NORTHWESTERN UNIVERSITY

Optically-Active Microcrystals and Devices through DNA-Programmable Assembly

A DISSERTATION

SUBMITTED TO THE GRADUATE SCHOOL

IN PARTIAL FULFILLMENT OF THE REQUIREMENTS

For the degree of

DOCTOR OF PHILOSOPHY

Field of Materials Science and Engineering

by

Lin Sun

EVANSTON, ILLINOIS

September 2020

ABSTRACT

Optically-Active Microcrystals and Devices through DNA-Programmable Assembly

Lin Sun

Colloidal crystals are promising candidates for nanophotonic applications due to their strong interactions with light and the capability to tailor such interactions through crystal design and engineering. DNA-programmable assembly, in particular, allows for precise structural control down to the sub-nanometer length scale. In this thesis, ways of designing, synthesizing, and utilizing DNA-assembled crystals as optical devices or components are presented.

Chapter 1 provides a brief overview of the uses of DNA-programmable assembly in nanophotonics, with a focus on how its control over crystal structure parameters makes it attractive for optical microdevice designs. Chapter 2 shows how such control can be exploited to study and determine the effects of nanoscale structure and lattice parameters on the light-matter interactions in colloidal crystals. Specifically, a comparison of the macroscopic optical properties of crystals with the same *bcc* lattice symmetry and macroscopic rhombic dodecahedron crystal habit but composed of octahedral and spherical nanoparticles, respectively, is provided. The first use of DNA-assembled crystals in making photonic crystals is presented and discussed in Chapter 3. The use of DNA molecules as spacer groups is a novel design parameter for photonic crystals, and a new set of design rules have emerged through simulations, which are detailed in this chapter. Importantly, a crystal composed of cubic nanoparticles is made according to these design rules, and it shows a broad reflectance stopband in the red and infra-red region, which underscores the advantages and utility of using DNA-programmable assembly techniques to make the photonic

crystals predicted by simulation. While the above two applications have benefited from the structural control at the nanoscale, control of mesoscale structural parameters, such as crystal orientation, size, shape and location on a substrate is equally crucial for integrating DNA-assembled crystals into devices. Chapter 4 describes a method for controlling colloidal crystal size and shape through the use of lithographically defined patterns to guide DNA-mediated assembly. Through a layer-by-layer assembly process on designated areas, the crystal's two-dimensional size and shape and height in the third dimension can be precisely controlled. Chapter 5 reports the incorporation of two-dimensional nucleation interfaces on a substrate to guide DNA-mediated nanoparticle crystallization into arrays of Wulff-shaped constructs with their orientation, shape and location dictated by the design of the interface. This unprecedented level of structural control is a significant step towards realizing complex, integrated devices based upon colloidal crystals. Finally, a brief conclusion and future outlook are given in Chapter 6. Taken together, the work reported in this dissertation has expanded the scope and capabilities of using DNA-programmable assembly in optical device fabrication.

Thesis Advisor: Professor Chad A. Mirkin

ACKNOWLEDGEMENTS

No success is achieved alone. And this is especially true for my graduate studies. This thesis would not have been possible without all the guidance, help, support and companionship I have received over the years. There are many people to whom I am eternally grateful.

I would first like to thank my advisor, Professor Chad A. Mirkin. It was a great honor to work with and learn from him. Chad has taught me the importance of asking meaningful questions, the ability to think critically about my own work and the work of others, the savviness to identify the key messages in projects, and the skills to communicate my work in an accessible and clear way. I am also grateful for the efficient environment that he has created, where I was given a tremendous amount of freedom to pursue my interests. My thesis work has been a wild blend of simulation, synthesis and characterization, and the group has never failed to provide the resources I need, including talented collaborators and state-of-the-art instrumentats. Chad's achievements have always served as a source of inspiration to me and many others, and working with him has encouraged me to believe in myself and strive for the best. I really value the lessons I have learned as his student, which I will carry with me for the rest of my career.

I am also grateful to Professor George C. Schatz, from whom I have received tremendous amount of guidance and support over the years. George not only has been a collaborator and a member of my thesis committee, but he has also been a second advisor to me. Thanks, George for always being accessable and supportive. Your endless curiosity is truly inspiring. I would also like to thank my other two committee members, Professor Teri W. Odom and Vinayak P. Dravid, for their valuable feedback and suggestions over the years.

Keeping such a large group well-functioning is no small task, and for that I am grateful to the current and previous office staff in the Mirkin lab: Dr. Sarah Hurst Petrosko, Dr. Sara M. Rupich, Dr. Tanushri Sengupta, Pamela Watson, Elizabeth Forest and Dr. Caroline Ko. Thank you all for keeping the group running smoothly.

Throughout my time at Northwestern, I worked closely with Dr. Haixin Lin. Haixin has always amazed anyone who has worked with him with his intellectual vigor. Moreover, he has always impressed me with his passion for science and attention to details. I am grateful for his wisdom with regard to both research and life issues. I have no doubt he will continue doing phenomenal work as a professor. I am also extremely grateful to my other two mentors, Dr. Daniel Park and Dr. Jessie Ku. Daniel recruited me into the group and taught me everything I needed to know to start my research in optics. Some of my work was made so much easier thanks to the simulation and experimental protocols that he established. Jessie taught me all of the basics about DNA-programmable assembly and inspired me to always think critically about the experiments I planned to do. Other collaborators include Dr. Michael B. Ross, Marc R. Bourgeois, Dr. Kevin Kohlstedt, Dr. Shuanzhi Wang, Wenjie Zhou, Jingshan Du, Yuanwei Li and Yueh-te Chu. I am so grateful to have worked with all of you.

My work would not be possible without all the state-of-the-art instrumentation and world-class support from the EPIC facility of Northwestern University's *NUANCE* Center and the Center for Nanoscale Materials (CNM) of Argonne National Laboratory. Special thanks goes to Dr. David Czaplewski and Dr. Ralu Divan from CNM for their training and guidance pertaining to nanofabrication.

I also made many friends while at Northwestern, who make for the best memories I have from the university. Thank you, Abha Gosavi, Jennifer Ferrer, Ran Li, Weizi Yuan, Yaoyao Chen, Yue Yin, Min Zhang, Xiankai Yu, Yeguang Xue, Jiazhen Chen, Haoxiang Yang, Liangjie Wu, Boran Ma, Wuliang Zhang, Mary Wang, Eileen Seo, Lam-Kiu Fong, Monica Guan, Youngeun Kim, Shuya Wang, Ziyin Huang, Qingyuan Lin, Pengcheng Chen and Taegon Oh. A special shout out tgoes o my roommate Tingting Liu, who beared with my nervous pacing, shower singing and exotic cooking in the time of lock-down. I'm really grateful to all of you for weathering through the ups and downs with me.

Last but not least, I thank my parents, who have always supported my decisions, even though it sometimes puts them through agony. It is truly amazing to have people who put my happiness and wellbeing above everything else in the world, and I am forever indebted to them for that. Thank you, mom and dad, for your unconditional love and unwavering support.

LIST OF ABBREVIATIONS

bcc	Body-Centered Cubic
CCD	Charge-coupled Device
DBR	Distributed Bragg Reflector
EMT	Effective Medium Theory
FDTD	Finite-difference Time-domain
FIB	Focused Ion Beam
GISAXS	Grazing-Incidence Small-Angle X-ray Scattering
HPLC	High-Performance Liquid Chromatography
LSPR	Localized Surface Plasmon Resonance
ML	Machine Learning
NP	Nanoparticle
PAE	Programmable Atom Equivalent
PC	Photonic Crystal
PDMS	Poly(dimethyl siloxane)
PPC	Plasmonic Photonic Crystal
QD	Quantum Dots
RIE	Reactive Ion Etching
SAXS	Small-Angle X-ray Scattering
sc	Simple Cubic
SEM	Scanning Electron Microscopy
SPP	Surface Plasmon Polariton
TEM	Transmission Electron Microscopy
TMM	Transfer Matrix Method
UCNP	Upconversion Nanoparticle
UV-Vis	Ultraviolet-visible

TABLE OF CONTENTS

LIST OF FIGURES

Figure 5.3. Crystal orientation is affected by both pattern orientation and strain in the [001] orientation. (a) Schematic illustration of the patterns and (b) the corresponding SEM images of crystals assembled on such patterns. The numbers on the top indicates the lattice constant (ap) in nm for each pattern design. The upper and lower rows of the patterns both have (001) lattice arrangement but are 45 degrees rotated with respect to each other, resulting in 45 degree rotation of the corresponding crystals with respect to each other, as shown in SEM images. The white square highlights the range into which lattice constants measured with crystals assembled free in solution (ai) fall, namely the range of ap that results in the least amount of strain. At smaller ap, and therefore lager compression strain, the crystals are rotated 45 degrees, which is separated by the black dashed line. (c-f) Detailed analysis of crystal grown on pattern with 60 nm lattice constant (ap) and 45-degree in-plane rotation. Top-down images of crystals before (c) and after (d) FIB cross-sectioning show that the cut is made along 45-degree in-plane direction. The crystals are tilted around 75 degrees from the top in order to observe the sectioned surface (e) and a corresponding drawing of the top layer of nanoparticles (f) are shown for comparison. (g-j) The same set of result for crystal grown on pattern with 75 nm lattice constant (ap) and 45-degree in-plane rotation. Top-down images of crystals before (g) and after (h) FIB cross-sectioning show that the cut is made along 45-degree in-plane direction. The crystals are tilted around 75 degrees from the top in order to observe the sectioned surface (i) and a corresponding drawing of the top two layers of nanoparticles (j) are shown for comparison. All

LIST OF TABLES

CHAPTER ONE

Overview of Fundamental Optical Studies of Single Crystalline Superlattices

1.1 Colloidal Crystals in Nanophotonics Applications

Nanophotonics have been actively researched due to the need to manipulate light beyond the diffraction limit in a wide range of technical applications, including optical integrated circuits, sensing, energy materials and nonlinear optics.[1] One effective approach for realizing sub-wavelength light manipulation is through noble metal nanoparticles (NPs), where light is confined to the vicinity of the NP through its localized surface plasmon resonance (LSPR).[1-6] Moreover, the LSPR can be effectively tuned by NP size, shape and composition.[7-10] Because of its ability to confine light into small volume and our ability to dictate the light-matter interaction as a result of the development of NP synthesis, plasmonic NPs have played a major role in a wide range of nanophotonics studies.[1, 11]

Besides the properties of a plasmonic NP, its dielectric environment and proximity to other plasmonic NPs can also impact the optical behavior significantly.[12] Moreover, photonic modes can arise in periodic structures or micron-sized cavities composed of plasmonic NPs.[13] Thus, realizing precise structural control is equally, if not more crucial to understanding and manipulating light-matter interaction at both the nanoscale and the microscale, in order to realize nanophotonic devices with plasmonic NPs.

1.2 Unique Advantages of DNA-Assembled Crystals in Nanophotonics

DNA-programmable assembly has been shown to be a robust way to build lattice structures of NPs with precise control over the structural properties on both the nano- and micro-scale (Figure 1.1) .[14] On the nanoscale, a wide variety of NPs size, shape, and composition can be used.[15, 16] In particular, more than 10 nanoparticle composition has been used as building blocks for DNA-programmable assembly. Different nanoparticle composition would provide additional

functionalities, such as magnetic, dielectric and excitonic properties. Moreover, the interparticle distance can be changed by changing the number of base pairs in the DNA linker strands.[16] On the microscale, various lattice symmetry and crystal habit can be designed.[16-19] This high tunability and precise control over the structural parameters of assembled superlattices has rendered DNA-programmable assembly an attractive way to build a new class of optical materials. These materials serve as an ideal system for systematic investigation of the structure-function relationship in an optically complicated system where plasmonic, excitonic, and photonic modes interact in a single cavity.[8, 20] The knowledge can then be used to inform rational design of technologically relevant optical metamaterials.

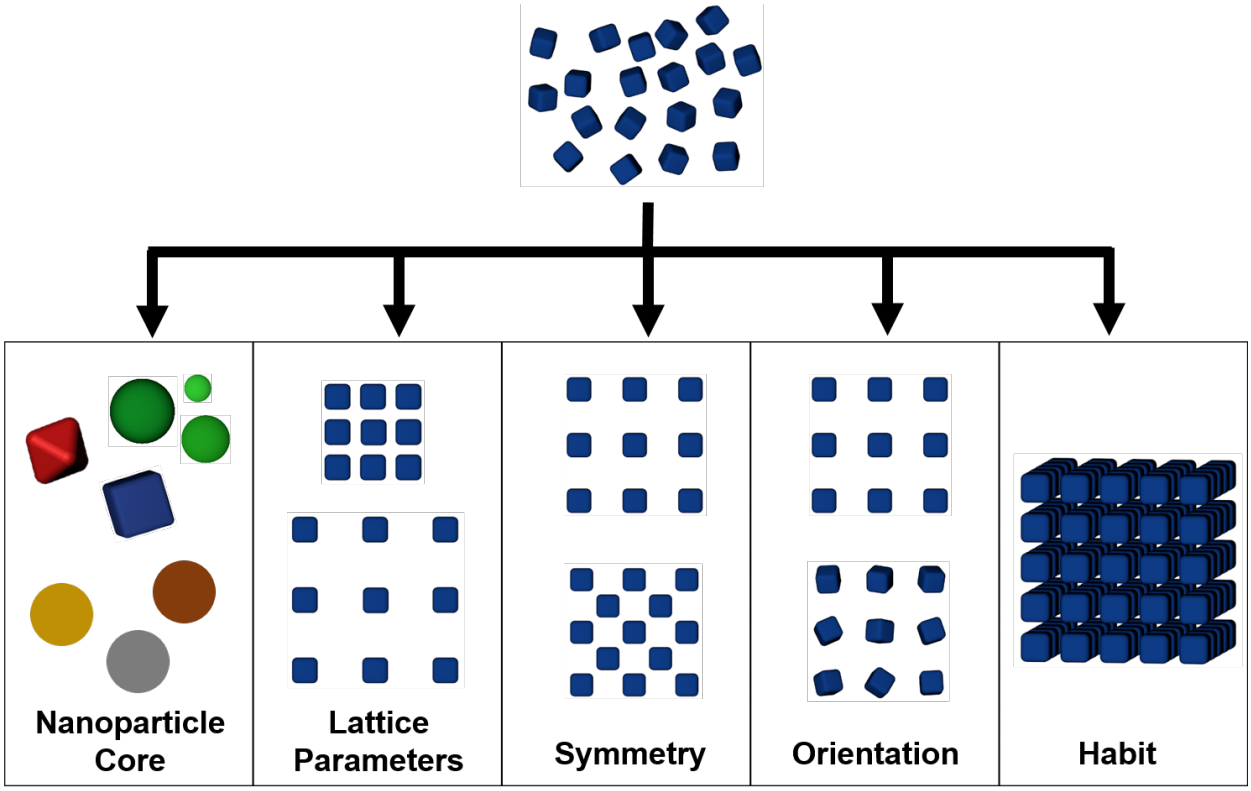

Figure 1.1. Schematic showing the different aspects of structural control attainable by DNA-programmable assembly.

Indeed, previous work explored the optical properties inside a single-crystalline rhombic dodecahedral DNA-assembled crystals composed of spherical gold (Au) NPs, with a particular focus on the interplay between plasmonic and photonic properties.[20] This pioneering work laid ground for using DNA-programmable assembly to make optical functional materials and initiated a rational approach to the structure-function establishment. Subsequently, empowered by the versatile assembly capabilities, a wide variety of properties and potential applications were investigated, including the effect of defects[21], plasmonic NP composition[22] and crystal habits[23].

1.3 Thesis Overview

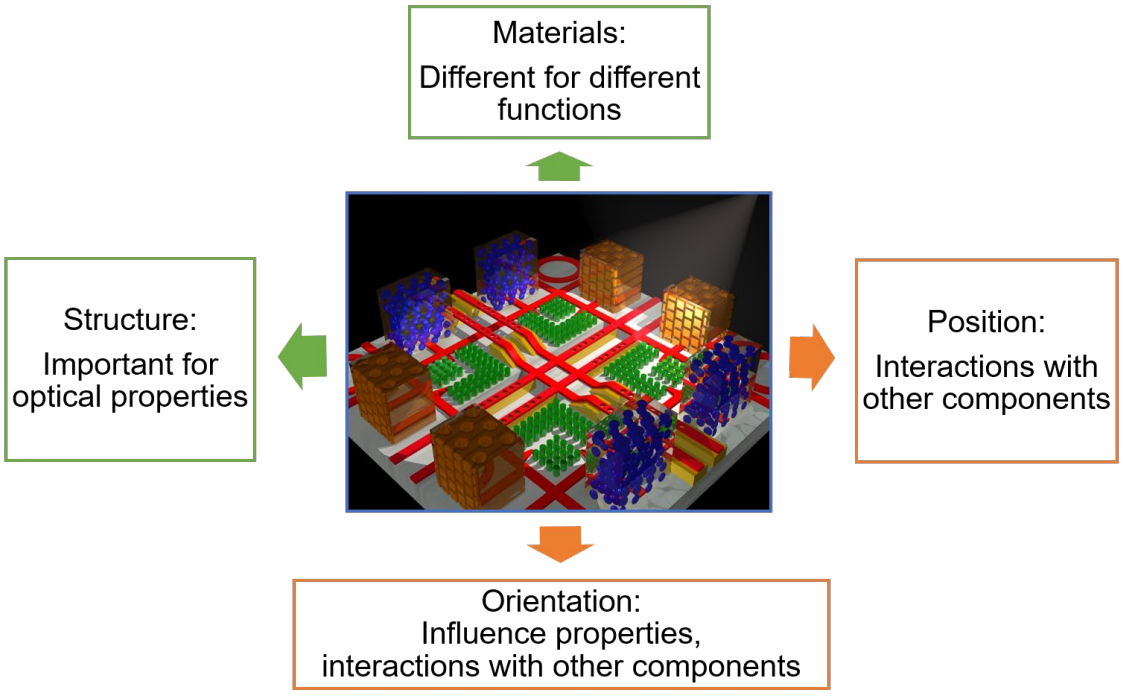

Figure 1.2. Overview of the structural control needed for optical integrated device fabrication. As highlighted in the green rectangles, DNA-programmable assembly has achieved precise structural control at the nanoscale, including control over the building block materials and lattice symmetry and constant. However, position and orientation of the superlattices (highlighted in orange rectangles) are yet to be achieved.

Albeit groundbreaking, all the above-mentioned work used spherical plasmonic NPs as building blocks and huge potential remains untapped. For examples, anisotropic NPs are often perceived to have better optical properties due to a stronger field confinement and polarization dependent properties.[24] Thus, a main part of this thesis addresses the optical properties that can be achieved via crystals composed of anisotropic NP building blocks. In Chapter 2, polarization-dependent optical properties of micro-crystals made with octahedral NPs were found to be a manifestation of individual NP anisotropy and the robustness of DNA-programmable assembly in arranging both NPs position and alignment. Chapter 3 illustrates an example of a simulation-driven approach for predicting and designing 3D photonic crystals. The results from our simulation is then corroborated by experimental demonstration, where cubic NPs were used to form a simple cubic lattice with predicted photonic stopband.

Another important direction is to further improve the structural control accessible to the DNA-programmable technique in order to allow fabrication of sophisticated materials and devices by design. The majority of research in the field has been done on lattices formed freely in solution, and great control over the nanoscale properties such as NP composition and lattice constant has been achieved. However, there is little control over mesoscale properties, such as the crystal orientation and location on a substrate (Figure 1.2). These control are especially important if sophisticated devices are desired, where individual elements need to not only perform their own functionality but also communicate with other elements. Thus, the other focus of this thesis is to explore and establish processes that allows such control (Chapter 4 and 5).

CHAPTER TWO

Polarization-Dependent Optical Response in Anisotropic Nanoparticle–DNA Superlattices

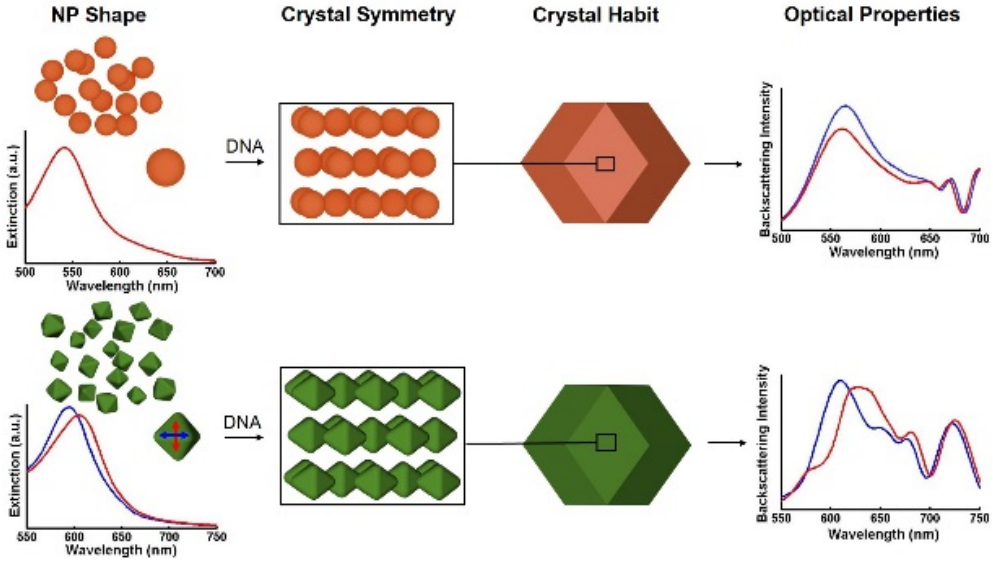

Note: Portions of the material in this chapter is published in the following article: Polarization-dependent optical response in anisotropic nanoparticle–DNA superlattices, *Nano Letters* **2017**. *4*, 2313-2318.
The article can be found on this link: https://pubs.acs.org/doi/abs/10.1021/acs.nanolett.6b05101.
Further permissions related to the material excerpted should be directed to the ACS
This work was done in collaboration with Dr. Haixin Lin, Dr. Daniel J. Park, Marc R. Bourgeois, Dr. Michael B. Ross, Dr. Jessie C. Ku and Dr. George C Schatz.

2.1 Abstract

DNA-programmable assembly has been used to prepare superlattices composed of octahedral and spherical nanoparticles, respectively. These superlattices have the same bcc lattice symmetry and macroscopic rhombic dodecahedron crystal habit but tunable lattice parameters by virtue of the DNA length, allowing one to study and determine the effect of nanoscale structure and lattice parameter on the light-matter interactions in the superlattices. Backscattering measurements and finite-difference time-domain simulations have been used to characterize these two classes of superlattices. Superlattices composed of octahedral nanoparticles exhibit polarization-dependent backscattering, but via a trend that is opposite to that observed in the polarization dependence for analogous superlattices composed of spherical nanoparticles. Electrodynamics simulations show that this polarization dependence is mainly due to the anisotropy of the nanoparticles, and is observed only if the octahedral nanoparticles are well-aligned within the superlattices. Both plasmonic and photonic modes are identified in such structures, both of which can be tuned by controlling the size and shape of the nanoparticle building blocks, the lattice parameters, and the overall size of the three-dimensional superlattices (without changing habit).

2.2 Introduction

Gold nanoparticles (NPs) are widely studied optical building blocks due to their strong interactions with visible light, which is confined into small volumes close to the NP surface due to localized surface plasmon resonance (LSPR) excitation.[1-6] The LSPR is sensitive to NP size, shape, composition, dielectric environment, and proximity to other plasmonic NPs.[7-10] Ordered arrays and other structures of plasmonic NPs exhibit a variety of interesting properties, such as the ability to guide light around sharp corners,[25] a broadband optical response,[26] Fano resonances,[27] and a negative index, which is important for the development of metamaterials.[28] Moreover, the optical properties of such ordered plasmonic structures can be tuned by changing the distance between individual NPs.[7-9, 29, 30] Therefore, great effort has been devoted to research on making two- and three-dimensional periodic structures of plasmonic NPs using top down[25, 26, 28] and bottom up[10, 31-33] techniques.

DNA-programmable assembly has emerged as a robust and flexible tool for synthesizing superlattices with control over NP size and shape, lattice structure, and crystal habit. In these structures, nanoparticles with different shapes,[15, 34] sizes,[16] and compositions[22, 34, 35] can be assembled, and also lattice symmetry and nanoparticle spacing can be tuned,[16, 18] giving rise to robust[36] and compositionally tunable thin film optical modes.[22] In addition, the micron length scales associated with well-formed superlattices lead to optical cavity modes, such as FP resonances[20] that arise due to interference of light travelling between the parallel top and bottom facets of the superlattice,[20, 37] and shape dependent scattering[23] that is dictated by the crystal habit (*i.e.* the size and shape of the micro- or macroscopic superlattice). In principle, one can uniquely use DNA-programmable methods to assemble different NP building blocks into macroscopic

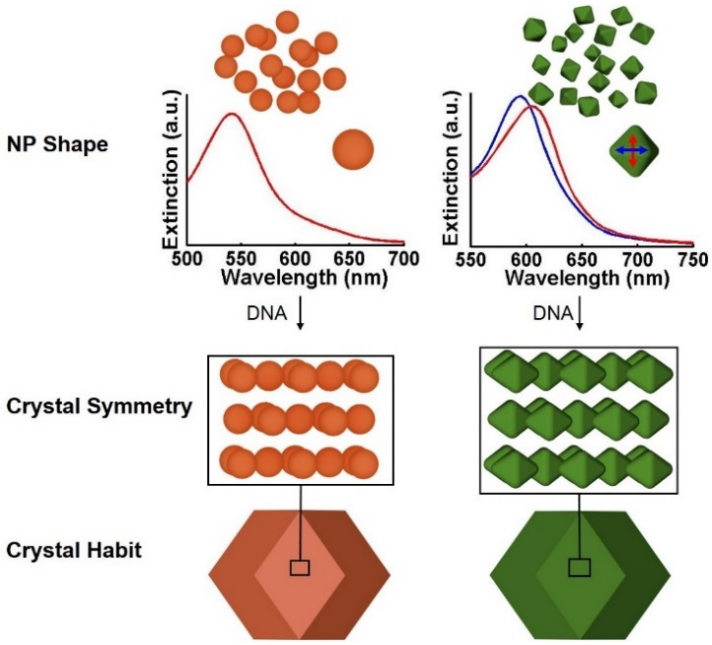

Figure 2.1. Schematic depiction of the structure of superlattices made from both spherical (orange) and octahedral (green) NPs. The shape of the NPs gives rise to different polarization dependence of their LSPRs. Both superlattices have bcc lattice structures and the exposed facets are the closest packed (110) planes for the rhombic dodecahedral crystal habit. Single nanoparticle extinction spectra were obtained from FDTD calculations with the refractive index of the dielectric environment set as 1.45. Note that different wavelength ranges are used in the spectra.

superlattices where the superlattices have the same crystal symmetry and macroscopic crystal habit, but that comprise different NP shapes. This type of comparison enables separation of the effect of NP shape from the effects of lattice symmetry and microscale faceting.

Herein, we show that octahedral and spherical NPs can be assembled into body-centered cubic (bcc) superlattices with identical rhombic dodecahedra crystal habits and similar lattice parameters, but different optical properties (Figure 2.1). These superlattices have been characterized by backscattering measurements and finite-difference time-domain (FDTD) simulations. In addition to focusing on the importance of the shape of the NPs, we can also use simulations and, in certain cases, experiment to independently assess the importance of lattice parameter and size of the microscale superlattices on optical response. Therefore, this DNA-programmable technique allows

one to disentangle contributions of the nanoscale building blocks from the microscale architecture to the optical properties of the superlattice. Importantly, superlattices composed of octahedral NPs exhibit polarization-dependent backscattering spectra at all volume fractions studied (5.1% - 20.3%), while the opposite polarization dependence behavior is seen in superlattices comprised of spherical NPs with volume fractions larger than 10%. Finally, it was found that the orientation and alignment of the NPs inside each superlattice is crucial for observing such polarization-dependent behavior.

2.3 Results and Discussion

We begin by using optical simulations to probe different types of resonances in the superlattices. Previous work done by our group has shown that both plasmonic modes and FP type photonic modes exist and interact in superlattices comprised of spherical NPs (Figure 2.2A).[20] These two types of modes couple strongly to each other, leading to band-gap behavior in some cases.[20, 38] Here, FDTD simulations with an infinite slab model were used to approximate the optical properties of the superlattices. This model matches well with the experimental setup, which is described in detail in the methods section. Two polarizations, 0º and 90º (perpendicular and horizontal to the long axis of the rhombic dodecahedron, respectively), are used to characterize the light polarization (Figure 2.2A).

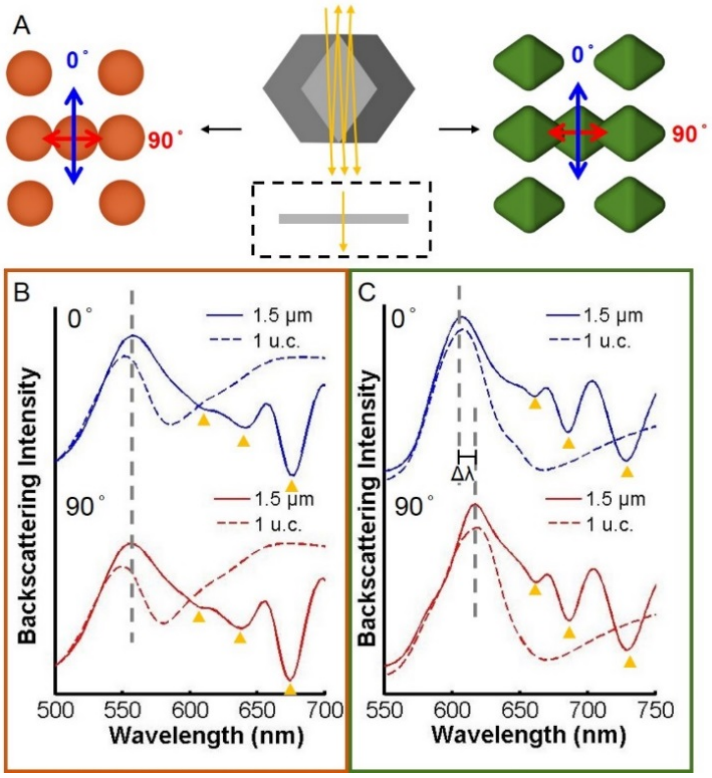

Figure 2.2. The optical modes of the superlattice consist of both plasmonic and FP modes. The roles of each mode are shown in the backscattering spectra. (A) Schematic depiction of the superlattice where both plasmonic and FP modes exist, in comparison to a thin slab with a thickness of only 1 u.c., which is too thin to support FP modes (center). Structures of a single unit cell of superlattices made from spherical (left) and octahedral (right) NPs along the (110) direction are shown, with the 0º and 90º indicating the corresponding polarizations of the incident light. (B) FDTD simulation of a spherical superlattice with the polarization along 0º (top, solid line) and 90º (bottom, solid line) as defined in (A). The grey dashed line indicates the maximum wavelength of the main peaks, which is the same for the two polarizations. The blue and red dashed lines are the spectra of the 1 u.c. thick slab, which shows that the location of the main peak is determined by the plasmonic modes. The dips at longer wavelength, as indicated by the yellow arrows, are FP modes. (C) The same simulations were performed for superlattices made from octahedral NPs, where there is a difference ($\Delta\lambda \sim 10$ nm) between the main peaks of the two polarizations.

Importantly, the LSPRs of the octahedral NPs along 0º and 90º are different due to anisotropy of the NP shape (shape anisotropy, Figure 2.1). In addition, the top and bottom facets of the superlattice adopt the (110) plane of the bcc lattice structure,[17] resulting in a smaller interparticle spacing between NPs in 90º compared to 0º. The anisotropy in the lattice structure (structure

anisotropy) would result in different interparticle interactions that depend on polarization, even for superlattices comprised of spherical NPs – with sufficient volume fractions – where the NP shape anisotropy is absent. The solid lines in Figures 2.2B-C show the simulated backscattering spectra of superlattices made from spherical and octahedral NPs, respectively. The average diameter of the spherical NPs is 40 ± 3.2 nm, while the edge length of octahedral NPs is 51 ± 2 nm. Tips of the octahedral NPs are rounded with an average radius of curvature of 4.8 ± 0.5 nm, a value determined from scanning electron microscopy (SEM) images of the as-synthesized NPs used in the experiments (Figure 2.5). These NP structural parameters are kept constant throughout this work. The interparticle spacing, defined as the NP surface-to-surface distance along the 90º direction, is 40 nm, and the thickness of the slab is set to be 1.5 μm. These parameters are set such that they fall within a range that can be realized experimentally.[16, 39-42]

The simulated spectra exhibit a convolution of plasmonic and FP modes, however, the influence of nano and micro-scale structure can be disentangled (Figure 2.2). FP modes are purely photonic modes that are determined by superlattice thickness and effective refractive index within the cavity. Therefore, we eliminate FP modes by simulating a 1 unit cell (u.c.) thick superlattice, where the superlattice is optically too thin to support any FP modes- such a structure should only exhibit the optical response of the plasmonic nanoparticles.[23] Indeed, only one peak is observed for the 1 u.c film (dashed lines, Figures 2.2B-C). Moreover, this peak is spectrally close to the main peak found in the thicker samples (1.5 μm). Therefore, the main peak in these figures is primarily determined by the plasmonic properties of a single layer of NPs, while the dips at longer wavelengths are from FP modes (orange arrows, Figures 2.2B-C).

From these simulations, we find that for the superlattices with spherical NPs there is negligible difference between the main peaks, namely the backscattering maximum around 560 nm, along the 0º and 90º polarizations. However, for the superlattices with octahedral NPs the main peak at around 610 nm red-shifts by $\Delta\lambda \sim 10$ nm when the polarization is aligned along 90º compared to 0º. This difference suggests the crucial role that shape anisotropy plays. Notably, Maxwell-Garnett effective medium theory (EMT), which has been used to quantitatively explain a variety of optical properties in spherical nanoparticle based superlattices,[20-22, 24] can no longer be applied to the superlattice made from octahedral NPs.

To experimentally demonstrate the different responses to the two polarizations in the two types of superlattices, spherical and octahedral NPs were assembled into bcc lattices with a rhombic dodecahedral crystal habit and ~2 μm parallel face-to-face dimensions (Figure 2.1). In particular, the directional DNA interaction will align octahedral NPs in a face-to-face manner,[15] as can be seen in the schematic drawing of a single unit cell superlattice in the (100) orientation (Figure 2.6A). After the assembly, the superlattices undergo a silica embedding process in order to preserve their structure in the solid-state,[43] enabling optical measurements and electron microscopy imaging. Small angle X-ray scattering (SAXS) was used to extract information on the crystal structure and lattice constant (in the solution- and in the solid-state), as well as to ensure their high crystallinity (Figure 2.6).

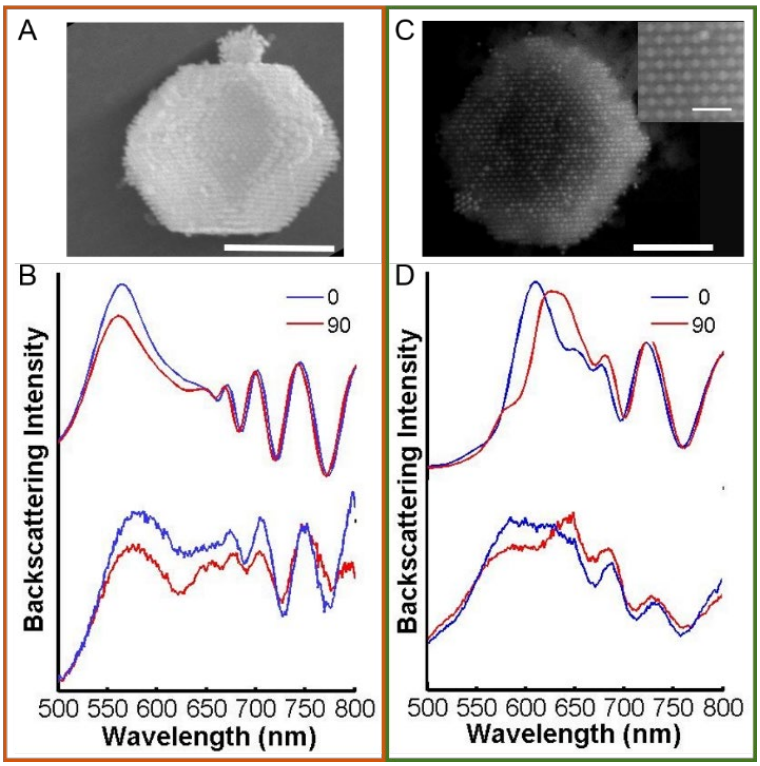

Figure 2.3. Experimental confirmation of the absence and presence of polarization-dependence in superlattices comprised of spherical and octahedral NPs, respectively. (A, B) SEM image of a superlattice consisting of spherical NPs and its backscattering spectra obtained from simulation (top) and experiment (bottom). (C, D) The same set of data for a superlattice consisting of octahedral NPs. Inset in (C) is a magnified area of the SEM image. The interparticle spacings are 29 and 37 nm for superlattices made of spherical and octahedral NPs, respectively. Scale bars are 1 μm for (A) and (C), and 200 nm for inset in (C).

Backscattering measurements were performed on these superlattices with a microscope-coupled spectrometer (see section 2.5.5 for more information). Figures 2.3A,C are SEM images of typical superlattices made from spherical and octahedral NPs, respectively, where the lattice constants, as measured by SAXS, are 69 and 102 nm, respectively. As such, the interparticle spacing is 29 nm for the spherical NPs and 37 nm for the octahedral NPs. The good agreement between simulation (top) and experiment (bottom) for both superlattices, Figures 2.3B,D, validates both the simulation model and the high quality and fidelity of the DNA-programmed NP

superlattices. Polarization dependence is primarily observed for the main peak as dictated by nanoscale effects, such as NP shape – which controls the LSPR – and structure anisotropy of the lattice – which affects particle-particle coupling. At wavelengths far from the main peak, both simulation and experiment show a much smaller difference between the FP modes at the two polarizations.

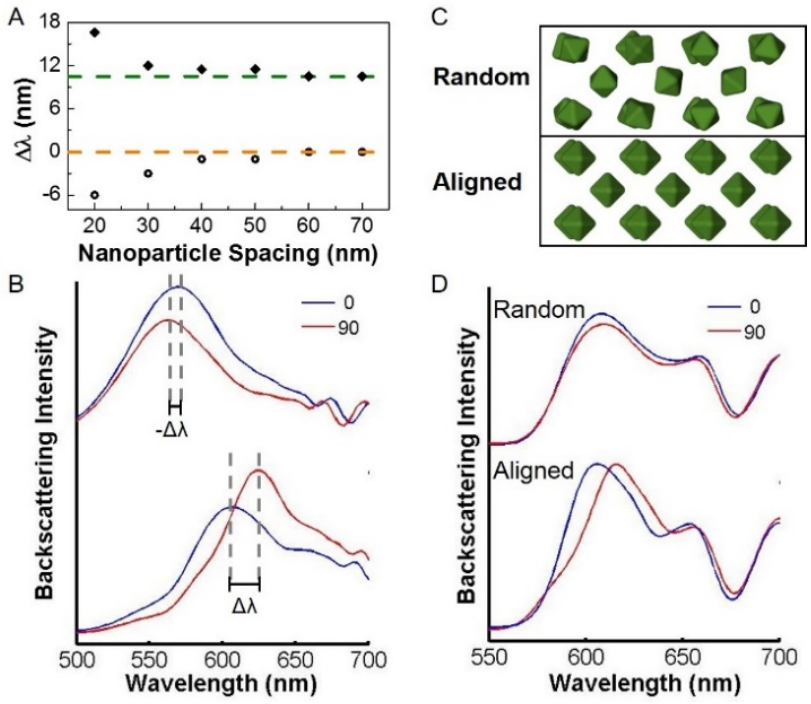

Figure 2.4. The effect of structural and NP shape anisotropy and NP alignment on polarization dependence. While keeping the NP size and shape the same, simulations show the effect of changing the interparticle spacing from 20 to 70 nm for spherical and aligned octahedral NPs. Differences between maxima of the main peaks at 90º and 0º polarization (Δλ) for all superlattices are summarized in (A). (B) Simulated spectra of spherical and aligned octahedral NPs with 20 nm interparticle spacing. Interestingly, for the superlattices consisting of spherical NPs, the peaks blue-shift at 90º compared to 0º, resulting in negative Δλ values as marked by the –Δλ. The opposite happens for the superlattices consisting of octahedral NPs. (C) In order to show the importance of alignment of the NPs, a set of simulations was set up with same set of parameters but for randomly oriented (top) and well-aligned (bottom) NPs. Interparticle spacing here is 70 nm. (D) The backscattering spectra from the set up in (C). The polarization dependence is lost in the former case.

To explore the effect of both shape and structure anisotropy, a set of superlattices where the interparticle spacing is varied from 20 to 70 nm and the superlattice thickness is held constant at 1.5 μm were simulated. Figure 2.4A summarizes the difference between the main peak along the 90º and 0º directions – namely, $\Delta\lambda = \lambda_{max}^{90} - \lambda_{max}^{0}$. A spectral representation can be seen in Figure 2.4B, where the backscattering spectra of superlattices made from spherical (top) and octahedral (bottom) NPs with 20 nm interparticle spacing are plotted. In contrast with the polarization-dependent red shift as seen in the superlattices with octahedral NPs, the main peak blue shifts when the polarization is changed from 0º to 90º in the superlattices with spherical NPs, resulting in negative values of Δλ. In fact, as the interparticle spacing decreases, λ_{max} along both 0º and 90º are red-shifted, though the shift is more significant along 0º for superlattices made of spherical NPs (Figure 2.12). This red-shift with decreasing NP separation is routinely observed and attributed to enhanced interparticle coupling.[8, 44, 45] However, the opposite trend (blue-shifting) is observed for the polarization dependence, by which we mean that although the NPs are more closely spaced (smaller interparticle spacing) along the 90º direction, λ_{max}^{90} is to the blue of λ_{max}^{0} for spherical NP superlattices.

Evidently, in this case, long-range coupling between many NPs plays an important role, necessitating explicit consideration of the dipole lattice sum. Under the assumption that each NP can be considered as a point dipole, this sum describes the near- and far-field coupling between NPs and is solely dependent on the geometric parameters of the lattice (i.e., the arrangement of the NPs). Section 2.6.2 provides details of the lattice sum approach, here presented in the context of a coupled dipole method that uses the modified long-wavelength approximation (MLWA) to describe particle polarizabilities.[46, 47] Applying this method to calculate the extinction spectra for

a (110) bcc lattice plane along 0º and 90º (Figure 2.7) shows that the blue-shift seen in superlattices made of spherical NPs is due to the difference in the lattice sums for the two polarization directions.[8, 9, 48] As the interparticle spacing increases (>60 nm), negligible polarization dependence is observed (Figure 4A), and the dipole lattice sums and extinction spectra (Figure 2.13) show that this is due to the smaller difference in the lattice sums along the different polarization directions for this spacing. Likewise, the larger red-shifts of λ_{max}^{0} compared to λ_{max}^{90} as the interparticle spacing decreases can be attributed to a larger difference in the lattice sums along the two polarizations.

For superlattices made of octahedral NPs, λ_{max}^{90} is to the red of λ_{max}^{0}. Although the dipole lattice sum is the same for the same NP arrangement, compared to the case of superlattices made of spherical NPs, octahedral NPs have different effective polarizabilities (α) along the different polarization axes. Larger values of α along the 90º (tip-to-tip) will result in a reduced (1/α) which would then intersect the dipole lattice sum at larger wavelength (Figure 2.9), which red-shifts the resonance position (λ_{max}). In other words, a stronger tip-to-tip coupling along 90º contributes to a more significant red-shift compared to edge-to-edge coupling along 0º as the interparticle spacing become small (Figure 2.16). As the interparticle spacing decreases, large plasmonic coupling plays an especially important role in the large red-shift observed in λ_{max}^{90}.

As a result, the effect of structure anisotropy (i.e. different dipole lattice sums) on the polarization dependence becomes significant for both superlattices made of spherical and anisotropic NPs, respectively, at close distances (Figure 2.4A), with Δλ becoming non-zero even for spherical NPs. The same trends are also demonstrated experimentally (see details in 2.6.6). From these data, we conclude that structural anisotropy is important only in close packed

superlattices (interparticle spacing < 40 nm, see Figure 2.10-2.12),[7, 21] while at larger interparticle spacings, the polarization dependence and lack thereof are determined by the NP shape anisotropy.

So far, the interparticle spacing of superlattices comprised of octahedral NPs that can be realized by DNA-mediated assembly falls within a region where the effect of NP shape anisotropy dominates, namely larger interparticle spacing. It is likely that alignment of the NP building blocks is necessary in order to achieve polarization-dependent far-field properties. The effect of NP alignment can be easily probed by simulation where the local orientation of the NP can be randomly varied while the location within the lattice symmetry and spacing remains fixed (Figure 2.4C). The results are then averaged over 10 randomized systems, similar to a model used previously to explore structural variation in spherical NP experiments, which provided strong agreement with experiment.[21] In order to prevent nearest neighbor NPs from touching each other in fully random orientations, a larger lattice constant, 135 nm, must be used, which corresponds to 70 nm interparticle spacing in the aligned superlattice. The results in Figure 2.4D illustrate that with larger interparticle spacing the polarization dependence is no longer observed for the randomized orientation superlattice. In other words, alignment of the NPs in the superlattice is necessary to generate a polarization-dependent plasmonic response, especially for larger interparticle spacing.

2.4 Conclusion

In conclusion, this work shows how one can uniquely use DNA-programmable assembly with electrodynamics simulations to interrogate specific structure-function relationships in well-defined microscopic crystals. The methodology allows one to focus on one set of parameters, isolated in

large part from the others, including particle size and shape, lattice parameters, and crystal habit size. In this work, we have used it to identify a polarization dependence observed in lattices formed from spherical particles due to the bcc lattice symmetry, and a much stronger polarization dependence with lattices constructed from octahedral particles. The origin of this strong polarization dependence derives from both the shape of the octahedral particle building blocks as well as their arrangement into a well-defined lattice, where they are both positionally and rotationally ordered by virtue of DNA-programmed assembly. Moreover, the incorporation of anisotropic NPs introduces additional interesting features that were not accessible with spherical NP-based structures. Polarization-dependent properties associated with the superlattices derived from octahedral NPs open paths to polarization-dependent optical micro devices and electromagnetic field enhancement applications. As such, the robustness and tunability of DNA-programmable assembly coupled to the introduction of anisotropic NP building blocks further expands the platform of DNA-programmable assembly as a promising tool for a wide range of applications, spanning sensing, metamaterials, and micro-optical systems.

2.5 Methods

2.5.1 NP Synthesis

51 nm octahedral NPs were synthesized through iterative reductive growth and oxidative dissolution reactions reported previously.[49] The size of the NPs was determined by both the method outlined in ref. 1 and SEM images (Figure 2.5).

Citrate stabilized spherical NPs with a diameter of 40 nm from British Biocell International (BBI) were purchased from Ted Pella.

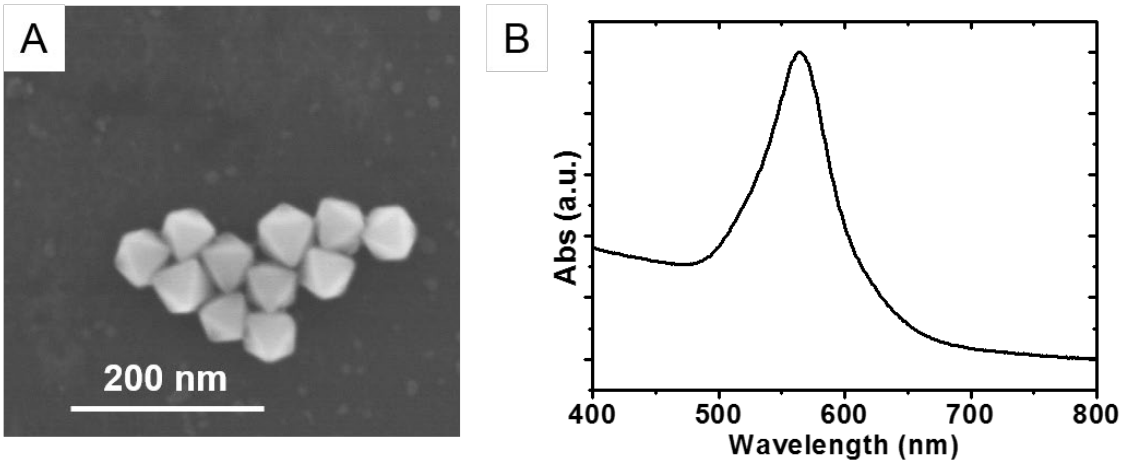

Figure 2.5. SEM image (A) and UV-Vis (B) spectrum of as-synthesized octahedral NPs. NPs were suspended in water during UV-Vis measurement.

2.5.2 DNA Synthesis and Design

All oligonucleotides used in this study were synthesized on a solid-support MM48 synthesizer (BioAutomation), where the reagents were purchased from Glen Research. Oligonucleotides with <70 bases were synthesized with a 5' trityl group and were purified with reverse-phase high-performance liquid chromatography (HPLC), followed by standard deprotection procedures. Longer oligonucleotides were synthesized without the 5' trityl group and were purified through polyacrylamide gel electrophoresis (PAGE). Details of these experiments can be found in the literature.

For octahedral NP assembly, self-complementary DNA strands were used.[39, 40] The DNA design composes two components, an "anchor" strand that attaches to the NPs through a gold-sulfur bond and a "linker" strand that on one end hybridizes to the "anchor" strand and on the other end, also called the "sticky end", hybridizes to a complimentary "linker" strand on a different NP. Table 2.1 summarizes the DNA sequences used for octahedral NP assembly. In order to vary the

DNA length, thus changing the interparticle spacing, one 40-base spacer block was added to the shorter "linker" strand ("d1") while two spacer blocks were added to the longer DNA design ("d2"). Each spacer block is duplexed with a complementary 40-base sequence ("duplexer") and separated by a single A "flexor".

Table 2.1. DNA design used for octahedral NP assembly. The 40-base spacer blocks are the segments in orange color. The duplexer strand is complimentary to each spacer block.

Name	Sequence (5' to 3')	Number of Bases
Anchor	TCA ACT ATT CCT ACC TAC AAA AAA AAA A C_6H_{12} SH	28
d1	GTA GGT AGG AAT AGT TGA ATT TTT TTT TTT TAC TGA GCA GCA CTG ATT TTT TTT TTT TTA GCG C	64
d2	GTA GGT AGG ATT AGT TGA ATT TTT TTT TTT TAC TGA GCA GCA CTG ATT TTT TTT TTT TTA TT TTT TTT TTT TAC TGA GCA GCA CTG ATT TTT TTT TTT TTA GCG C	105
40-base duplexer	AAA AAA AAA AAA ATC AGT GCT GCT CAG TAA AAA AAA AAA A	40

F or the spherical NP assembly, non-self-complementary DNA strands were used, as denoted by "A" and "B" in Table 2.1. Again, the anchor strands are attached to the spherical NPs onto which the corresponding linker, pre-hybridized to the duplexer strand, is hybridized.

Table 2.2. DNA design used for spherical NP assembly. Sp18 denotes Spacer Phosphoramidite 18, a commercially available hexaethyleneglycol phosphate spacer manufactured by Glen Research, which is compatible with conventional phosphoramidite DNA synthesis. Again the 20-base spacer region is colored in green.

Name	Sequence	Number of Bases
A anchor	TCA ACT ATT CCT ACC TAC $(Sp18)_2$ SH	18
B anchor	TCC ACT CAT ACT CAG CAA $(Sp18)_2$ SH	18
A linker	GTA GGT AGG AAT AGT TGA Sp18 TT ACT GAG CAG CAC TGA TTT Sp18 TTTCCTT	45
B linker	TTG CTG AGT ATG AGT GGA Sp18 TT ACT GAG CAG CAC TGA TTT Sp18 AAGGAAA	45
20-base duplexer	AAA TCA GTG CTG CTC AGT AA	20

2.5.3 NP Functionalization and Assembly

Octahedral NPs were functionalized in a solution with 0.5 M NaCl concentration according to methods described previously.[39, 40] NP concentration was determined by a Cary 5000 UV-Vis spectrometer (Agilent) and an appropriate ratio of DNA anchor strands was added. For octahedral NPs, after the NP functionalization, an excess amount of DNA linker strand is then added into the NP solution and the samples were annealed at 40℃ for 30 minutes to ensure hybridization. The solution was then cooled down to room temperature.

Spherical NPs were functionalized with thiolated anchor strands in an approximate ratio of 4 nmol per 1 mL NPs after which the NPs were salt aged to 0.5 M NaCl.[41] Excess DNA was removed with three rounds of centrifugation, after which, the NP concentration was determined with UV-Vis. 600 pre-hybridized linker strands per NP were then added.

After functionalization and hybridization, a slow-cooling process[17] was performed using a Veriti Thermal Cycler 96-well instrument (Life Technologies) at a cooling rate of 0.1°C/10 min from 65 °C to 25 °C such that single-crystalline rhombic dodecahedral superlattices are achieved.

After single-crystalline rhombic dodecahedral superlattices are synthesized, a silica embedding process was applied in order to transfer the superlattice into solid phase.[50] First, 2 μL of 3- (trimethoxysilyl) propyl acrylate (TMSPA, Gelest) was added to as-synthesized superlattice solution and vigorously stirred for 20 mins, before adding 4 μL of tetraethyl orthosilicate (TEOS, Sigma–Aldrich). The solution-based superlattices were then stirred for more than 12 hours upon the addition of TEOS. Finally, the superlattices was purified by several rounds of sedimentation, removal of supernatant and resuspension in water.

2.5.4 Superlattice Characterization

Silica-embedded superlattices were then examined by small angle X-ray scattering (SAXS) at Argonne National Laboratory's Advanced Photon Source. Information on the crystallinity and lattice structure can be understood, and its lattice constant *a* can be extracted, through the following formulas:

$$d_{110} = \frac{\lambda}{2sin\theta}$$

$$a = \sqrt{h^2 + k^2 + l^2}d = \sqrt{2}d_{110}$$

Here d_{110} is the spacing between (110) planes, λ is the X-ray wavelength, and θ is the scattering angle. Figure 2.6B shows the SAXS data of octahedral NP superlattices assembled by d1 or d2 DNA.

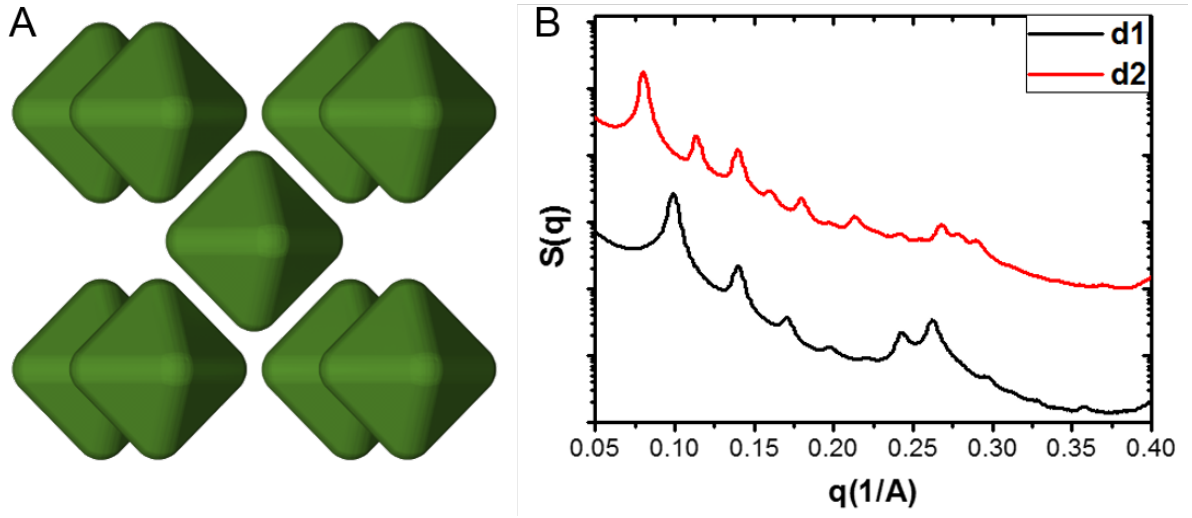

Figure 2.6. Schematic representation of a single unit cell of octahedral NP superlattice in the (100) orientation (A) and the SAXS data for the two samples used (B).

2.5.5 Optical Measurements

Silica embedded superlattices were first drop cast onto plasma cleaned Indium Tin Oxide (ITO) coated glass slides and the solvent was fully evaporated, this resulted in a population of superlattices with their top surfaces lying parallel to the substrate. Superlattices were then observed and located with both a Zeiss Axio Observer.Z1 microscope and a Hitachi SU8030 SEM to ensure proper orientation. A coverslip deposited with anti-reflection coating purchased from Evaporated Coatings Inc. is then fixed close to the sample by carbon tape at the corners. Subsequently, immersion oil with refractive index matching that of silica was slowly injected in-between the coverslip and the glass slide, such that the samples were fully immersed in the oil. This effectively provides an optically homogeneous background for the silica-embedded superlattices. A Xenon lamp (XBO 75) with a broad-band spectrum (300 – 1100 nm) was used as the light source, and a linear polarizer was used to polarize the incident light. In bright field (BF) reflection mode, the sizes of field-stop and aperture were minimized in order to minimize the angle of incident light. A

50× objective (N.A. 0.8) was used to collect light from only the center of the superlattices. A spectrometer with 50 g/mm grating (Princeton Instrument) and a charge coupled device (PyLoN) were connected to the microscope and were used to collect the backscattering spectra. A slit (50 μm) was used to extract the backscattering spectrum from a thin line at the center of the superlattice, which enables the use of the thin slab model in FDTD to simulate this system.[20] Finally, a background spectrum was chosen from a clean region near the superlattice and was used to remove the signal from the background in the backscattering spectrum.

2.5.6 FDTD Simulation Setup

FDTD simulations were run with a commercial package Lumerical FDTD Solutions v.8.12.631. The dielectric function of gold was adopted from the experimental data obtained by Johnson and Christy.[51] The refractive index of silica was assumed to be 1.45.[52] An infinite thin slab model was used, where a (110) bcc unit cell was repeated in the xy-plane by applying periodic boundary conditions. A PML boundary condition was used in the z direction, which was also the light propagation direction. The length of the superlattice in the z direction can be adjusted to be either 1.5 μm or similar to the actual superlattice thickness as estimated by SEM images. The infinite thin slab model is based on the assumption that light reflected from only the center of the superlattice, namely its top flat surface, but not from its slanted side surfaces. The validity of this model in the spherical NP superlattice case was previously shown by D. Park *et al.*.[20]

2.6 Supplementary Analysis

2.6.1 Spherical NP Superlattice Polarization Dependence Spectrum

Since there is no polarization dependence of the spherical NP itself, the polarization dependence of the spherical NP superlattices can only come from structural anisotropy. As shown in Figure 2.7, where only NPs on the (110) plane of a bcc unit cell is drawn, although the distance in the 90˚direction is smaller than that in the 0˚, the distance between NPs in the 35.3˚orientation is the smallest. Thus, experiment and simulation were performed with 15˚increment in polarization between 0˚and 90˚, except one extra point at roughly 35.3˚, as shown in Figure 2.7.

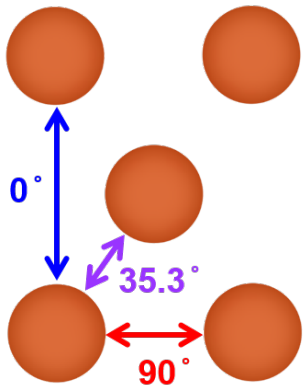

Figure 2.7. Schematic drawing of only NPs on the (110) plane of a single u.c. of the superlattice along the (110) direction. The nearest neighbors of the NP at the bottom left corner is defined to be in the 0˚, 35.3˚, and 90˚orientations.

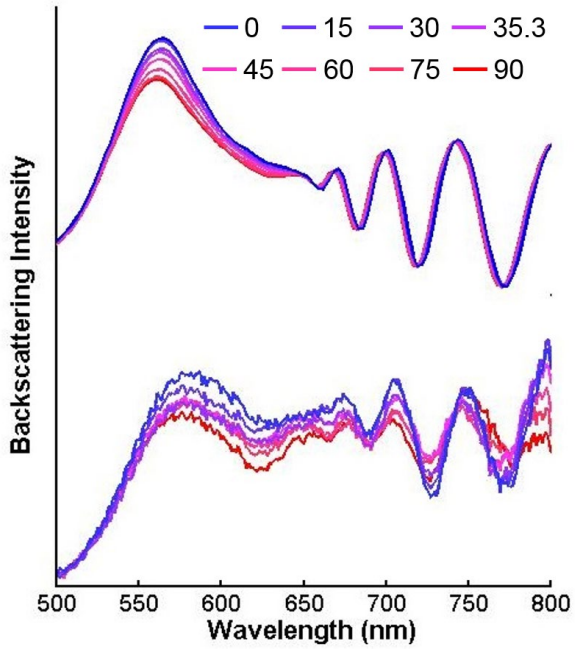

Figure 2.8. Simulation (top) and experimental (bottom) result for the same sample shown in Figure 3 in the main text. The polarizations were varied from 0˚ to 90˚ in steps of 15˚.

Interestingly, contrary to the simple case of a metallic NP dimer interaction, where the LSPR red (blue)-shifts when illuminated with longitudinal (transverse) polarized light, and the red (blue) -shifting becomes more significant at smaller interparticle distance, the optical response of the 2D bcc lattice is not directly related to the interparticle distance. Instead, the main peak gradually blue shifts from 90˚ to 0˚.

2.6.2 Coupled Dipole Calculation

In order to further understand the spectral shift in spherical NP superlattices, a single (110) plane of bcc NP lattice (interparticle spacing 20 nm) is examined within the context of the coupled dipole approximation. Each NP (40 nm in diameter) was modelled as a point dipole with polarizability, which describes response of the NP to the electric field of light, α_0 computed using

the Au dielectric function data of Johnson and Christy.[51] Radiative damping and dynamic depolarization were included in the model by using the modified long wavelength approximation (MLWA) (to account for damping/depolarization effects) to rewrite the dipole polarizability as:

$$\alpha_{NP} = \frac{\alpha_0}{1 - \frac{2}{3} ik^3 \alpha_0 - \frac{k^2}{R} \alpha_0}$$

where k is the wavevector of the incident light in the surrounding medium, and R is the sphere radius.

When excited by an external field $\overrightarrow{E_0}$, the NPs in a lattice re-radiate scattered waves in proportion to the magnitude of their induced dipole moment. The net electric field acting on each NP is then the sum of the incident field plus the radiated fields from all other dipoles in the array. For incident light directed along the normal in an infinite array in the x-y plane, this leads to effective polarization components:

$$P_i = \frac{E_0^i}{\frac{1}{\alpha_{NP}} + S_i} \qquad i = x, y$$

The lattice sums, S_i, are given by

$$S_x = \sum_j e^{ikr_j} \left[\frac{(1 - ikr_j)(3cos^2\theta_j - 1)}{r_j^3} + \frac{k^2 sin^2\theta_j}{r_j} \right]$$

$$S_y = \sum_j e^{ikr_j} \left[\frac{(1 - ikr_j)(3sin^2\theta_j - 1)}{r_j^3} + \frac{k^2 cos^2\theta_j}{r_j} \right]$$

where r_j is the distance between the dipole located at the origin and the other j dipoles in the lattice, and θ_j is the angle between $\vec{r_j}$ and $\hat{x}$. The extinction cross-section per dipole is then:

$$C_{ext} = \frac{4\pi k}{\left|\overrightarrow{E_0}\right|^2} Im\left(\overrightarrow{E_0}^* \cdot \vec{P}\right)$$

The location of maximum extinction is where the denominator ($\frac{1}{\alpha} + S_i$) becomes zero, which in this case is largely determined by when the real parts of the lattice sum and the inverse effective lattice polarizability are equal.[47]

As an application of these expressions, the real and imaginary parts of the calculated dipole sum in both 0˚ and 90˚ polarizations are plotted in Figure 2.9A, together with the inverse of the polarizability. Based on these results, the extinction cross section at three different directions of the lattice: 0˚, 35.3˚, and 90˚ are plotted in Figure 2.9B. Importantly, the same trend is observed as for the case for a 3D superlattice simulated by FDTD, where the main peak blue shifts gradually from 90˚ to 35.3˚ and finally 0˚.

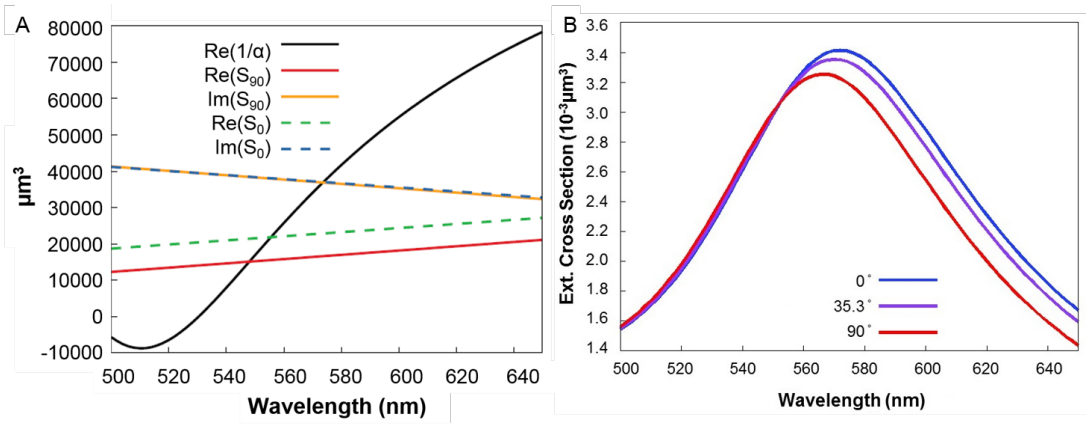

Figure 2.9. (A). Plot of the real and imaginary parts of the lattice sums for 0˚ (S_0) and 90˚ (S_{90}) polarization, and for 20 nm separation. Also plotted is the inverse of the polarizability. Although Im(S_0) and Im(S_{90}) overlaps with each other, there is an obvious difference between Re(S_0) and Re(S_{90}) that eventually determines the peak location. (B). Calculated extinction cross section at the three polarizations. Despite the simplified case of only considering a single layer, this trend matches well with the FDTD simulation of the 3D bcc superlattice.

2.6.3 Backscattering Spectra of Superlattices with Varying Lattice Constants

Backscattering spectra from spherical and octahedral NP superlattices with the interparticle distance varying from 20 to 70 nm were simulated and are shown in Figure 2.10 and 2.11,

respectively. As the interparticle distance increases, the difference between the main peak wavelength between 0˚and 90˚is negligible for the spherical NP superlattices. However, similarly spaced octahedral NP superlattices still exhibit polarization dependence (Figure 2.11).

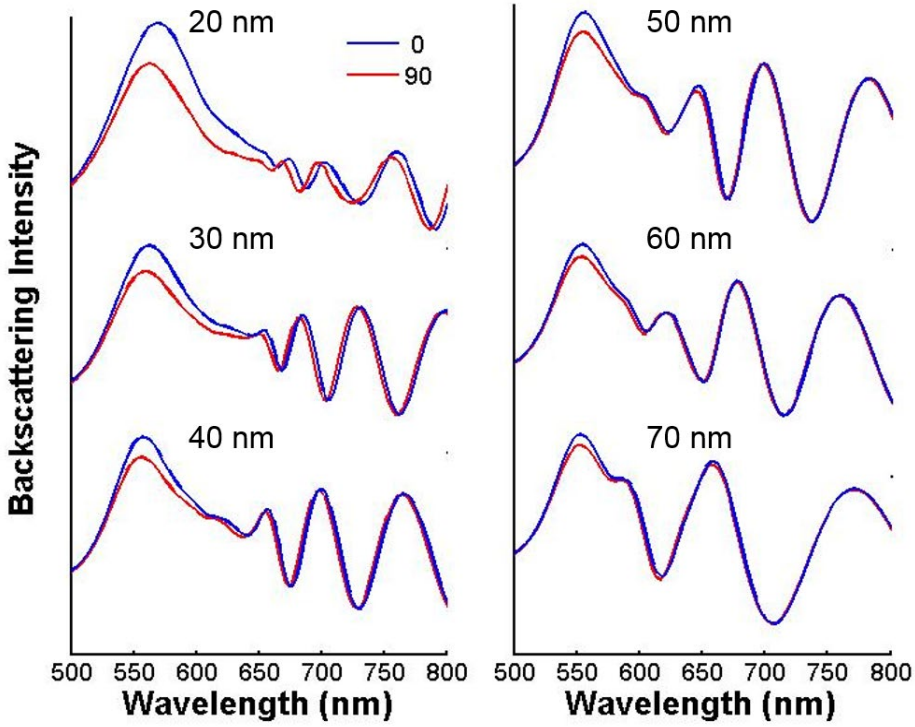

Figure 2.10. Simulated backscattering spectra of spherical NP superlattices with the interparticle spacing varying from 20 to 70 nm as labeled in the plots.

The peak wavelength λ_{max} of both superlattices along both polarizations as a function of interparticle spacing are summarized in Figure 2.12. As the interparticle spacing decreases, λ_{max} red shifts in all cases.

Coupled dipole calculations were employed again to investigate the mechanism for loss of polarization dependence in spherical NP superlattices with large interparticle spacing. The lattice constant (interparticle spacing) utilized here is 120 nm (80 nm). As shown in Figure 2.13, the imaginary part of the lattice sum along the 0º and 90º directions are again overlapped, while the

difference between the real part of the lattice sums are much reduced in comparison to those illustrated in Figure 2.9. Moreover, the polarizability intersects the real part of the dipole lattice sum further away from the extinction maxima, reducing the influence of the intersection position in the extinction maxima. As a result, the extinction spectra show little polarization dependence.

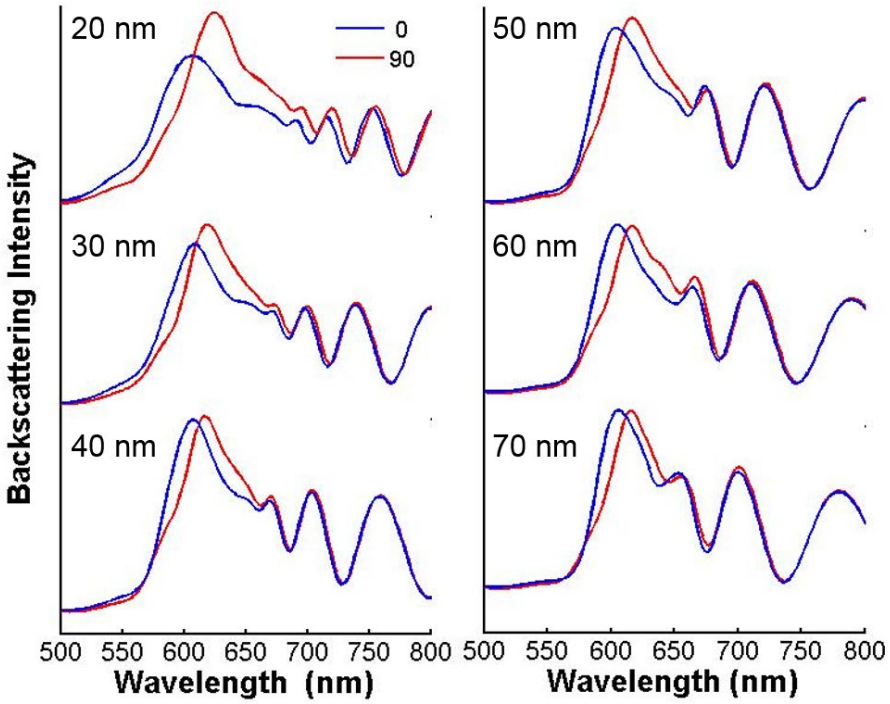

Figure 2.11. Simulated backscattering spectra of octahedral NP superlattices with the interparticle spacing varying from 20 to 70 nm as labeled in the plots.

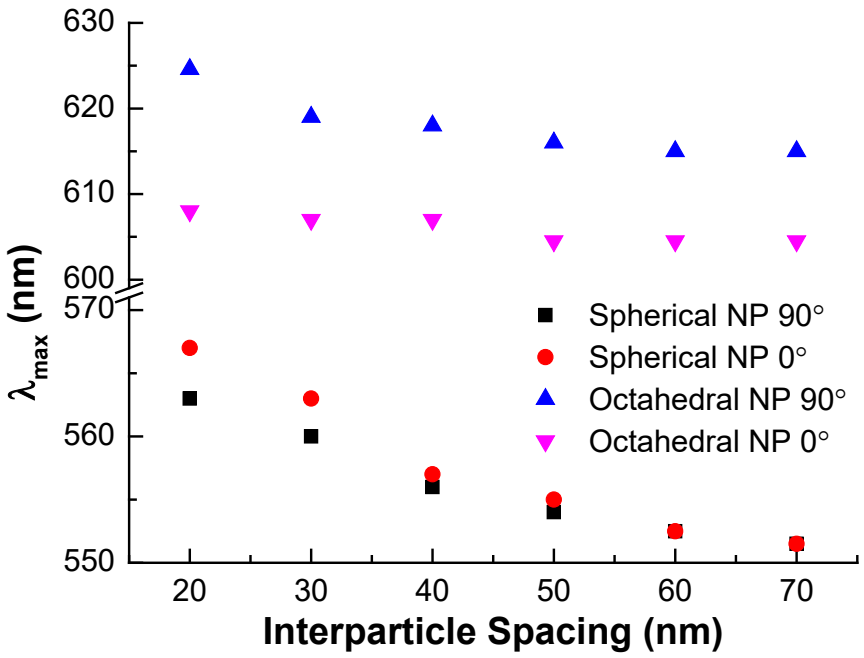

Figure 2.12. Summary of λmax of spherical and octahedral NP superlattices with the interparticle spacing varying from 20 to 70 nm. The main peaks red shift in all cases as the interparticle spacing is decreased.

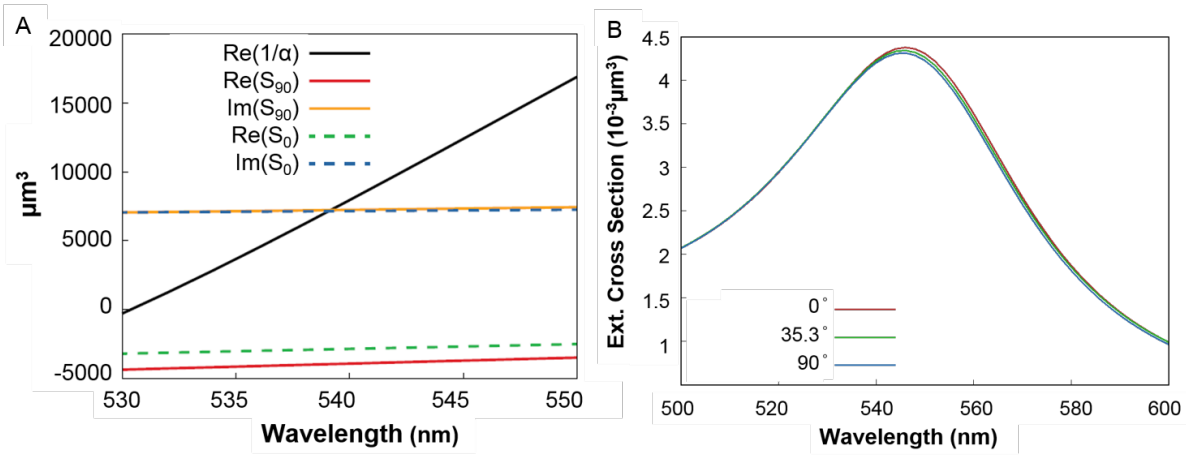

Figure 2.13. (A). Plot of the real and imaginary parts of the lattice sums in the 0˚(S_0) and 90˚(S_{90}) directions and the inverse polarizability from the coupled dipole method. Interparticle spacing used here is 80 nm. In this case, Im(S_0) and Im(S_{90}) still overlap with each other, but the difference between Re(S_0) and Re(S_{90}) becomes greatly reduced compared to Figure S5. (B). Calculated extinction cross sections for the three polarizations. This shows that due to the decreasing

difference between the dipole sums at larger interparticle spacing, the structure anisotropy is lost in spherical NP superlattices.

2.6.4 Electric Field Distribution inside the Superlattices

In order to obtain a qualitative understanding of the NP coupling strength of spherical and octahedral NP superlattices along the two polarizations, a single layer of octahedral NP lattice is simulated (Figure 2.14), and electric field distributions of a single unit cell perpendicular to the light injection direction are plotted in Figure 2.15 and 2.16 for spherical and octahedral NP superlattices, respectively. The interparticle spacings are 20 nm for both cases. The wavelengths are chosen to be 558 and 610 nm, close to the main extinction peaks of spherical and octahedral NP superlattices, respectively. The field strength in the middle of two nearest neighbor particles along 90º when the light polarization is 90º, label as point X in Figure 2.16A, is much stronger than that along 0º with 0º light polarization (point Y in Figure 2.16B) for the octahedral NPs superlattices. Note that points X, Y are essentially the same due to symmetry, but are labeled differently for clarity, namely X is associated with 90º polarization while Y 0º. In contrast, the field strengths of the corresponding points in spherical NP superlattices, namely points X and Y in Figure 2.15, are significantly weaker and show the opposite trend: field intensity at point Y is slightly larger, by less than an order of magnitude, compared to point X in Figure 2.15. Therefore, we conclude that the coupling in the 90º (tip-to-tip coupling) is stronger than that in the 0º (edge-to-edge coupling) for octahedral NP superlattices.

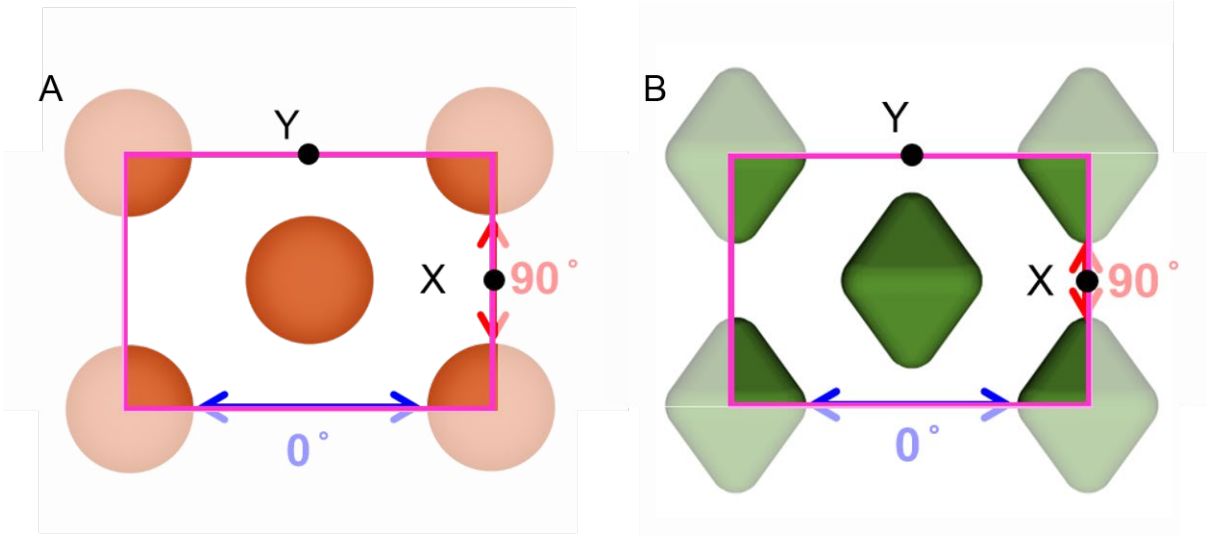

Figure 2.14. Schematic drawing of a single unit cell of NPs on the (110) plane of spherical and octahedral NP superlattices, respectively. Field intensity distributions inside the magenta square are plotted in the following two figures.

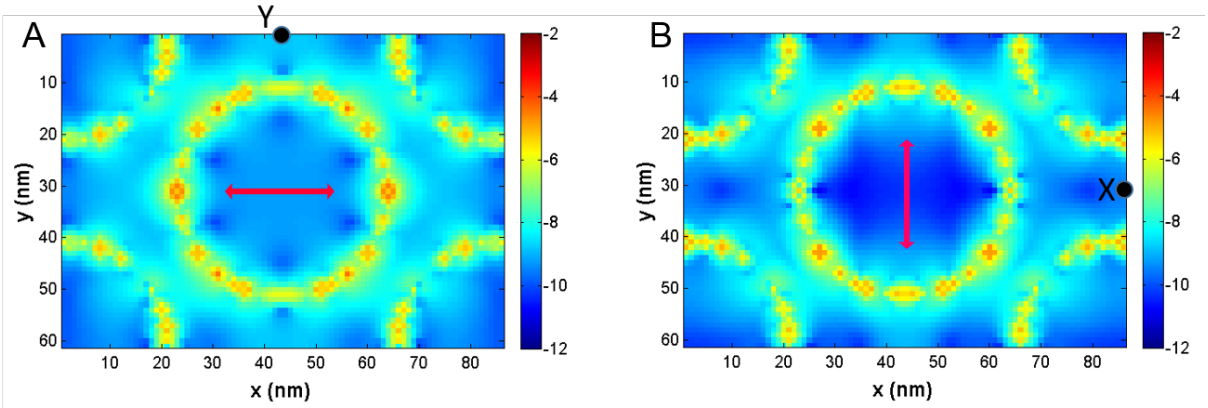

Figure 2.15. Electric field intensity in a single unit cell of one (110) plane of spherical NP superlattices when light is polarized in 0º (A) and 90º (B). Light wavelength is 558 nm, close to the main peak location and injection direction is perpendicular to the plane. Red arrows in the center denote light polarization directions. Point Y denotes the middle between two nearest neighbor particles in the 0º and point X denotes that in the 90º. The field intensity at Y is slightly larger than at X in this case. Log scale is used.

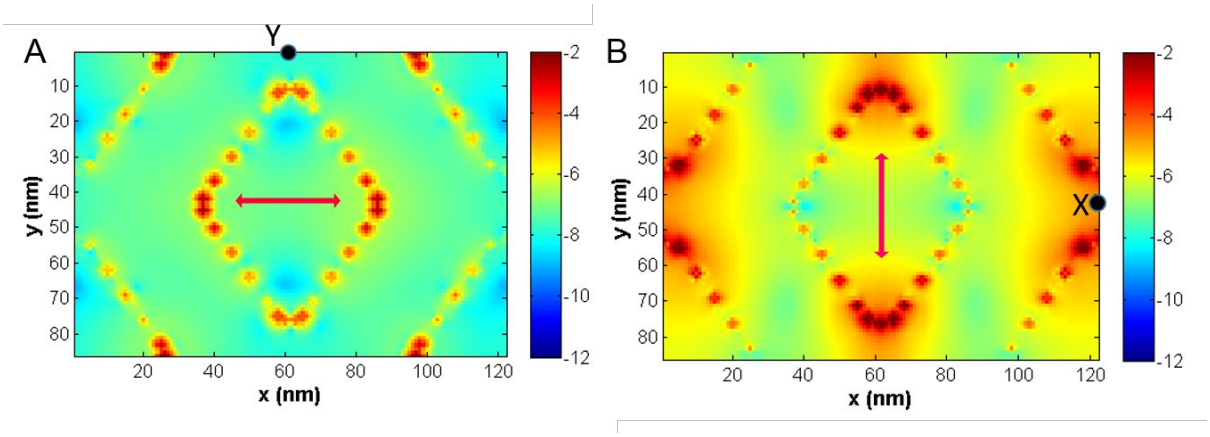

Figure 2.16. Electric field intensity in a single unit cell of one (110) plane of octahedral NP superlattices when light is polarized in 0º (A) and 90º (B). Light wavelength is 610 nm, close to the main peak location and injection direction is perpendicular to the plane. Red arrows in the center denote light polarization directions. Point Y denotes the middle between two nearest neighbor particles in the 0º and point X denotes that in the 90º. The field intensity at X is much larger than at Y in this case, indicating stronger tip-to-tip coupling along 90º than edge-to-edge coupling along 0º. Log scale is used.

2.6.5 Polarization Dependence Spectra for Octahedral NP Superlattice

Polarization dependence for octahedral NP superlattices is studied in details by simulating the structure with 15˚increment in polarization between 0˚and 90˚(Figure 2.17). The interparticle spacing is 37 nm and superlattice thickness is fixed at 1.5 μm. The insert shows the extinction spectra of a single octahedral NP with the same polarizations. Similar to the case of spherical NP superlattices, the peak wavelength gradually changes from λ_{max}^{0} to λ_{max}^{90}. This trend is in well accordance with the gradual change of dipole lattice sum and nanoparitlce polarizability from 0˚ to 90˚.

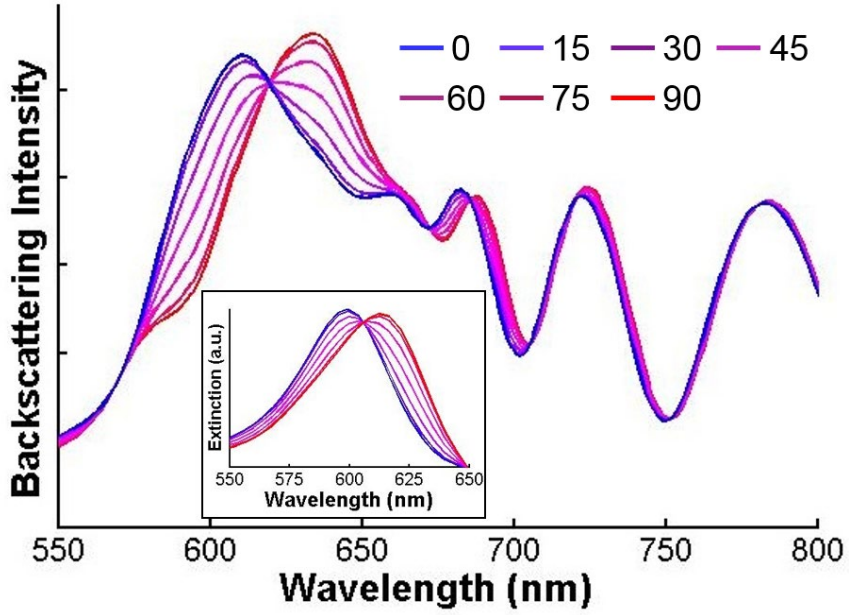

Figure 2.17. Simulation result for octahedral NP superlattice with the same NP size, 37 nm interparticle spacing and 1.5 μm thickness. Insert shows the extinction spectra of a single octahedral NP. The polarizations were varied from 0˚ to 90˚ in steps of 15˚.

2.6.6 Results for Superlattice with a Larger Lattice Constant

Octahedral NP superlattices with the same batch of NPs (51 nm with 4.8 nm rounding) and larger interparticle spacing (61 nm) were also examined. Figure 2.18A shows the SEM image of one sample. The same set of simulation and experiment as described in previous sections were performed. As can be seen in Figure 2.18B, the difference in wavelength, $\Delta\lambda$, for the main peak is maintained even in the superlattice where the NPs are further separated apart.

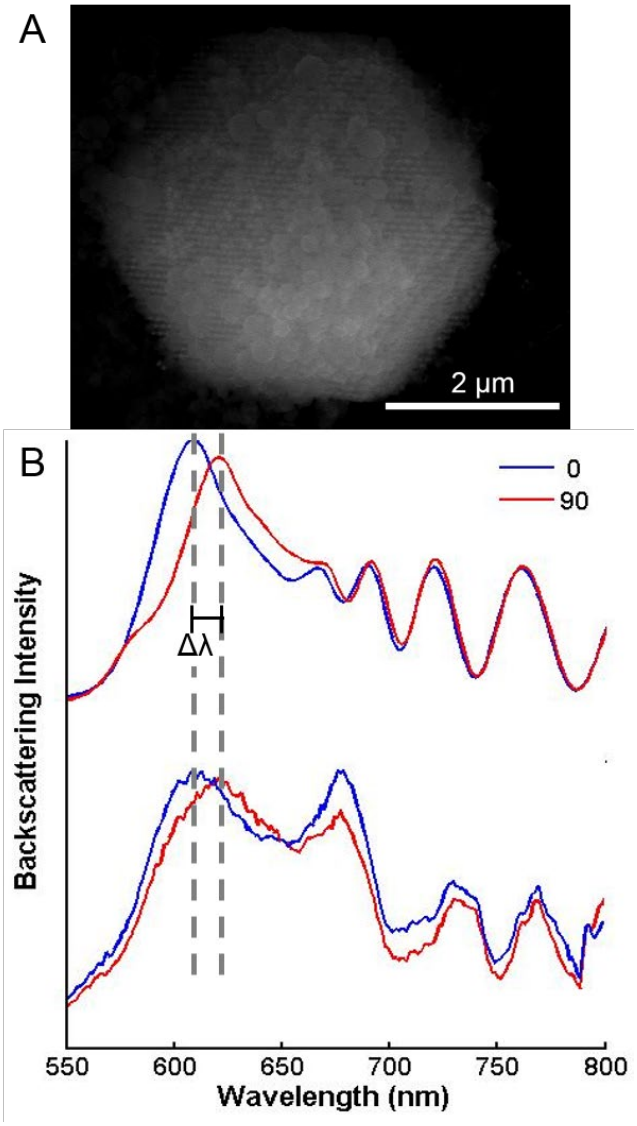

Figure 2.18. SEM image of an octahedral NP superlattice with interparticle spacing as 61 nm (A), and its backscattering spectra from both simulation (B, top) and experiment (B, bottom). Δλ is shown to denote the difference between the main peak wavelengths for the two polarizations.

CHAPTER THREE

Design Principles for Photonic Crystals Based on Plasmonic Nanoparticle Superlattices

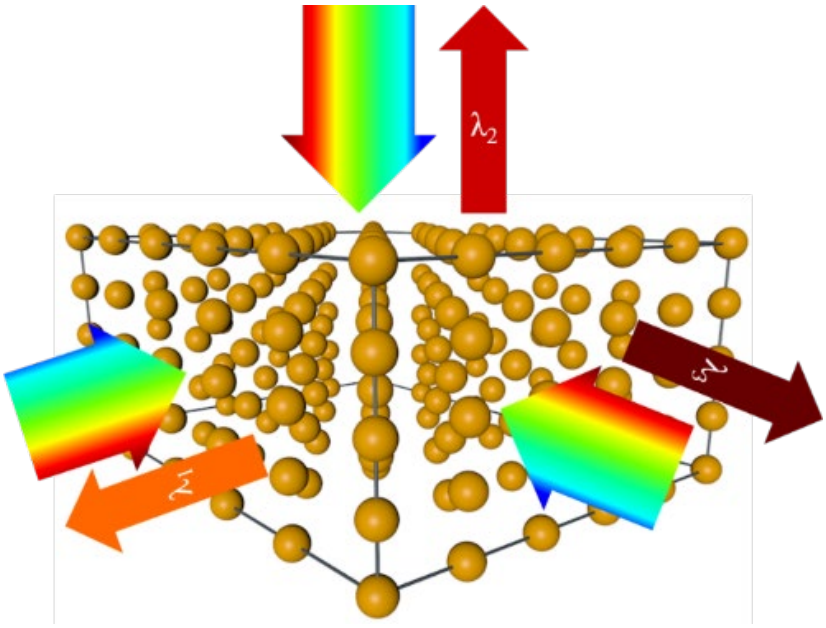

Note: Portions of the material in this chapter is published in the following articles:

1. Design principles for photonic crystals based on plasmonic nanoparticle superlattices, *Proceedings of the National Academy Sciences USA* **2018**, *115 (48)*, 7242-7247
2. Design principles for nanoparticle based photonic crystals, *Active Photonic Platforms X* **2018**, *10721*, 1072122

This work was done in collaboration with Dr. Haixin Lin, Dr. Daniel J. Park, Dr. Kevin Kohlstedt and Dr. George C Schatz.

3.1 Abstract

Photonic crystals have been widely studied due to their broad technological applications in lasers, sensors, optical telecommunications, and display devices. Typically, photonic crystals are periodic structures of *touching* dielectric materials with alternating high and low refractive indices, and to date, the variables of interest have focused primarily on crystal symmetry and the refractive indices of the constituent materials, primarily polymers and semiconductors. In contrast, FDTD simulations suggest that plasmonic nanoparticle superlattices with spacer groups offer a promising new route to photonic crystals due to the controllable spacing of the nanoparticles and the high refractive index of the lattices, even far away from the plasmon frequency where losses are low. Herein, the stopband features of 13 Bravais lattices are characterized and compared, resulting in paradigm-shifting design principles for photonic crystals. Based on these design rules, a simple cubic structure with a ~130 nm lattice parameter is predicted to have a broad photonic stopband, a property confirmed by synthesizing the structure via DNA programmable assembly and characterizing it by reflectance measurements. We show through simulation that a maximum reflectance of more than 0.99 can be achieved in these plasmonic photonic crystals by optimizing the nanoparticle composition and structural parameters.

3.2 Introduction

Photonic crystals (PCs) are materials with periodically varied refractive indices, in which optical control is achieved by refractive index contrast and diffraction. When the effective wavelength of light satisfies the Bragg criterion (when the wavelength is twice the periodicity), light propagation in certain directions inside the material is “forbidden”[53]. This gives rise to a photonic band gap (PBG) conceptually analogous to the electronic band gap in semiconductors.

PCs have been intensively studied for use in a wide range of technologies, such as semiconductor lasers, optical integrated circuits, optical switches, and solar cells[54-56]. In addition, they are commercially used for light emitting diodes, sensors, and optical fibers.

Conventionally, PCs are structures made of dielectric materials (e.g. polymers and semiconductors) and prepared via top-down[57, 58] or bottom-up fabrication processes[59, 60]. In general, bottom-up techniques are attractive because they are often simpler, less expensive, and more scalable[60, 61]. PCs made with bottom-up processes are typically close-packed or touching, and the techniques used to make them provide little control over crystal symmetry and lattice parameter[62].

Thus far, the primary considerations in designing PCs have been crystal symmetry and the choice of dielectric materials, in order to increase the index contrast between the high- and low-index materials, which is crucial for achieving good photonic properties (see section 3.6.1 for detailed explanation)[63-65]. However, there remain several intrinsic challenges, including overcoming the strain that results from interfacing materials with large lattice mismatches[66], poor crystal quality[63], and low index contrast[65, 67]. Moreover, since the high-index materials are closely spaced and sometimes touching[54, 64], planes along the light propagation direction are always composed of a mixture of both high- and low-index materials - there is no well-defined separation between the high- and low-index layers, which reduces the index contrast. Hence, alternative fabrication methods that incorporate high-index materials and allow spatial separation of the high- and low-index materials may help solve challenges in PC fabrication and property tailoring.

With the advent of methods for chemically programming the formation of colloidal crystals[14, 68], additional variables can be used to tune PC properties. For example, interparticle distance, which can be finely tuned with some of the emerging techniques for particle assembly[16,

[18], represents a yet-to-be explored parameter that could prove useful in PC design. Herein, we use FDTD simulations and take into account the Bragg criterion, to study the origin of the PBG along certain directions for 13 of the 14 Bravais lattices comprised of Au nanoparticles (NPs). From this analysis, general design principles are established, and based on these design rules, a simple cubic structure with a ~130 nm lattice parameter is predicted to exhibit a broad photonic stopband, a property confirmed by synthesizing it via DNA programmable assembly[14, 16, 69] and characterizing it by reflectance measurements. Most of the data pertain to Au NPs, but the lessons learned extend to other plasmonically active materials. Importantly, we show through simulation that a maximum reflectance of >0.99 can be achieved by optimizing NP composition and crystal structural parameters, despite the concern that metallic plasmonic NPs are lossy.

3.3 Results and Discussion

Because the NP size is smaller than the free electron mean-free-path, the free electrons in Au NPs are confined and interact strongly with light, giving rise to a localized surface plasmon resonance (LSPR) that can be used to focus light beyond the diffraction limit[70]. The frequency of the LSPR is highly dependent upon the NP's size and shape, the dielectric environment, and presence of neighboring plasmonic NPs[12, 48]. Besides having local control over detailed properties at the nanoscale, the macroscopic properties of the NP ensemble, such as its effective refractive index (n_{eff}), can also be tuned by various structural parameters[71]. Particularly, within a range of volume fraction where plasmonic coupling is not too strong, the n_{eff} of spherical NP ensembles can be calculated using Maxwell–Garnett effective medium theory (EMT)[8], allowing qualitative understanding of the structure dependence of their optical properties. Although metal NPs are

absorptive close to the plasmon resonance frequency, EMT studies have shown that the real part of the permittivity can be enhanced well away from the plasmon frequency, where absorption is relatively small. Also, the optical response associated with plasmonic NPs is so strong that it is possible to use lattices with relatively low volume fraction (i.e., the NPs are highly separated) in constructing functional photonic lattices. Therefore, ensembles of plasmonic NPs serve as a promising candidate for the high-index material in PCs (Plasmonic PCs, PPCs, Figure 3.1). Although a high effective index can be realized in plasmonic NP ensembles and there has been extensive work on plasmonic NP assemblies[68, 72, 73], large stopbands are not typically observed in such structures due to the dense-packed arrangements of NPs[10, 74]. This analysis is consistent with the conclusion that plasmonic NPs must be well-separated to design effective PPCs.

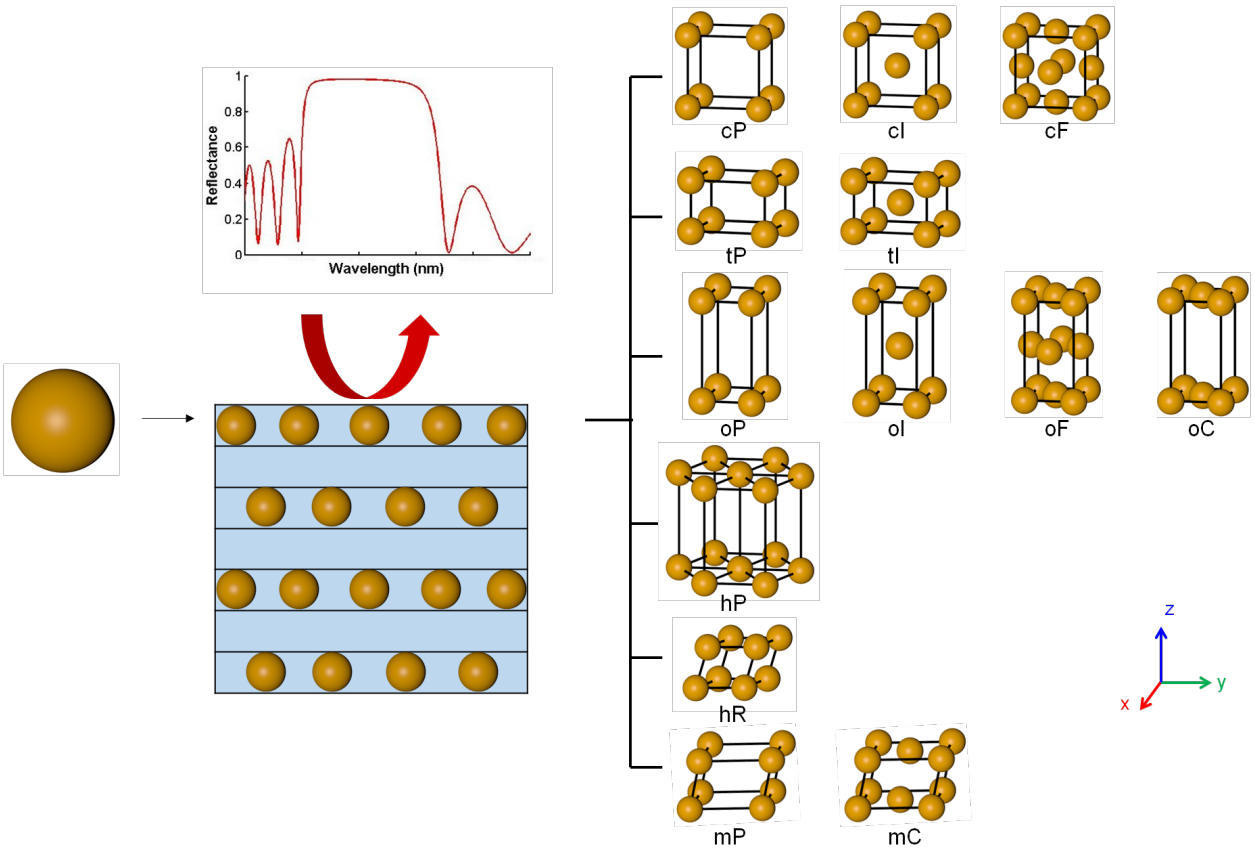

Figure 3.1. Schematic representation describing the design of plasmonic PCs with Au NPs. The stopband features that are generated by light incident normal to the x-y plane are investigated. Along the z-direction, the superlattice can be viewed as alternating NP and dielectric layers with high and low indices, respectively. 13 out of 14 Bravais lattices are studied. In the layered structure scheme, the NPs are embedded in a homogeneous matrix.

Conceptually, a periodic structure can be achieved by building a crystal where the NPs are located at each lattice site and embedded in a homogeneous dielectric medium. For a chosen direction relative to the crystal lattice, each crystalline plane contains a layer of NPs that serves as the high-index layer, and the medium between each lattice plane serves as the low-index layer. The crystal can have different lattice symmetries and lattice constants, which in turn will affect the effective refractive index (n_{eff}) of the NP layer and the periodicity. To systematically investigate the effect of structural parameters on the photonic properties and provide guidelines for the construction of PPCs with large PBGs along selected directions, we have studied the optical properties of 13 out of the 14 Bravais lattices to identify the roles each lattice parameter plays (Figure 3.1). In particular, finite-difference time-domain (FDTD) simulations are carried out to investigate how the lattice parameters of PPCs - the lattice constants in all three dimensions and the angle - affect the photonic stopband features. We setup lattices with spherical Au NPs (diameter 108 nm), all embedded in a silica matrix (as such structures can be made experimentally). Cases with different NP sizes are examined in section 3.6.11. To minimize computational time and keep the simulations tractable, we found 7 layers of NPs sufficiently represented the thin PPC films (Figure 3.9 and 3.10) and were used in all simulations unless otherwise specified. Normal incidence of light (z-direction) onto the (001) plane (x-y plane) of the lattice is investigated (Figure 3.1); cases with different angles of incidence are discussed in section 3.6.10.

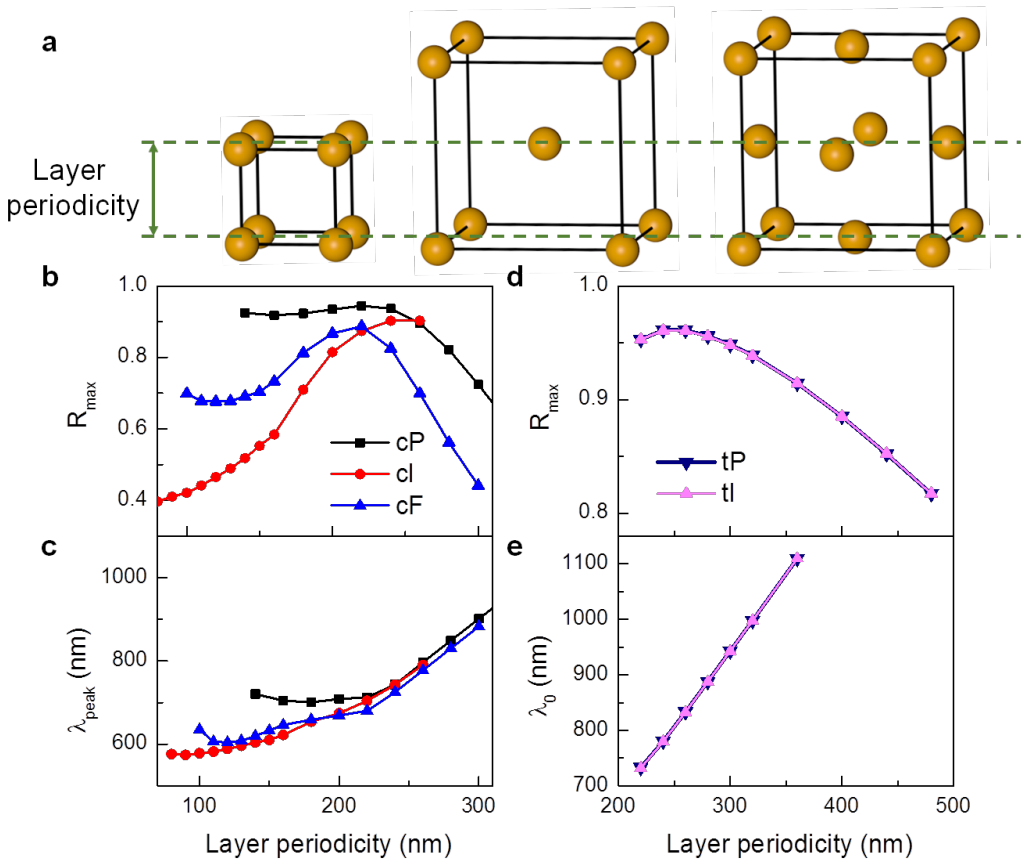

Figure 3.2. Layer periodicity dictates the location of the photonic stopband. **a**, If the superlattice is viewed as alternating layers that do and do not contain the NPs, then the layer periodicity is defined as the spacing between two adjacent layers that contain NPs. **b,c**, Dependence of maximum reflectance (R_{max}, **b**) and its corresponding wavelength (λ_{peak}, **c**) on the layer periodicity of simple cubic (cP), body-centered-cubic (cI) and face-centered-cubic (cF) superlattices. **d,e**, Dependence of R_{max} (**d**) and center wavelength (λ_0, **e**) of tetragonal (tP) and body-centered-tetragonal (tI) lattices. The lattice constant within each layer is kept constant at 200 nm. Only the λ values of a reflectance larger than 0.9 is considered as the stopband and its λ_0 plotted as a function of layer periodicity in **e**.

Rule 1: Layer periodicity, as compared to the lattice constant along the light propagation direction, dictates the location of the photonic stopband.

Figure 3.2 summarizes the maximum reflectance (R_{max}) of the stopband and the peak wavelength, at which R_{max} is obtained, for simple cubic (cP), body-centered-cubic (cI) and face-

centered-cubic (cF) lattices as a function of the periodicity of each layer along the z-direction (Figure 3.2a). In other words, a single cI or cF unit cell has three layers (top, middle, bottom), and the periodicity of each layer in the z-direction is half of the lattice constant (Figure 3.2a). A clear trend between the peak wavelengths and layer spacing is observed between the three lattice types (Figure 3.2b and 3.2c). It is remarkable how the peak wavelengths and maximum reflectance share similar values and trends, especially above 200 nm layer spacings. As the lattice constant increases, the peak wavelength increases and R_{max} increases until it reaches a maximum value, then decreases, as expected from our analysis in section 3.6.1. This demonstrates the importance of controlling the lattice constant, which is not easily achievable with conventional fabrication techniques. When the properties are plotted as a function of lattice constant (Figure 3.11), the correspondence between the three lattice types becomes weak. This suggests that instead of the lattice constant in the z-direction (c), the spacing between each NP layer in the light propagation direction (layer periodicity) should be considered as the periodicity of the PC (Figure 3.2a).

The above point is directly shown in lattices with larger layer periodicity (>200 nm, Figure 3.2a), where the peak wavelength increases almost linearly, compared to the slow change at smaller periodicities. This complication arises because plasmonic NPs are used as building blocks. As seen more clearly in section 3.6.3, where the reflection spectra of superlattices with cP crystal structure and different lattice constants are shown, the stopband overlaps with the plasmonic modes of the NP lattice at smaller lattice constants (140 - 200 nm). In this situation, the exact wavelength of the stopband becomes hard to predict. We simplify the discussion further by focusing on lattices where the plasmonic modes and stopband are spectrally separated. This also allows us to later test the feasibility of using EMT to estimate the n_{eff} and reproduce the reflectance

spectra, since the EMT prediction is less accurate on the blue side of the LSPR where quadrupole modes are important in the NP response and there is more significant absorption. In addition, as the lattice constant further increases and the first-order Bragg peak red shifts, a second-order peak arises (Figure 3.11 and 3.19). For simplicity, only first-order peaks are considered.

Although the cubic lattice system can provide insight into the structure-function relationship of PPCs, the situation is limited due to the high crystal symmetry in the cubic lattice system, prompting the investigation of other lattice symmetries. Next, we move to investigate tetragonal crystal systems. Compared to the cP lattice, c is different from the lattice constant in the x-y plane (a), which allows more freedom in teasing out the structure-function relationship. Figure 3.2d shows the dependence of the R_{max} on the layer periodicity of both tetragonal lattices (tP) while keeping a constant (200 nm). The largest R_{max} is reached with $c \sim 240$ nm. Further inspection shows that the periodicity at which the largest R_{max} is obtained involves an optimization of both layer periodicity and layer number (Figure 3.18). To further determine the characteristics of the stopband, we study only those with their R_{max} larger than 0.9 and define the band width ($\Delta\lambda$) to be the width of the band with reflectance ≥ 0.9. Figure 3.2e demonstrates again that the wavelength of the center of the band (λ_0) depends linearly on the layer periodicity. Although $\Delta\lambda$ increases, the normalized band width $\Delta\lambda/\lambda_0$ decreases due to the faster increase in λ_0 (Figure 3.16). Interestingly, the properties of body-centered-tetragonal (tI) lattices are almost identical to a tetragonal counterpart with the same layer periodicity, which we emphasize again is not c but $c/2$ in tI lattices. This indicates that the properties of the stopband may be independent of the relative position of the NPs between different layers, as discussed below.

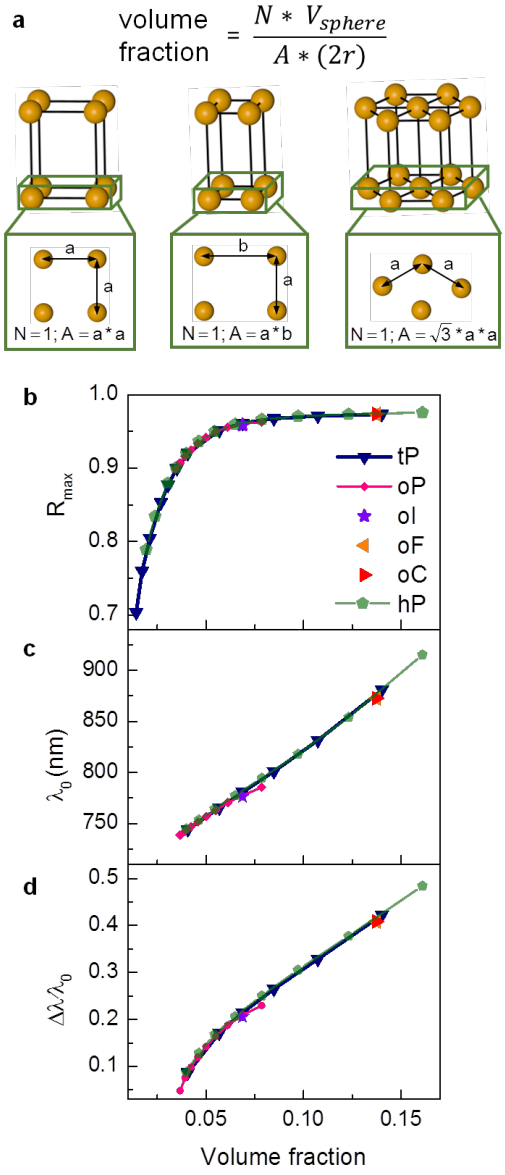

Figure 3.3. The volume fraction of each NP layer dictates the R_{max}, λ_0, and $\Delta\lambda/\lambda_0$ of the stopband. **a**, The volume fraction within each NP layer is defined in the top equation, where N is the number of NPs in each unit cell, V_{sphere} is the volume of the NP, and A*(2r) is the volume of a unit cell, where A is the area of the facet in the x-y plane of the unit cell, r is the radius of the NP and thus the diameter of the NP defines the thickness of the NP layer. **b-d**, R_{max} (**b**), λ_0 (**c**) and normalized bandwidth ($\Delta\lambda/\lambda_0$, **d**) of tetragonal (tP), orthorhombic (oP) and hexagonal (hP) lattices as a function of volume fraction within each NP layer. One lattice constant within the NP layer is chosen for body, face, base-centered-orthorhombic (oI, oF, oC, respectively), and the stopband features show good agreement with the oP lattices, as predicted. The layer periodicity of all data points is 240 nm.

Rule 2: The volume fraction, rather than the exact NP arrangement, of each NP layer dictates the bandwidth.

Now that layer periodicity has been identified as a key structural parameter, we investigate the relationship between *a* (with fixed layer periodicity) and stopband features in Figure 3.20. As *a* increases, R_{max}, λ_0 and $\Delta\lambda/\lambda_0$ all decrease, due to the reduced index contrast between the NP and the silica layer as the amount of Au in the NP layer is diluted by increasing *a*. Next, we explore the stopband features of orthorhombic (oP) and hexagonal (hP) lattices and compare them to that of the tetragonal structures (Figure 3.3). The layer periodicity is kept constant at 240 nm for all lattice types. From the perspective of the NP arrangement in each layer, the NPs are arranged in squares, in rectangles with the length of one side fixed (b = 250 nm), and in diamonds with 60º angle, while *a* is varied for tP, oP, and hP lattices, respectively (Figure 3.3a). To enable comparison between different lattice symmetries, the properties are plotted against the NP volume fraction within each NP layer (Figure 3.3a). A striking fact is that all of the plots for the three different lattice structures overlap. The stopband is dictated by the volume fraction rather than the exact arrangement of the NPs within each layer for fixed NP size and layer periodicity. We see in Figure 3b, as volume fraction increases, the R_{max} increases monotonically until it saturates at ~ 0.97, and the 0.03 loss is due to absorption by the material (Figure 3.24). Interestingly, λ_0 and $\Delta\lambda/\lambda_0$ increase with increasing volume fraction (decreasing lattice constant); this is a consequence of the low-energy band edge experiencing a blue-shift while the high-energy edge remains relatively unchanged (Figure 3.21-3.23).

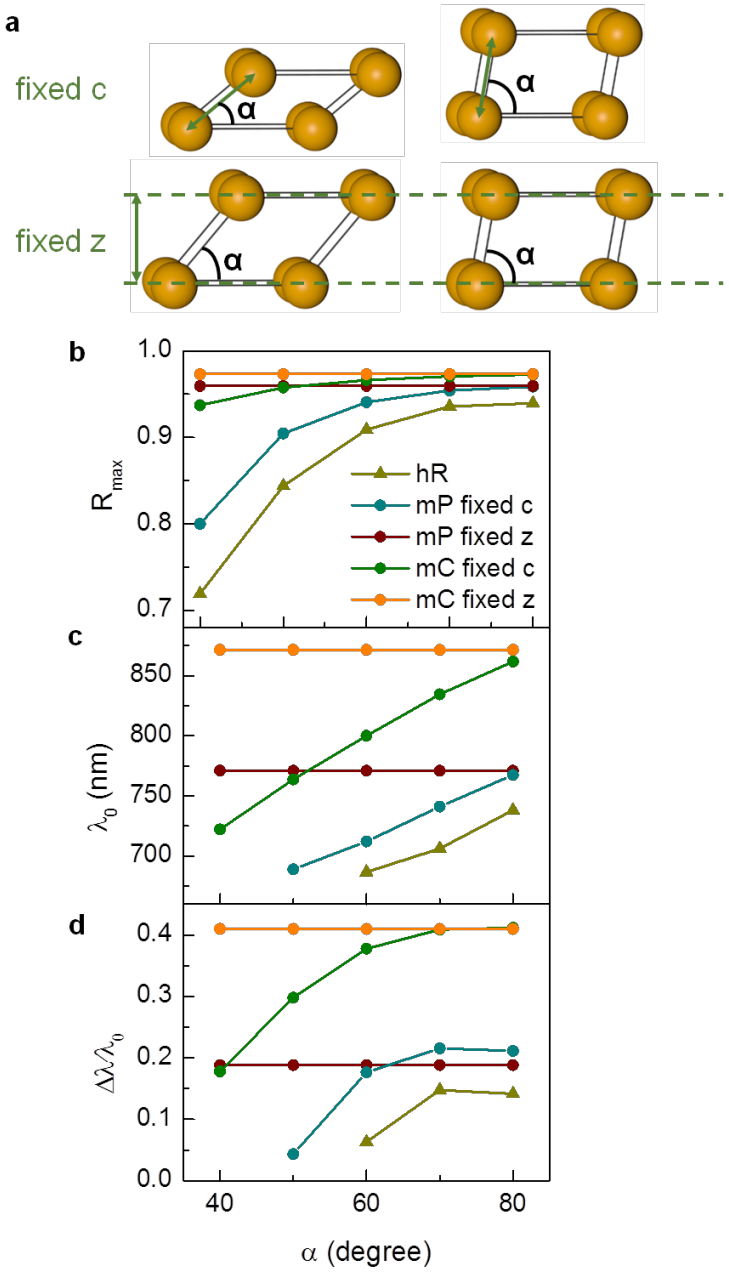

Figure 3.4. The registry between NP layers has a negligible effect on the stopband features. **a.** Two sets of structural parameters in monoclinic and base-centered monoclinic (mP and mC, respectively) lattices with either fixed layer periodicity (fixed z) or fixed lattice constant *c* (fixed c) while changing the angle. **b-d**, R_{max} (**b**), λ_0 (**c**) and normalized bandwidth ($\Delta\lambda/\lambda_0$, **d**) of trigonal (hR), mP, and mC lattices with either fixed c or z as a function of the angle α. In the fixed c (z) case, *c* (*z*) is 240 nm.

Rule 3: The nanoparticle registry between layers does not affect stopband features

Features of the stopband of trigonal lattices (hR) are summarized in Figure 3.4b-d. Here, the lattice constant is fixed at 240 nm while the angle is changed from 40 to 80º, and both R_{max} and λ_0 increase (Figure 3.4b-d and 3.25). So far, we have shown the important roles that layer periodicity and volume fraction in each layer play, while the exact arrangement of NPs in each layer has negligible influence. However, the effect of registry between different layers has not been considered. While our observations in all the body-centered and face-centered structures (cubic and tetragonal) indicate that registry plays a trivial role, its effect can be studied more clearly in monoclinic lattices. A monoclinic lattice (mP) allows even more degrees of freedom, where all three lattice constants (a, b and c) and the angle (α) between layers can be independently varied. Two sets of simulations are performed where the lattice constants in each layer are fixed at a = 250 nm and b = 160 nm, while the lattice constant in the [001] direction is set such that either the layer periodicity (fixed z) or c (fixed c) is kept constant. R_{max}, λ_0 and $\Delta\lambda/\lambda_0$ of the lattice with fixed c demonstrate a similar trend to that of the trigonal lattice; in comparison, those of the fixed z lattices are constant, and the reflectance spectra overlap at all α (Figure 3.26 and 3.27). This proves that the registry between different layers indeed does not affect the stopband features of the lattice. This observation coincides with our expectation that the relative arrangement of NPs in each layer and between layers does not matter (when the NPs are spaced such that no strong plasmonic interaction occurs).

To further explore this concept, we discuss the feasibility of using EMT combined with the transfer matrix method[75] (EMT + TMM) to reproduce the spectra calculated by FDTD (Figure 3.31). The good qualitative agreement between the EMT + TMM and FDTD results indicates that

the superlattice properties in the z-direction can be treated as alternating layers of high (NP)- and low (dielectric)-index materials.

We have derived guidelines to design PPCs from analysis of the stopband features along one dimension; however, the results can be applied to any direction for a three dimensional (3D) PPC. 3D PPCs offer more compact design and are sought-after for applications involving all-optical integrated circuits[60]. Here, we explore experimental methods for realizing such 3D PPCs. DNA-programmable assembly is a promising emerging method for making PPCs since it provides fine control and even sub-nm tunability over particle spacing[16, 18, 69, 76]. Moreover, interparticle spacing can be dynamically tuned after PC formation[18, 77], enabling dynamic tuning of the stopband location. Here, as proof-of-concept, we use micron-sized simple cubic superlattices with well-faceted cubic crystal habits[40] made from DNA-functionalized cubic NPs to experimentally explore this concept. The cubic crystal habit facilitates the alignment of the microcrystal with its (001) facet facing up. Specifically, cubic NPs with 88 ± 4 nm edge length and 5 ± 1 nm corner rounding were used, and the lattice constant as measured by small angle X-ray scattering was 134 nm (Figure 3.7). The simulation results for a superlattice made of spherical NPs with the same volume and lattice constants show the existence of a broad stopband (Figure 3.5b, top), a property that is observed both experimentally and through simulation in the cubic NP superlattice (Figure 3.5b, bottom). Moreover, the experimentally observed stopband matches remarkably well with the simulation prediction, emphasizing that the design rules articulated above are not limited to spherical particles. Indeed, as in section 3.6.13, NPs with different shapes can be used as the building blocks for superlattices that demonstrate similar stopband properties. Although only a cP lattice is studied experimentally, other lattice structures (over 500 different crystals spanning over

30 different crystal symmetries) have been made through DNA-programmable assembly[14, 16]. For lattices with symmetries that do not belong to the cubic lattice system, one can obtain different stopband properties using different crystal orientations of the same superlattice.

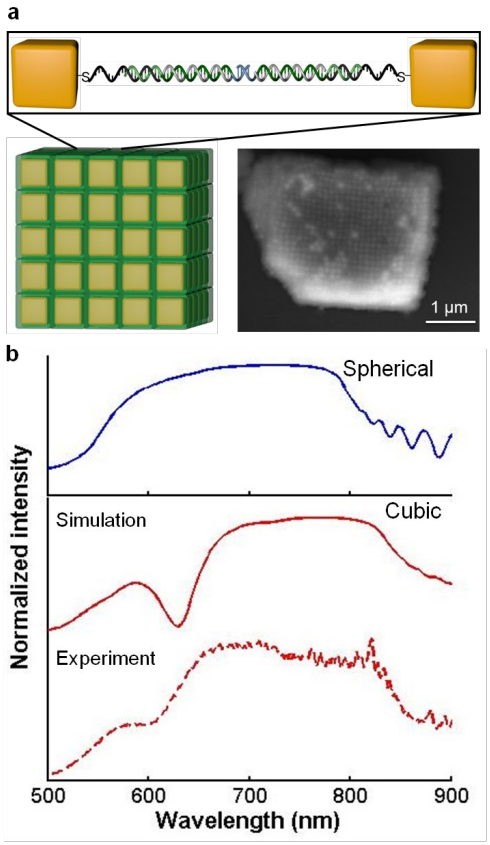

Figure 3.5. Experimental measurement and FDTD simulations of cubic NP superlattices. **a**, Schematic representation (bottom-left) and scanning electron microscope (bottom-right) image of a superlattice made through DNA-programmable assembly of nanocubes, after encasing in silica. The Au nanocube building blocks have an 88 nm edge length and a 5 nm corner rounding. The lattice constant of the superlattice is 134 nm and defined by the duplex DNA interconnects An enlarged view of one hybridized DNA-pair between nearest neighbor nanocubes in a lattice is shown in the top image. **b**, Simulation result of a simple cubic superlattice with spherical NPs that has the same lattice constant and volume fraction as the superlattice shown in **a** (top) and simulation and experimental results for the superlattice shown in **a** (bottom).

Building photonic crystals with materials other than Au

We noted earlier that R_{max} is limited by absorption, largely because Au NPs are lossy. Simulation results show that among Au, Ag, Al, and Cu, the superlattices composed of Ag NPs show the highest reflection and lowest loss. In this case, R_{max} reaches 0.986 (Figure 3.41), and this can be further increased by optimizing structural properties. One simulation result shows that an R_{max} greater than 0.996 can be achieved (Figure 3.42). The performances of these plasmonic NPs are compared with other metallic NPs with poor plasmonic properties (Figure 3.43). The stopband features of superlattices made of Ti NPs are much weaker (Figure 3.43 and 3.44) than those of superlattices made of Au NPs with similar structures. Additionally, to benchmark our technique with conventional PC fabrication methods (where dielectric materials are in general used), we investigated the stopband features of lattices made with various dielectric NPs through simulation (Figure 3.45-3.53). These lattices obey the same design principles derived above. However, the stopbands of crystals made with dielectric NPs saturate much more slowly, and the band widths are much narrower compared to the metallic NP ones with the exact same lattice parameters. Finally, we explore the effect of the dielectric medium in Figure 3.54 and note that with the same superlattice, the spectral location of the stopband can be tuned by immersing or embedding it in a different dielectric medium[62].

3.4 Conclusions

Through a systematic study of the stopband features of 13 Bravais lattice structures along the z-direction, we have shown, for the first time, that non-touching PPC superlattices can be treated as periodically alternating layers of high- and low-index materials along the light

propagation direction. We have identified two key parameters that dictate the stopband features: the layer periodicity and the volume fraction of each NP layer. Interestingly, when the NPs are spaced sufficiently far away such that strong plasmonic coupling is minimized, the exact arrangement of NPs in each layer and the registry between different layers have negligible influence on the stopband properties. From a fabrication standpoint, this work conclusively shows that DNA-programmable assembly is especially and perhaps uniquely useful for making 3D PPCs, since it provides control over the spacing between NPs and lattice symmetry. The high tunability of the stopband features realized through this technique (by changing lattice parameters, NP size and composition, and the dielectric matrix) should lead to PPCs with interesting applications as novel cavities and filters. Compared to PCs made with purely dielectric materials, PPCs are smaller in size and lighter in weight[78]. For example, with simple cubic lattices, a saturated stopband is realized for a superlattice with a lattice constant of only 140 nm and a 7 layer thickness (the total thickness is ~ 1 μm). Importantly, the volume fraction of the metal for a lattice with 200 nm particle spacing is less than 0.10. Moreover, the technique, which allows one to explore the combined effects of both the PBG and the plasmonic properties of NPs, hold promise for making and exploring PPC materials that may prove useful in plasmonic cavity structures[79, 80], optical nanocircuits[81], and low-loss metamaterials[82].

3.5 Methods

3.5.1 Finite-Difference Time-Domain (FDTD) Simulation

FDTD simulations were run with a commercial package Lumerical FDTD Solutions v.8.12.631. The dielectric functions of gold, silver, aluminum and copper were adopted from the

experimental data obtained by Johnson and Christy (JC)[51], Shiles *et al.*[83] and Hagemann *et al*[84], respectively. The refractive index of silica was assumed to be 1.46. In order to obtain the reflectance spectra, an infinite thin slab model was used, unless otherwise specified, where periodic boundary conditions were adopted in the x and y directions such that a simple cubic unit cell was repeated infinitely in the x-y plane. A perfectly matched layer boundary condition was used in the z direction, which was also the light propagation direction. The length of the superlattice in the z direction was determined by the number of layers and the lattice constant in the z direction. The infinite thin slab model assumes that only the center of the reflected light is collected, namely not counting light reflected at the edge and side of the photonic crystals. The validity of this model for our experimental setup and DNA-nanoparticle (NP) superlattice was previously demonstrated in the literature.[20] Illumination with light occurs in air (n_0 = 1), and the crystal is assumed to lie on top of a glass substrate (n_s = 1.44). For band-structure calculations, a single unit cell for the simple cubic lattices and four unit cells for the diamond lattice were simulated with Bloch boundary conditions. More than ten dipole sources with random orientation and location within the simulation region were used to excite all optical modes in the lattices. More than ten randomly located time monitors were used to collect the signal in the time domain, and Fourier transform was performed to convert data into the frequency domain.

3.5.2 Nanoparticle Synthesis and Characterization

Gold nanocubes (88 nm edge length, >95% were cube shaped with a <5% variation in size) were synthesized according to a seed-mediated method[85]. The uniform seeds prepared *via* iterative reductive growth and oxidative dissolution reactions are critical to the uniformity of the final

products. Particle uniformity was characterized based on statistical analysis of Hitachi H8100 transmission electron microscope (TEM) images (Figure 3.6).

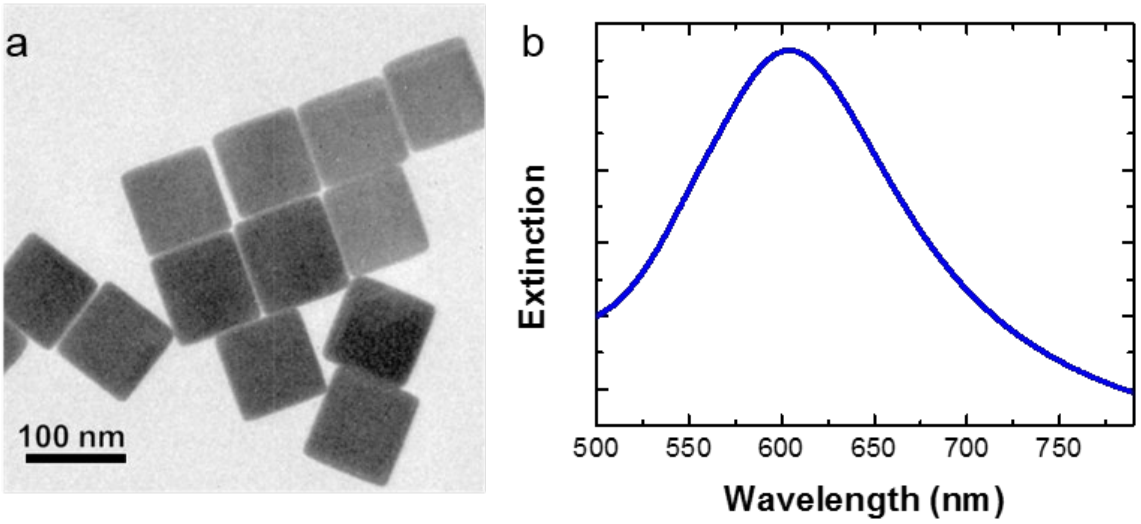

Figure 3.6. Characterization of 88 nm nanocubes. A representative TEM image (a) and UV-Vis spectrum (b) of the monodisperse nanocubes.

3.5.3 DNA Design, Synthesis and Purification

DNA strands used in this work were designed according to the literature recommendations[86, 87]. Detailed DNA sequences can be found in Table 3.1. They have three key components: an anchor strand, a linker strand, and duplexer strands. The anchor strand with a thiol group allows them to be adsorbed onto gold nanoparticles, a dA_{10} region that increase the flexibility (light gray)[41], and a region that can hybridize to the linker strand (dark gray). The linker strand contains three regions: an 18-base sequence (dark blue) complementary to the dark gray region of the anchor strand; some repeated 40-base spacer sequences (dark green) which are designed for conveniently controlling the length of the "DNA bonds"; and a 4-base self-complementary sticky end (light blue) which determines the interaction between the assembling

nanoparticles. Each region is separated by a single base A to provide some flexibility. The duplexer strands (light green) can hybridize to the 40-base spacer sequences in the linker strand (dark green).

Table 3.1. DNA sequences used in this work. The three regions of linker strand are highlighted with different color.

	DNA sequence (5'–3')	Number of base
Anchor strand	TCA ACT ATT CCT ACC TAC AAA AAA AAA A SH	28
Linker strand	GTA GGT AGG AAT AGT TGA A TTTTTTTTTTT ACT GAG CAG CAC TGA TTTTTTTTTTTT A GCGC	64
Duplexer strand	AAAAAAAAAAAAA TCA GTG CTG CTC AGT AAAAAAAAAAAA	40

DNA strands in this work were synthesized on a solid-support with a MM48 synthesizer (BioAutomation) on a solid-support with reagents purchased from Glen Research and purified via reverse-phase high-performance liquid chromatography (HPLC; Agilent). Matrix-assisted laser desorption ionization time-of-flight mass spectrometry (MALDI-TOF-MS) was used to confirm the molecular weight and purity of HPLC-purified DNA. Concentration was determined by UV-vis spectrometry. The extinction coefficient of each DNA strand was calculated with OligoAnalyzer tool from Integrated DNA Technologies.

3.5.4 Nanoparticle Functionalization and Assembly

Nanocubes were chemically functionalized with anchor strand through literature procedures[16, 86, 87]. The as-synthesized nanocubes were collected by centrifugation and washed with H_2O. This process was repeated. After removing the supernatant, the colloid was re-dispersed

in an aqueous solution of the desalted anchor strand (2 OD_{260} of DNA for 1 OD_{SPR} of nanocube). Note that this strand prior to use was maintained in the reduced state with dithiolthreitol (DTT, Sigma Aldirich). Both the DTT and salt must be removed prior to particle modification[88]. Then, the mixture was brought into 0.01 M phosphate buffer solution (PBS) and 0.01% sodium dodecyl sulfate (SDS) solution and was agitated on a shaker (~1000 rpm) for 0.5 hour. Then, the nanocubes were treated by slow addition of NaCl, which is leads to increased DNA loading[88]. The salt concentration of the nanocube solution was successively increased from 0.05 M to 0.1 M to 0.2 M to 0.3 M to 0.4 M to 0.5 M NaCl using a 2 M NaCl stock solution. These additions were done sequentially with 10 s sonication and 0.5 hour shaking between each salt addition. The colloid was treated with overnight shaking after the final salt addition to insure maximum DNA loading. Free DNA strands were removed by three rounds of centrifugation with 0.01% SDS solution. The final pellet was re-suspensed in a solution contained 0.01% SDS, 0.01 M PBS and 0.5 M NaCl.

The DNA linker strand was mixed with duplexer strand in a solution containing 0.5 M NaCl and 0.01 M PBS, and then incubated at 40 ºC for 0.5 hour for pre-hybridization. The duplexed DNA linker solution was then added into the functionalized nanocube colloid in excess to the amount of the anchor strands on particle surface. The mixture was allowed to incubate overnight at room temperature to form aggregates. 150 μL solutions with aggregates were pipetted into 150 μL PCR 8-tube strips (Life Technologies) and placed into a thermal cycler (Life Technologies). The temperature of the thermal cycler was first increased to 60 ºC, and then slowly cooled to room temperature in a rate of 0.1 °C per 10 minutes. The slow cooling rate provides sufficient time for the superlattice to reach equilibrium during the assembly process[17].

3.5.5 Superlattice Characterization

Nanocube superlattices were embedded in silica before electron microscope, optical microscope and small angle X-ray scattering (SAXS) characterization. This method can preserve crystal symmetry and lattice parameter when superlattices are transferred from solvent[50]. Scanning electron microscope (SEM; Hitachi SU8030) and scanning transmission electron microscope (Hitach HD2300) were used to observe the morphologies of nanocube superlattice. SAXS experiments, which reveal lattice parameters (Figure 3.7), were performed at the DuPont-Northwestern-Dow Collaborative Access Team (DND-CAT) beamline of the Advanced Photon Source at Argonne National Laboratory. X-rays with λ= 1.24 Å (E = 10 keV) were used.

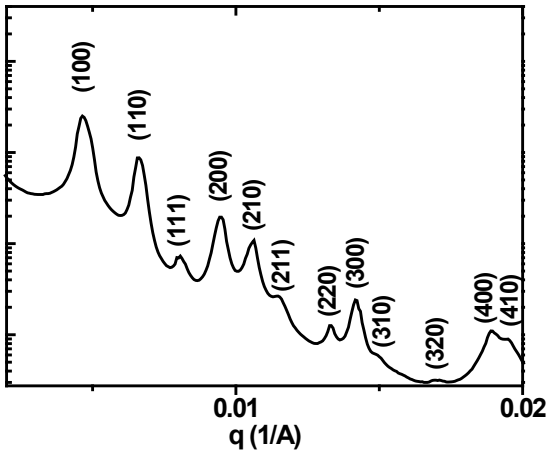

Figure 3.7. SAXS data of nanocube superlattice. The lattice parameter of the nanocube superlattice is 134 nm based on the SAXS data.

3.5.6 Optical Measurements

Silica embedded superlattices[50] were first drop cast onto plasma cleaned Indium Tin Oxide (ITO) coated glass slides, and the solvent was fully evaporated, resulting in a population of superlattices with their flat surfaces lying parallel to the substrate. Superlattices were then observed and located with both a Zeiss Axio Observer.Z1 microscope and a Hitachi SU8030 SEM to ensure proper orientation and a flat top surface. A coverslip deposited with anti-reflection coating purchased from Evaporated Coatings Inc. is then fixed close to the sample by carbon tape at the corners. Subsequently, immersion oil with a refractive index matching that of silica was slowly injected in-between the coverslip and the glass slide, such that the samples were fully immersed in the oil. This effectively provides an optically homogeneous background for the silica-embedded superlattices. A Xenon lamp (XBO 75) with a broad-band spectrum (300 – 1100 nm) was used as the light source. In bright field (BF) reflection mode, the sizes of field-stop and aperture were minimized to minimize the angle of incident light. A 50× objective (N.A. 0.8) was used to collect

light from only the center of the superlattices. A spectrometer with 50 g/mm grating (Princeton Instrument) and a charge coupled device (PyLoN) were connected to the microscope and were used to collect the backscattering spectra. A slit (50 μm) was used to extract the backscattering spectrum from a thin line at the center of the superlattice, which enables the use of the thin slab model in FDTD to simulate this system[20]. Finally, a background spectrum was chosen from a clean region near the superlattice and was used to remove the signal from the background in the backscattering spectrum.

3.6 Supplementary Analysis

3.6.1 Considerations in Designing Photonic Crystals

In the one-dimensional case, the PC can be viewed as periodically alternating layers of high- and low-index materials or a distributed Bragg reflector[89], and the PBG can be identified as the spectral region with high reflectance (low transmittance) in the far-field spectra, in other words a stopband in the reflectance spectra. For incident angles perpendicular to the layers, the Bragg condition is best met when the optical length of each layer of the PC is a quarter of the relevant wavelength, equation (3.1).

$$\frac{\lambda_0}{4} = d_h n_h = d_l n_l \tag{3.1}$$

Here, λ_0 is the center wavelength of the photonic band, and d_h, n_h and d_l, n_l are the thicknesses and refractive indices of the high- and low-index materials, respectively[37]. The higher the contrast between the high and low refractive indices, the broader the photonic band width, as governed by equation (3.2):

$$\frac{\Delta\lambda_0}{\lambda_0} = \frac{4}{\pi} \arcsin\left(\frac{n_h - n_l}{n_h + n_l}\right) \tag{3.2}$$

where $\Delta\lambda_0$ and λ_0 are the width and center frequency of the band[90]. The maximum reflectance (R_{max}) is not only dependent on the index contrast but also on the number of layers through the equation:

$$R_{max} = \left[\frac{n_0(n_h)^{2N} - n_s(n_l)^{2N}}{n_0(n_h)^{2N} + n_s(n_l)^{2N}}\right]^2 \tag{3.3}$$

n_0 and n_s are the indices of the top and bottom layers outside of the crystal, and N is the number of layers of the high-index material[37].

For all of the fabrication methods for photonic crystals, a critical parameter for achieving large PBG and high reflectance is the refractive index contrast between the high- and low-index materials, the importance of which can be seen in equations (3.1)-(3.3) above[63-65]. Moreover, as can be seen in equation (3.1), in order to satisfy the Bragg condition at certain wavelengths, the thickness of each layer can be reduced by using materials with a higher index, which is important for the miniaturization of devices.

3.6.2 Spectra of a Single Nanoparticle

For a systematic investigation of the effect of lattice parameters on the stopband features, FDTD simulations are performed where spherical Au NPs with 54 nm radius are arranged in a lattice structure, unless otherwise specified. Figure 3.8 shows the absorption, scattering, and extinction spectra of a single spherical NP in silica host.

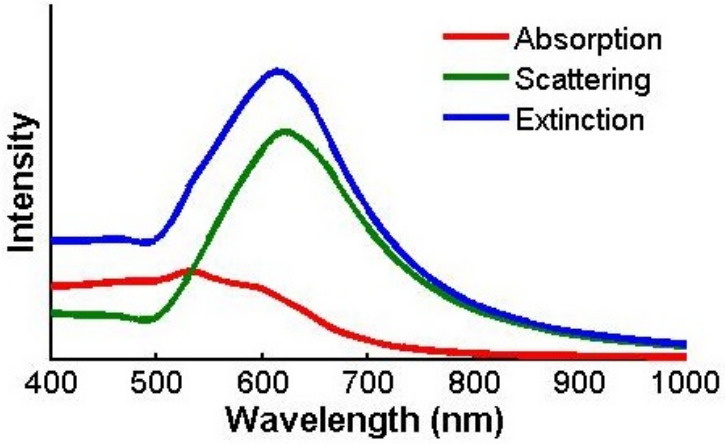

Figure 3.8. Absorption, scattering, and extinction spectra of a single NP. The radius of the spherical NP is 54 nm. The NP is modeled to be in silica with a refractive index of 1.46.

3.6.3 Results for Cubic Superlattices

The dependence on N can be seen in Figure 3.9, where the reflection spectra of superlattices with simple cubic (cP) lattice symmetry, 200 nm lattice constant but different number of layers (1 – 20) are shown. The stop band between 600 – 770 nm saturates at only 7 layers. However, as the lattice constants increases, more layers are needed for the reflection band to saturate (Figure 3.10). To keep the computational time reasonable, the exact dependence on the number of layers is not examined, and 7 layers of superlattices are used (i.e. $N = 7$) in all simulations throughout the main text, unless otherwise specified.

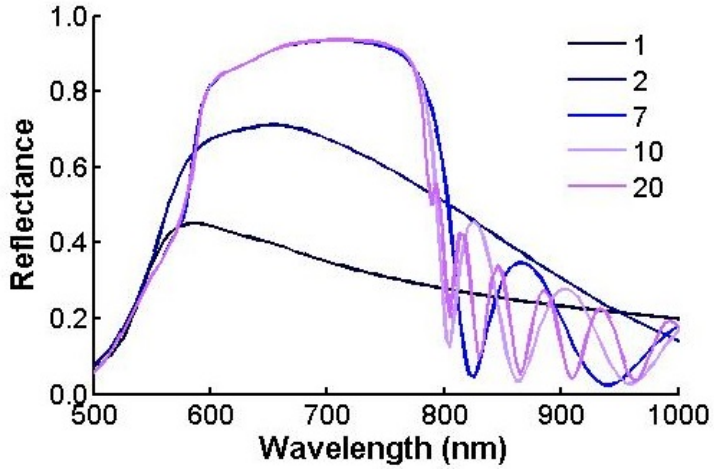

Figure 3.9. Thickness dependence of the reflectance spectra. The spherical NP radius is 54 nm, and the crystal has simple cubic symmetry and a 200 nm lattice constant. The number of layers is shown in the legend. The reflectance spectra resemble that of dielectric photonic crystals. When there is only one layer, the structure is not periodic in the light propagation direction, thus no Bragg reflection occurs. As the number of layers increases, the reflection band appears and saturates quickly. The number of layers at which the stop-band saturates is 7 in this case.

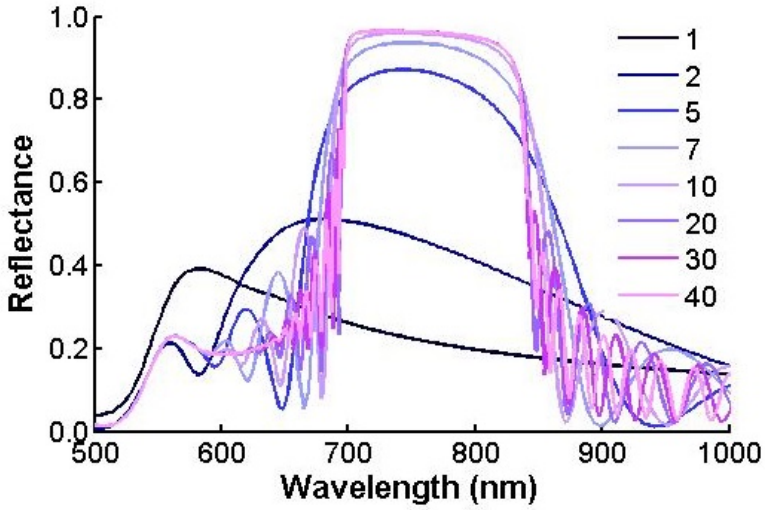

Figure 3.10. Thickness dependence of the reflectance spectra of a crystal with larger lattice constant. The NP radius is 54 nm, and the crystal has simple cubic symmetry and a 240 nm lattice constant. Again, the number of layer is shown in the legend. In contrast with the superlattice with a smaller lattice constant (Supplementary Fig. 4), the stop-band is not saturated until the number of layers exceeds at least 10.

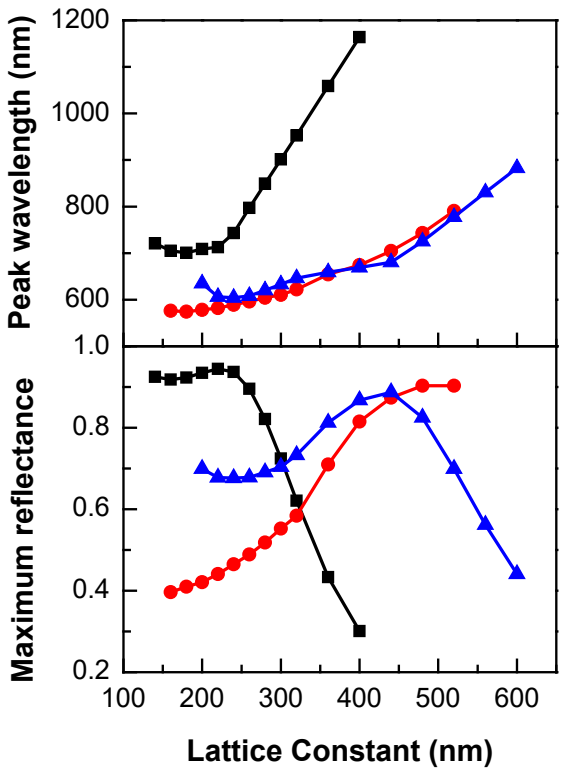

Figure 3.11. Dependence of maximum reflectance and its corresponding wavelength on the lattice constant of cP, cI and cF lattices. The NP radius is 54 nm, and 7 layers are used. The spectra of these data points are shown below.

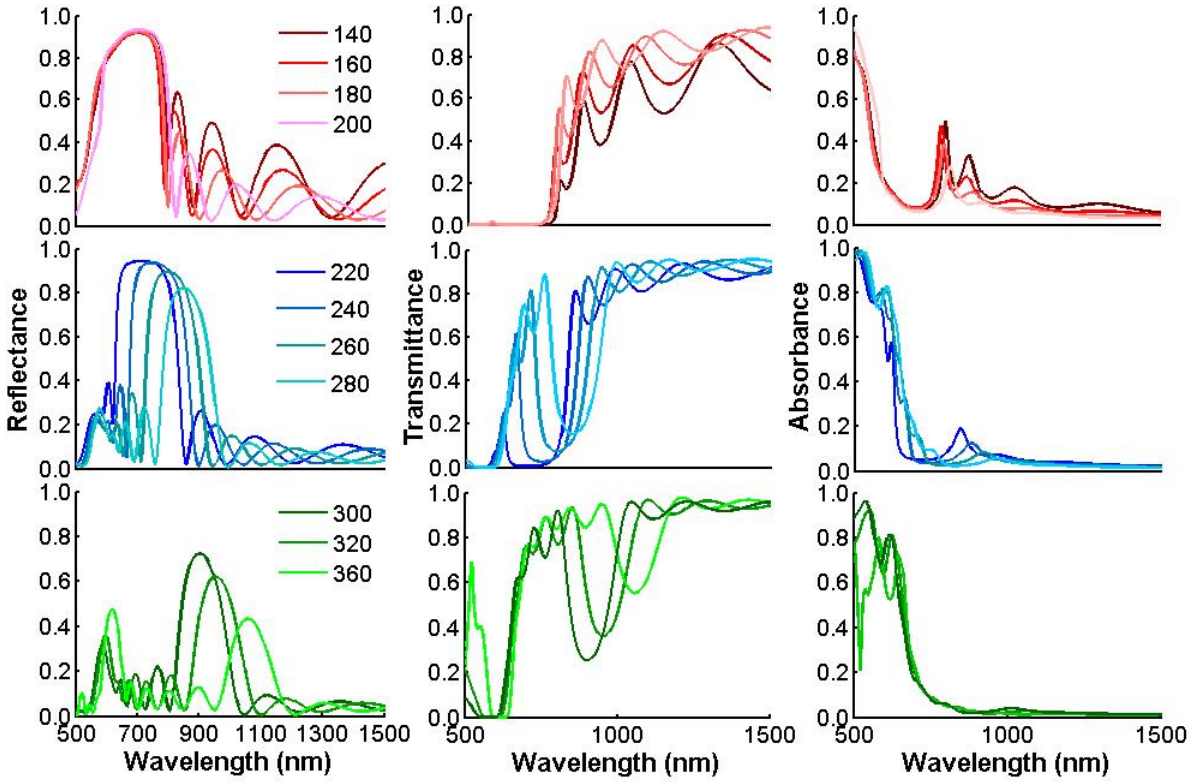

Figure 3.12. Dependence on lattice constant of the reflectance, transmittance and absorbance spectra of cP lattices. The NP radius is 54 nm, and the layer number is fixed at 7. Lattice constants are shown in the legends. The range of lattice constants was chosen so that strong near-field coupling between NPs is avoided. As can be seen, the LSPR peak overlaps with the photonic band when the lattice constant is at or below 200 nm (top), while it is separated at a lattice constant equal to or larger than 220 nm (middle). When the lattice constant further increases beyond 300 nm, the first order peak further red shifts and a second order peak arises close to the LSPR (bottom).

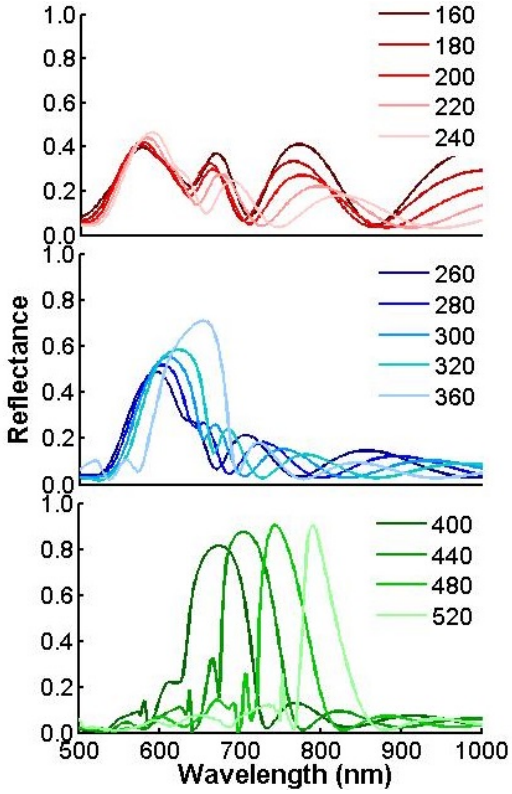

Figure 3.13. The reflectance spectra dependence on lattice constant for cI lattices. The NP radius is 54 nm, and the lattices have 7 layers, namely 3 unit cells. Lattice constants are shown in the legends.

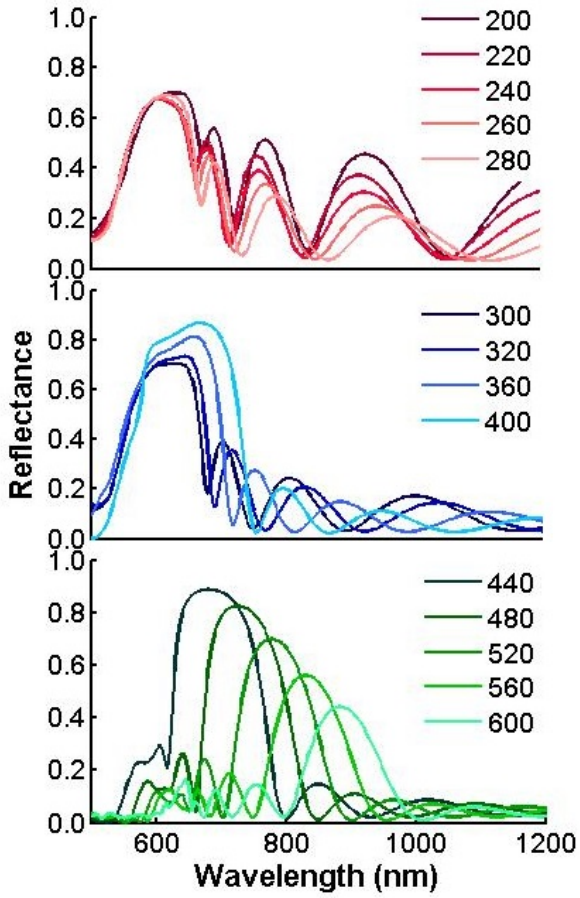

Figure 3.14. Dependence on lattice constant of the reflectance spectra of cF lattices. The NP radius is 54 nm, and the lattices have 7 layers. Lattice constants are shown in the legends.

3.6.4 Results of Tetragonal Superlattices

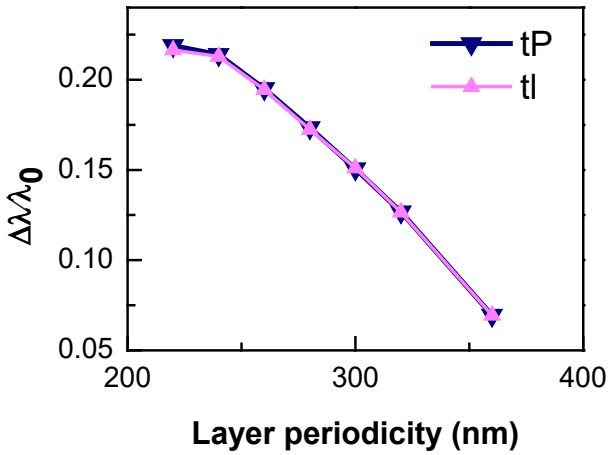

Figure 3.15. Dependence of the bandwidth on the layer periodicity of tP and tI lattices. The NP radius is 54 nm, and the lattices have 7 layers. The lattice constant within each layer is kept at 200 nm. The reflectance spectra of the data points are shown below.

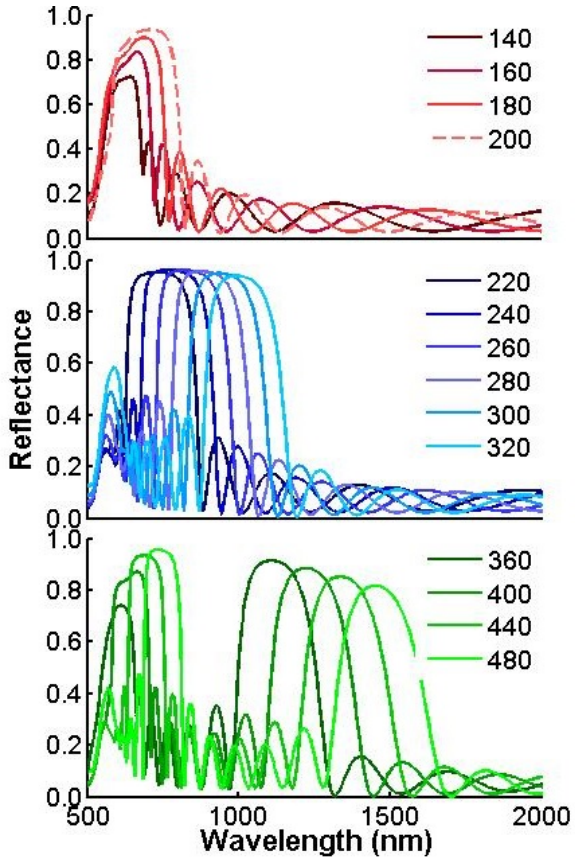

Figure 3.16. Dependence on the layer periodicity of the reflectance spectra of tP lattices. The NP radius is 54 nm, and the lattices have 7 layers. Lattice constants in each metallic layer (*a*) is kept at 200 nm. Layer periodicities are shown in the legends. Interestingly, as the layer periodicities increase, the Bragg band starts from being convoluted with LSPR (140 – 200 nm), to separated (220 – 320 nm), to producing second order band that's convoluted with LSPR (360 – 400 nm), to second order band separated from LSRP (440 – 480 nm).

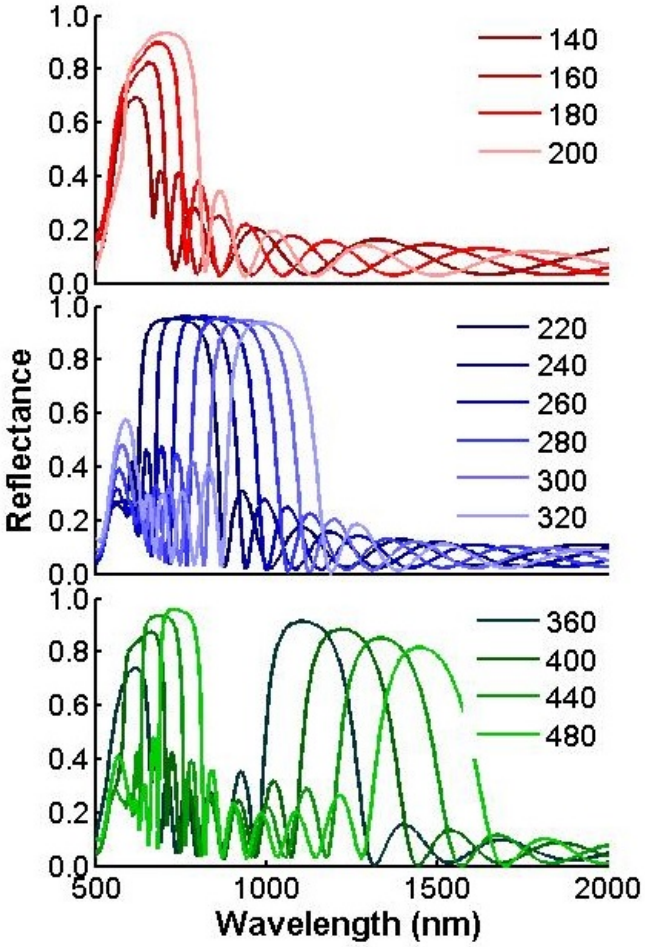

Figure 3.17. Dependence on the layer periodicity of the reflectance spectra of tI lattices. The NP radius is 54 nm, and the lattices have 7 layers. Lattice constants in the x-y plane (*a*) is kept at 200 nm. Layer periodicities are shown in the legends. Notice how similar the spectra are compared to the ones in Supplementary Figure 11. Similarly, as the layer periodicities increase, the Bragg band starts from being convoluted with LSPR (140 – 200 nm), to separated (220 – 320 nm), to producing second order band that's convoluted with LSPR (360 – 400 nm), to second order band separated from LSRP (440 – 480 nm).

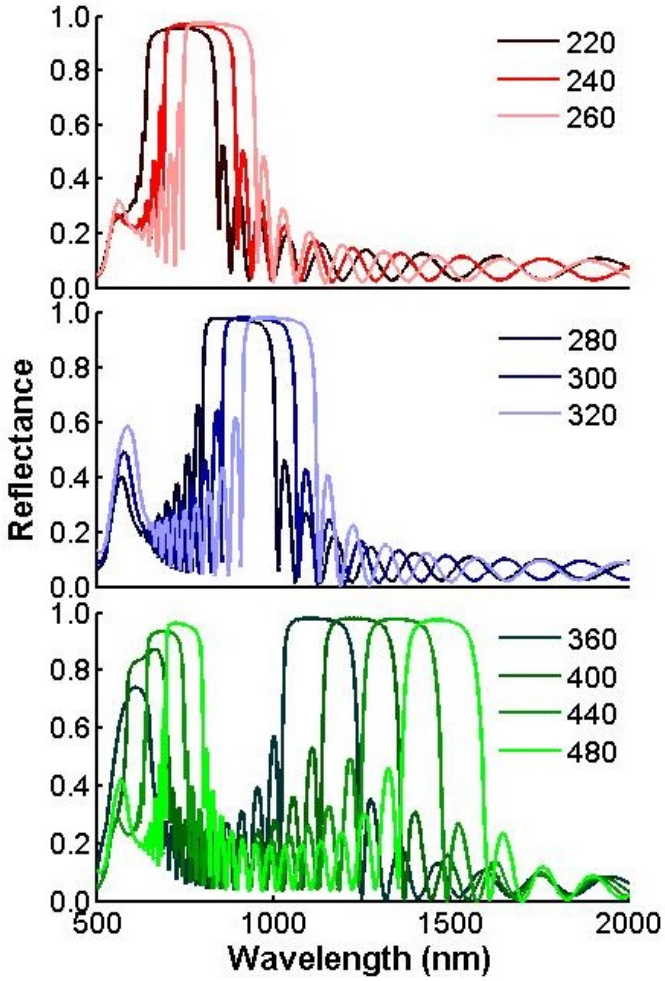

Figure 3.18. Dependence on the layer periodicity of the reflectance spectra of tP lattices with 15 layers. The NP radius is 54 nm. This time the lattices have 15 layers. Lattice constant in each metallic layer (*a*) is kept at 200 nm. Layer periodicities are shown in the legends. As the layer periodicities increase, the Bragg band starts from being separated from LSPR (220 – 320 nm), to producing second order band that's convoluted with LSPR (360 – 400 nm), to second order band separated from LSRP (440 – 480 nm).

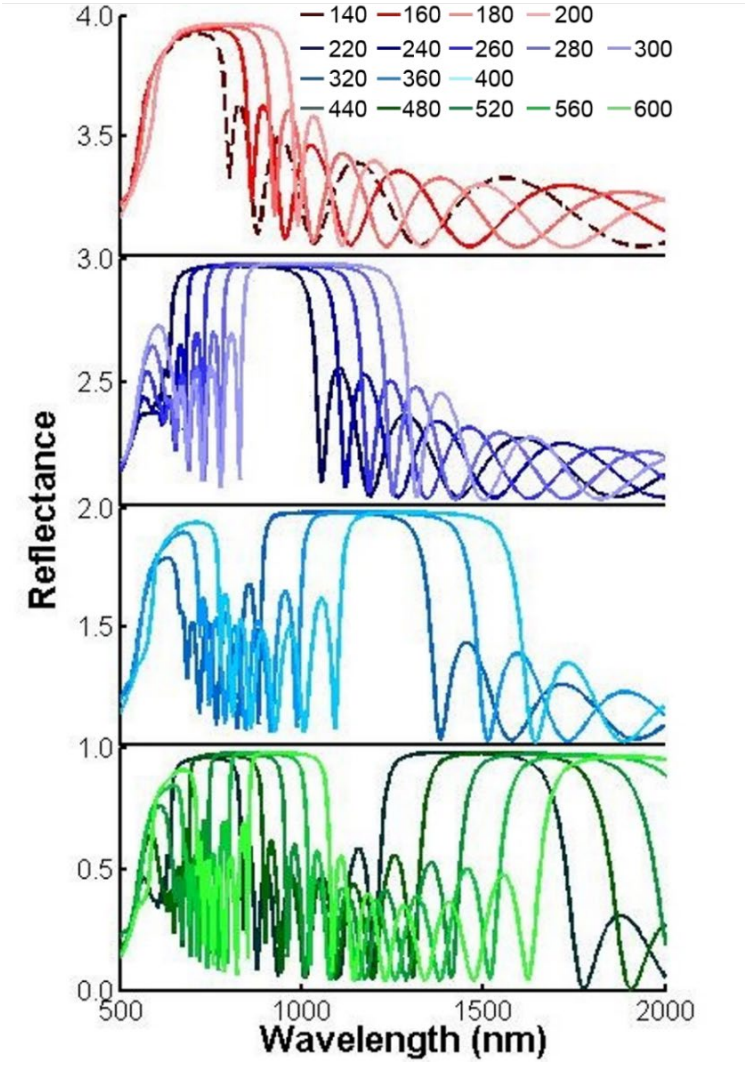

Figure 3.19. Dependence on the layer periodicity of the reflectance spectra of tP lattices with a = 140 nm. The NP radius is 54 nm, and the lattices have 7 layers. Lattice constant in the x-y plane (*a*) is kept at 140 nm, which is smaller than that shown in the Supplementary Figure 11. Layer periodicities are shown in the legends. In this case, large Bragg reflection band is observed for all layer periodicities investigated. More interestingly, as the layer periodicities increase, the Bragg band starts from being convoluted with LSPR (140 – 200 nm), to separated (220 – 300 nm), to producing second order band that's convoluted with LSPR (320 – 400 nm), to second order band separated from LSRP (440 – 600 nm).

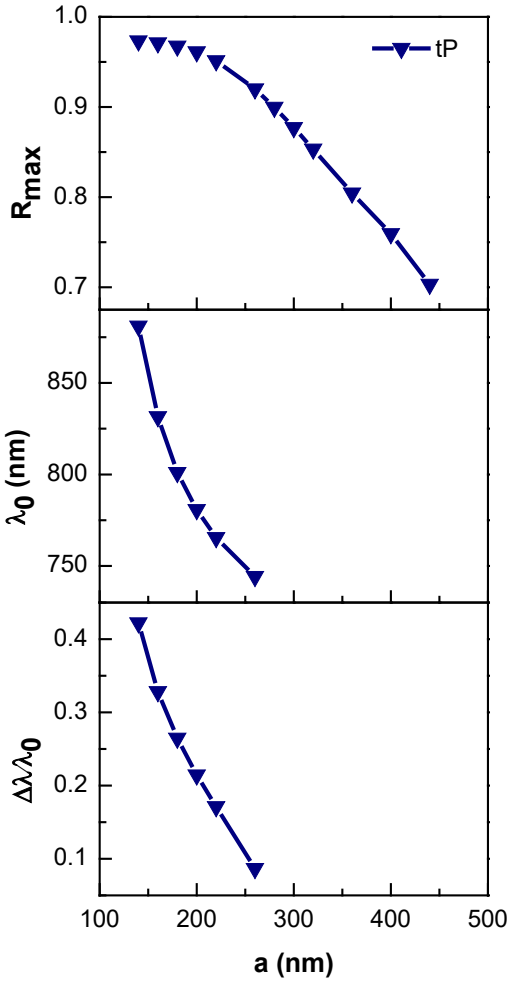

Figure 3.20. Dependence of maximum reflectance, λ_0, and $\Delta\lambda/\lambda_0$ on the lattice constant (a) in each layer of tP lattices. The NP radius is 54 nm, and the lattices have 7 layers. Layer periodicity is kept at 240 nm.

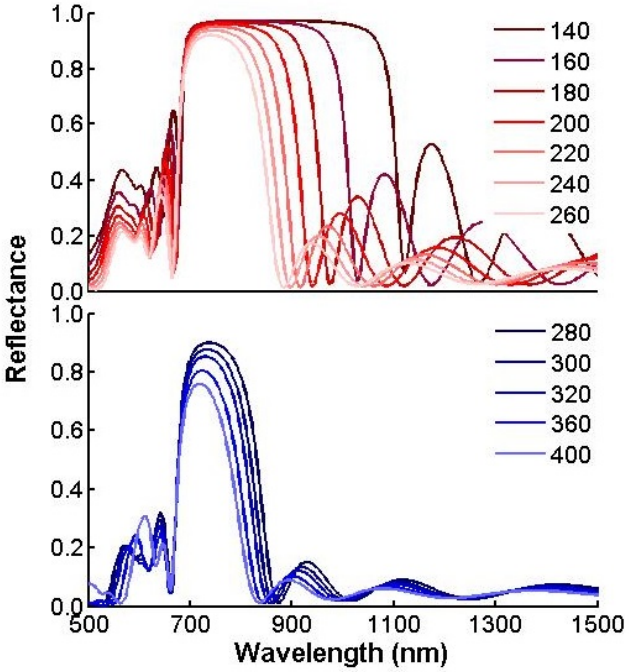

Figure 3.21. Dependence of the reflectance spectra on the lattice constant in each layer of tP lattices. The NP radius is 54 nm, and the lattices have 7 layers. Layer periodicity is kept at 240 nm. Lattice constants in each metallic layer are shown in the legends. Interestingly, as the lattice constants in each layer increase, the lower energy side of all the reflection bands seems to be at the same wavelength, while the band width and reflectance on the rest of the band decreases.

3.6.5 Results of Orthorhombic Superlattices

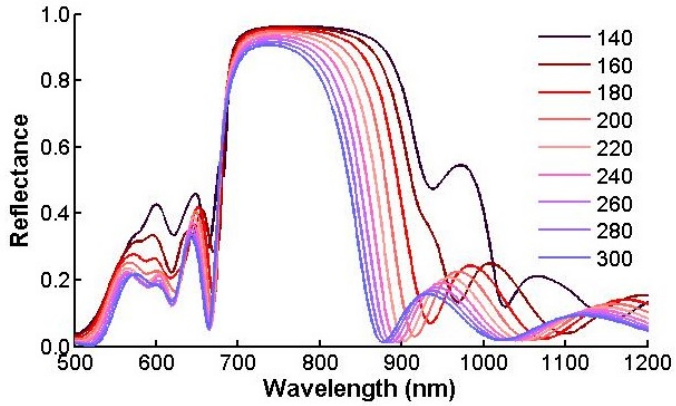

Figure 3.22. The reflectance spectra dependence on the lattice constant in each layer of oP lattices. The NP radius is 54 nm, and the lattices have 7 layers. Layer periodicity is kept at 240 nm. One lattice constant in each metallic layer (*a*) is kept constant at 250 nm, while the other (*b*) is shown in the legends. Again, the higher energy side of all the reflection bands seems to be at the same wavelength, while the band width and reflectance on the rest of the band decreases.

3.6.6 Results of Hexagonal Superlattices

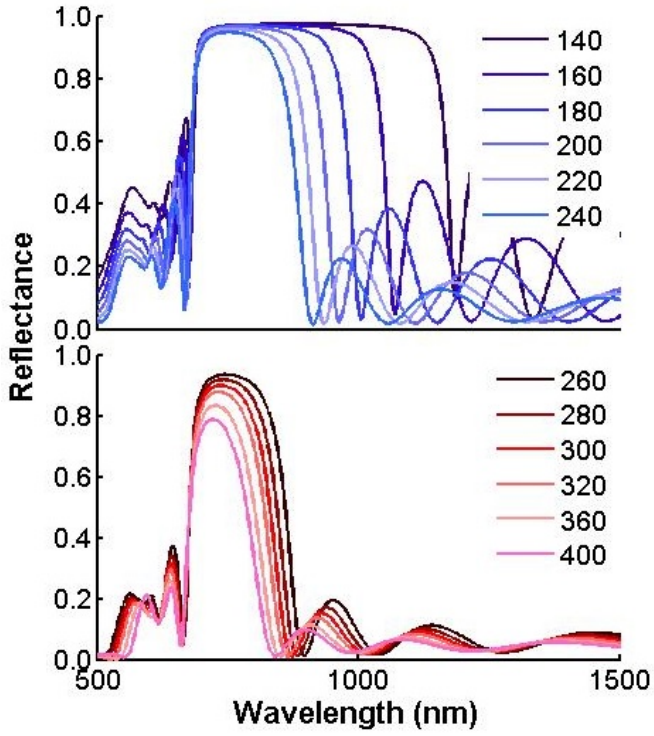

Figure 3.23. Dependence on the NP spacing in each layer of the reflectance spectra of hP lattices. The NP radius is 54 nm, and the lattices have 7 layers. Layer periodicity is kept at 240 nm. Lattice constant in each layer is shown in the legends. The higher energy side of all the reflection bands seems to be at the same wavelength, while the band width and reflectance on the rest of the band decreases.

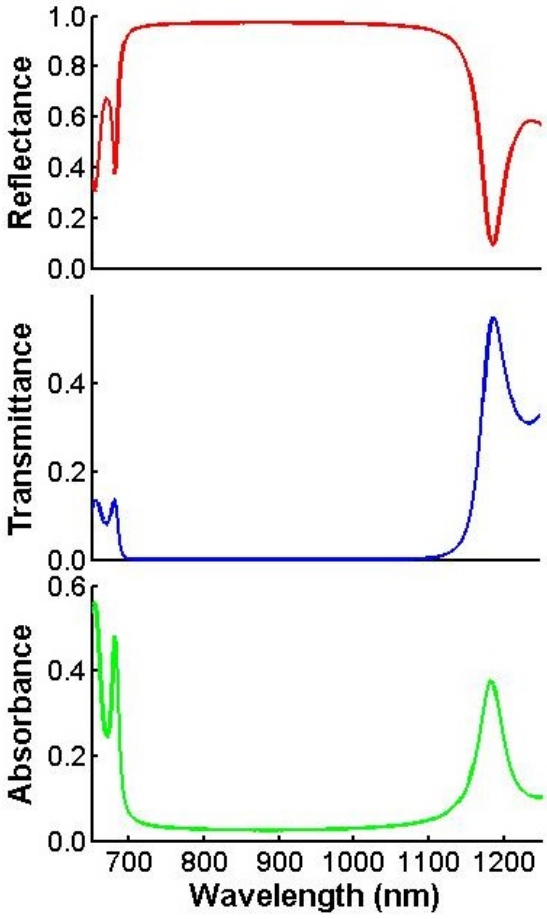

Figure 3.24. Reflectance, transmittance and absorbance of a hP lattice. The NP radius is 54 nm, and the lattices have 7 layers. The lattice constant in each layer is 140 nm, and the layer periodicity is 240 nm. This is the same lattice with the largest volume fraction in the previous figure. The highest reflectance is ~97%, due to the material absorption, as can be seen in absorbance spectrum (bottom).

3.6.7 Results of Trigonal Superlattices

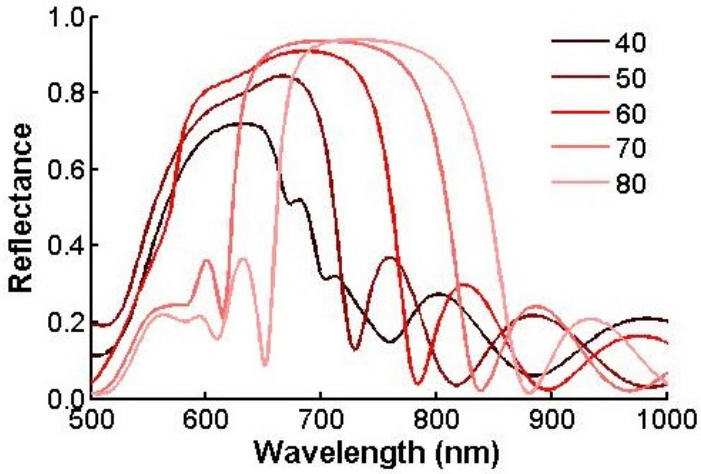

Figure 3.25. Dependence on the angle between each layer of the reflectance spectra of hR lattices. The NP radius is 54 nm, and the lattices have 7 layers. Layer periodicity is kept at 240 nm. Lattice constant in each layer is shown in the legend.

3.6.8 Results of Monoclinic Superlattices

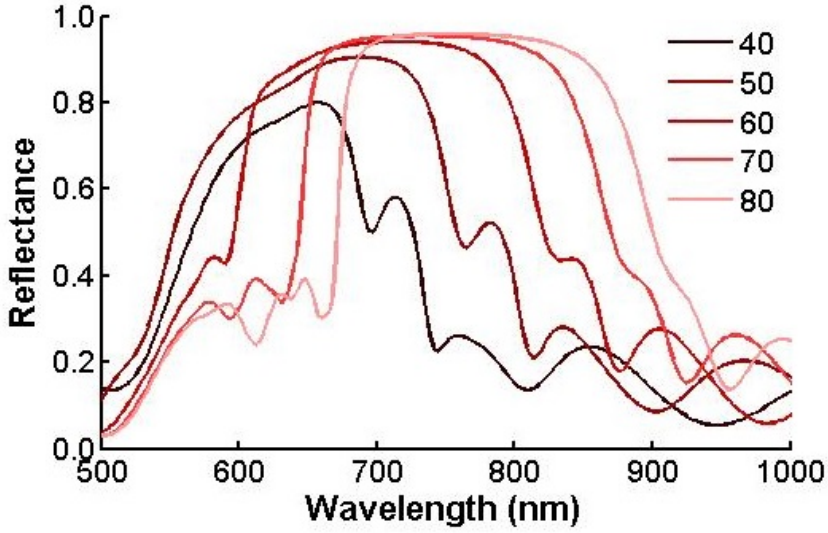

Figure 3.26. Dependence on the angle between each layer of the reflectance spectra of mP lattices with fixed c. The NP radius is 54 nm, and the lattices have 7 layers. The three monoclinic lattice constants are kept constant. The angle is shown in the legend.

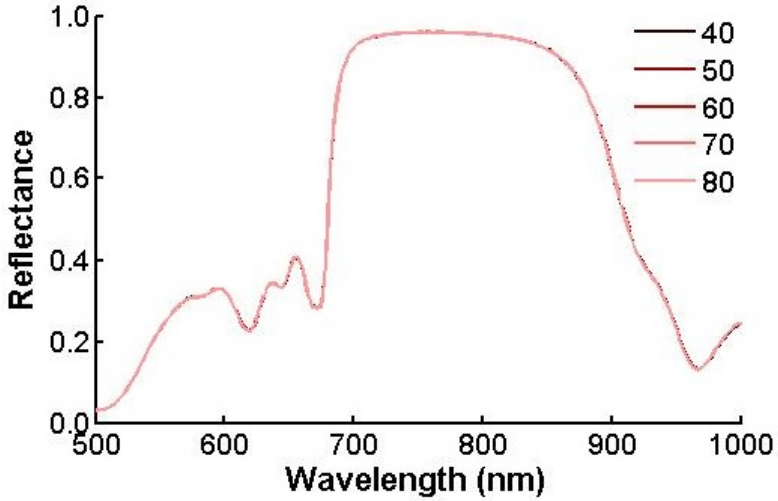

Figure 3.27. Dependence on the angle between each layer of the reflectance spectra of mP lattices with fixed z. The NP radius is 54 nm, and the lattices have 7 layers. The lattice constant in each layer and the layer periodicity are kept constant. The angle is shown in the legend. All the spectra are exactly on top of each other.

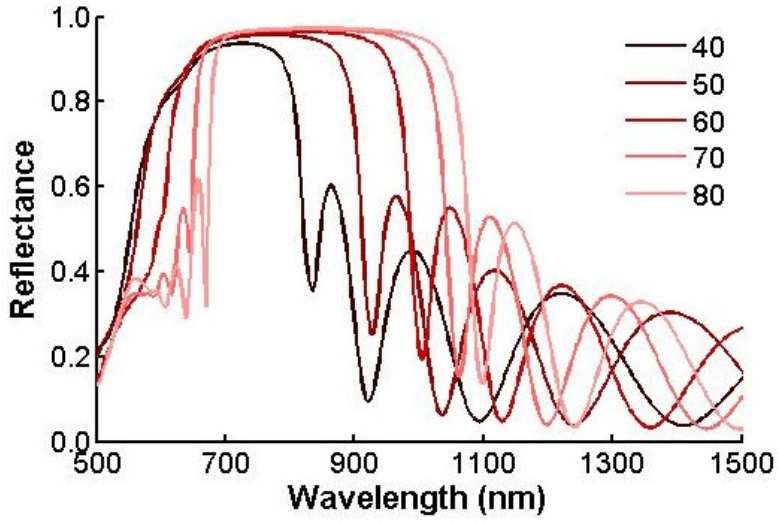

Figure 3.28. Dependence on the angle between each layer of the reflectance spectra of mC lattices with fixed c. The NP radius is 54 nm, and the lattices have 7 layers. The three monoclinic lattice constants are kept constant. The angle is shown in the legend. The reflectance of the mC lattices is higher than that of its monoclinic counterpart because of higher volume fraction in each layer.

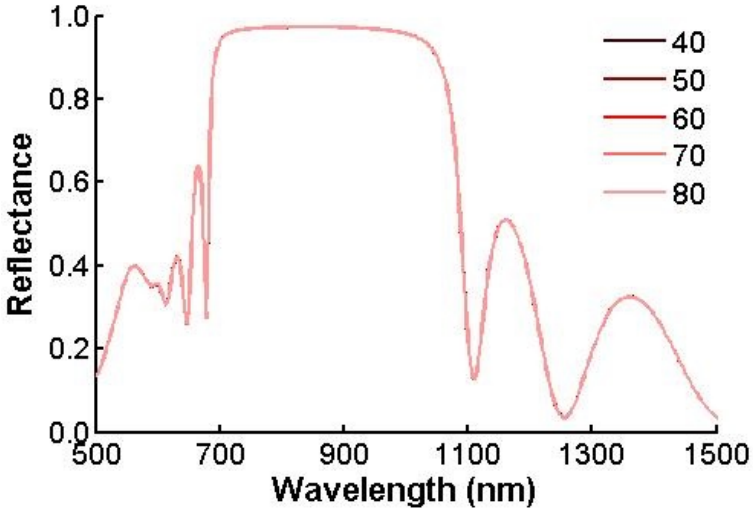

Figure 3.29. Dependence on the angle between each layer of the reflectance spectra of mC lattices with fixed z. The NP radius is 54 nm, and the lattices have 7 layers. The lattice constant in each layer and the layer periodicity are kept constant. The angle is shown in the legend. All the spectra are exactly on top of each other. The reflectance of the mC lattices is higher than that of its monoclinic counterpart because of higher volume fraction in each layer.

3.6.9 Reflectance with Effective Medium Theory and Transfer Matrix Method

Since the volume fraction, rather than the exact arrangement of the NPs, within each NP layer affects the properties of the stop-band, one can use the Maxwell-Garnett Effective Medium Theory (EMT)[20] to obtain the effective index n_{eff} of the NP layer, followed by using the Transfer Matrix Method (TMM)[75], as commonly used in layered dielectric films, to calculate the reflectance and transmittance of the superlattices. The n_{eff} is only dependent on the dielectric constants of the composite materials and the volume fraction by the equation:

$$\frac{\varepsilon_{eff} - \varepsilon_{matrix}}{\varepsilon_{eff} + 2\varepsilon_{matrix}} = FF * \frac{\varepsilon_{Au} - \varepsilon_{matrix}}{\varepsilon_{Au} + 2\varepsilon_{matrix}} \tag{3.4}$$

where *FF* is the fill factor (volume fraction of Au) in each layer, as explained in Figure 3.3 and Figure 3.30. ε_{Au} and ε_{matrix} are the dielectric constant of Au and the background matrix (Au is embedded in silica in this case). The ε_{eff} is the effective dielectric constant of the layer and n_{eff} can then be calculated as the square root of ε_{eff}. The real and imaginary part of the n_{eff} of the NP layers in three simple cubic lattices with 200, 240, and 300 nm lattice constant (*a*) are show in Figure 3.30. As can be seen, the smaller the lattice constant (hence larger *FF*), the larger the real part of n_{eff}, which is important since large index contrast is desired.

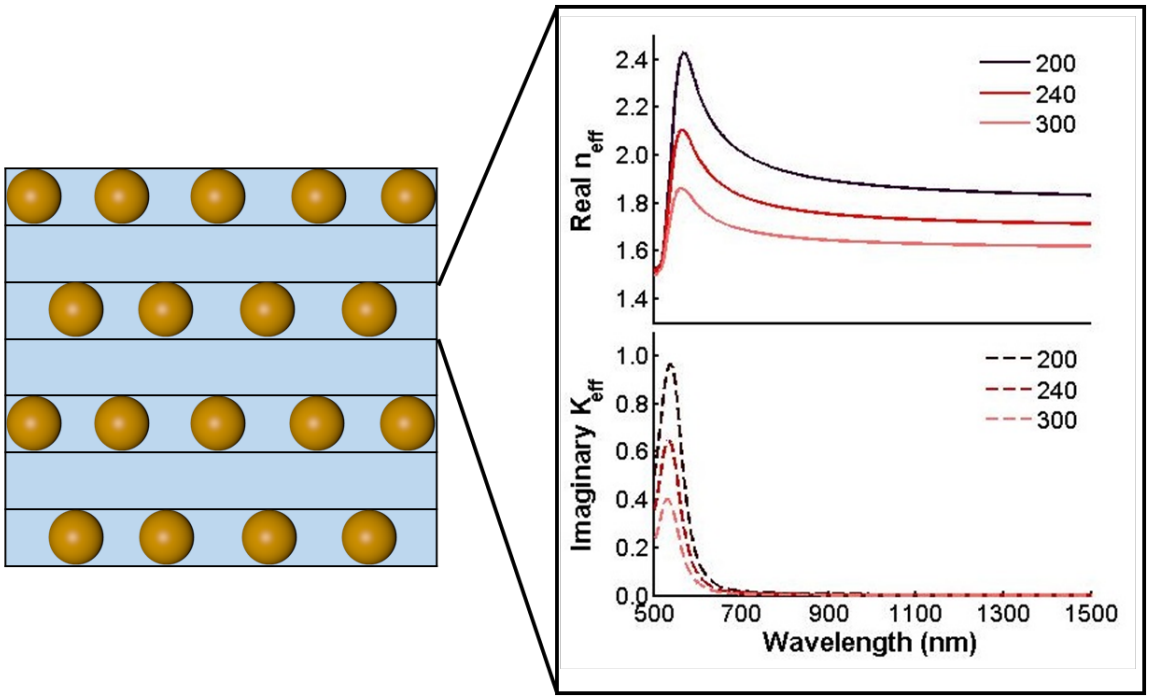

Figure 3.30. The real and imaginary part of the effective index calculated with EMT. Here the thickness of the NP layer is twice that of the NP radius. Simple cubic superlattices are used and the lattice constants are shown in the legend.

Now that we know both n_{eff} and n_{si} (1.46), one can calculate the reflectance, transmittance and absorbance of the layered structure by using the TMM. Figure 3.31 compares the results calculated through the EMT+TMM codes (done in Matlab) and FDTD of the three superlattices mentioned in the previous paragraph. Overall there is good agreement between the two methods, especially at longer wavelength. The EMT+TMM method underestimates the strength of the stop-band, likely because of blurring of the index contrast. In other words, the full FDTD calculation sees much larger dielectric contrasts. The agreement at shorter wavelength (around or below the NP LSPR at ~600 nm) is poorer mostly due to the limitation in EMT. For example, the quadrupole mode at ~ 550 nm is not predicted by EMT. And when a = 200 nm, the LSPR and stop-band is separate with EMT methods, while the two couple with FDTD.

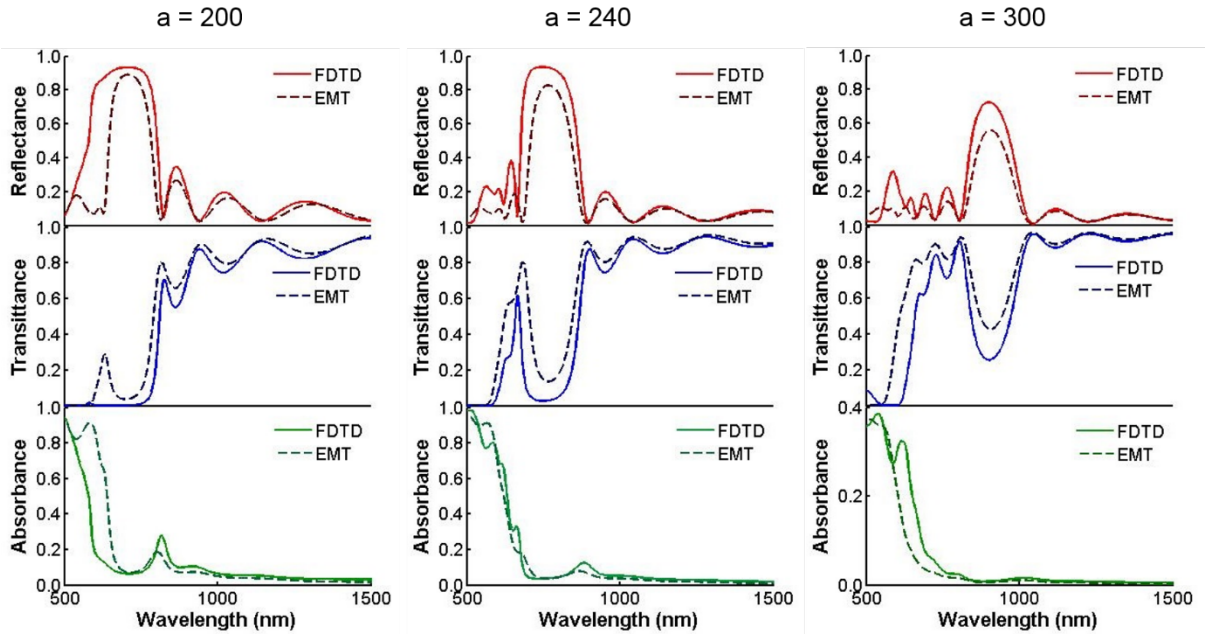

Figure 3.31. Comparison between FDTD and EMT methods. Reflectance (top), transmittance (middle) and absorbance (bottom) spectra of simple cubic superlattices with 7 layers and 200 (left), 240 (center) and 300 (right) nm.

3.6.10 Angle-Dependent Reflectance Spectra

The dependence of reflectance on the incidence angle is investigated through simulation and plotted in Figure 3.32. NPs with 54 nm in radius are arranged in cP lattice with 300 nm lattice constant and 30 layers, in order to ensure sufficient number of layers are used and the reflectance is saturated. The stopband, which is the red-colored broad band in Figure 3.32, blue-shifts as the angle of incidence increases. This is because as the angle of incidence increases, the effective layer periodicity along the light propagation direction decreases, thus the stopband shifts shorter wavelength. The stopband exists up until ~ 50° then gradually disappears at steep angle of incidence, due to the fact the distinction between high- and low-index materials become blurred along a certain range of angles.

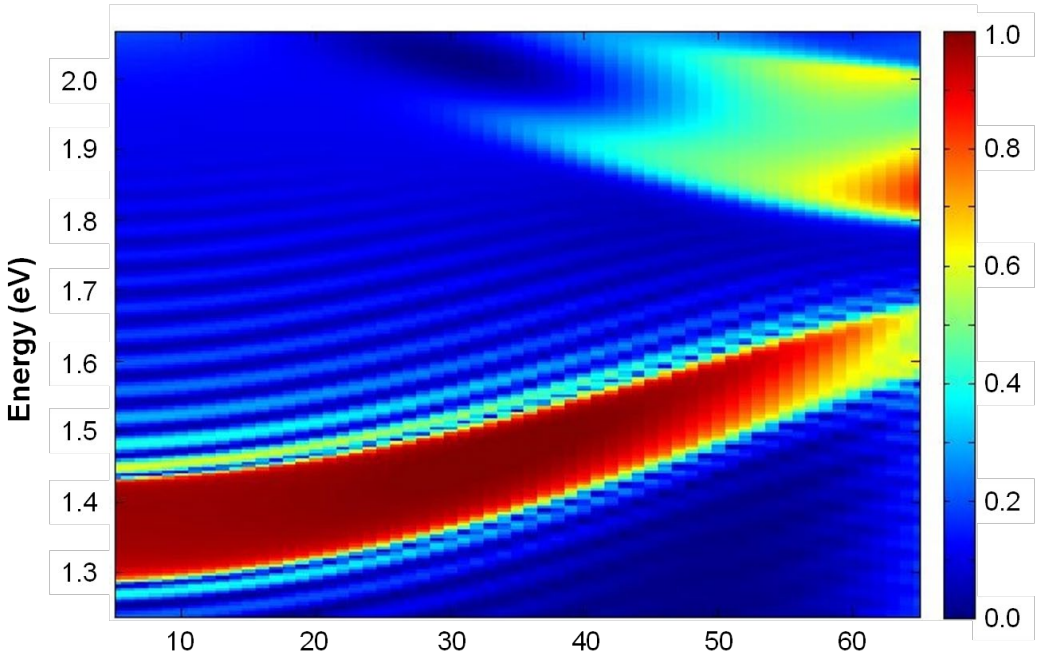

Figure 3.32. Angle-dependent reflectance spectra of simple cubic superlattices. The NPs are 54 nm in radius, and the lattice constant is 300 nm. 30 layers are simulated to ensure sufficient layer number. The stopband blue-shifts as the angle of incidence increases, which can be rationalized since the layer periodicity decreases accordingly. At steep angles (> 50°) the definition between the high- and low-index layers along the light propagation becomes blurry, thus the stopband gradually disappears.

3.6.11 Effect of Nanoparticle Size

The effect of NP size is explored by using cP lattices with the same densities (i.e. constant volume fractions of the overall superlattice) and 7 layers, we compare the photonic properties of superlattices made with nine different NP sizes (10 – 90 nm in radius) and four volume fractions (8.2%, 10%, 15%, 20%). The lattice constants are summarized in Table 3.2.

Table 3.2. Lattice constants in nanometers used for different NP radius (r) and volume fractions (vf) for simple cubic superlattices. Lattice constants are in nm.

r(nm) / vf (%)	10	20	30	40	50	60	70	80	90
8.2	37	74	111	148	185	222	259	296	333
10	35	69	104	139	174	208	243	278	313
15	30	61	91	121	152	182	212	243	273
20	28	55	83	110	138	165	193	220	248

No reflectance larger than 0.9 is observed in 10-40 nm NP superlattices at all six volume fractions (Figure .3.33). For superlattices with 50-90 nm NPs, R_{max} increases to a saturation value Figure 3.35b). Moreover, the larger the NP size, the more the stopband is to the red, which is true for all volume fractions (Figure 3.34 and 3.35c). This is likely because that at a constant volume fraction, the layer periodicity is larger for larger NP size, thus λ_0 increases as predicted by equation (3.4). Likewise, the stopband blue shifts as the volume fraction increases, due to smaller layer periodicity at larger volume fraction. From Figure 35 we see that at sufficient volume fraction both the R_{max} and $\Delta\lambda/\lambda_0$ increases with larger NPs. Thus, at a constant Au volume fraction, larger NPs are more suitable for optimizing PPCs performance.

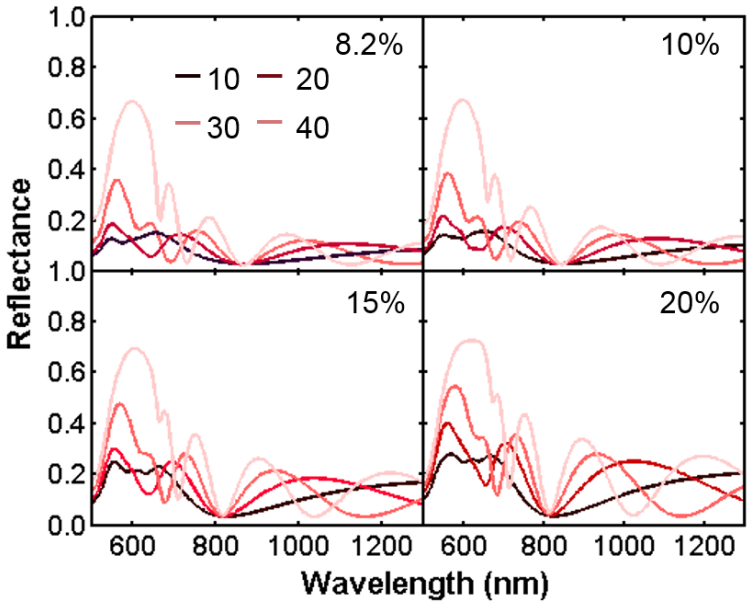

Figure 3.33. Reflectance spectra of simple cubic superlattices with small NP building blocks at four volume fractions. The NP size is indicated in the legend, and the volume fraction is shown in the top-right corner of each plot. The lattices have 7 layers. No reflectance larger than 0.9 exists when the three sizes of NPs are used at all four volume fractions.

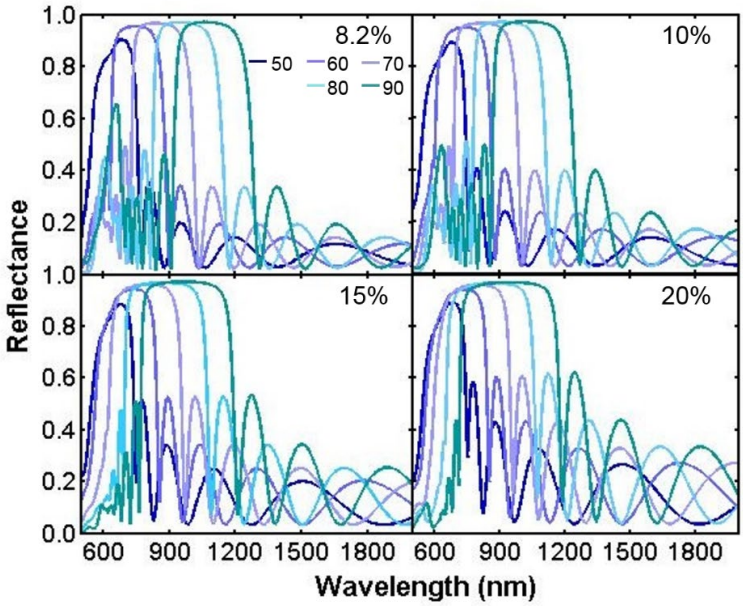

Figure 3.34. Reflectance spectra of simple cubic superlattice with larger NP building blocks at four volume fractions. The NP size is indicated in the legend, and the volume fraction is shown in the top-right corner of each plot. The lattices have 7 layers. As is evident, the stop-band becomes broader with larger NP building blocks.

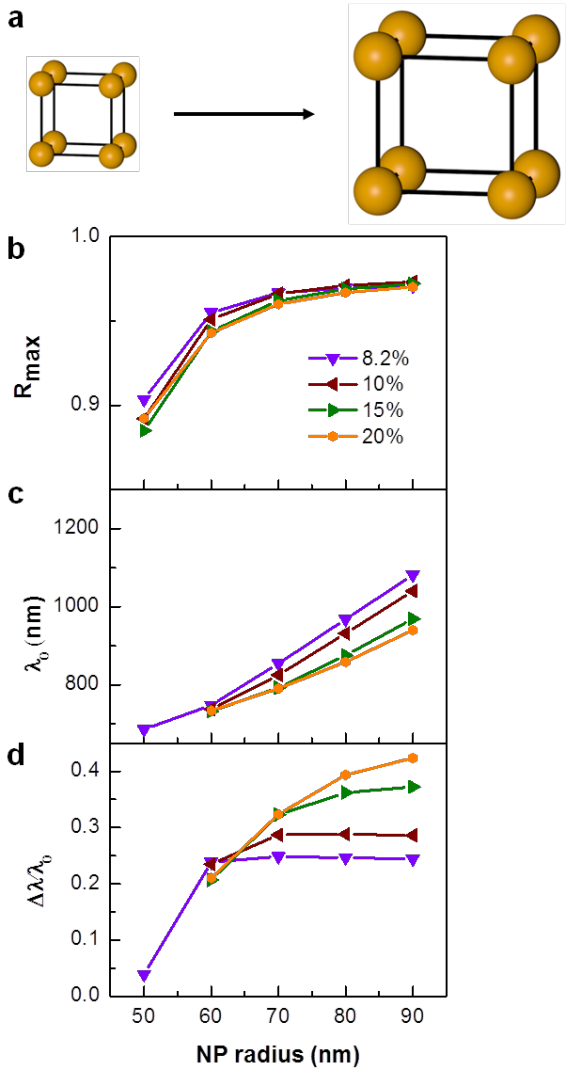

Figure 3.35. NP size as a design parameter for PPCs. a, At the same volume fraction and lattice symmetry (simple cubic), the effect of the NP size on the stopband features is explored. **b-d**, The dependence of R_{max} (**b**), λ_0 (**c**) and $\Delta\lambda/\lambda_0$ (**d**) on NP size of four different volume fractions as shown in the legend.

3.6.12 Bandstructure of PPCs

The stop-band that is observed in the reflectance spectra can also be viewed in the band diagram of the corresponding superlattice. To avoid interband transitions in Au, the Drude model is used to generate the dielectric constant of Au:

$$\varepsilon_D(\omega) = \varepsilon_\infty - \frac{\omega_D^2}{\omega^2 + i\gamma_D\omega} \tag{3.5}$$

where ε_∞ = 11.4577, ω_D = 9.4027 eV, and γ_D = 0.08314 eV. The calculated refractive index is compared with the experimental results from Johnson and Christy in Figure 3.36.

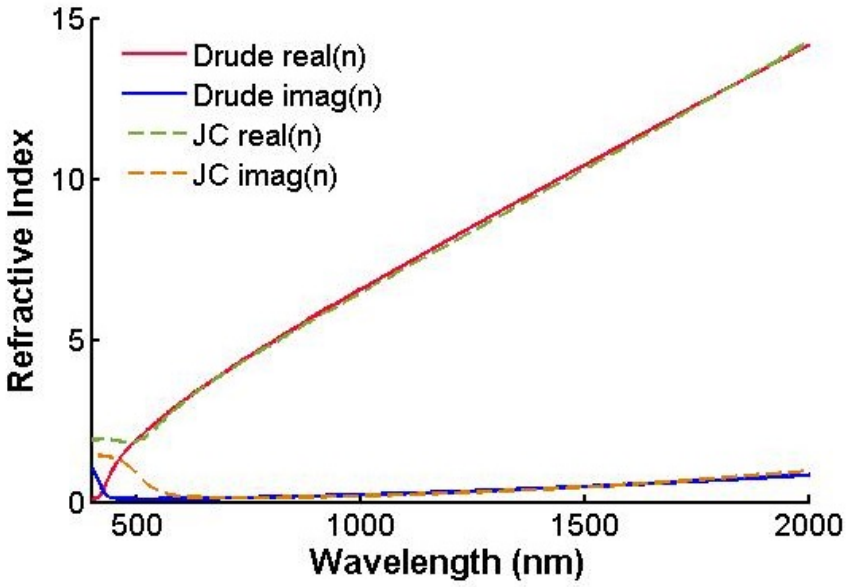

Figure 3.36. Comparison between the refractive indexes obtained from Drude model and experimental results. The real ("Drude real(n)") and imaginary ("Drude imag(n)") part of the refractive index from the Drude model fits well with the real ("JC real(n)") and imaginary ("JC imag(n)") part of the experimental results reported by Johnson and Christy [51].

By importing the Drude model as the material property, a single simple cubic unit cell of spherical gold NP with 54 nm radius is simulated. Bloch boundary conditions are used in all three dimensions and the dispersion relation in the ΓX direction is investigated. The unit cell is excited with multiple randomly distributed dipole sources. The electric field as a function of time is collected by multiple randomly placed monitors and Fourier-transformed to produce the dispersion relation (Figure 3.37).

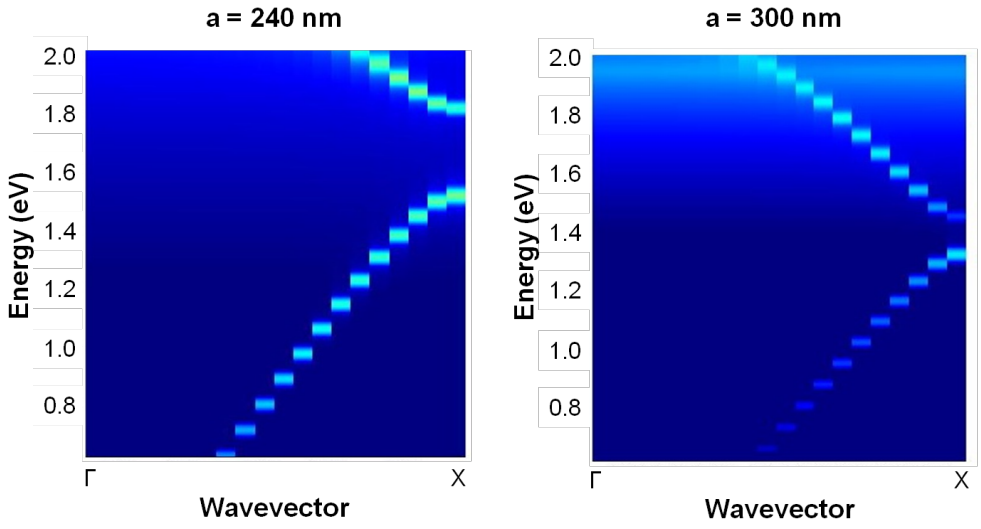

Figure 3.37. Band diagram of simple cubic lattice with two different lattice constants. The lattice constants are labeled on top of the band diagram.

Large Ag NPs with larger lattice constant are also investigated in order to separate the photonic band gap from the NP LSPR. Figure 3.38 shows the bandstructure of a cP lattice with 180 nm NP and 300 nm lattice constant. A broad bandgap exists in the ΓX direction but gradually closes up in other directions. This shows a similar trend to our angle-dependent study shown in Figure 3.32. A full photonic band gap is observed in a diamond lattice, as can be seen in the case of a diamond lattice made of 180 nm Ag NPs and 500 nm lattice constant, in order to avoid NP

touching (Figure 3.39). The band gap is 0.42 eV, which is larger than similar structures made with the same volume fraction of high-indexed dielectric materials, as reported by Ho *et al.*[91]

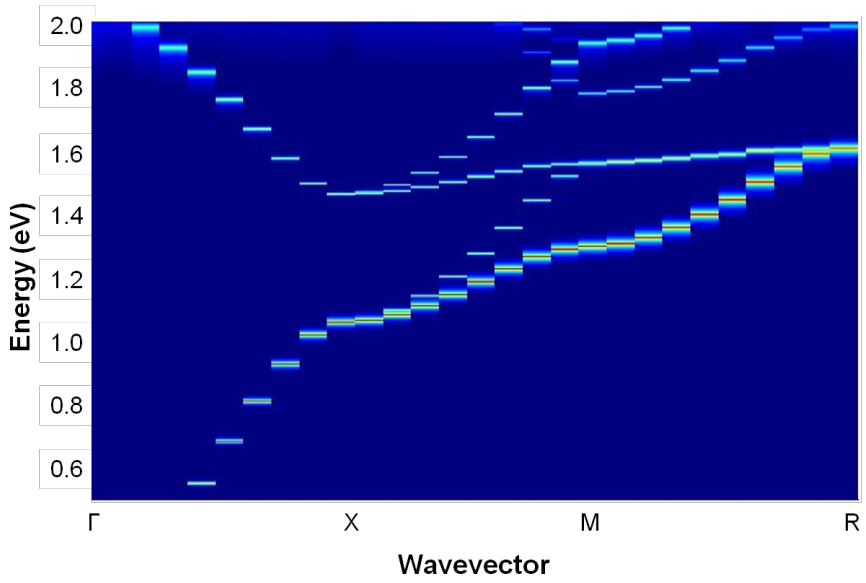

Figure 3.38. Band diagram of simple cubic lattice made of Ag NPs. The NPs are 90 nm in radius and the lattice constant is 300 nm.

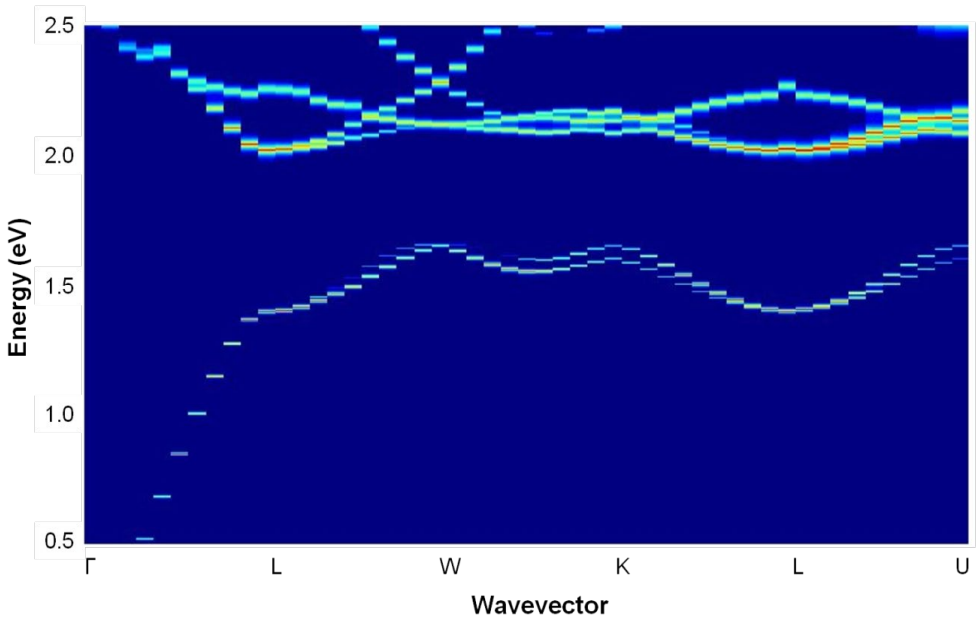

Figure 3.39. Band diagram of diamond lattice made of Ag NPs. The NPs are 90 nm in radius and the lattice constant is 500 nm.

3.6.13 Effect of NP Shape

In order to investigate the effect of NP shape through simulation, spherical, cubic and octahedral NPs of the same volume are used as building blocks. The radius of the spherical NP is 54 nm, the edge length and rounding are 88 and 5 nm for cubic NP and 112 and 5 nm for octahedral NP. Simple cubic lattice structure with 200 nm lattice constant is used such that all the superlattices with different NP shape share the same volume fraction too. Once again, 7 layers are used in the calculations. Figure 3.40 shows the reflectance spectra of the three superlattices. Here, we see that the stop-band exists in all three spectra, which indicates that the same general guidelines that are discussed in the main text can be applied to other NP shapes.

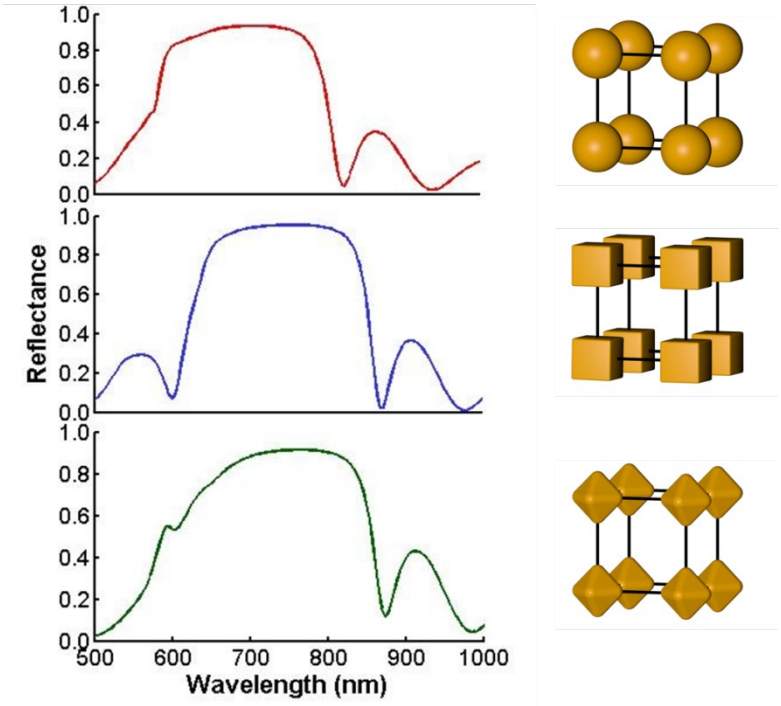

Figure 3.40. Reflectance spectra of simple cubic superlattice with spherical (top), cubic (middle) and octahedral (bottom) NPs. The three types of NP building blocks have the same volume and their corresponding superlattices have the same lattice constant and volume fraction. A stop-band is observed in all spectra.

3.6.14 Performance of PPCs with Different NP Composition

In the main text, we pointed out that one factor that might hinder the wide application of PPCs is the reduced reflectance due to material absorption, as might be resulted from the large absorption that is in general observed with Au NPs. Therefore, we perform a set of simulations on superlattices with the same geometry as the experimental sample, namely a simple cubic lattice structure, 134 nm lattice constant, 88 nm cubic NP with 5 nm rounding, but different materials (Ag, Au, Al, Cu). Again, only 7 layers are probed. Figure 3.41 shows the reflectance, transmittance and absorbance spectra. Obviously, the stop band of Ag shows the highest reflectance and lowest absorption, followed by Au, Cu and lastly Al. We note that this trend might not hold true in superlattice with different lattice parameters, due to reasons such as the fact that material loss is dependent on the NP size and its dielectric environment and the effective indices depend on wavelength. Interestingly, the stopband can be tuned to cover visible range by using Al NPs. The highest reflectance of the Ag NP superlattices reaches ~0.986 and might be further increased by adjusting the lattice parameters and layer number. Indeed, the simulated spectra of a tetragonal Ag NP superlattice with 134 nm in-plane lattice constant, 300 nm layer periodicity and 15 layers are plotted in Figure 3.42, in which the largest reflectance reaches more than 0.996. This large value is comparable to that of high-quality dielectric PCs and indicates the suitability of the Ag NP superlattices in a wide range of applications.

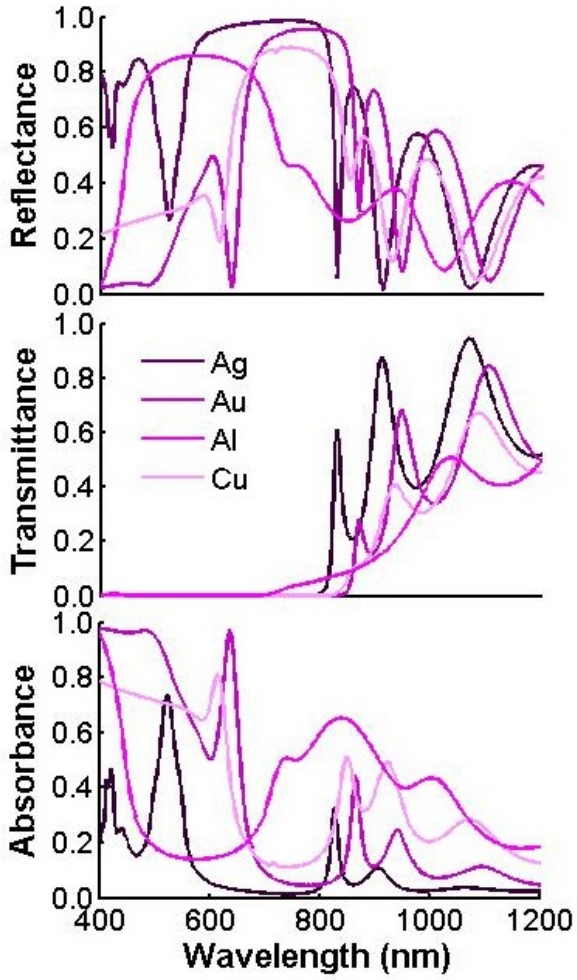

Figure 3.41. Reflectance (top), transmittance (middle) and absorbance (bottom) spectra of simple cubic superlattice with Ag, Au, Al, and Cu NPs. Ag NP superlattice shows the largest reflectance and lowest loss at its stop-band wavelengths. The lattice constant is kept at 134 nm, and the number of layers is 7. Cubic NPs with 88 nm edge length and 5 nm rounding are used.

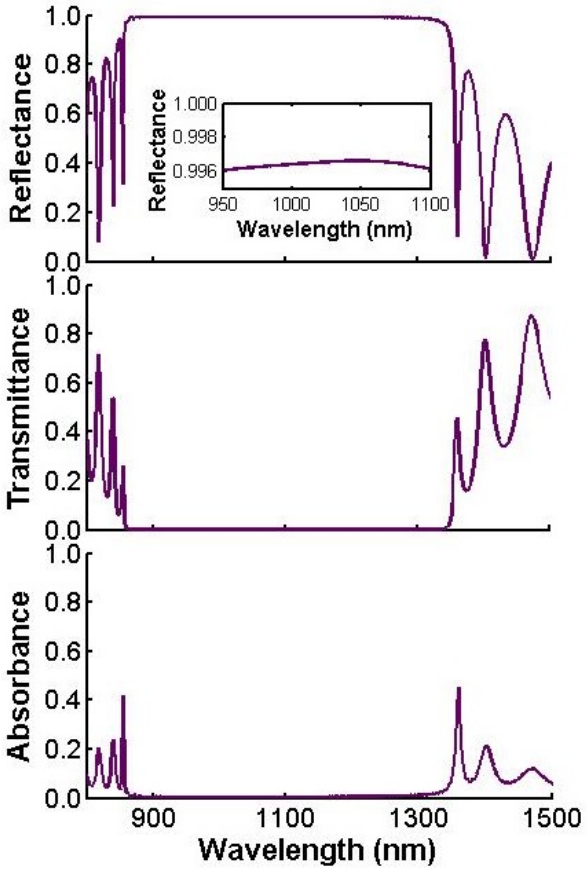

Figure 3.42. Reflectance (top), transmittance (middle) and absorbance (bottom) spectra of tetragonal superlattice with Ag NPs. The R_{max} for this structure is ~ 0.996. The structural parameters for this superlattice are a = 140 nm, c = 300 nm, 15 layers. Cubic NPs with 88 nm edge length and 5 nm rounding are used.

3.6.15 Performance of PCs with Different Metallic NPs

So far, we have derived the design rules by varying the lattice parameters, which can be experimentally enabled by programming the spacer groups. The NP building blocks also serve as an important design parameter. Although the aforementioned design rules are derived based on gold spherical NPs, they hold true for lattices assembled from other NP building blocks [92]. Thus, we investigated how the NP composition affects the stopband properties. Towards that end, we compare the reflectance spectra of the same simple cubic lattices (200 nm lattice constant, 7 layers, silica dielectric medium) made with different NP compositions ranging from plasmonic, metallic but with poor plasmonic properties, and dielectric materials. Figure 3.43 shows the reflectance spectra calculated by FDTD and EMT+TMM (solid and dashed line, respectively) of lattices composed of plasmonic NPs (top panel, Al, Cu, Ag, Au) and metallic NPs with poor plasmonic properties (bottom panel, Sn, Cr, Fe, Ti). Interestingly, the stopband properties of lattices made with plasmonic NPs are in general stronger as compared to those of metallic NP with poor plasmonic properties. Figure 3.44 shows the real and imaginary (top and bottom panel, respectively) part of the effective index of the NP layers in each case as calculated by EMT. Layers composed of plasmonic NPs in general have larger effective indices, which is likely the main reason for their better stopband properties in Figure 3.43.

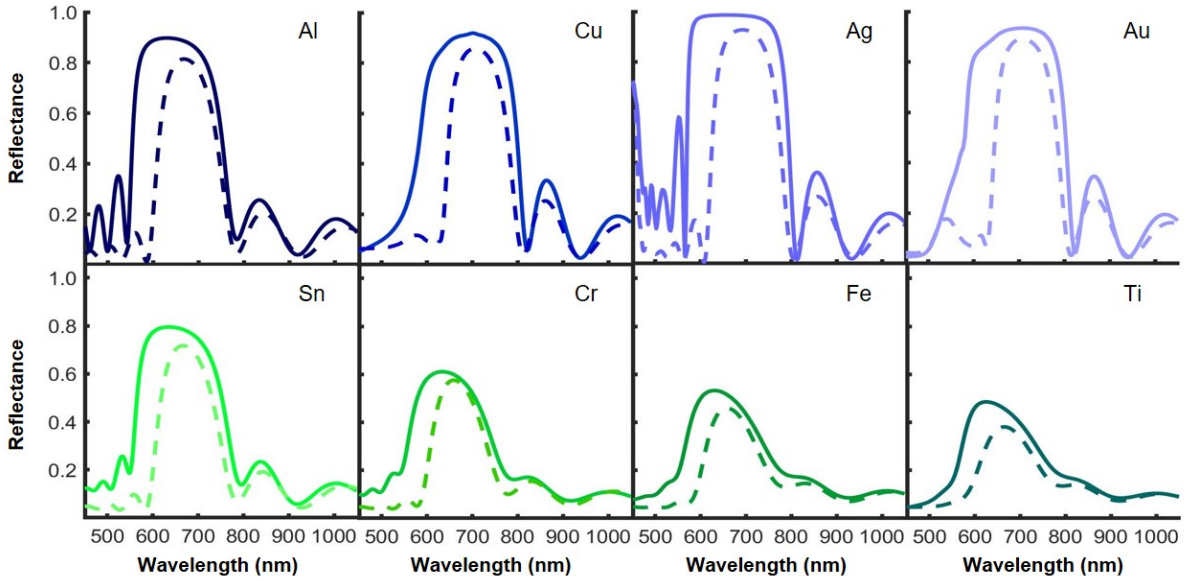

Figure 3.43. Reflectance spectra of lattices made with plasmonic (top panel) and metallic NPs with poor plasmonic properties (bottom panel) as calculated by both FDTD (solid line) and EMT+TMM (dashed line). The lattice parameters are fixed as cubic lattice with a 200 nm lattice constant. All NPs are spherical with 54 nm radius, and the dielectric medium has refractive index of 1.46. 7 layers are simulated.

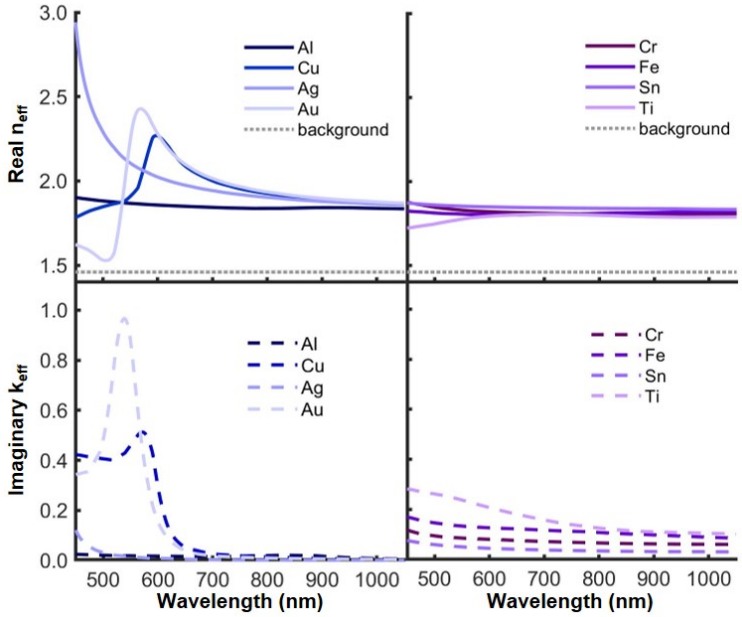

Figure 3.44. Real (top panel) and imaginary (bottom panel) part of the effective indices as calculated by EMT. The lattices are made with plasmonic (left) and metallic NPs with poor plasmonic properties (right). The lattice parameters are fixed as cubic lattice with a 200 nm lattice constant. All NPs are spherical with 54 nm radius, and the dielectric medium has refractive index

of 1.46. 7 layers are simulated. The grey dotted line in the top panel is the index used for the dielectric background (silica).

3.6.16 Performance of PC with Dielectric NPs

In order to benchmark our technique with conventional PC fabrication methods, simulations are done with dielectric NP building blocks. Specifically, the NPs have 54 nm radius and their material is set to be dielectric with a constant positive refractive index. The NPs are arranged into lattice structures in the same manner as the metallic NP superlattices discussed in the main text. The dielectric NP superlattices show similar behavior as its metallic counterpart, such as a stronger stopband with larger number of layers (Figure 3.45), a red-shift as the lattice constant increase (Figure 3.46). They also obey well the design principles derived with metallic NP superlattices (Figure 3.48-3.50). Importantly however, a larger number of layers are needed for the stopband to saturate, and the bandwidth is smaller in the dielectric NP superlattice compared to the metallic.

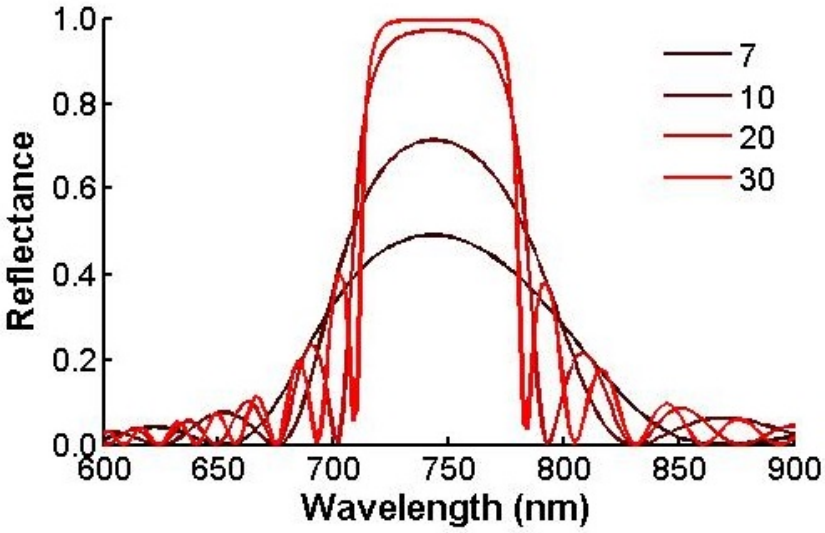

Figure 3.45. Thickness dependence of the reflectance spectra of dielectric NP superlattices. The NP radius is 54 nm, the crystal has simple cubic symmetry and 240 nm lattice constant. The number of layers is shown in the legend. The dielectric index of the NPs is fixed at 4. The reflection spectra resemble that of superlattices made with metallic NPs with the exact same lattice

parameters. A larger number of layers is required to achieve high reflectance (> 0.9), and the stopband does not saturate even for 30 layers.

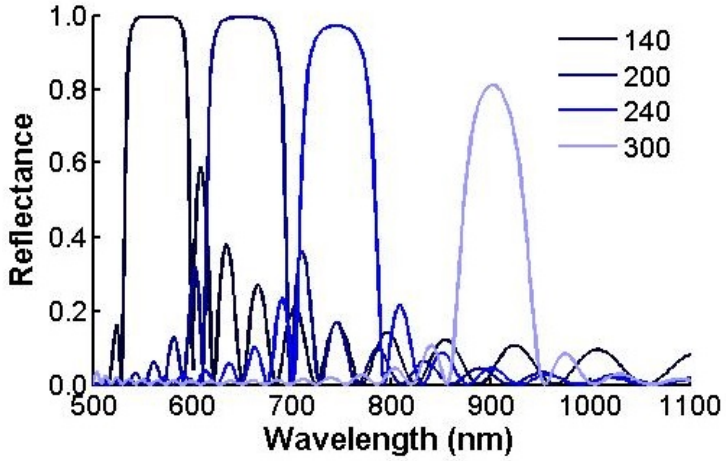

Figure 3.46. Dependence on the lattice constant of the reflectance spectra of dielectric NP superlattices. The NP radius is 54 nm, and the crystal has simple cubic symmetry. The number of layers is fixed at 20. The dielectric constant of the NPs is 4. The lattice constant is shown in the legend. The stopband red shifts as the lattice constant increases, similar to the case of plasmonic nanoparticle superlattice.

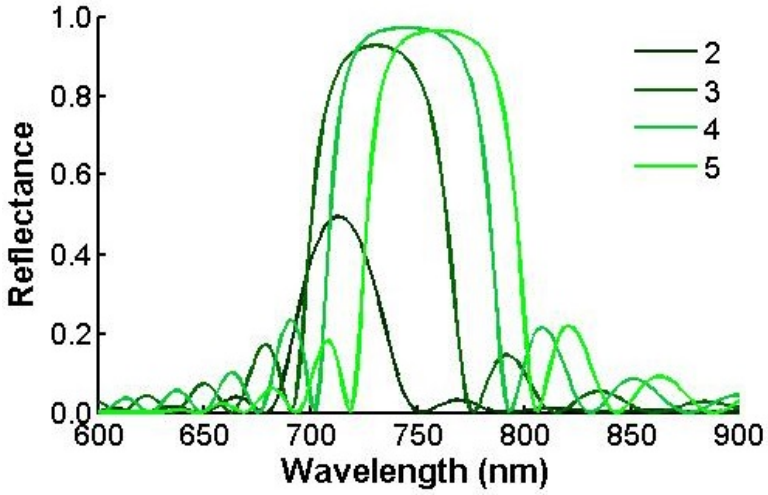

Figure 3.47. Dependence on the dielectric index of the reflectance spectra of dielectric NP superlattices. The NP radius is 54 nm, and the crystal has simple cubic symmetry and 240 nm lattice constant. The number of layers is fixed at 20. The dielectric index of the nanoparticles is shown in the legend. As the index increase, there is a slight red-shift in the stopband location.

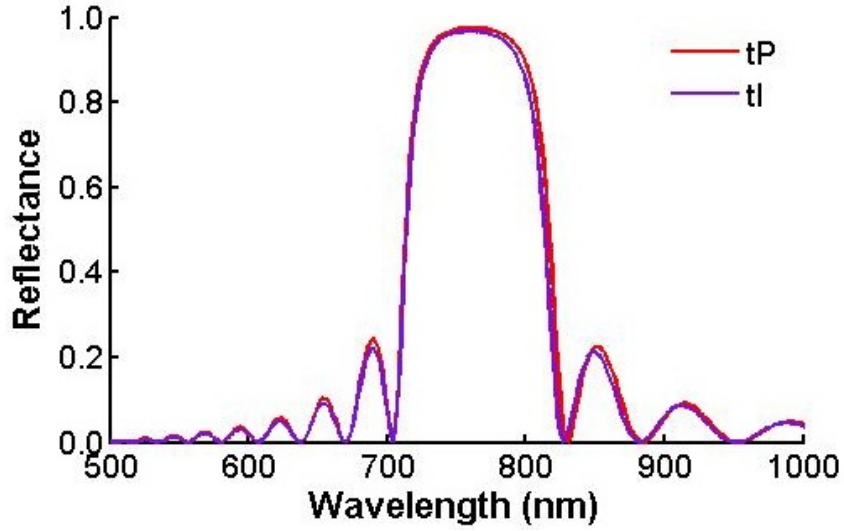

Figure 3.48. Effect of layer periodicity on the reflectance spectra of dielectric NP superlattices. The NP radius is 54 nm, and the dielectric constant is 4. The superlattice has 200 nm in-plane lattice constant and 15 layers. The lattice symmetry is shown in the legend. The two spectra coincides with each other well, indicating again that layer periodicity, rather than lattice constant in z-direction, determines the stopband features.

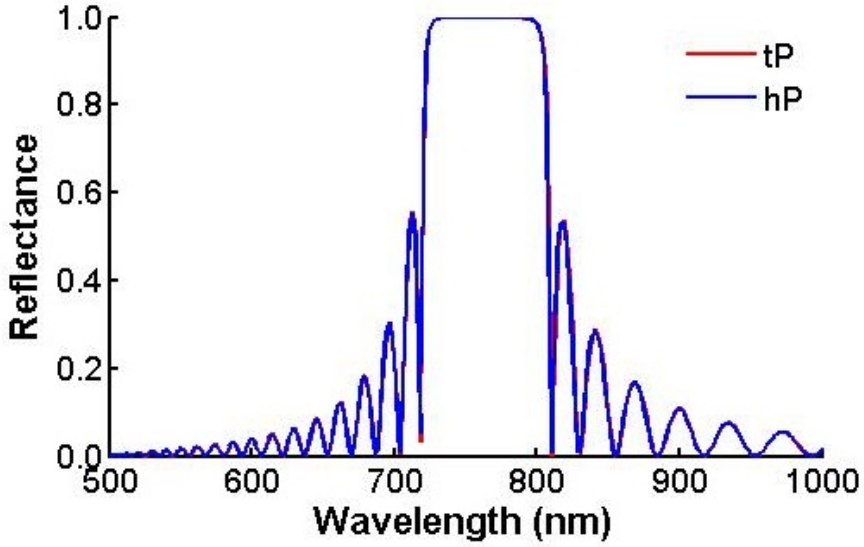

Figure 3.49. Effect of NP arrangement in each layer on the reflectance spectra of dielectric NP superlattices. The NP radius is 54 nm, and the dielectric constant is 4. The superlattice has 240 nm layer periodicity and 20 layers. The lattice symmetry is shown in the legend. The two spectra overlap with each other, indicating again that the exact arrangement of nanoparticles in each layer does not affect the stopband features.

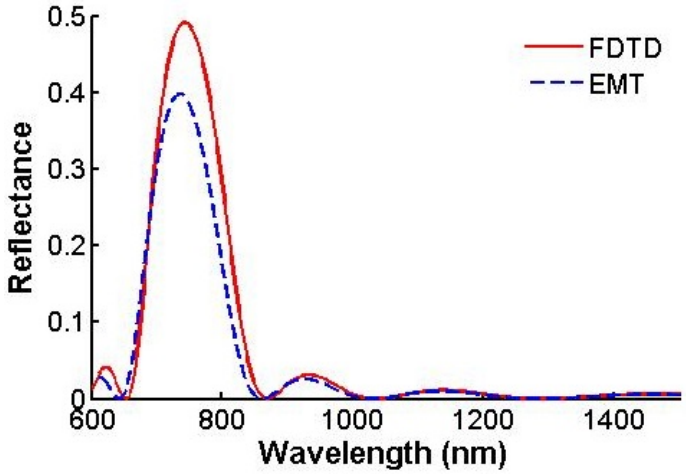

Figure 3.50. Comparison between reflectance spectra from FDTD and EMT+TMM methods. The EMT+TMM method is done in the exact same manner as described in section 5 of this SI, except that the inclusion material is dielectric instead of Au. The NP radius is 54 nm and its dielectric constant is 4. The superlattice has simple cubic lattice symmetry, 240 nm lattice constant and 7 layers. Consequently, volume fraction in the NP layer is ~ 21.2% and resulting refractive index of the layer is ~ 1.8 (independent of wavelength).

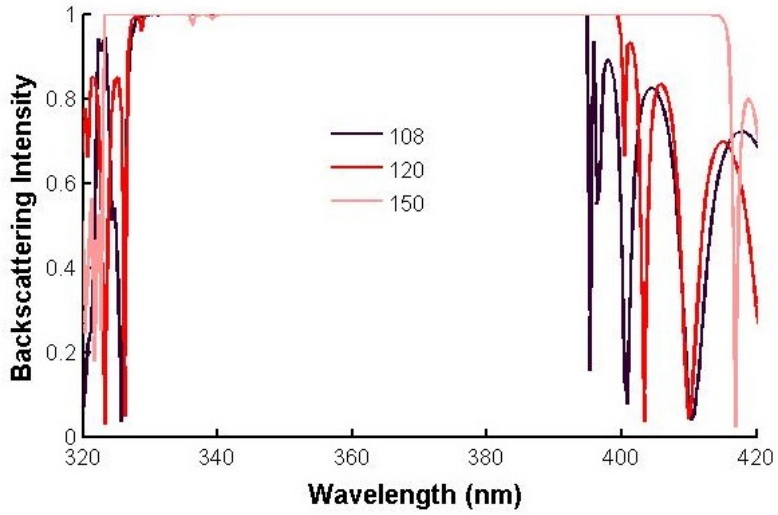

Figure 3.51. The stopband features can be improved by the use of spacer group. Dielectric NPs are also used to demonstrate the importance of having spacer groups (i.e. having NPs well-separated). The superlattice has tetragonal symmetry with a = 140 nm and 7 layers. The radius and dielectric constant of the NPs are 54 nm and 4, respectively. The lattice constant in the z direction (c) is shown in the legend. When c = 108 nm, adjacent NP layers are touching. The bandwidth increases as the NP layers are further separated.

In Figure 3.52, the reflectance spectra calculated by FDTD and EMT+TMM (solid and dashed line, respectively) of lattices composed of dielectric NPs are compared. Again we see that the stopband is in general weaker (i.e. lower maximum reflectance and narrower bandwidth) or missing in the case of SiO_2 NPs than those of lattices made with plasmonic NPs. This is because the real part of the effective indices are lower (Figure 3.53). Indeed, lattice made with Al_2O_3 shows the strongest stopband among all the dielectric NP lattices (Figure 3.52), which corresponds to the largest real part of effective index.

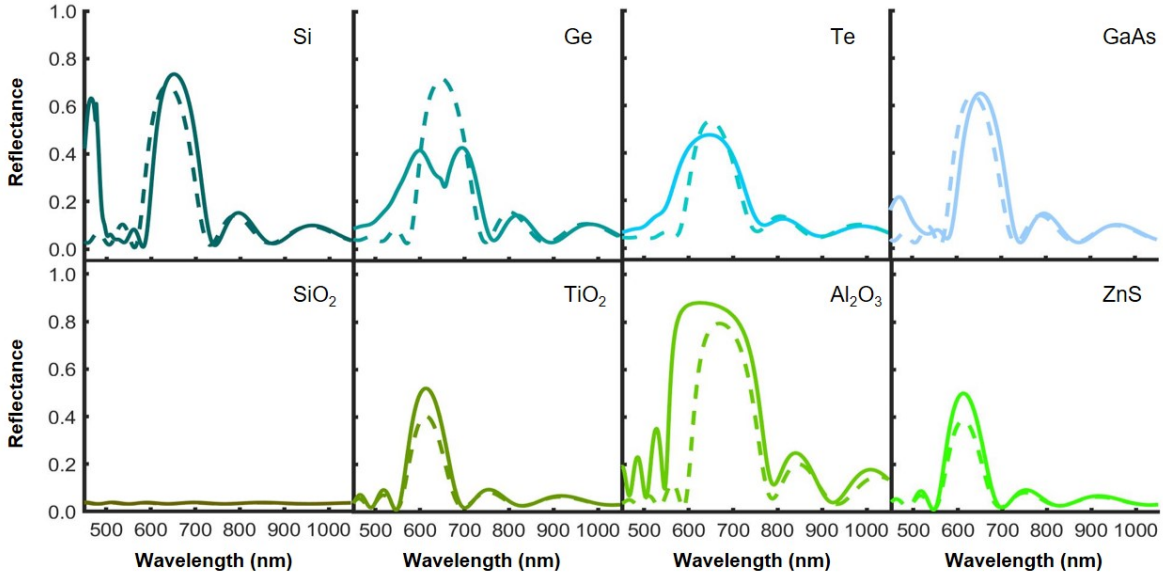

Figure 3.52. Reflectance spectra of lattices made with different dielectric NPs as calculated by both FDTD (solid line) and EMT+TMM (dashed line). The lattice parameters are fixed as cubic lattice with a 200 nm lattice constant. All NPs are spherical with 54 nm radius, and the dielectric medium has refractive index of 1.46. 7 layers are simulated.

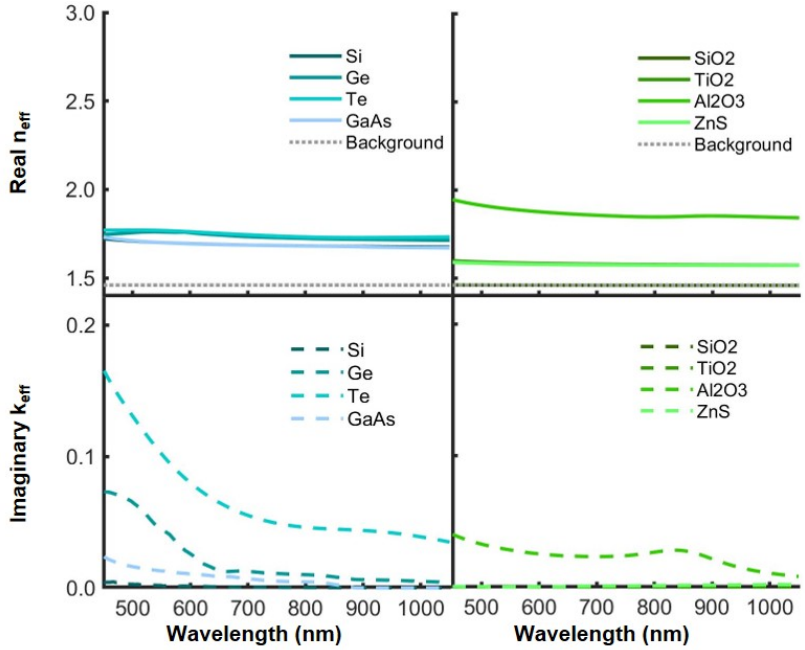

Figure 3.53. Real (top panel) and imaginary (bottom panel) part of the effective indices as calculated by EMT. The lattices are made with different dielectric NPs (shown in legend). The lattice parameters are fixed as cubic lattice with a 200 nm lattice constant. All NPs are spherical with 54 nm radius, and the dielectric medium has refractive index of 1.46. 7 layers are simulated. The grey dotted line in the top panel is the index used for the dielectric background (silica).

3.6.17 Effect of Dielectric Medium

The superlattice can have a different dielectric medium. Experimentally, this can be easily achieved by immersing the superlattices in different index-matching oils. Thus, we investigate through simulation the effect of a different dielectric medium. Again, the superlattice is set to have the same structural properties with 88 nm edge length and 5 nm rounding Au nanocubes, simple cubic lattice structure, 134 nm lattice constants and 7 layers. Figure 3.54 summarizes the reflectance, transmittance and absorbance spectra of the superlattices with different dielectric medium. Obviously, the spectral location of the stop-band can be easily tuned by changing the

dielectric medium. Moreover, the larger the dielectric medium, the broader the stop-band, which might be due to larger index contrast between the metal and dielectric layer.

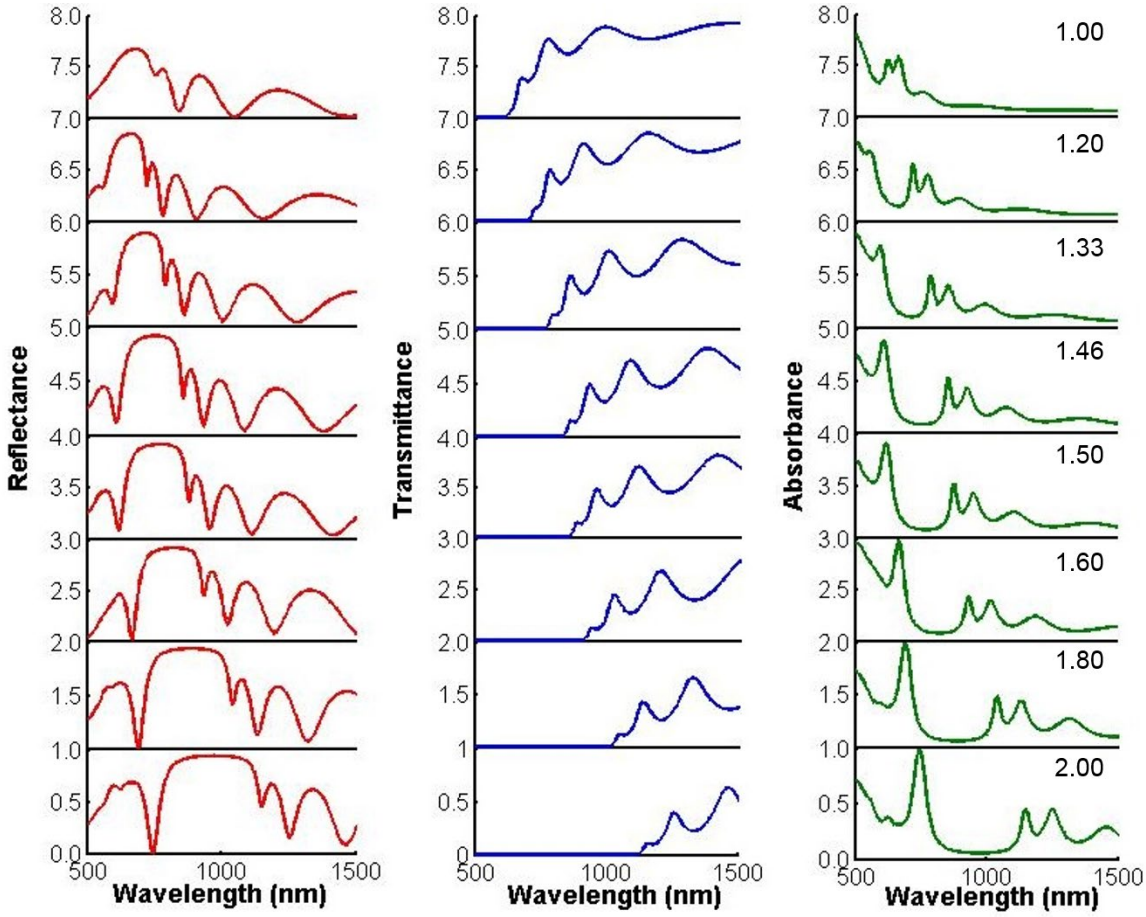

Figure 3.54. Reflectance (left), transmittance (middle) and absorbance (right) spectra of superlattice with different dielectric media. The superlattice parameters are fixed, namely nanocubes with 88 nm edge length and 5 nm rounding, 134 nm lattice constant and 7 layers are used. The refractive index of the dielectric medium is shown on the top-right corner of the absorbance spectra.

CHAPTER FOUR

Controlling Crystal Shape with Template-Guided Assembly

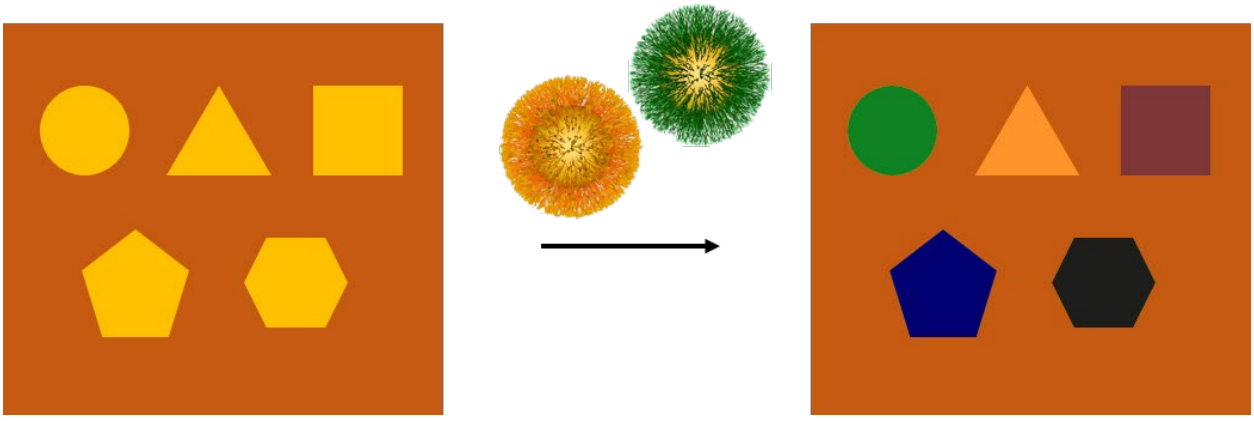

4.1 Abstract

DNA-programmable assembly has shown promise in making three dimensional optical materials with precise control over the crystal structural parameters at the nanoscale, however, control over the crystal size, shape and location on a substrate is yet to be realized. Here, by assembling DNA-nanoparticle superlattices inside lithographically defined templates in a layer-by-layer fashion, we show control over the two dimensional shape and height in the third dimension of the superlattice. These additional structural control is a step closer to realizing sophisticated optical devices with DNA-programmable assembly.

4.2 Introduction

DNA-assembled colloidal crystals have been found to show optical properties that have both fundamental scientific interests and practical functional potential.[8, 20, 21, 23, 80, 92, 93] Importantly, the high structural control and tunability have provided DNA-programmable assembly an unique advantage in tailoring optical functionalities. However, the majority of work has been focused on lattices freely assembled in solution, which does not allow control over the lattice size, shape and location on a substrate. However, these mesoscale parameters are as crucial to optical applications as the nanoscale parameters. For example, the crystal shape plays a significant role in the optical properties of the superlattices, since light reflection and refraction at each crystal facet can give rise to additional photonic modes. Indeed, previous work done in our group has shown that crystal habit can be an additional design parameter for optical properties.[23] When excitonic molecules are present, crystal-habit-driven directional emission was also observed.[80] Conventional, only four crystal habits have been achieve through DNA-assembled crystals,[17, 40] limiting the design of optical properties with crystal habit. Therefore, it is of great interest to develop a procedure where

superlattices with any defined crystal shape and size can be reliably assembled. Additionally, for sophisticated device fabrication, multiple elements, each with specific purposes need to be incorporated into one platform in a synergic manner. Namely, these elements need to not only perform their own tasks but also be able to communicate with other elements. Thus, their relative orientation and position on a substrate is also crucial. I will talk about orientation control in the next chapter, but here I provide a facile method to fabricate DNA-nanoparticles with control over the lattice size, shape and location on a substrate.

4.3 Results and Discussion

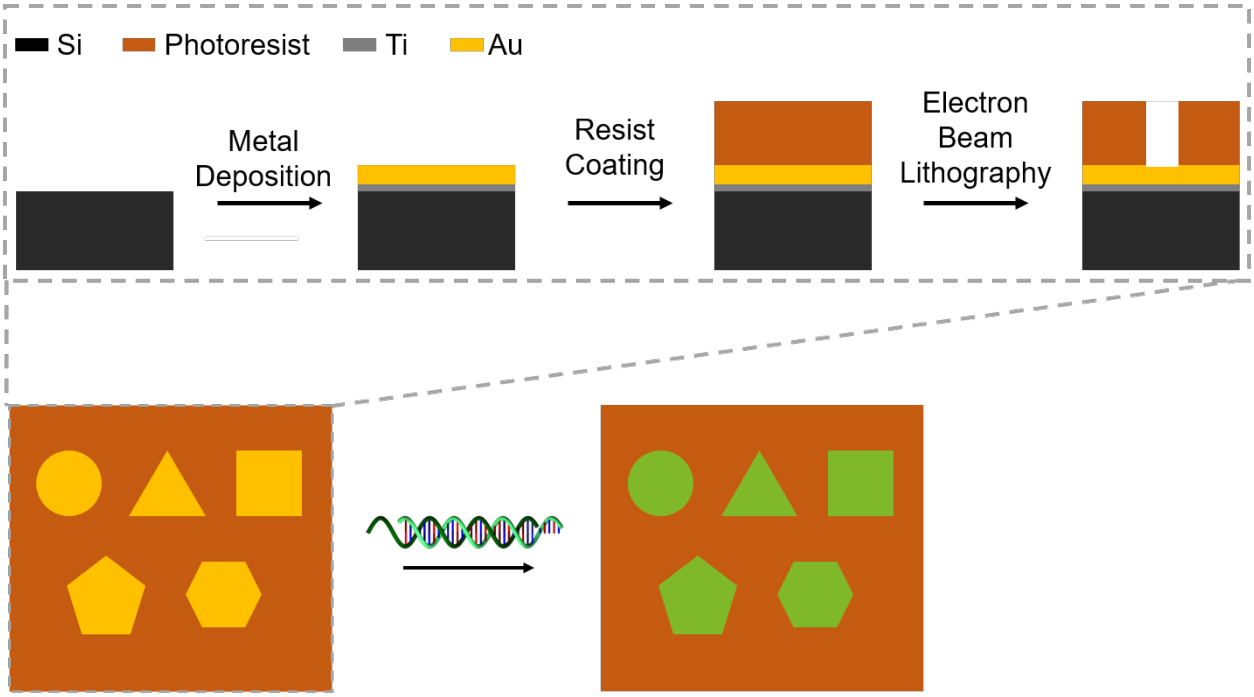

Figure 4.1. Schematic drawing of the assembly process. Blue arrow denotes electron beam. Two types of pattern are going to be tested. The one on the left is a micron-sized pattern (hexagon), and the one on the right is many individual posts, whose size is similar to the NPs and which make up a micron-sized pattern (square). The PMMA can be kept to confine the superlattice assembly (left) or removed after a lift-off process.

The two-dimensional (2D) size and shape and the location of crystals on a substrate can be defined by incorporating top-down nanolithography techniques. Specifically. patterned substrates

can be fabricated using electron beam lithography (EBL) under processes well-established in the literature (Figure 4.1). A thin layer of Au (8 - 15 nm) with 2 nm Ti adhesion layer is first deposited onto ultra-flat silicon substrates (*NOVA Electronic Materials LLC*), followed by spin coating a layer of poly(methyl methacrylate) (PMMA, *Microchem*) with controlled thickness. The PMMA coated substrate is then patterned by EBL with pre-designed shapes. After resist development, the patterned substrate will have trenches with exposed Au at the bottom and PMMA walls, which will allow confinement of the growth of the superlattice to within the trenches (Figure 4.1). A stepwise assembly process[19] can then be adopted to grow *bcc* DNA-NP superlattices in a layer-by-layer fashion. With this method, the crystal shape in the plane parallel to the substrate is determined by the two dimensional (2D) pattern and the superlattice thickness is defined by the number of deposited layers. SEM and grazing-incidence small-angle X-ray scattering (GISAXS) can be used to characterize the structural properties of the superlattices.

Table 4.1. DNA sequences used for assembly. DNA B was in general used to be attached to the substrates, and both DNA A and B were attached to nanoparticles.

Strand Name	Sequence (5' – 3')
Anchor Strands	
Anchor A-SH	TCA ACT ATT CCT ACC TAC $(sp18)_2$ SH
Anchor B-SH	TCC ACT CAT ACT CAG CAA $(sp18)_2$ SH
Linker Strands	
Linker A-n=0	GTA GGT AGG AAT AGT TGA (sp18) TTTCCTT
Linker B-n=0	TTG CTG AGT ATG AGT GGA (sp18) AAGGAAA

Spherical Au NPs with 10 nm in diameter are used to assemble all the superlattices. Oligonucleotides were synthesized with a 5' trityl group and were purified with reverse-phase

high-performance liquid chromatography (HPLC), followed by standard deprotection procedures. The DNA strands are examined by a matrix assisted laser desorption ionization-time of flight mass spectrometry (MALDI-TOF MS) to ensure high quality of DNA. The DNA sequences are summarized in Table 4.1. The substrate is functionalized with anchor and linker A, and complementary DNA strands (DNA A and B) are coated onto NPs to make reactant solution containing PAE A and B under a 0.5 M salt concentration. The substrate is subsequently submerged in PAE A and B solution alternatively for 1.5 hours each. In-between each submersion, the substrate is dipped in clean 0.5 M salt solution to wash off unbound PAEs. After the assembly, the substrate in annealed at temperature slightly below its melting temperature in 0.5 M salt solution for 15 minutes. *bcc* lattices with a surface-to-surface spacing of about 15 nm is assembled, which corresponds to a 17 nm lattice constant. The as-assembled superlattices then undergo a silica embedding process in order to transfer into solid phase.[43]

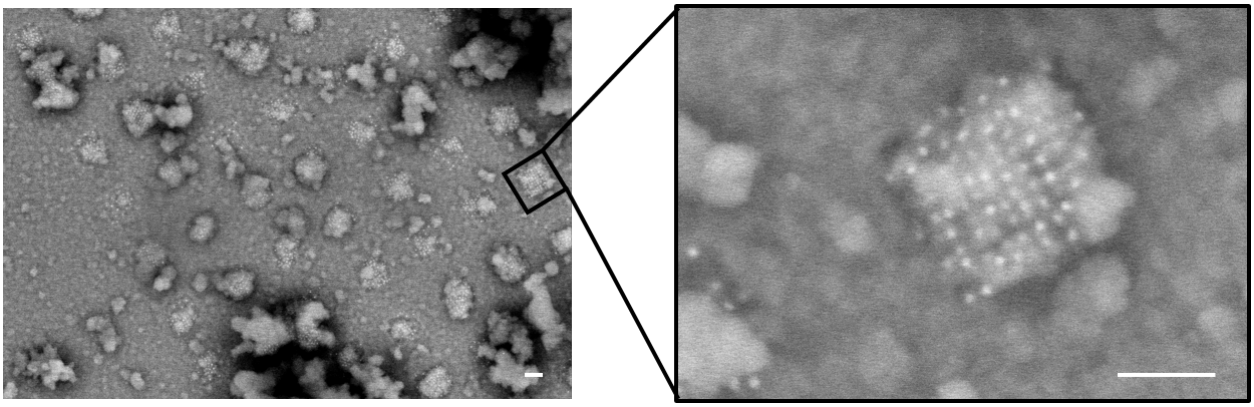

Figure 4.2 Superlattices assembled inside squares with 100 nm edge length and 200 nm spacing between neighboring trenches. 5 layers of PAEs are deposited. The scale bar is 100 nm.

As a proof of concept, superlattices are grown in square-shaped patterns with various edge lengths. The PMMA wall height is about 50 nm. SEM images of superlattices grown in squares as

small as 100 nm are shown in Figure 4.2. When the pattern edge lengths fall below 100 nm, there is no lattice formation. Lattice formation is observed when the edge length is 100 nm, but the yield is pretty low (Figure 4.2). Moreover, 5 layers of PAEs are assembled, resulting in a total crystal height of ~ 42.5 nm, shorter than the PMMA wall. Namely, crystals are well confined inside the trenches. As the trench edge length increases to 200 nm, we see crystals form in all trenches (Figure 4.2). 8 layers of PAEs are deposited this time, resulting in a 68 nm height, which is taller than the PMMA wall. We see the crystals grew out of the PMMA wall confinement and can even form "bridges" between neighboring lattices. Moreover, although we expect the lattices to grow along the (100) orientation from the layer-by-layer assembly process, lattices with different orientations, such as (100), (110) and (111) are observed (Figure 4.2).

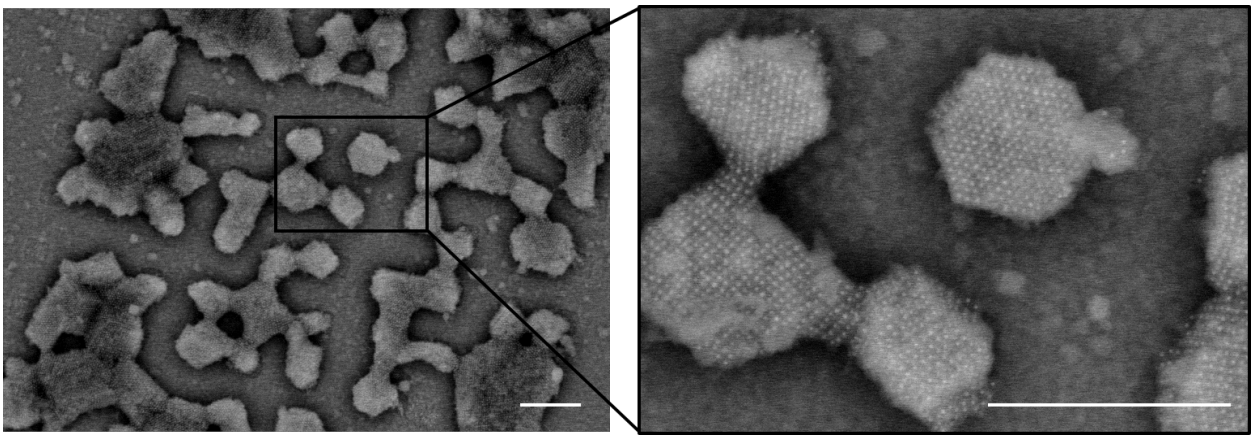

Figure 4.2. Superlattices assembled inside squares with 200 nm edge length and 500 nm spacing between neighboring trenches. 8 layers of PAEs are deposited. The scale bar is 500 nm.

As the trench size further increases, single crystalline superlattices can be assembled in trenches up to 400 nm in edge length (Figure 4.3-4.4). Moreover, the edge-to-edge spacing between neighboring squares can be tuned, as shown in Figure 4.3. From Figure 4.3a-c, the spacing is varied from 300 nm to 500 nm while the edge length is kept constant at 300 nm. The smallest

distance to prevent bridge formation and result in individual unconnected lattices at each site is ~ 500 nm.

Finally, we see that although the pattern edge length increases, the size of the crystals that outgrow the PMMA confinement is similar (Figure 4.4). More statistical studies need to be done in order to understand the assembly process. Nonetheless, the majority of crystals seem to retain the square shape (Figure 4.4).

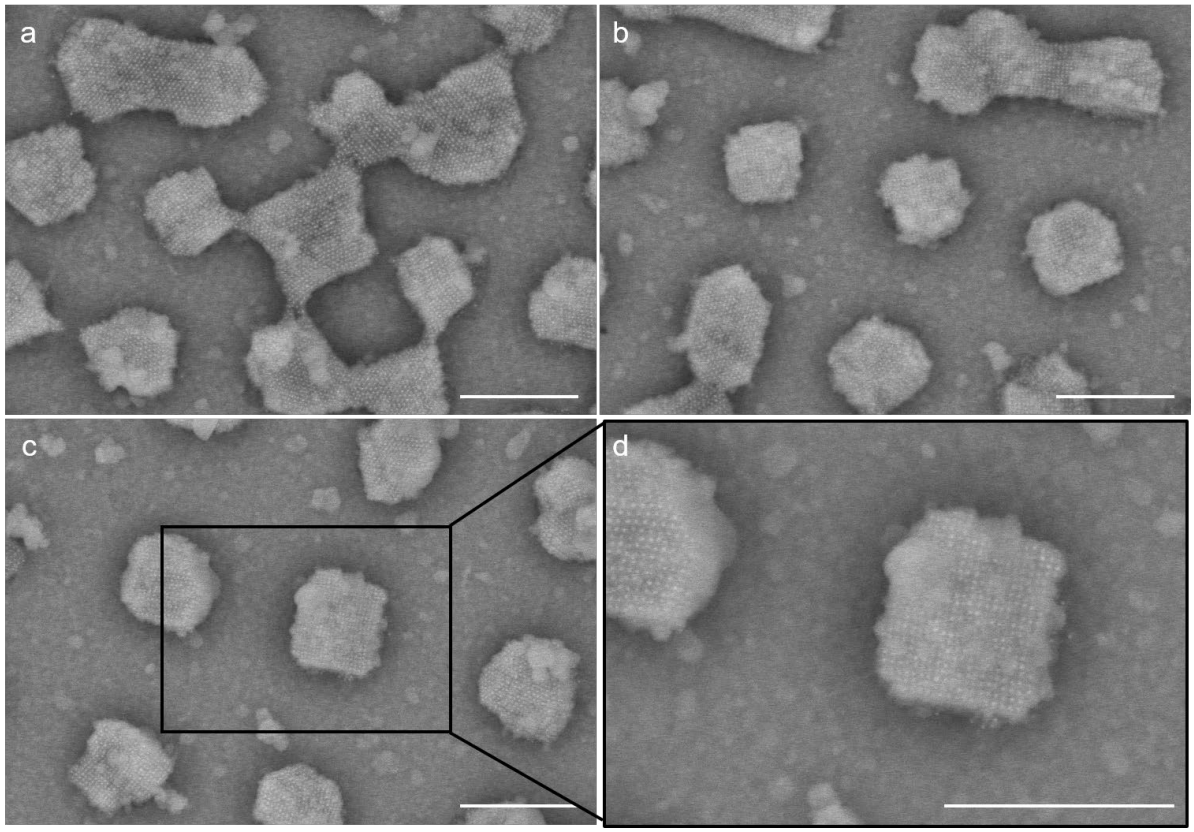

Figure 4.3. Superlattices assembled inside squares with edge length of 300 nm and changing edge-to-edge spacing from 300 nm (a), 400 nm (b) to 500 nm (c). An enlarged view of one crystal in (c) is shown in (d). 8 layers of PAEs are deposited. The scale bar is 500 nm.

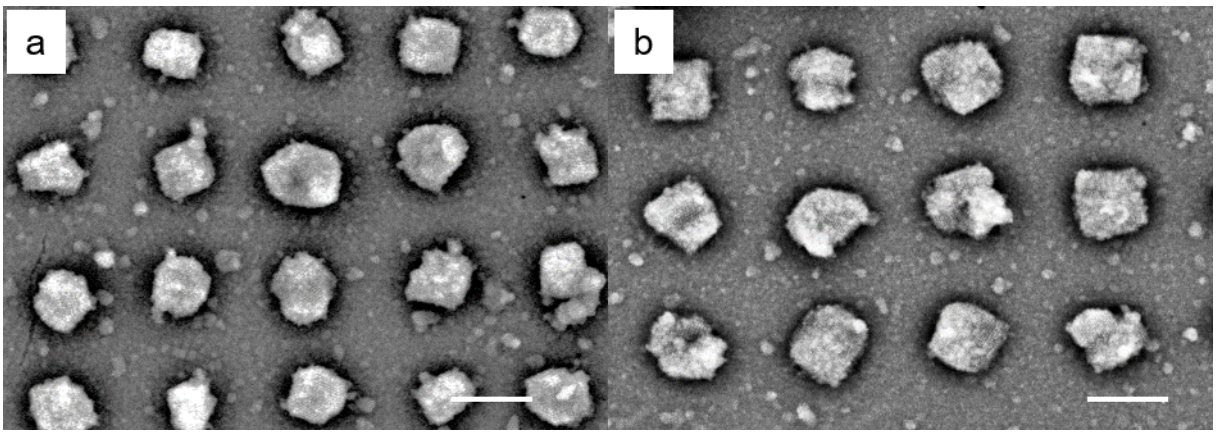

Figure 4.4. Superlattices assembled inside squares with edge length of 300 nm (a) and 400 nm (b) and 500 nm edge-to-edge spacings. 8 layers of PAEs are deposited. The scale bar is 500 nm.

We can further increase the trench size into the micrometer range. Figure 4.5 shows a range of shapes, the size of which is equivalent to being inscribed in a circle with 2 μm in diameter. Polycrystalline samples are assembled, but the overall shapes are maintained. Optimal conditions can be found through further studies to increase crystallinity and reduce the crystal edge roughness.

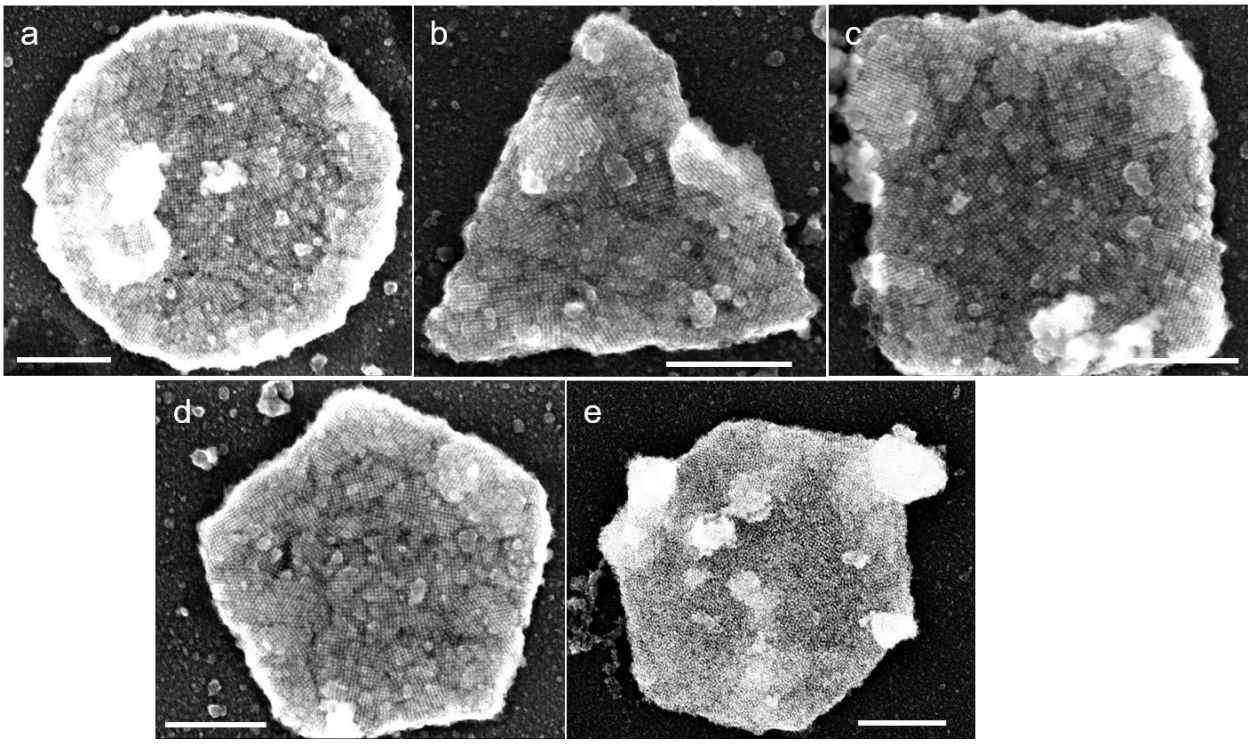

Figure 4.5. SEM images of superlattices assembled in micron-sized patterns. PMMA was not removed. 5 layers of. Scale bar: 500 nm.

4.4 Conclusion

In summary, a facile method to make DNA-assembled nanoparticle lattices with defined 2D shape and height in the third dimension has been developed. Further investigation can potentially shed light on the assembly kinetics to help explain the different orientations the lattices adopted as well as the bridging phenomena between different lattices. Moreover, the crystallinity and wall roughness can also be improved with optimized PMMA choices and assembly conditions.

CHAPTER FIVE

Wulff-Shaped Superlattice Array with Controlled Orientation and Position Assembled on Substrate

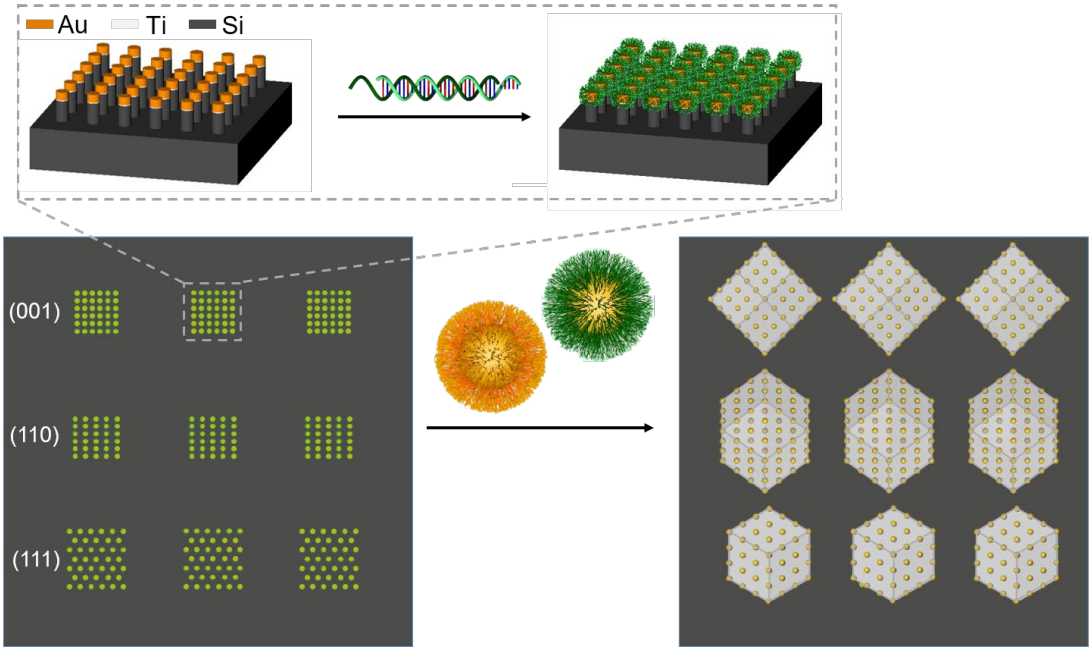

This work was done in collaboration with Dr. Haixin Lin, Yuanwei Li, Wenjie Zhou and Jingshan Du.

5.1 Abstract

Colloidal crystals have emerged as promising candidates for building optical micro-devices. Techniques now exist for synthesizing colloidal crystals with robust control over the nanoscale features (e.g., lattice symmetry), however, the ability to tune macroscale structural features, such as lattice orientations and the relative positions of crystals to one another, has yet to be realized. Here, we draw inspiration from epitaxial growth strategies in atomic crystallization and prepare two-dimensional nucleation interfaces on a substrate to be used in conjunction with DNA-mediated nanoparticle crystallization, which both allows powerful engineering over substrate/crystal lattice mismatch not achieved in atomic epitaxy and forms arrays of Wulff-shaped nanoparticle crystals, with control over single crystal orientation and location. The ability to easily manipulate lattice mismatch provides unique opportunities to study both colloidal and atomic epitaxy. And the unprecedented level of structural control is a significant step towards realizing complex, integrated devices with colloidal crystal components.

5.2 Introduction

Colloidal crystals, a type of artificial crystals formed by ordered assembly of colloidal particles, exhibit unique optical[94], electrical[95], mechanical[96, 97] and biological[98] properties due to the tailored interactions among particle building blocks. Conventionally, particle assembly mediated by solvent evaporation[99, 100], chemical linkers[101], electrostatics[73, 102] and external fields[103] have been used to synthesize colloidal crystals with a variety of structures and compositions. Among these strategies, DNA-mediated assembly has developed into a robust tool for crystal engineering that resulted in crystals with over 50 different symmetries[104], more than 10 types of chemically distinct building blocks, and 4 distinguished well-defined crystal habits[105-107]. With powerful control over the symmetry and crystal habit, DNA-mediated crystal engineering has

pushed the development of colloidal crystals towards unique applications, especially in nanophotonics. In particular, several types of DNA-assembled colloidal crystals with tailored structures down to the nanoscale have been demonstrated as promising optical elements, such as polarizers[93], waveguides[108], emitters[109] and reflectors[108]. Due to their small size (micron-scale), such colloidal crystals may further be integrated into high-density optical circuits for optical computing[110]. However, since crystal orientation, shape and location with respect to other structures can also significantly affect the optical light path, control over these properties of each individual colloidal crystal is needed in order to realize the eventual practical use of colloidal crystal optical devices[111]. So far, the majority of colloidal crystal assembly has been done either in solution[104] or on a substrate with limited control over the crystal orientation and location[112-114] and a synthetic approach needs to be developed that allows such unprecedented high level of structural control.

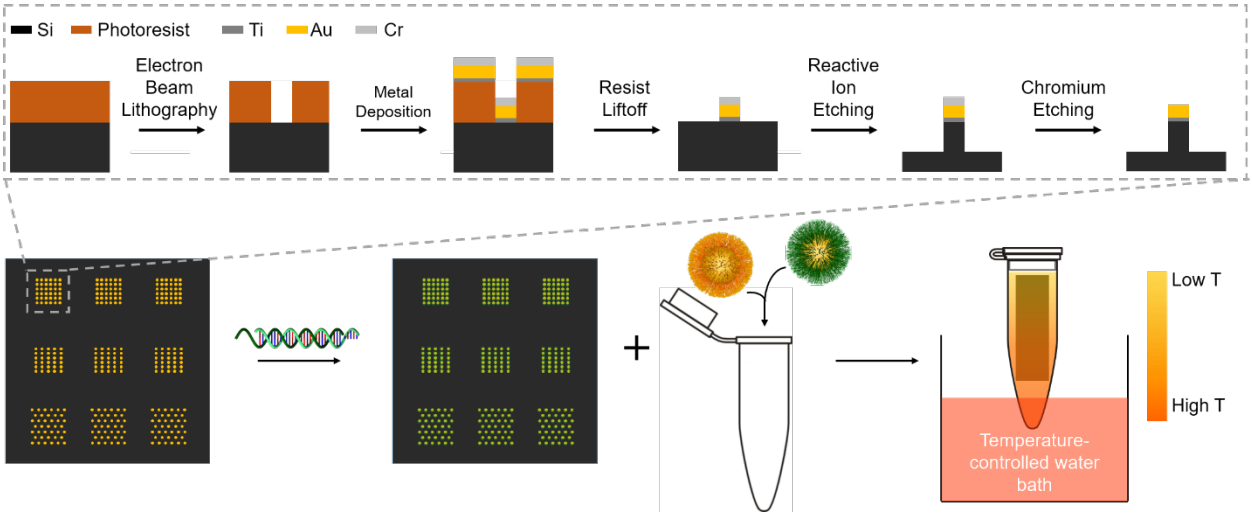

Figure 5.1. Schematic representation of the experiment process and setup. The substrates are fabricated through a sequence of processes shown in the dashed square on the top of the figure. The patterned substrates are then functionalized with a dense layer of DNA B (green-colored DNA), followed by submerging into a mixed solution of nanoparticles coated with complimentary DNA A and B. This solution is then partially submerged in a temperature-controlled water bath to create a temperature gradient, and the water bath is slowly cooled.

5.3 Results and Discussion

In this work, we report a novel strategy to control the location, shape, and orientation of individually addressable colloidal crystals using a combination of pattern-guided epitaxy[112, 115-117] with a temperature gradient[118] incorporated slow cooling method[119], as illustrated in Figure 5.1. Silicon (Si) wafers with lithographically defined patterns resembling the (001), (110) and (111) lattice planes of a body-centered cubic (*bcc*) NP crystals were fabricated (Figure 5.5). The patterns are composed of arrays of gold (Au) posts of ~ 30 nm in height and diameter, sitting on top of high aspect ratio Si nanopillars (Figure 5.6). This elevated-post design effectively prevents any steric hindrance imposed by the substrates (Figure 5.7). On each substrate, a micrometer sized thin strip is also patterned and deposited with the metal layers together with the post arrays. The substrates were then functionalized with DNA linkers (DNA B) and placed in a solution containing an equal concentration of 30 nm Au NPs with 30 nm in diameter, which are coated with complementary DNA linkers (DNA A and B). The solution is heated up to above the melting temperature and slowly cooled to room temperature[119]. A temperature gradient[118] is also incorporated to facilitate assembly on substrate (Figure 5.1). The post arrays on the substrate serves as "seeds" for epitaxial growth, which directs the NP assembly in the orientation perpendicular to lattice plane defined by the pattern. The micron-sized Au strip also provides nucleation sites for crystal assembly[120]. Additionally, this process yields crystals assembled freely in solution as a by-product from excess NPs that are not deposited on substrates. After the reaction solution reaches room temperature, both crystals grown in solution and on substrate undergo a silica embedding process separately[50] in order to be transferred to solid state, enabling direct visualization under electron microscopes.

Small angle X-ray scattering (SAXS) (Figure 5.8a) together with SEM characterization (Figure 5.8b) were used to investigate the lattice symmetry of crystals freely assembled in solution.

Our results reveal that these crystals adopt *bcc* lattice symmetry and rhombic dodecahedral (RD) habit, which is the expected Wulff equilibrium shape for the NP and DNA design[119]. The RD-shaped crystals are enclosed by the closest-packed (110) planes, which are the intrinsic structural parameters that are determined by the specific NP and DNA used[16] and serve as guide for to our substrate pattern design. When a substrate with unpatterned micrometer-sized Au film is used, we see that crystals selectively grow on top of the Au film (Figure 5.2a), but there is little control over their positions and orientations (Figure 5.9). In contrast, arrays of crystals grow on locations defined by the pattern on substrate (Figure 5.2b). Additionally, crystals grown on (001), (110) or (111) patterns (Figure 5.2c-e) also show orientation-specific crystal shapes (Figure 5.2f-h). These shapes are a manifestation of orientation-specific Wulff structure enclosed by (110) facets. They can be viewed as parts of an RD cut by the substrate lattice plane (Figure 5.10). Moreover, upon observing close observation of the SEM images in Figure 5.2f-h, we can see that the nanoparticle indeed assemble in a way that follows the crystal orientation defined by the underlying pattern. Namely, orientation control in the direction perpendicular to the substrate (the z-axis) is achieved as a consequence of the crystals growing along the orientation perpendicular to the lattice plane as defined by the pattern. Naturally, the pattern also dictates the crystal orientation parallel to the substrate (the x-y plane), as can be directly viewed in Figure 5.11 for the case in [001] orientation. The only caveat is the case of (111) pattern, where there are two degenerate crystal orientations due to their symmetry in the x-y plane (Figure 5.12). Importantly, the overall square shape of the pattern has very little impact and does not lead to a square-shaped crystal (Figure 5.2 and Figure 5.11-5.12), neither is the size of the crystal dictated by the size of the pattern (Figure 5.13). In essence, although the substrate patterns serve as nucleation sites for epitaxial assembly, the grown

crystals are thermodynamic product with its shape and size dictated by the growth condition, such as NP and DNA used[40, 107, 119, 121].

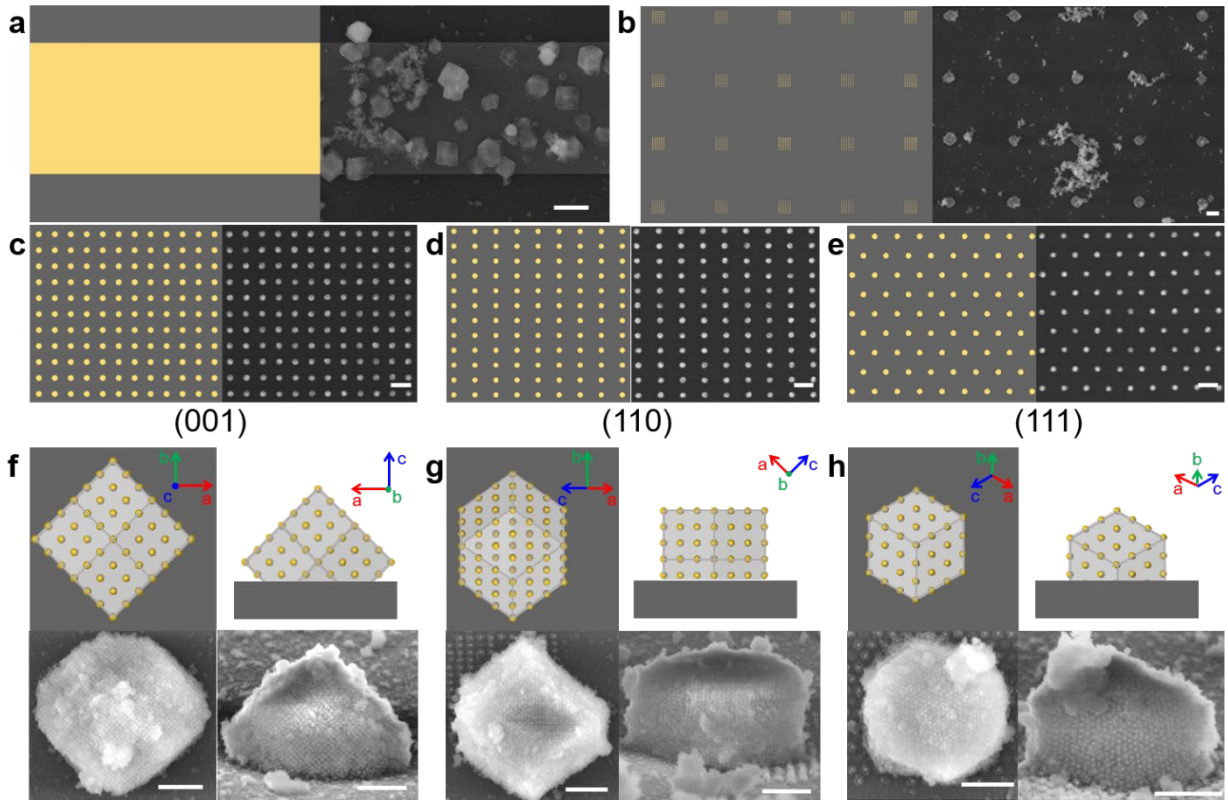

Figure 5.2. Arrays of Wulff-shaped nanoparticle crystal with controlled orientation and location epitaxially grown on patterned substrates. Crystals assemble on micron-sized gold strip randomly without any control in their orientation and location (a), as compared to the ones grown on patterned substrate with specified orientation, shape and location (b). A schematic presentation of the pattern design and an SEM image of assembled crystals of both cases are shown on the left and right part, respectively. (c-e) Schematic illustration (left) and SEM images (right) of the pattern design imitating the (001), (110) and (111) crystals planes, respectively. (f-h) Schematic illustration (top row) and SEM images (bottom row) of the top-down and side view of epitaxially grown crystals along [001], [110] and [111] orientations, respectively. The side view is 75 degrees tilted from the top-down view in the scheme and SEM images, respectively. All crystals are imaged after silica embedding, and the while debris seen at the surface of crystals and substrates are silica too Scale bars: (a-b) 2 µm, (c-e) 100 nm, (f-h) 500 nm.

To further investigate the effect of pattern design on the epitaxial growth, we systematically varied the lattice constant of the (001), (110) and (111) patterns. Specifically, Figure 5.3a shows

two rows of patterns with lattice constant (a_p) ranging from 50 nm to 85 nm from left to right. Both rows have (001) patterns but with the in-plane orientation rotated 45 degrees with respect to each other. The intrinsic lattice constant (a_i) as obtained from SAXS measurement of crystals freely assembled in solution is about 78 nm (Figure 5.8), and the two patterns with closest a_p (i.e. 75 and 80 nm) are highlighted in Figure 5.3a by the white square. Interestingly, all crystals still take on the shape expected for growth along the [001] orientation, even when the a_p is as small as 50 nm, which corresponds to a theoretical 56% lattice mismatch (Figure 5.3b). This is a significantly larger lattice mismatch compared to atomic systems, where epitaxial growth only occurs when the lattice mismatch between the deposited material and the substrate is small, reportedly less than 15%[122]. Additionally, we observe a 45-degree rotation in the x-y plane of crystal at smaller a_p. For both rows shown in Figure 5.3b, the rotation occurs when a_p changes from 65 to 70 nm, as indicated by the dashed black line.

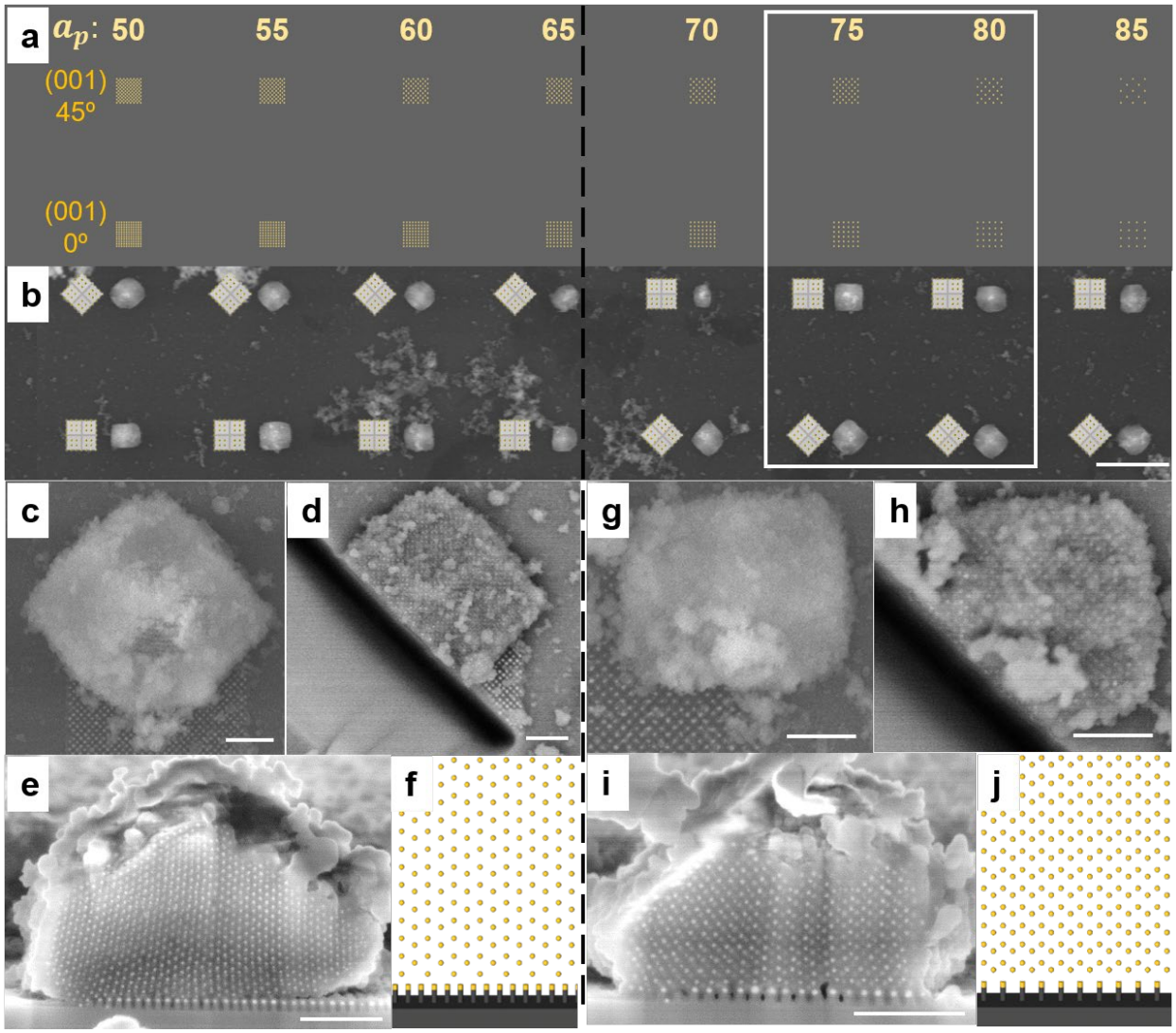

Figure 5.3. Crystal orientation is affected by both pattern orientation and strain in the [001] orientation. (a) Schematic illustration of the patterns and (b) the corresponding SEM images of crystals assembled on such patterns. The numbers on the top indicates the lattice constant (a_p) in nm for each pattern design. The upper and lower rows of the patterns both have (001) lattice arrangement but are 45 degrees rotated with respect to each other, resulting in 45 degree rotation of the corresponding crystals with respect to each other, as shown in SEM images. The white square highlights the range into which lattice constants measured with crystals assembled free in solution (a_i) fall, namely the range of a_p that results in the least amount of strain. At smaller a_p, and therefore lager compression strain, the crystals are rotated 45 degrees, which is separated by the black dashed line. (c-f) Detailed analysis of crystal grown on pattern with 60 nm lattice constant (a_p) and 45-degree in-plane rotation. Top-down images of crystals before (c) and after (d) FIB cross-sectioning show that the cut is made along 45-degree in-plane direction. The crystals are tilted around 75 degrees from the top in order to observe the sectioned surface (e) and a corresponding drawing of the top layer of nanoparticles (f) are shown for comparison. (g-j) The

same set of result for crystal grown on pattern with 75 nm lattice constant (a_p) and 45-degree in-plane rotation. Top-down images of crystals before (g) and after (h) FIB cross-sectioning show that the cut is made along 45-degree in-plane direction. The crystals are tilted around 75 degrees from the top in order to observe the sectioned surface (i) and a corresponding drawing of the top two layers of nanoparticles (j) are shown for comparison. All crystals are embedded in silica before SEM imaging, and the while debris seen at the surface of crystals and substrates are silica too. Scale bars: (b) 5 μm, (c-j) 500 nm.

To understand the origin of this rotation, focused ion beam (FIB) is utilized to expose the crystal cross sections by removing part of the crystal and its underlying substrate. This enables us to directly view of the crystal inner structure and shed light on the interaction between the pattern and the crystal. Figure 5.3b-j shows examples of crystals grown on patterns with 60 and 75 nm a_p before (top left) and after (top right) FIB sectioning, respectively. Both patterns have 45 degrees in-plane rotation, and the cut is made along 45-degree in-plane direction (namely, along the (100) plane defined by the pattern). The cross-sectional SEM image (Figure 5.3e and 5.3i) is taken by viewing the structure at a 75-degree angle from the top of the crystal (furthest from the substrate). When there is little mismatch between the crystal and pattern, namely a_p is close to a_i (Figure 5.3g-j), the cross section is essentially the (001) plane of the lattice (see Figure 5.14 for a detailed illustration). The lattice constant of the epitaxially grown crystal (a_c) is defined as the average spacing between nearest neighbor particles on each (001) plane of the crystal. We see that a_c is close to a_p near the interface between the crystal and substrate and gradually relaxes as the crystal grows further away from the substrate, a phenomenon commonly observed in conventional atomic epitaxy[123]. In comparison, when a_p is much smaller than a_i (Figure 5.3b-f), the cross section maintains a (110) lattice plane (Figure 5.3e and 5.14b). Specifically, in the direction parallel to the substrate on the cross section is the (110) orientation of the crystal with the interparticle spacing

about twice of a_p. This results in an a_c about $\sqrt{2}$ times of a_p at locations close to the substrate and gradually relaxes to a_i. The reason for this rotation and the difference in a_p and a_c is a balance between the two main drive forces: first, the large binding energy between complementary DNA strands has served as the main driving force for DNA-mediate assemblies[16, 104]. Consequently, one guiding principle in DNA-mediated assembly is that the thermodynamic products are structures that maximize the binding between complementary DNA strands[16]. Thus, the first layer of NPs deposited on the pattern will fall at the center of the square that is defined by four neighboring Au posts (Figure 5.15), as one would expect for epitaxial assembly along the [001] orientation. We will call these sites the *proper sites* as they maximize complementary DNA hybridization. On the other hand, hydrodynamic radii of the DNA-grafted nanoparticles calculated from a *bcc* lattice with a_i = 78 nm is ~ 34 nm, which will result in a 3 nm overlap of the same type of DNA if all the *proper sites* are filled on pattern with a 65 nm a_p. And the overlap can be as large as 18 nm when a_p = 50 nm (Figure 5.15). The resulting large electrostatic and steric repulsion between charged DNA strands will prevent NPs from coming too close and filling every suitable site when a_p is too small. Consequently, the first layer of NPs deposited on the substrate take up suitable sites alternatively, effectively maximizing hybridization between complementary DNA strands without crowding (Figure 5.15). This essentially redefines the pattern, resulting in a larger lattice constant ($\sqrt{2}$ times of the original) and a 45-degree in-plane rotation from the original pattern (Figure 5.14-5.15). Compared to conventional wisdom where small lattice mismatch is sought after for the epitaxial growth of high quality heterostructures[122], our finding provides a new direction for strain engineering with large lattice mismatch in atomic epitaxy. Another point to note is that the lattices seem to always be contracting as it grows further from the substrate, this is a consequence of the

silica embedding process[50] (Figure 5.16-5.17). Importantly, when a_p is close to a_i, the yield of crystals epitaxially grown on substrate with expected shape is close to 100%, regardless of its in-plane rotation (Figure 5.11, 5.19-5.20).

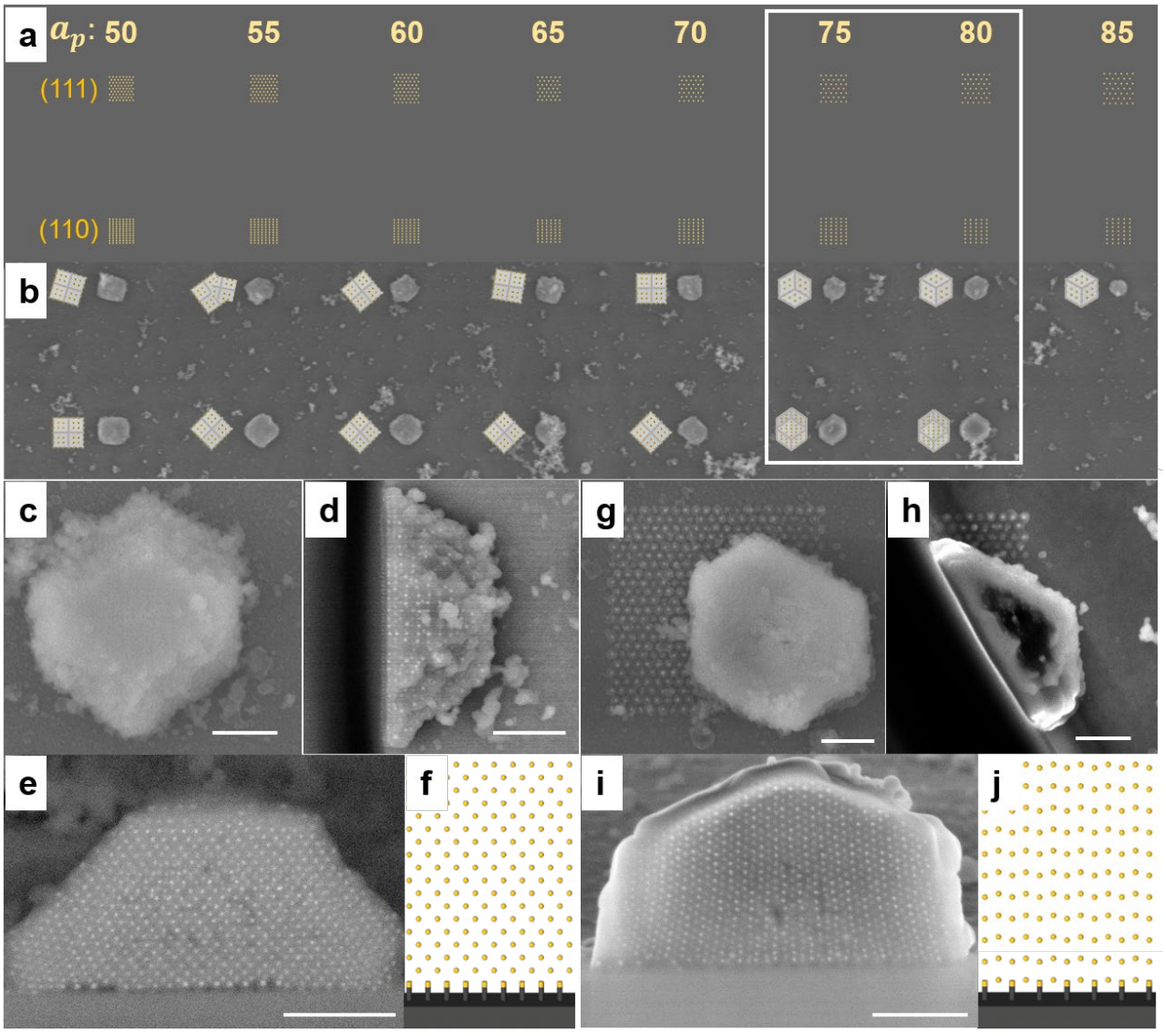

Figure 5.4. Substrate guided epitaxial growth only occurs on patterns with the least amount of strain in the [110] and [111] orientations. (a) Schematic illustration of the patterns and (b) the corresponding SEM images of crystals assembled on these patterns. The numbers on the top indicates the a_p in nm. The upper and lower rows of the patterns have (111) and (110) lattice arrangement, respectively. The white square highlights the range of a_p into which a_i falls, namely

the patterns that result in the least amount of strain. As we can see in the SEM images, epitaxial assembly along the desired orientation only occurs when the a_p is close to the a_i (i.e. within the white square). (c-f) Detailed analysis of crystal grown on a (110) pattern with 75 nm lattice constant (a_p). Top-down images of crystals before (c) and after (d) FIB cross-sectioning show that the cut is made along the 90-degree in-plane direction for (110) pattern. The crystals are tilted around 75 degrees from the top in order to observe the sectioned surface (e) and a corresponding drawing of the top layer of nanoparticles (f) are shown for comparison. (g-j) The same set of result for crystal grown on a (111) pattern with 75 nm lattice constant (a_p). Top-down images of crystals before (g) and after (h) FIB cross-sectioning show that the cut is made along the 120-degree for (111) pattern. The crystals are tilted around 75 degrees from the top in order to observe the sectioned surface (i) and a corresponding drawing of the top two layers of nanoparticles (j) are shown for comparison. All crystals are embedded in silica before SEM imaging, and the while debris seen at the surface of crystals and substrates are silica too. Scale bars: (b) 5 μm, (c-j) 500 nm.

In the [110] and [111] orientations, we only observe epitaxial assembly when a_p is close to a_i, i.e. the lattice mismatch is small. Figure 5.4a-b shows two rows of patterns with (111) (top) and (110) (bottom) symmetries. Patterns with a_p close to a_i are highlighted in the white rectangle. Again, we use FIB to expose the cross sections of crystals grown on the (110) and (111) patterns and observed them at an angle of 75 degrees from the top of the crystal (Figure 5.4b-j). The cut is made along the 90-degree direction for (110) pattern (i.e. the $(1\bar{1}0)$ plane, Figure 5.4d) and 120-degree for (111) pattern (i.e. the $(\bar{1}\bar{1}2)$ plane, Figure 5.4h). A closer investigation of the two samples in Figure 5.20 shows that both crystals grow epitaxially on patterns with a_p = 75 nm. For (110) patterns with smaller a_p, the majority of crystals attain shapes that resemble the shapes of crystals grown along the [001] orientation (Figure 5.4b and 5.21). In particular, the crystals are all aligned as if a_p = 55 - 70 nm (Figure 5.21). Again this can be rationalized by visualizing the deposition geometry of the each layer. Each deposited layer of DNA A-grafted nanoparticles will fit into the center of four DNA B-grafted nanoparticles (or posts for the first layer of nanoparticles) that define a square, and so will DNA B-grafted nanoparticles fit into the center of four DNA A-

grafted nanoparticles. With hydrodynamic radii of 34 nm, this layer of NPs will likely be located 31 nm above the posts plane when a_p = 70 nm, and as much as 48 nm when a_p = 55 nm. These spacing between the layers defined by the two types of nanoparticles resembles the corresponding spacing along the [001] orientation. Namely, crystals essentially grow along [001], rather than <110> orientation, with tensile strain in the x-axis and compression strain in the y-axis (Figure 5.22). The term strain here is defined as how much the position of the NPs differ from the theoretical positions predicted by the corresponding lattice. Since there is no binding between nanoparticles in the same plane, the tensile strain in this case is beneficial as it provides some room to alleviate the compression train the NPs suffer in the y-axis. When a_p = 50 nm, the periodicity of posts along the x-axis is around 71 nm, close to 68 nm where the NPs are just touching. Thus, some of the crystals assembled on these patterns adopt a 45-degree rotation, similar to the case with (001) pattern with small a_p. Although the structural analysis is enabled by visualizing the crystal in a layer-by-layer manner, we emphasize that this in no way suggests that the crystals grew in a layer-by-layer fashion. For (111) pattern, there is a mixture of polycrystalline and single crystalline structures (Figure 5.4b and 5.23). But upon closer inspection, we see all crystals grew along the [001] orientations, but with three different in-plane orientations. Even the polycrystalline samples seem to have grown along the [001] orientation, but their polycrystallinity is a result of grains with different in-plane orientations. This is because at smaller a_p, the first deposited layer of nanoparticles could adopt a (100) symmetry, which has three identical in-plane orientations due to the symmetry of the pattern (Figure 5.24). Although the yield of epitaxial growth along the [110] orientation is close to 100% (Figure 5.21), the yield along the [111] orientation is only about 40%

(Figure 5.23). Additional discussion with FIB sectioned samples are presented in the supplementary information (Figure 5.25-2.32).

Conceptually, this procedure can be applied to other systems, for example, with different NP size, shape, and composition, or different DNA designs[16, 40, 124]. Figure 5.33-5.36 show that when 20 nm spherical NPs coated with the same A and B DNA design are used, the expected orientation control is observed. We thus foresee that this technique can be expanded to other lattice symmetries or NP shapes to control lattice orientation and attain symmetry-specific crystal shapes[40, 107].

5.4 Conclusion

In conclusion, by combining epitaxial growth on patterned substrates with a slow-cooling method, arrays of Wulff-construction-shaped crystals can be grown along specific crystal orientation at predefined locations on a substrate. In particular, we showed that *bcc* crystals can epitaxially grow along [001], [110] and [111] orientations into orientation-specific shapes. FIB was used to reveal the cross section of crystal and shed light on the interactions between substrates and crystals. We saw that under large compression strain, the first layer of deposited nanoparticles reconstruct the (001) pattern into one with larger lattice constants and a 45-degree in-plane rotation, while the epitaxial growth along the [110] and [111] orientations only occurred when the strain is small. Our findings provide additional considerations that can be beneficial to strain engineering in atomic epitaxy. Importantly, close to 100% yield was achieved in the [001] and [110] orientations. Hence this method provides a level of structural control that has not been previously reported in the field of colloidal crystal engineering. Upon further development with

the conventional wisdom established in the DNA-programmable assembly field, this technique can be used fabricated crystals of a variety of tailored size and shape with controlled orientation and location. We envision that this technique can be beneficial for a wide range of applications including chemical and biological sensors [125], optoelectronic devices [8] and optical integrated circuits [111].

5.5 Methods

5.5.1 DNA Design and Synthesis

All oligonucleotides were synthesized on a Mermaid 48 DNA Synthesizer (BioAutomation) using standard protocol and reagents purchased from Glen Research. Strands were synthesized from 3' end on controlled pore glass (CPG) beads. After synthesis, the oligonucleotide strands were cleaved from the CPG beads with either 30% ammonium hydroxide solution or a 1:1 mixture of 30% ammonium hydroxide and 40% aqueous methylamine solution. The strands were then purified using an automated reverse-phase high-performance liquid chromatography (HPLC; Shimadzu) on an Agilent C18 column (5 μm, 250x4.6 mm). Finally, the 4,4'-dimethoxytrityl (DMT) protecting groups on the DNA strands were removed by setting in 20% acetic acid for 1 hour before extracting all organic contents with ethyl acetate. All final products were examined with matrix-assisted laser desorption ionization time-of-flight mass spectrometry (MALDI-TOF-MS; Bruker) to ensure the correct molecular weight and high purity of synthesized DNA.

Table 5.1. DNA sequences used for assembly. DNA B was in general used to be attached to the substrates, and both DNA A and B were attached to nanoparticles.

Strand Name	Sequence (5' – 3')
Anchor Strands	
Anchor A-SH	TCA ACT ATT CCT ACC TAC $(sp18)_x$ SH
Anchor B-SH	TCC ACT CAT ACT CAG CAA $(sp18)_x$ SH
Linker Strands	
Linker A-n=1	GTA GGT AGG AAT AGT TGA (sp18) TT ACT GAG CAG CAC TGA TTT (sp18) TTTCCTT
Linker B-n=1	TTG CTG AGT ATG AGT GGA (sp18) TT ACT GAG CAG CAC TGA TTT (sp18) AAGGAAA
Linker A-n=2	GTA GGT AGG AAT AGT TGA (sp18) TT ACT GAG CAG CAC TGA TTT (sp18) TT ACT GAG CAG CAC TGA TTT (sp18) TTTCCTT
Linker B-n=2	TTG CTG AGT ATG AGT GGA (sp18) TT ACT GAG CAG CAC TGA TTT (sp18) TT ACT GAG CAG CAC TGA TTT (sp18) AAGGAAA
Duplexer Strand	
Duplexer d20	AAA TCA GTG CTG CTC AGT AA

The table above summarizes the DNA sequences used in this work (Table 5.1). Two types of DNA stands (denoted A and B) that are complementary to each other were used in order to assemble *bcc* lattices with thermodynamic shapes[119]. The entire sequence coated onto each nanoparticle can be viewed in three parts. First, a thiolated anchor strand that was directly attached to the nanoparticles via the gold-thiol bond. A desired number (x = 2 or 5) of hexaethylene glycols (sp18s) were included close to the 3' propyl thiol in order to increase the flexibility of DNA, which will improve grafting density and crystallization ability[112]. Second, linker strands that contain a region complementary to the corresponding anchor strands on one end, a spacer region that

includes certain number (n = 1 or 2) of 20-base sequence, and a 7-base single-stranded sticky end region on the other end. Last, 20-base duplexer strands were hybridized onto the spacer region of the linker strands. The spacer region is designed to tune the length of the DNA, while the sticky end engages in the hybridization with complementary sticky end region on neighboring nanoparticles and drives the aggregation of complementary DNA-coated nanoparticles. The DNA coated nanoparticles are also commonly called programmable atom equivalents (PAE) due to the striking similarity between DNA-mediated assembly and traditional atomic crystal formation.

5.5.2 Substrate Design and Fabrication

In order to facilitate epitaxial growth of crystals on substrates, the patterned arrays should resemble the desired crystal lattice plane ((001), (110), and (111)). For a pattern with lattice constant a_p, the posts are arranged according to Figure 5.5. Additionally, Au posts with size close to the size of the nanoparticles used (20 or 30 nm) are also desired.

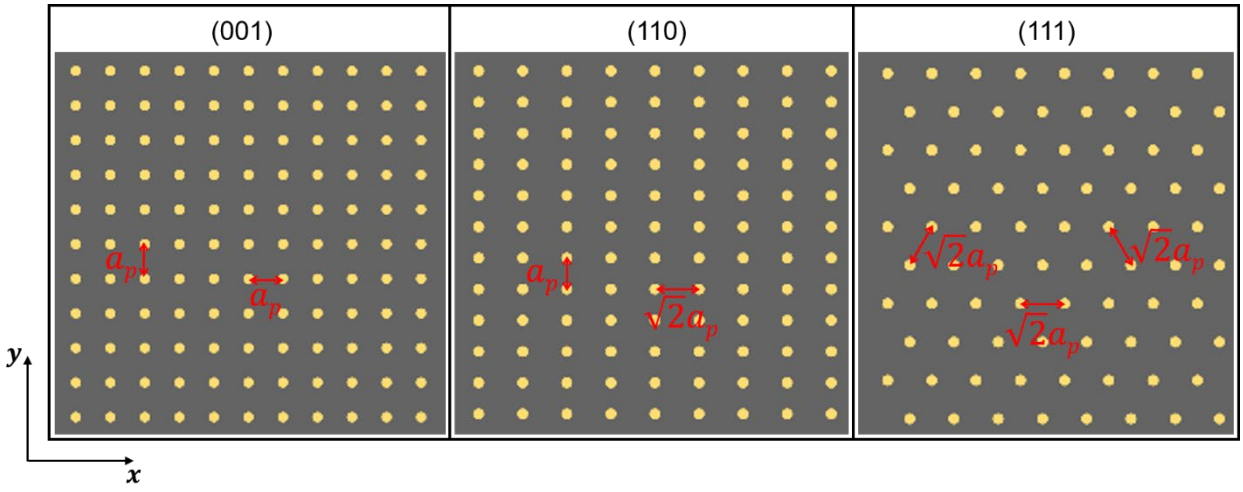

Figure 5.5. Schematic drawings of the pattern design for the three crystal planes, (001), (110) and (111) from left to right. a_p is the lattice constant of the pattern.

Moreover, the Au posts were made to sit on top of a pillar that is at least about 20 nm tall. This is because in the [110] orientation, the first deposited layer of PAEs lies on the same level as the posts (Figure 5.6). Hence the Au posts have to be sufficient far from the substrate in order to make room for DNA strands coated at the bottom of the incoming PAEs. In other words, high aspect ratio pillars containing Au post sitting on top of another posts are desired (Figure 5.6b).

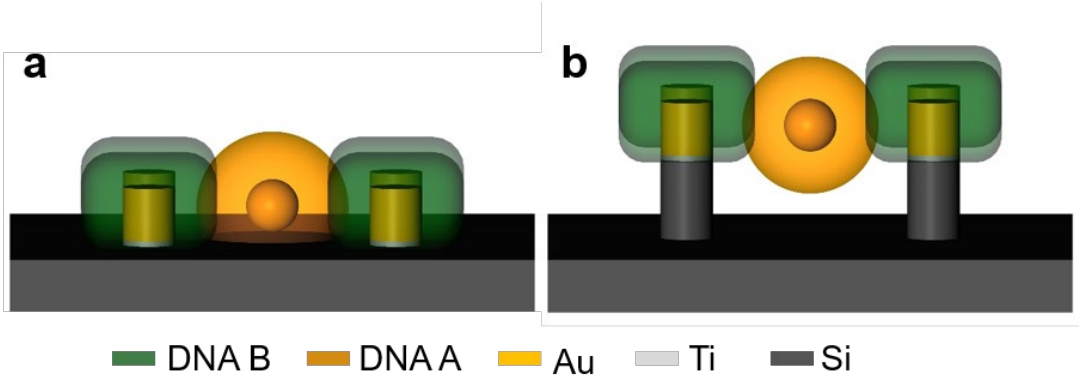

Figure 5.6. A tilted view of the first layer of nanoparticle deposited on (110) pattern. As the first layer of PAEs lie on the same level as the Au posts, the Au posts should be raised from the substrate to make space for the DNA coated at the bottom of the PAEs (b), such that the substrate is not physically hindering the PAEs (a).

For fabrication of the patterned substrate, 150 mm p-type prime grade (100) Silicon wafers were purchased from NOVA Electronic Materials. A thin layer of Poly(methyl methacrylate) (PMMA) resist (PMMA 950 A4, MicroChem) was coated onto pristine wafers through spin coating at 4500 rpm for 1 min and postbaking at 180 ℃ for 5 mins. The resulting resist film thickness was ~ 190 nm. JBX-8100FS (JEOL) electron-beam lithography (EBL) system was used for high throughput patterning. Substrate development was subsequently done through sonication in cold (4 ℃) MIBK/IPA in 1:3 ratio for 1 min, thoroughly rinsed in IPA, and dried under nitrogen. Oxygen plasma cleaning was performed on developed substrates for 30 s, in order to remove any remaining resist scums. The final film thickness was reduced to ~ 150 nm before metal deposition

in a Temescal FC2000 electron-beam evaporator. A film of Ti (2 or 5 nm), Au (20 or 30 nm), and Cr (10 nm) were subsequently deposited. The 10 nm Cr layer is used as protection layer for subsequent processing, as will be detailed in the following paragraphs. The remaining PMMA mask was finally removed through a liftoff process in hot (~ 80 ℃) Remover PG (MicroChem): the substrates were soaked in the hot Remover PG for ~ 10 hours, sonicated in hot Remover PG, Acetone and nanopure water, and dried in nitrogen.

Subsequently, a reactive ion etching (RIE) process was done to recess the substrate. Specifically, RIE was performed in Oxford PlasmaLab 100 with 50 sccm CHF_3, 2 sccm O_2, 50 W DC power under 20 ℃ temperature and 8 mTorr pressure for 8 – 12 minutes. This process effectively etched away Si and the whole substrate was recessed by more than 50 nm, except area of the posts that were protected by the Cr protection layer.

Finally, the Cr protection layer was removed through a wet etching process. The substrate was immersed in Chrome Etchant 1020 (Transene) for 40 minutes, followed by rinsing in copious amount of water. Figure 5.7 shows scanning electron microscope (SEM) images of the patterns before and after the wet etching process.

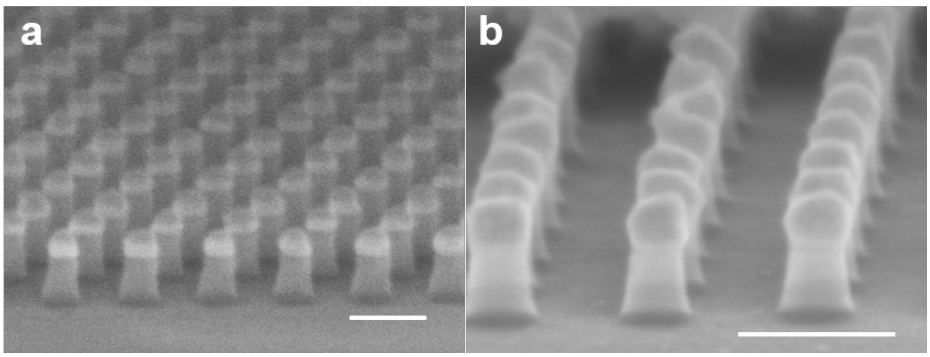

Figure 5.7. SEM images of the post arrays before (a) and after (b) wet etching process. In (a), the brightest portion of the pillars is Au, and the dark cap is Cr. In (b), the Cr cap on top of Au is gone. Both samples are tilted around 75 degrees. Scale bars are 100 nm.

5.5.3 Substrate and Nanoparticle Functionalization and Assembly

Thiolated anchor strands (A-SH and B-SH) were treated in 100 mM dithiothreitol for 1 hour in order to remove the 3'-propylmercaptan protecting group. The strands were then desalted using a size exclusion column (GE Healthcare).

Immediately before functionalization, the substrates were treated with O_2 plasma cleaning (50 W power and ~20 mTorr pressure), brief (~ 10 s) sonication in $NaBH_4$ solutions (20 mg $NaBH_4$ in 50 ml H_2O), followed by rinsing in H_2O. The salt concentration of the anchor stands B-SH solution was brought up to 1 M to maximize DNA loading on the posts, and a large excess amount (more than 10×) of DNA was always used for substrate functionalization. The substrate incubation solution was sonicated briefly (~ 10 s) to remove any air bubble and left for at least 4 hours.

For nanoparticle functionalization, 20 and 30 nm in diameter citric-capped Au nanoparticles (Ted Pella) were directly mixed with desalted anchor strands (A-SH and B-SH) under the ratio of roughly 1 OD of DNA per 1 mL of nanoparticles. After incubating for 2-4 hours, the solution underwent a "salt aging" process[88] to gradually bring up the final NaCl concentration to 0.5 M by increasing the solution salt concentration by 0.1 M at every 30 mins interval. After bringing the salt concentration to 0.5 M, the solution was incubated in a shaker under 37 ℃ and 130 rpm for ~ 10 hours. Surfactants, salt, and excess DNA strands unbound to nanoparticles were washed away by three rounds of centrifugation inside a 100 kDa membrane filter centrifuge tubes (Millipore). 0.01 % sodium dodecyl sulfate (SDS) in Nanopure water solution was used for resuspension of nanoparticles after each round of centrifugation. Finally, the salt concentration of the DNA-coated nanoparticle solution was brought up to 0.5 M salt concentration. Concentration of the nanoparticles was measured with a Cary 5000 UV-Vis-NIR spectrophotometer with

nanoparticle extinction coefficients found on Ted Pella's website (http://www.tedpella.com/gold_html/gold-tec.htm).

The next step is preparing DNA linker (Linker A/B-n=1/2) stock solution. The notation "n=1" (or "n=2") indicates the number of duplexed blocks inserted in the linker. Thus, n equivalents of duplexer strands were first mixed with linker strands together to bring the final duplexed DNA concentration to 10 μM in 0.5 M salt. The mixture was shaken at 300 rpm and 45 ℃ for 30 mins, before slowly cooled down to room temperature. The stock solution was used for subsequent assembly and can be stored in freezer for future use.

Finally, programmable atom equivalents (PAE) were made by hybridizing duplexed linker strands onto anchor-coated nanoparticles under a molar ratio of 1:400 and 1:900 for 20 and 30 nm nanoparticles, respectively. An appropriate amount of NaCl solution was added to bring the PAE salt concentration down to 2 nM. For linker hybridization on substrates, the linker stock solution was diluted to from 10 μM to 1 μM while keeping salt concentration constant. The substrates were dipped in 0.5 M NaCl solution to remove excess DNA anchor strands, before immersion in 1 μM DNA linker solution. The mixtures were again shaken at 300 rpm and 45 ℃ for 30 mins, before cooling down to room temperature. 2.5 mL of PAE A/B solution were added into 5 ml Eppendorf tubes and vortexed briefly to ensure even mixture, before adding the functionalized substrates. The tube was partially submerged in a temperature-controlled water bath, which was slowly cooled from 60 ℃ to 28 ℃ under a cooling rate of 0.01 ℃ per minute (Figure 5.1). This provides a temperature gradient inside the tube (~5 ℃ from bottom to top when the water bath temperature is 50 ℃, and the difference increases with higher water bath temperature), such that as the

temperature decreased, aggregated PAEs that settled down at the bottom of the tube were melted and diffused back to the top of the tube to replenish lost PAEs.

5.5.4 Post-Assembly Processing and Characterization

After slow cooling was completed, lots of crystals were also assembled freely in solution as by products, together with crystals assembled on substates. We examined the quality and lattice parameters of these freely assembled crystals through two processes: Small-Angle X-ray Scattering (SAXS) and SEM.

SAXS experiments were performed on as-assembled crystals conducted at the DuPont-Northwestern-Dow Collaborative Access Team (DND-CAT) beamline 5ID-D at the Advanced Photon Source (APS) at Argonne National Laboratory. The exact procedure had been described abundantly in literature[107, 126]. In particular, 10 keV (wavelength 1.24 Å) collimated X-ray beam illuminated on ~ 60 μL of the sample loaded in a 1.5 mm quartz capillary (Charles Supper), producing two dimensional scattering data that was later converted to one dimensional data through radial averaging. Due to the large contrast, the X-ray signal was predominantly scattered by the Au nanoparticles and oligonucleotides were considered transparent. Namely, the parameters of nanoparticle crystals were directly calculated from SAXS signals.

Before characterization with SEM, crystals assembled both freely in solution and on substrates underwent a silica embedding process to facilitate transition from solution to solid state[50]. Crystals assembled in solution sedimented at the bottom of the reaction tube, which were extracted and resuspended in 1 mL of 0.5 M NaCl solutions. Due to the large amount of crystals, 4 μL of N-(trimethoxysilyl)-propyl-N,N,N-trimethylammonium chloride (TMSPA, Gelest) was added. Vigorous agitation were needed to resuspend sedimented crystals, before incubating the

solution for 20 min on a rotary shaker at 700 rpm under room temperature. Subsequently, 8 μL of triethoxysilane (TES) was added to the solution and the solution was left in the shaker for at least 12 hours. After silica embedding, the samples were washed with three rounds of centrifugation, supernatant removal, and resuspension in Nanopure water in order to get rid of excess silica formed in solution. For substrates, nonspecifically attached PAEs were washed away by rinsing the substrates with 0.5 M NaCl solution before submerging in 5 mL of 0.5 M salt solution. The same shaking process was performed with substrates except with 10 μL TMSPA and 20 μL TES. Finally, the substrates were washed with Nanopure water and gently blown dried with Nitrogen.

In order to investigate how the crystal growth was affected by the substrate pattern, FIB cross-sectioning was used to cut through the crystals so that the crystal cross-section can be examined with SEM. FIB cross-sectioning was performed with a FEI Nova 600 NanoLab DualBeamTM-SEM/FIB system at Center for Nanoscale Materials (CNM) of Argonne National Laboratory. 30 keV Ga ion beam was used, and the beam current was set at 28 pA – 0.24 nA during milling.

5.6 Supplementary Discussions

5.6.1 Characterization of Crystals Assembled in Solution

Figure 5.8 shows the SAXS spectrum (a) and SEM image (b) of crystals freely assembled in solution and composed of 30 nm NP and n=2 DNA linker. The SAXS spectrum shown here is taken before silica embedding. For bcc structures, the first three peaks correspond to [110], [200], [211] crystalline orientations. We use the location of the first peak to calculate the lattice constant through the equation below:

$$a = \sqrt{2} * \frac{2\pi}{q_0}$$

and corroborate with the second and third peaks. The lattice constant calculated from SAXS data (a_i) is ~ 77.9 nm. In order to image crystals freely assembled in solution, the silica embedded samples are drop casted onto a silicon substrate and screened through in order to be located. From Figure 5.8b we see that all crystals adopt rhombic dodecahedral (RD) shape, but their location and orientation are random.

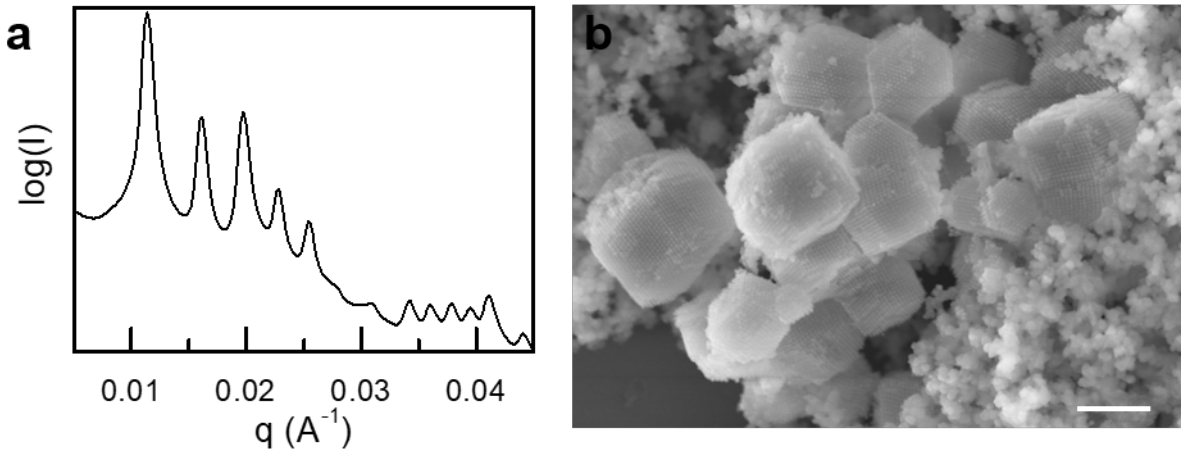

Figure 5.8. SAXS spectrum of 30 nm crystals assembled with DNA linker n=2 before silica embedding (a), and SEM image of the crystals after silica embedding and drop cast onto a silicon substrate (b). The scale bar is 1 μm.

5.6.2 Crystals Assembled on Unpatterned Au Strips

Micron-sized Au strips (5 - 10 μm wide and 200 - 300 μm long) are patterned together with post arrays to serve as controls. During each assembly process, the Au strips are also functionalized with DNA B and NP crystal growth occurs. The assembly is selective and only occurs on the Au strip (as compared to the rest of the substrate without Au). Depending on a variety of reasons, such as the DNA-loading density on the Au strip, surface hydrophilicity, PAE concentration and cooling rate, a multitude of deposition behavior is observed, including layer-by-layer growth (Figure 5.9a),

layer-by-layer followed by island growth (Figure 5.9b-d) and island growth (Figure 5.9e-f). Interestingly, when there is a higher density of growth (Figure 5.9a and 5.9d), crystals grow predominantly in the [100] orientation, since the lattice plane contains the most densely packed A type PAEs and therefore the largest binding affinity towards the Au strip that has been coated with complementary Linker B[114]. As the crystal density becomes sparse, we observe crystals in all three orientations (Figure 5.9b, c, e-f). There is little control on neither the crystal location nor orientation.

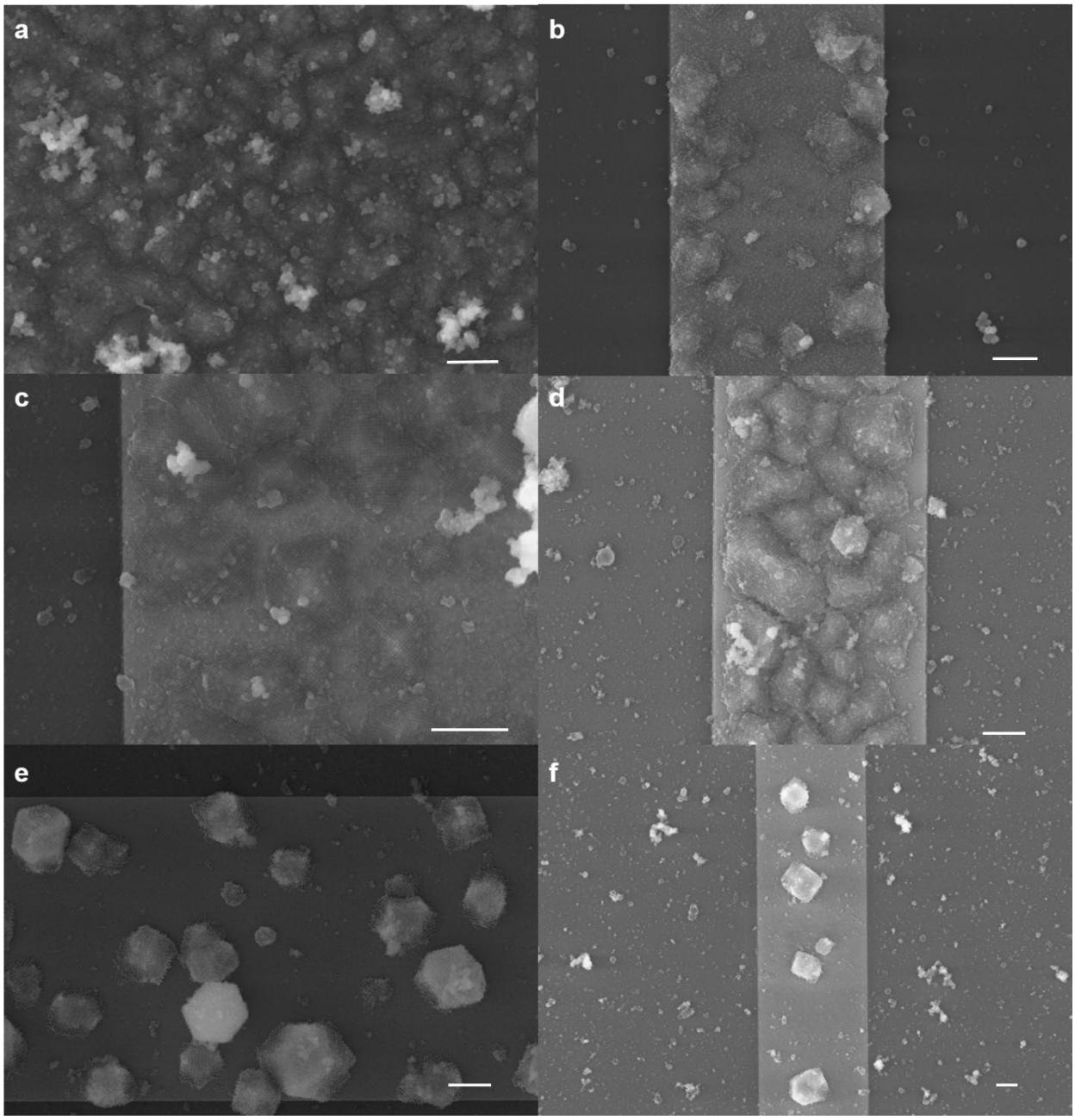

Figure 5.9. Crystals assembled on unpatterned Au strips. Depending on the assembly condition, different types of growth processes are observed. In all cases, there is little control on the crystal orientation and exact growth location. The scale bars are 1 μm.

5.6.3 Shapes of Crystals along Different Orientations

In a slow cooling process, thermodynamic product of bcc crystals in solution adopts an RD habit[119]. When a 2D pattern is introduced as the "seeding" layer for epitaxial growth, the slow cooling process would still produce crystals with partial Wulff polyhedral habit (i.e. part of RD). In order to visualize this, we can start with a full RD crystal, and each pattern on the substrate is as if we are cutting the crystal along the crystal planes resembled by the pattern symmetry, resulting in orientation-specific crystal shapes (Figure 5.10).

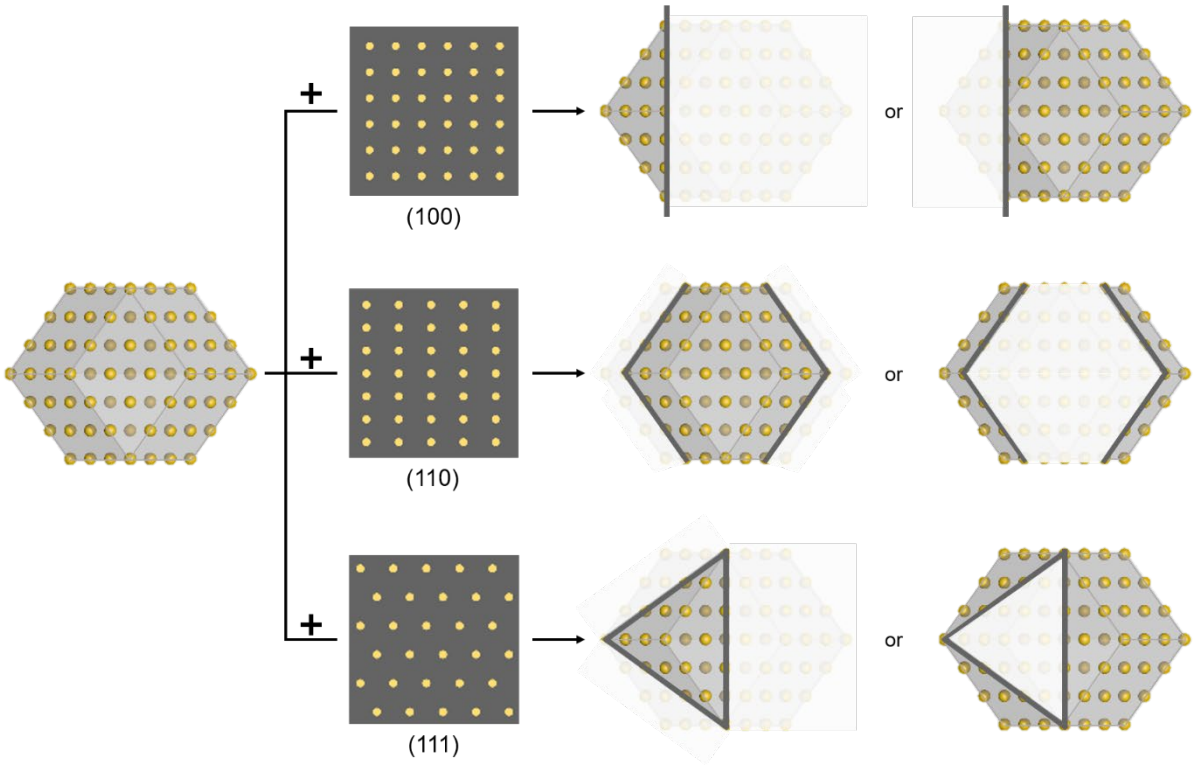

Figure 5.10. In order to rationalize the orientation-specific shapes, we can visualize it as if a full RD is cut by a specific lattice plane as defined by the symmetry of the pattern. The resulting shape, which is the shape of epitaxially grown crystals, is shown as the uncovered part. While the "missing" part which is as if cut off by the substrate is shown as the shaded regions.

5.6.4 In-Plane Orientation Control

From close-up SEM images of a single crystal (Figure 5.1f-h), we can see that the crystal grows in the lattice orientation perpendicular to the lattice plane defined by the pattern. Namely, the orientation in the z-axis is controlled by the pattern symmetry. Figure 5.11 shows that we also have control over the orientation of the crystals in the x-y plane. In Figure 5.11, both (a) and (c) are patterns of (001) lattice planes, however, the patterns in (a) are rotated 45 degrees with respect to the ones in (c). As a result, we see that the corresponding assembled crystals are 45 degrees rotated with respect to each other in (b) and (d).This effectively shows that we can control the in-plane crystal orientation by pattern design. Note that although the patterns in both design (a) and (c) have an overall square shape, the shape of the assembled crystal does not follow that of the pattern.

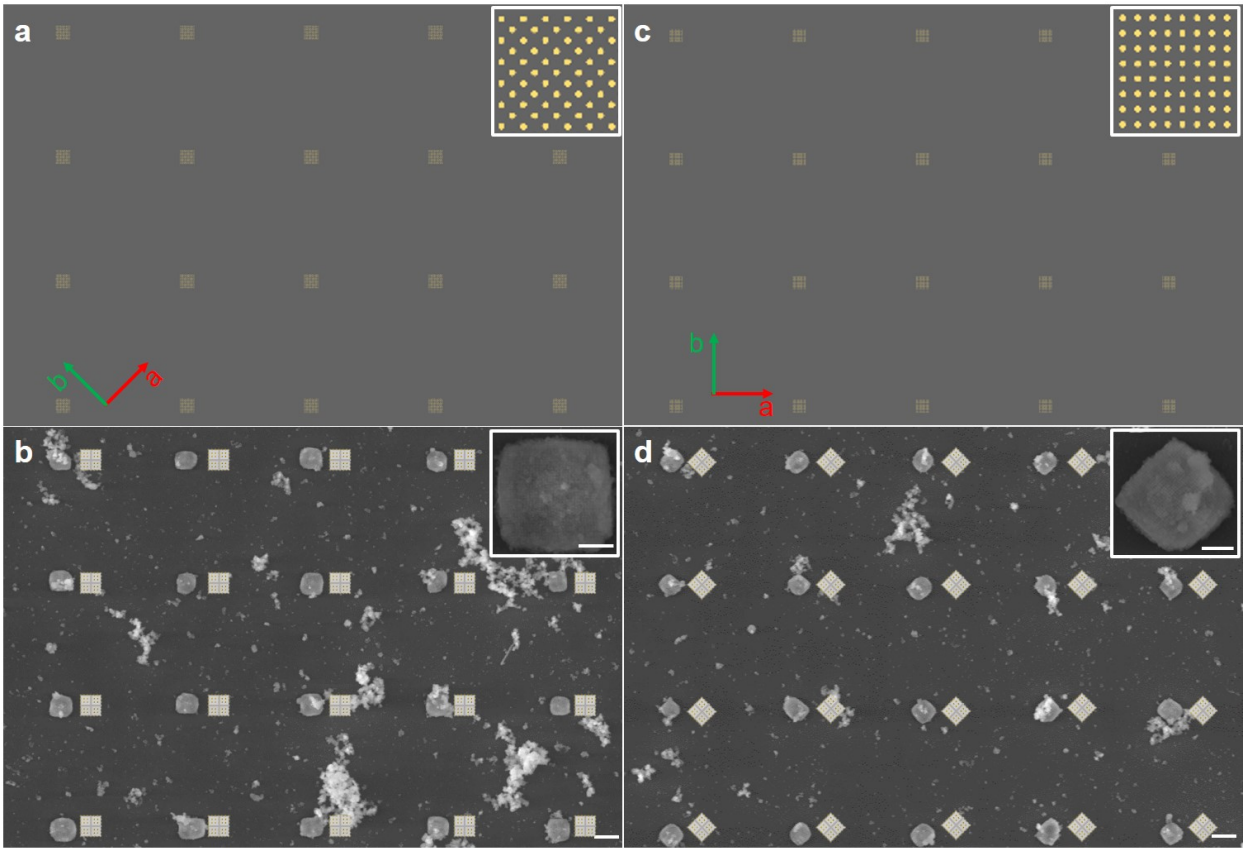

Figure 5.11. Schematic representation of the (001) substrate pattern with one (a) rotated 45 degrees with respect to the other (c). SEM images of the corresponding crystals also obey a 45-degree rotation from (b) to (d). The inset shows an enlarged image of each case. The scale bars are 2 μm and 500 nm (inset).

In the main text, we have discussed the effect of pattern symmetry and strain on the epitaxially assembled crystals in the [001] and [110] orientations and established a one-to-one correlation between the pattern and the crystal orientation. In the case of [111], however, two directions are allowed due to symmetry and there is no control over which direction the crystal undertakes (Figure 5.12).

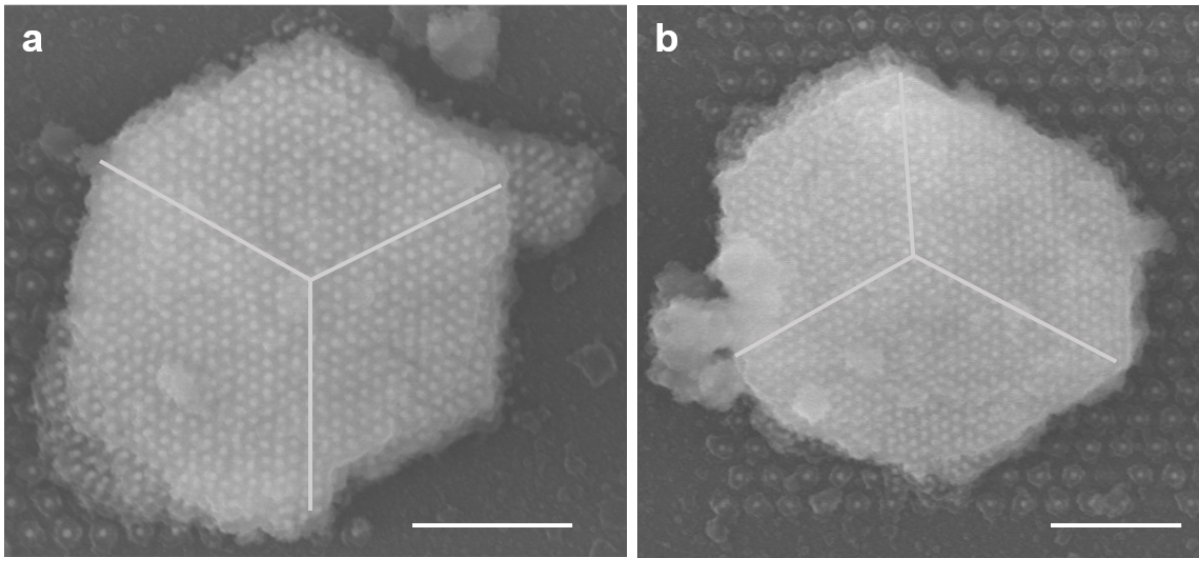

Figure 5.12. SEM images of crystals assembled in the [111] orientation. Both samples are assembled on the same substrate with 30 nm nanoparticle, n=2 linker, pattern lattice constant a = 75 nm. The edges at the top of the crystals are highlighted with white lines. Scale bars are 500 nm.

5.6.5 Size of the Pattern Does not Determine the Size of the Crystal

While we can easily control the overall size of the pattern, it does not affect the size of the crystal (Figure 5.13). Rather, since these crystals are thermodynamic products, their sizes are dependent on the growth conditions, such as NP size, concentration, and slow cooling rate. In

Figure 5.13, when using (001) pattern with 2 μm edge length (as compared to 1 μm edge length at all other cases), we see that multiple nucleation sites take place on the pattern. A single crystal epitaxially grows at each site, but these crystals do not grow big enough into one coherent single crystal with an overall pyramid shape.

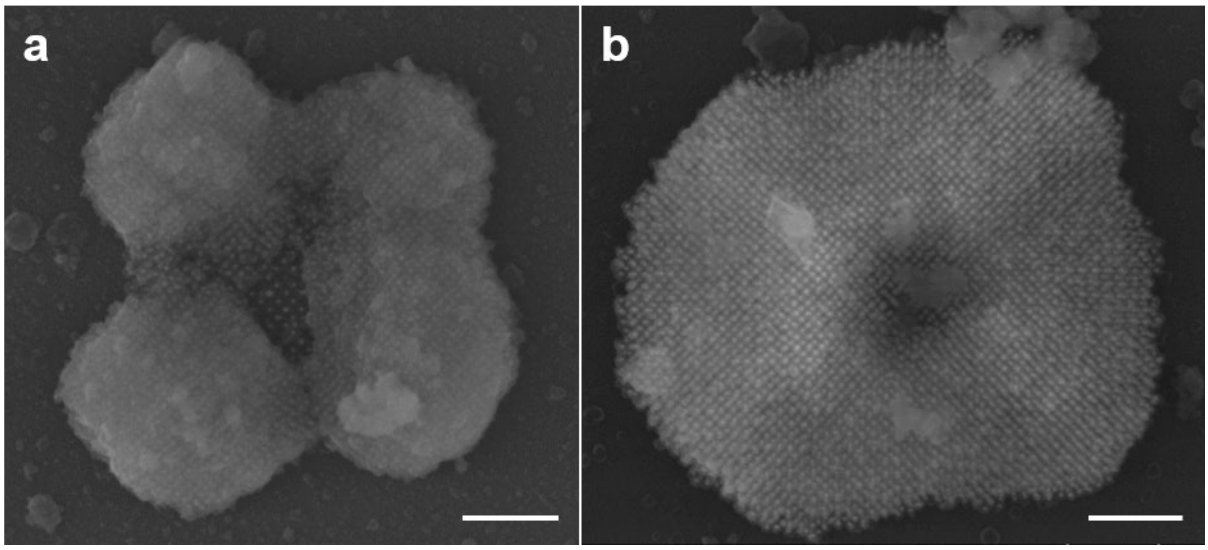

Figure 5.13. SEM images of crystals assembled in the (001) orientation. The edge length of the pattern is 2 μm, compared to the other cases where the edge length is only 1 μm. We see that multiple crystals nucleate and epitaxially grow on the pattern, but they do not grow large enough to form a single large crystal. Scale bars are 500 nm.

5.6.6 Additional Analysis of (001) Crystal Cross Sections

The lattice parameter change during the silica embedding process has created an extra layer of complication in understanding the interactions between pattern and crystal, rendering a direct point-to-point analysis difficult. Thus, we provide both SEM and schematics at different orientation to facilitate the understanding. To aid visualization of the schematics, PAE A and B are color coded as orange and green spheres, respectively. Figure 5.14a shows the SEM images of the 75 nm a_p sample from Figure 5.3c taken at 52 and 75 degrees from the top (upper row) and schematic drawings of the lattice structure at four different angles (0, 52, 75, 90 degrees, lower

row). From the 0-degree schematic (Figure 5.14a, bottom-left), we see that the cross section is composed of both types of PAEs at two different planes, which can be observed from the SEM image of the crystal tilted at 75 degrees due to a difference in contrast. When tilted at 52 degrees, the two planes of PAEs seem to align in an almost straight line. And when the crystal is tilted at 90 degrees, we can see the cross-sectional plane is indeed (001).

Figure 5.14b shows the same set of data of the 60 nm a_p sample from Figure 5.3b, namely sample with large lattice mismatch. From the 0-degree schematic (Figure 5.14b, bottom left), we see that both types of PAE are on the same plane, but different from the patterned posts. This is in well agreement with the 75-degree SEM image, where all PAEs show similar contrast. Again, when the crystal is tilted at 90 degrees, we can see the cross-sectional plane is indeed (110).

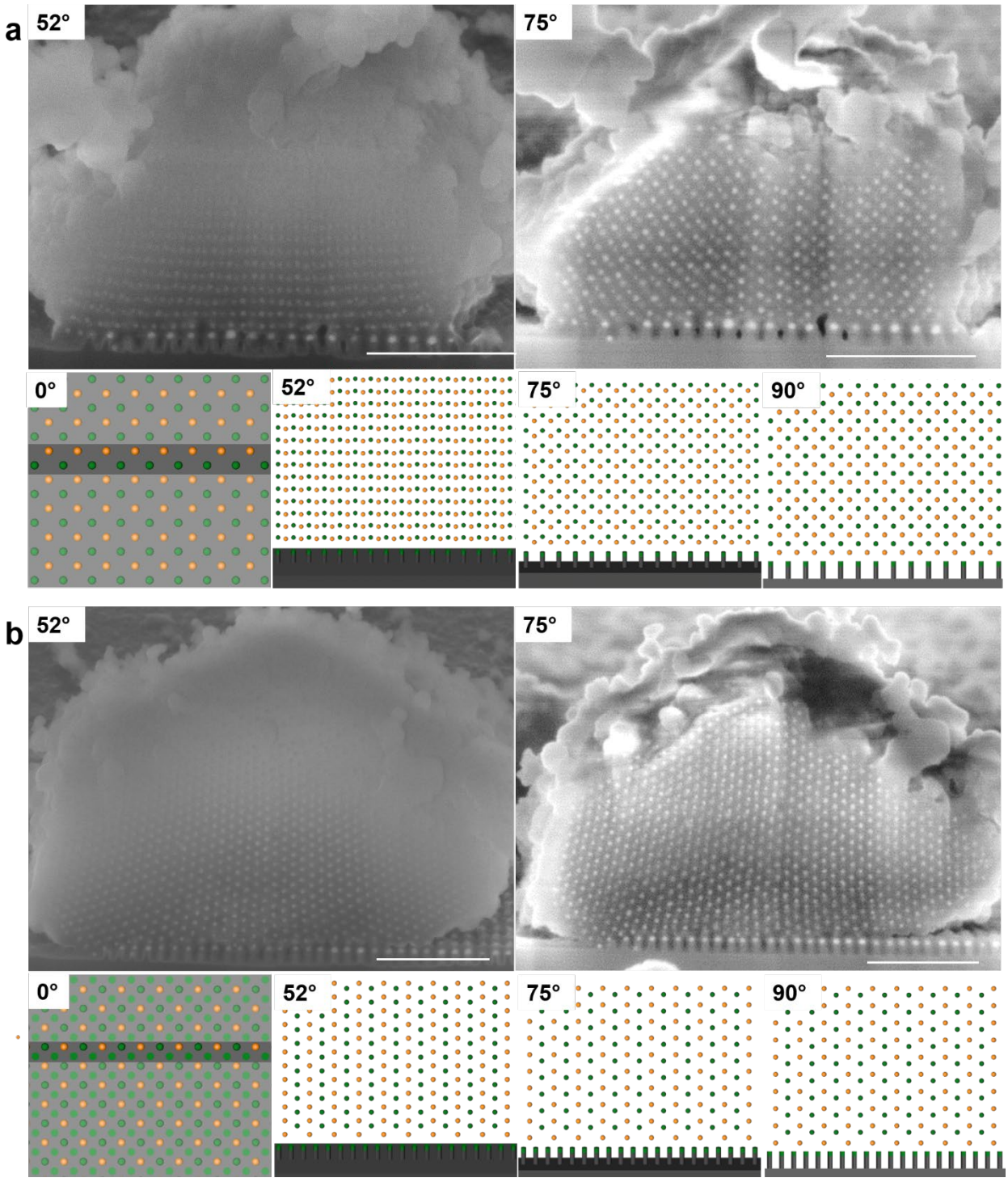

Figure 5.14. SEM images (upper row) and schematic drawings (lower row) of crystals with small (a) and large (b) lattice mismatch tilted at different degrees from the top of the crystal (furthest from the substrate). The degree of tilt is shown on the top-left corner of every image. The cross section is highlighted in the 0-degree drawings by adding shades to the rest of the lattice. There

are the same sample shown in Fig. 3b, c and the a_p are 75 nm (a) and 60 nm (b), respectively. The scale bars are 500 nm.

5.6.7 Pattern with Small a_p is Redefined by the First Layer of PAEs

We have shown that when the lattice constant is too small and there is too much compression strain, there will be overlap between the same type of DNA strands if all of the *optimum sites* are filled. This can be viewed in Fig. 5.15a, where the DNA is denoted by the partially transparent orange shell. The a_p of each pattern is labeled on the top of each drawing. When a_p = 50 or 65 nm, an example of the overlap between neighboring DNA shells is highlighted by the red ellipse. This overlap will give rise to repulsion between neighboring NPs such that only half of the positions defined by the substrate pattern are filled with NPs (Fig. 5.15b). The image on the left of Fig. S11b shows the pattern (green circles) and the potential sites (white empty circles) for NP deposition based on the complementary contact model, where complementary DNA strand hybridization is maximized during assembly[9]. The pattern is rotated 45 degrees, and its lattice constant is defined by the neighboring posts (shown as *a* and *b* in Fig. S11b). However, if every site defined by the white empty circles is filled, it will result in a large repulsion between neighboring NPs. Therefore, the first layer of NPs only deposits at alternating sites, effectively redefining the substrate pattern, as illustrated in the schematics on the right in Fig. S11b. The new pattern defined by the first layer is rotated 45 degrees from the original pattern and has a new lattice constant (shown as *a'* and *b'* in Fig. S11b) that is $\sqrt{2}$ times a_p. Thus, for a_p ranging from 50 to 65 nm, the redefined a_p' is between 71 and 92 nm, covering a similar range as the 65 - 85 nm examples shown in Figure 2a.

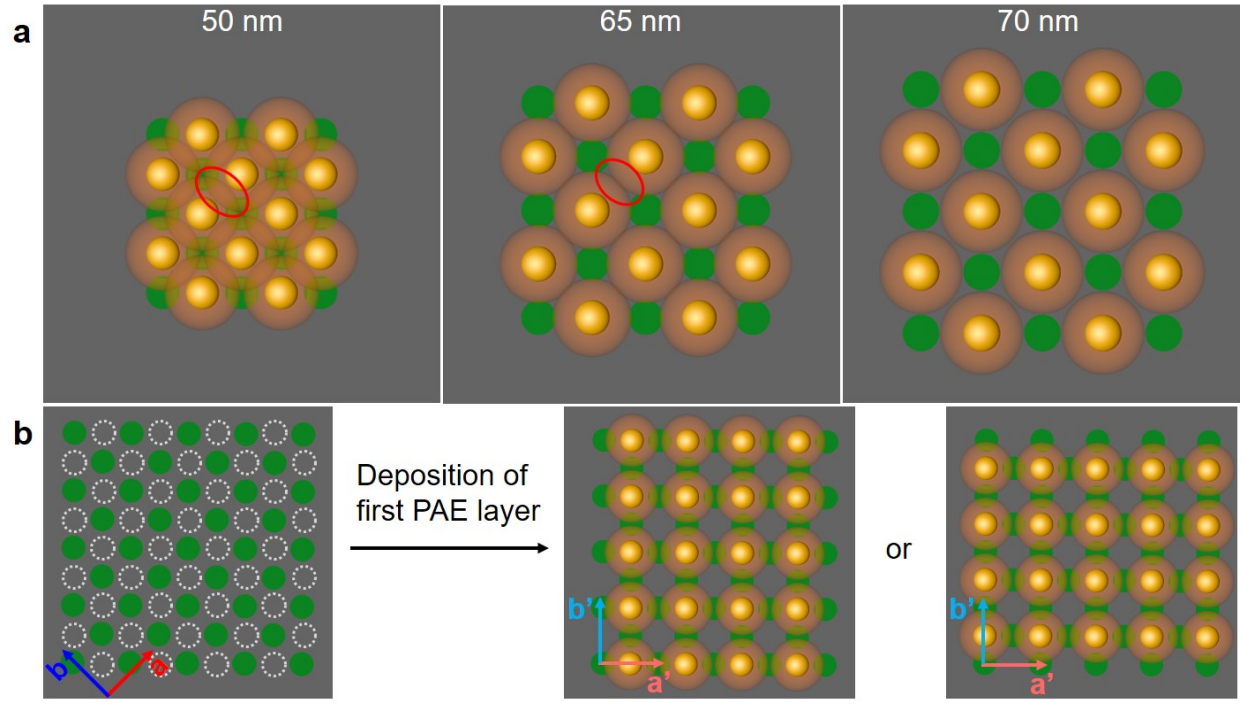

Figure 5.15. Schematic illustration of the redefinition of the substrate pattern by the first layer of NPs. (a) Schematics of the pattern and first NP layer if the NPs are deposited only according to the complementary contact model. The a_p of the pattern is labelled on the top of each drawing. The partially transparent orange spheres indicate the DNA shells. (b) Again, in order to maximize DNA binding, the first layer of NPs likely deposit at the locations defined by the gray empty circles in the image on the left. But, due to the large lattice mismatch between the substrate and the crystal and the large repulsion between NPs with the same type of DNA, only half of the positions were filled by the first layer of NPs, as shown in the images on the right, effectively redefining the pattern.

5.6.8 Effect of Silica Embedding on the Crystal

In all the cross-sectional images, we can see a decrease in the lattice constant from the substrate to the top of the epitaxially grown crystals, regardless of a_p. For example, although a_i is around 79 nm, the crystal still seems to "shrink" as it grows further from the substrate with 70 nm lattice constant. This is because crystals contract during the silica embedding process [50]. Indeed, we can see from the SAXS measurement, the lattice constant of 30 nm nanoparticle crystal with

n=2 linker after silica embedding (solid line) is 67.8 nm, as compared to 77.9 nm from the same batch of crystals measured before silica embedding (a_s, dashed line). It is worth mentioning that this shrinkage has no effect on the assembly process since it occurs afterwards, so a_i, rather than a_s, should be used to guide our analysis of the assembly process.

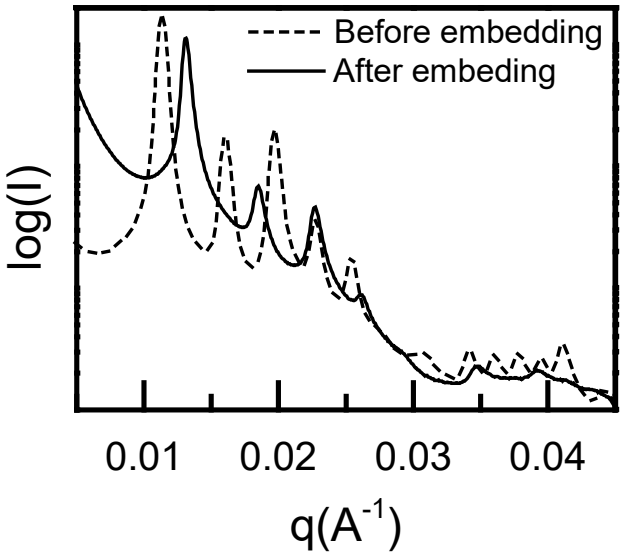

Figure 5.16. SAXS spectrum of silica-embedded 30 nm nanoparticle crystals with n=2 linker assembled freely in solution (solid line). The new calculated lattice constant a_s is 67.8 nm, much smaller than the lattice constant obtained from measuring the same batch of crystals before silica embedding (a_i, dashed line). The dashed line is the same data shown in Figure 5.8a.

When the crystal is larger, the shrinkage induced by silica embedding can be absorbed by the crystal, and we can only observe the shrinkage in cross-sectional images. In contrast, this shrinkage might be directly observed in smaller lattices and it might even break the lattice up. Figure 5.17a shows a superlattice partially grown on a (111) pattern. The $a_p$is 75 nm, similar to the a_i. However, since the superlattice only grows into a few layers, we can clearly see the lattice parameter decreases in upper layers of the crystal. In Figure 5.17b, a superlattice is partially grown along the [110] orientation. The overall shape of the superlattice resembles that of a partially grown

crystal in the [110] orientation, however, there is a laceration in the lattice, which is likely caused by the silica embedding process.

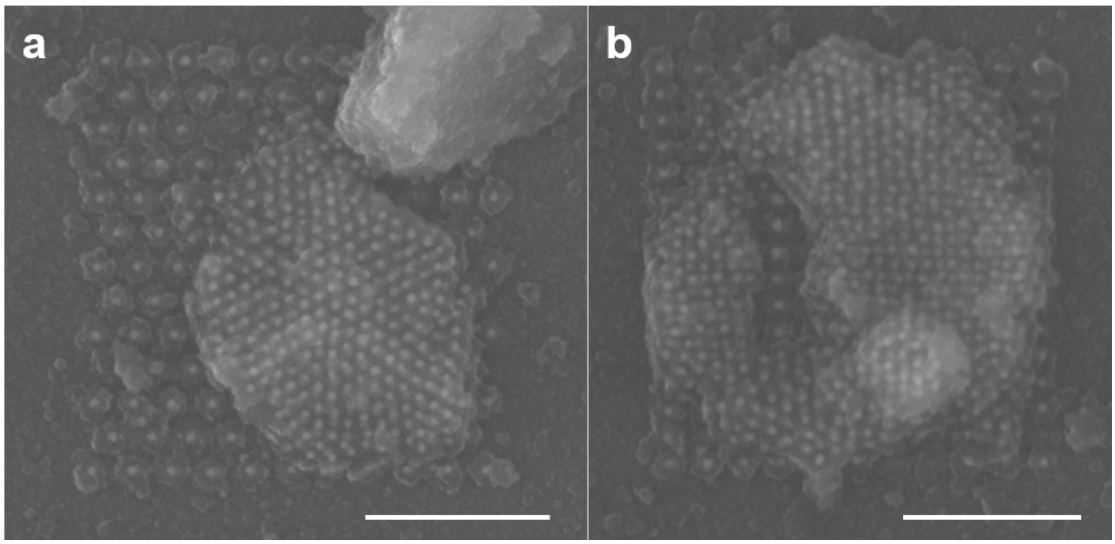

Figure 5.17. SEM images of a partially grown lattice along the [111] (a) and [110] (b) orientations. Due to the small number of layers, we can directly see the lattice shrinking in upper layers in (a). In (b), the overall lattice shape resembles that of a crystal along the [110] orientation, but there is a huge laceration inside the lattice that is likely caused by silica embedding. Scale bars are 500 nm.

5.6.9 Yield of Crystals Epitaxially Grown in the [001] Orientation

When a_p is close to a_i (as indicated by the white squares in Figure 5.18 and 5.19), the yields for epitaxially grown crystals in the [001] orientation for both 0- and 45-degree rotations are 100%.

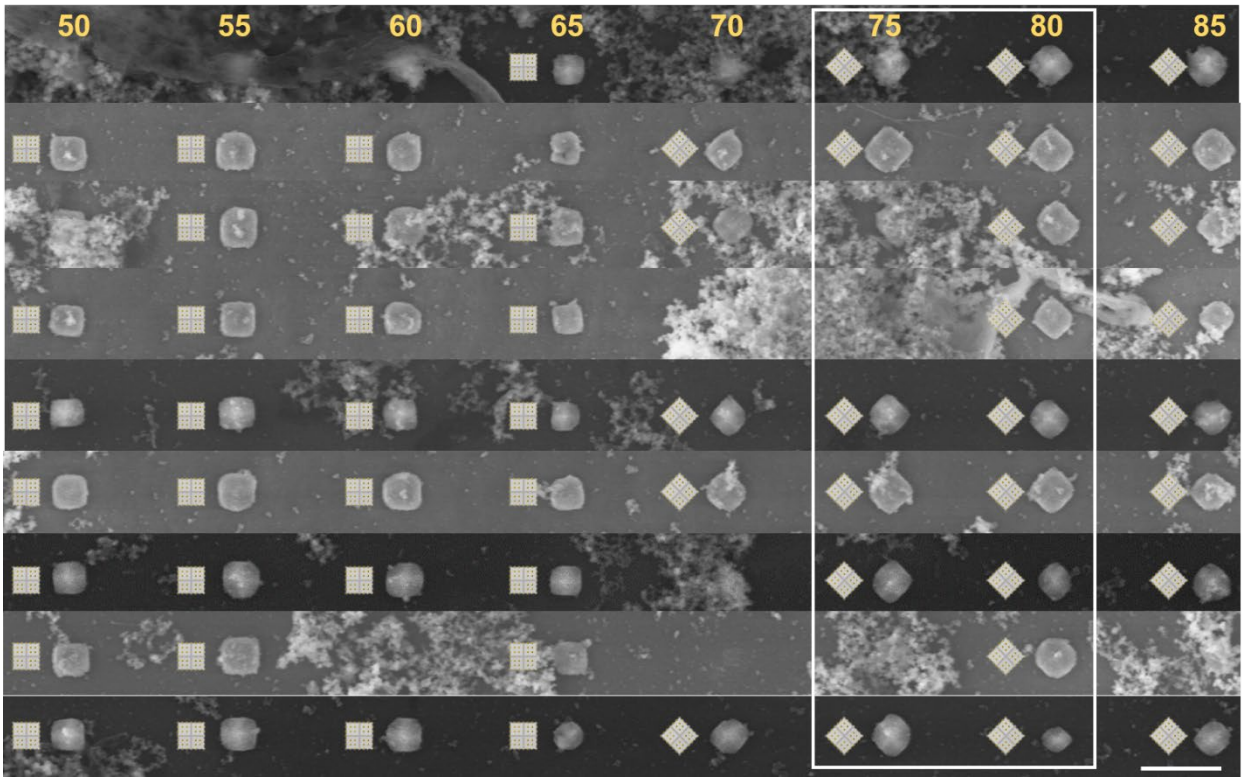

Figure 5.18. SEM images of crystals assembled along the [001] orientation on (001) pattern with a_p ranging from 50 - 85 nm. The white square highlights patterns with a_p close to a_i. Scale bar is 5 µm.

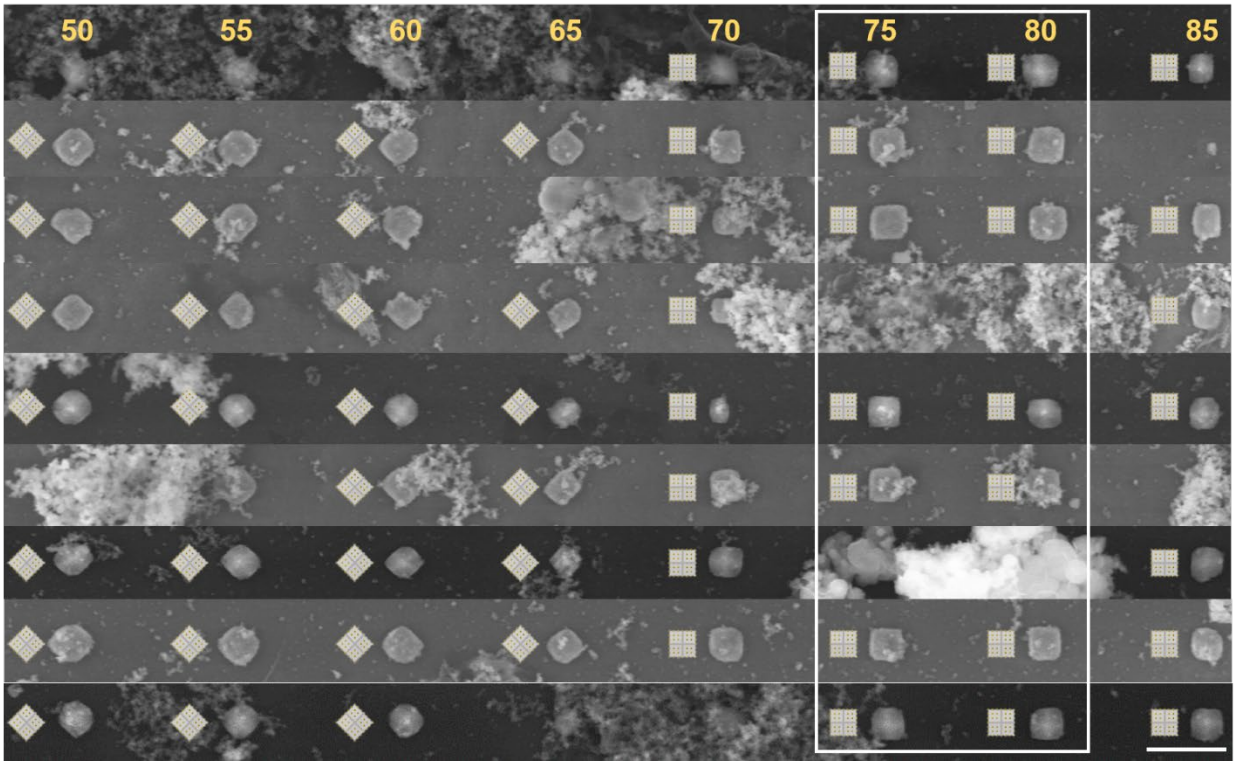

Figure 5.19. SEM images of crystals assembled along the [001] orientation on (001) pattern with 45-degree in-plane rotation and a_p ranging from 50 - 85 nm. The white square highlights patterns with a_p close to a_i. Scale bar is 5 μm.

5.6.10 Additional Analysis of (110) and (111) Crystal Cross Sections

Similar to Figure 5.15, cross sections of the (110) and (111) samples shown in Figure 5.4b and c are analyzed from different tilt angles. Figure 5.20a shows SEM images of the (110) sample tilted at 52 and 75 degrees from the top (upper rows) and schematic drawings of the lattice structure at four different angles (0, 52, 75, 90 degrees, lower row). To aid visualization of the schematics, PAE A and B are color coded as orange and green spheres, respectively. From the 0-degree schematic (Figure 5.14a, bottom-left), we see that the cross section is composed of both types of PAEs at the same plane, which can be seen from the SEM image of the crystal tilted at 75 degrees

- all NPs have similar contrast. Again, when the crystal is tilted at 90 degrees, we can see the cross-sectional plane is indeed$(1\bar{1}0)$.

Figure 5.20b shows the same set of data for the (111) sample (Figure 5.4c). From the 0-degree drawing (bottom-left), we see that there are essentially four equivalent layers. Our choice of the two layers for the cross-sectional image, as highlighted in the 0-degree cartoon and drawn in the 52-, 75- and 90-degree cartoons, is arbitrary. The cross-sectional plane is $(\bar{1}\bar{1}2)$.

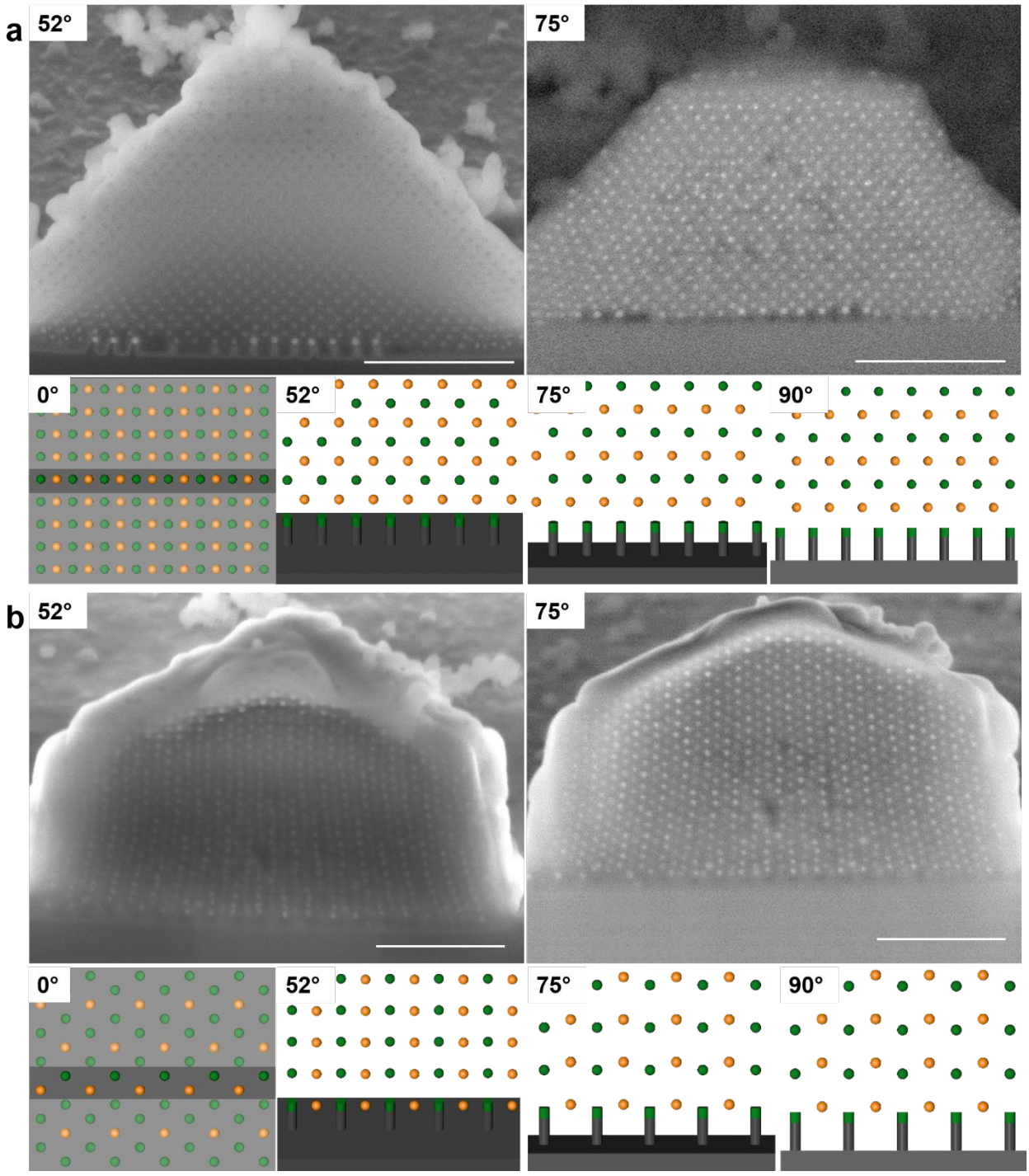

Figure 5.20. SEM images (upper row) and schematic drawings (lower row) of crystals grown on (110) (a) and (111) (b) pattern tilted at different degrees from the top of the crystal (furthest from the substrate). The degree of tilt is shown on the top-left corner of every image. The cross section is highlighted in the 0-degree drawings by adding shades to the rest of the lattice. They are the same samples shown in Fig. 4b, c and the a_p are both 75 nm. The scale bars are 500 nm.

5.6.11 Yield of Crystals Epitaxially Grown in the [110] Orientation

When a_p is close to a_i (as indicated by the white squares in Figure 5.21), the yield for epitaxially grown crystals in the [110] orientation is close to 100%. For a_p = 55 - 70 nm, crystals seem to identify the pattern as (001) plane with 0-degree rotation and grow along the [001] orientation.

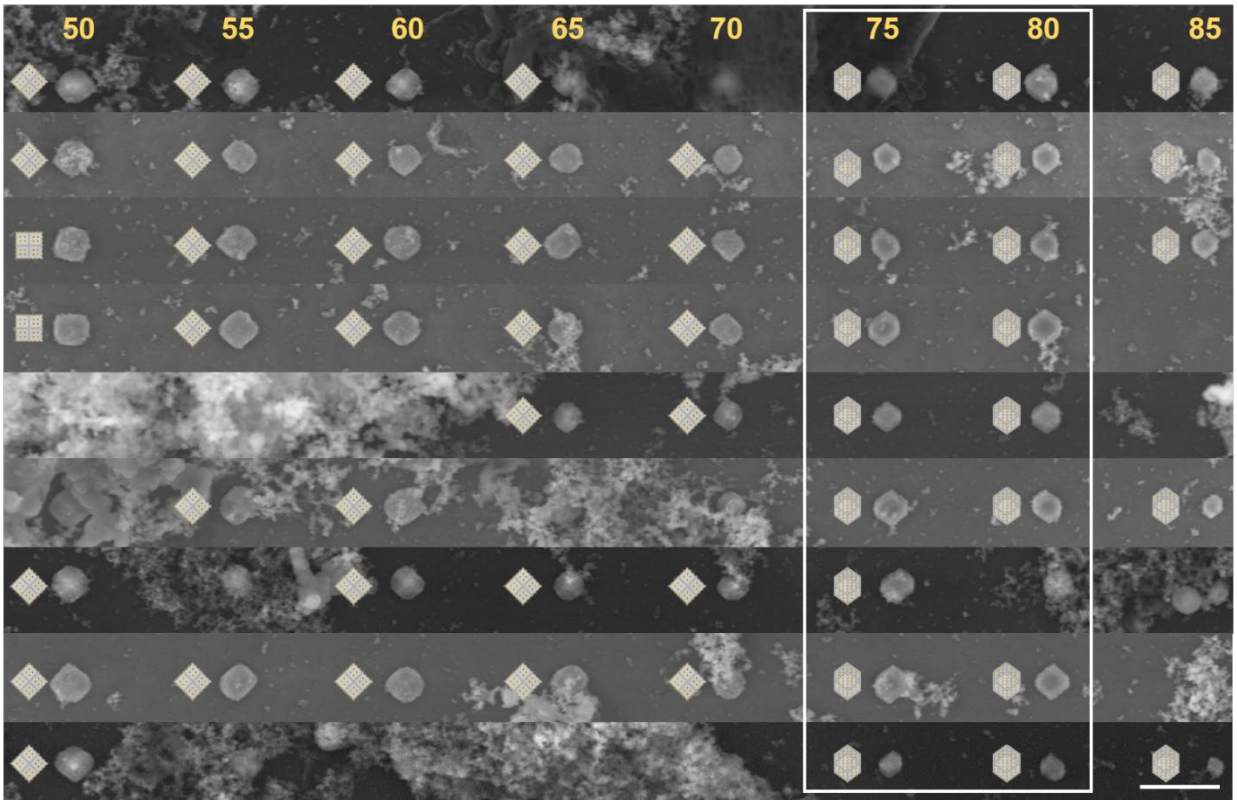

Figure 5.21. SEM images of crystals assembled on (110) pattern with a_p ranging from 50 - 85 nm. The white square highlights patterns with a_p close to a_i. Scale bar is 5 µm.

5.6.12 Analysis of Crystals Assembled on (110) Pattern with Small a_p

Figure 5.22a shows a schematic of the deposition geometry between different layers assembled on (110) patterns with 55 - 70 nm a_p. The A-type PAEs (orange sphere) will fit into the center of four B-type PAEs (green spheres) that define a square. For a 55 nm a_p, the distance

between neighboring B-type PAEs are 55 and 78 ($\sqrt{2}$ of 55) nm, respectively. With hydrodynamic radii of 34 nm, the center-to-center distance between binding A- and B-type PAEs are 68 nm. Consequently, the spacing between layers defined by the two types of PAEs is 48 nm, as indicated by the dashed double arrow. This distance is similar to the interlayer distance along the [001] orientation, which is half of a_p, i.e. 39 nm. Each layer of the PAEs will experience compressive strain in one direction and tensile strain in the other. The term strain here is defined as how much the position of the NPs differ from the theoretical positions predicted by the corresponding lattice. Since there is no binding between PAEs at the same layer, the concept of tensile strain is beneficial as it will provide additional room to accommodate the compression strain experienced along the other direction.

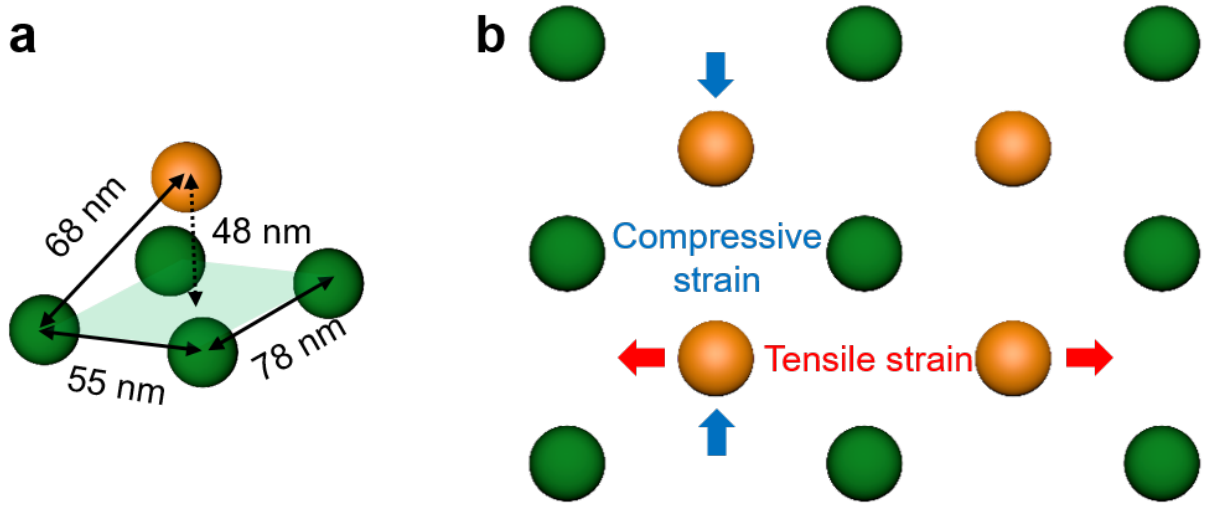

Figure 5.22. Schematic illustration of the deposition geometry of PAES on (110) pattern with compression strain. (a) Illustration of one PAE A deposited on top of the square defined by four neighboring PAE B. The numbers next to each double arrow indicates the spacing between the two PAEs. The spacing between the layers occupied by the two types of PAEs is indicated by the dashed line. (b) Top-down view of a few units of the two PAE layers shown in (a), which shows the anisotropic in-plane strain each layer is experiencing.

5.6.13 Yield of Crystals Epitaxially Grown in the [111] Orientation

When a_p is close to a_i (as indicated by the white squares in Figure 5.23), the yield for epitaxially grown crystals in the [111] orientation is only about 40%, much lower than the other two orientations. For smaller a_p, crystals seem to grow along the [001] orientation but with three major in-plane orientations. The reason is explained in Figure 5.24.

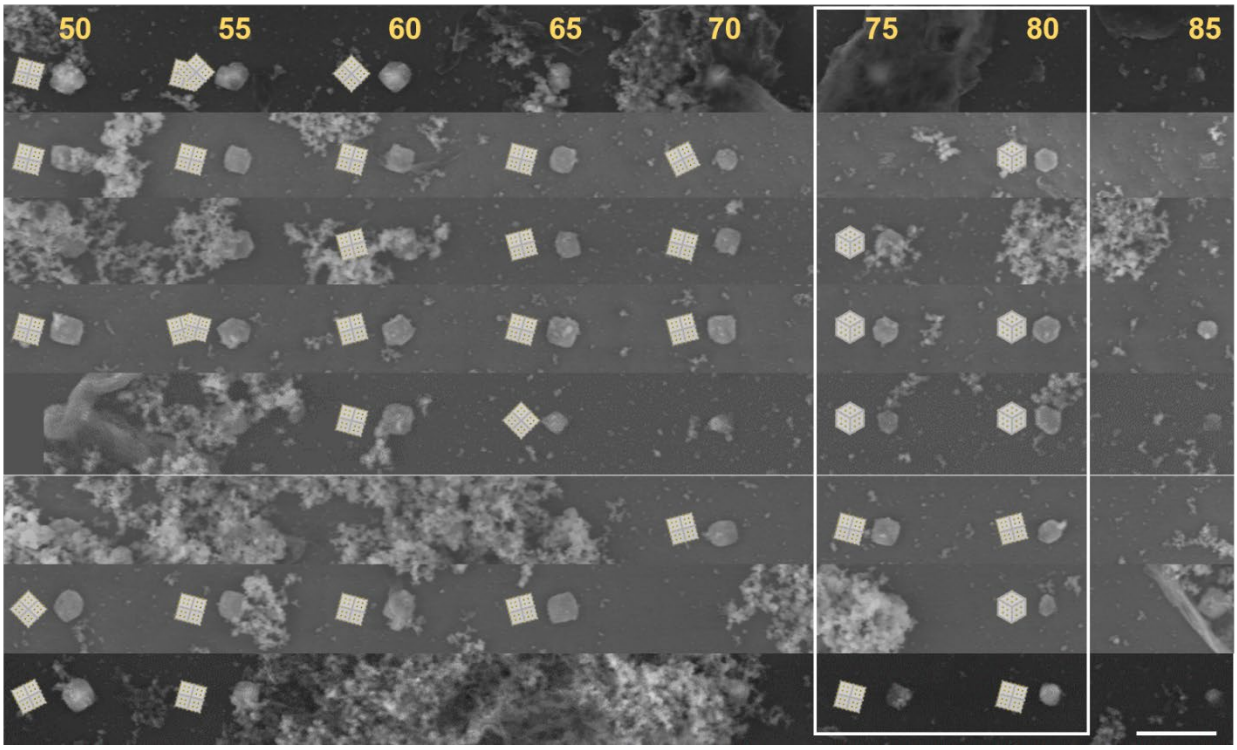

Figure 5.23. SEM images of crystals assembled on (111) pattern with a_p ranging from 50 - 85 nm. The white square highlights patterns with a_p close to a_i. Scale bar is 5 μm.

5.6.14 Analysis of Crystals Assembled on (111) Pattern with Small a_p

Fig. 5.24a shows a schematic of a unit cell along the (111) orientation with no strain. The NP A in the middle is bound to eight neighboring NP Bs (i.e. the coordination number is eight). In contrast, at small a_p (55 nm in Fig. 5.24b), the spacing between different NP layers increases in order to maintain the 68 nm interparticle spacing. As a result, two of the eight NP Bs become too

far to bind to the NP A in the middle (Fig. 5.24b), effectively reducing the coordination number from eight to six and consequently decreasing the hybridization between complementary DNA. Therefore, the deposition geometry of the first layer of NPs on (111) patterns with 50 – 70 nm a_p follows a strained (001) symmetry, as shown in Fig. 5.24c. The white empty circles indicate the theoretical geometry if there is negligible strain and the first layer of NPs follows the (111) geometry of the pattern (green circles). But since the a_p is much smaller, the first layer of NPs (orange spheres) instead follow a strained (001) pattern with three identical in-plane orientations due to the symmetry of the pattern.

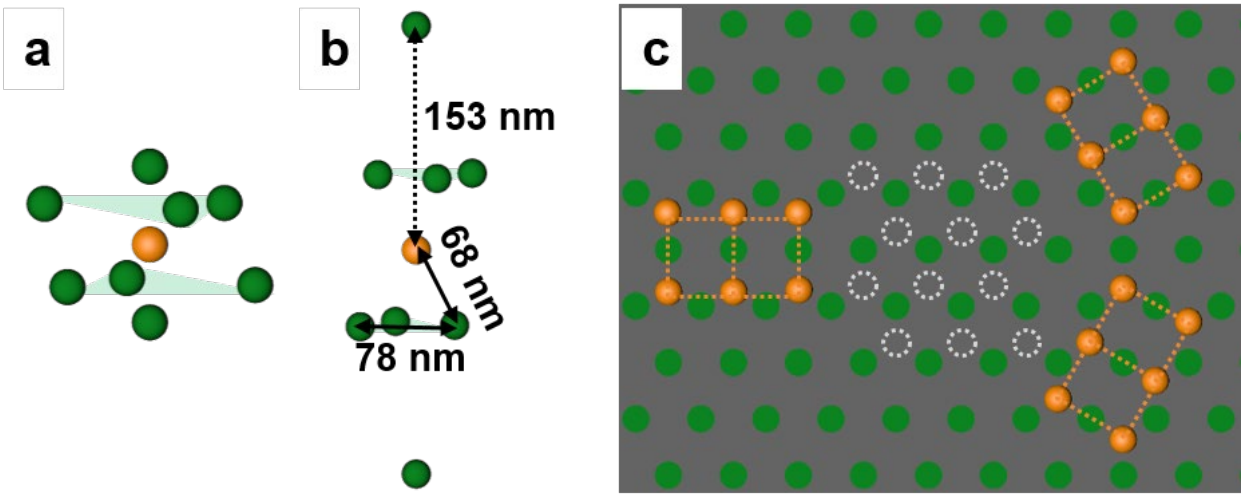

Figure 5.24 Schematics of (a) A unit cell with no strain along the (111) orientation; (b) the geometry of NPs with small a_p and (c) the resulting deposition geometries of the first layer of NPs on (111) patterns. The white empty circles indicate the theoretical geometry defined by the pattern (green circles), and the orange spheres show the actual deposition geometry of the first layer of NPs, which follows a strained (001) pattern with three identical in-plane orientations due to the symmetry of the pattern.

5.6.15 Additional Structural Analysis with More FIB-Sectioned Samples

Figure 5.25-30 show some additional FIB-cut examples grown along the [001] orientation with different lattice constants, and Figure 5.31 - 5.32 are examples of crystals grown on (110) and (111) planes but along the [001] orientation because of the small a_p.

Specifically, Figure 5.25 - 5.26 have (001) pattern with 55 nm a_p and 0-degree rotation. The cross sections between the two samples share great resemblance, which is also similar to Figure 5.2b. These samples are essentially equivalent in terms of orientation and cutting direction, and their cross sections are all (110) lattice planes.

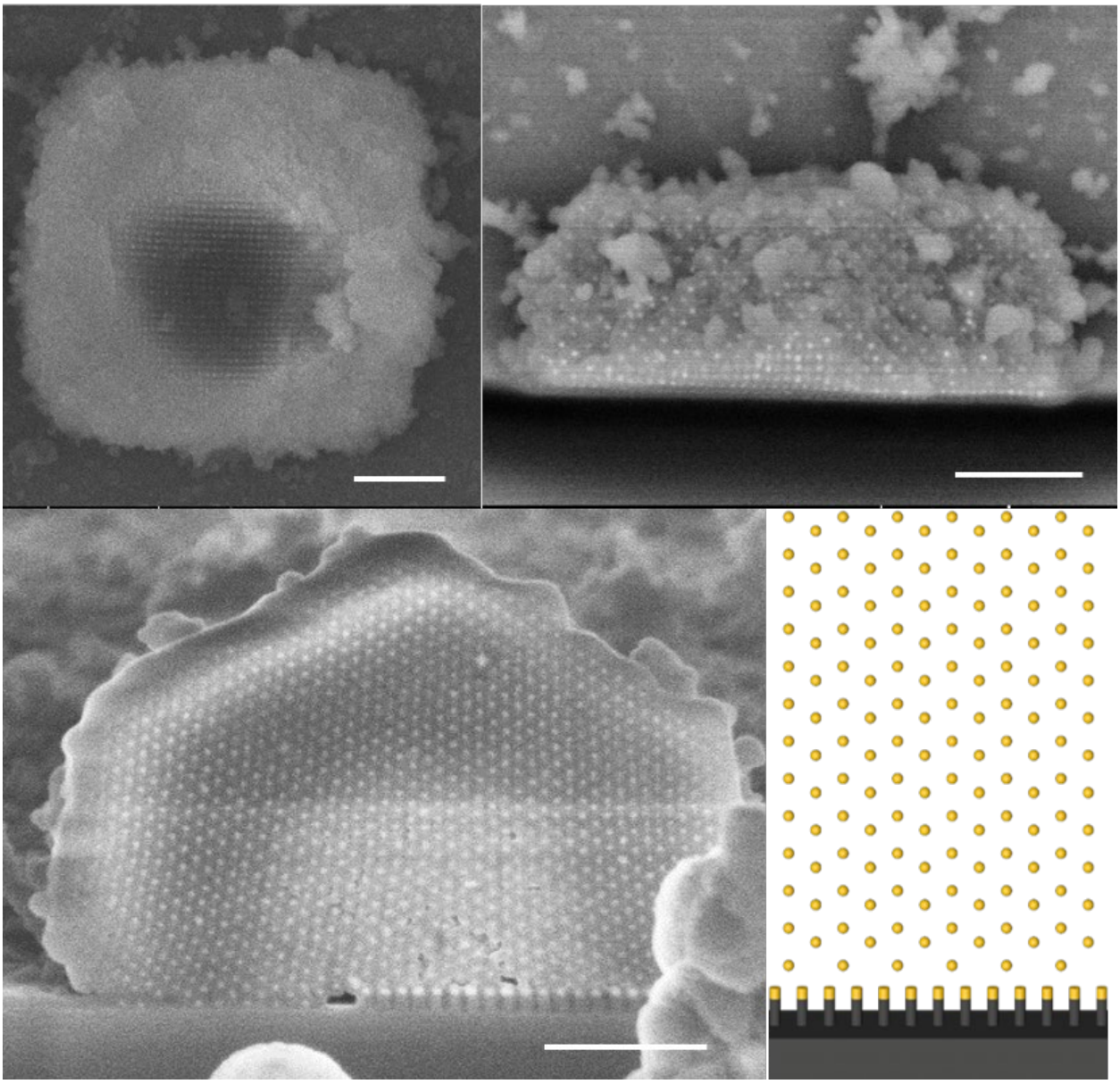

Figure 5.25. Top-down SEM images of crystals before (top left) and after (top right) FIB milling. The crystals are tilted around 75 degrees from the top-down view in order to observe the sectioned surface (bottom left) and a corresponding drawing of the top layer of nanoparticles (bottom right) is shown for comparison. The (001) pattern lattice constant and rotation are 55 nm and 0 degrees. Scale bars are 500 nm.

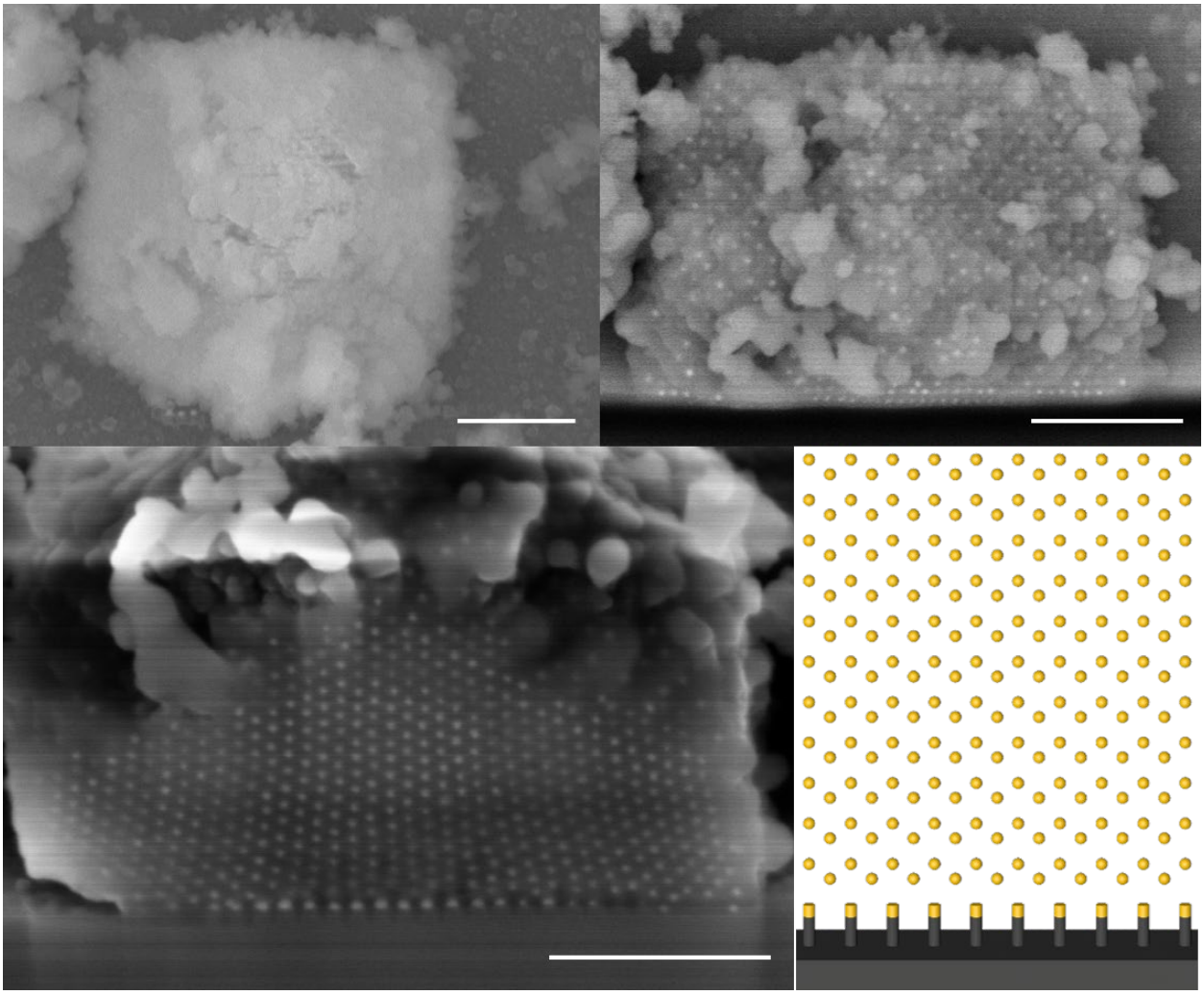

Figure 5.26. Another example of the (001) pattern with 55 nm lattice constant and 0-degree rotation. Top-down SEM images of crystals before (top left) and after (top right) FIB milling. The crystals are tilted around 75 degrees from the top-down view in order to observe the sectioned surface (bottom left) and a corresponding drawing of the top layer of nanoparticles (bottom right) is shown for comparison. Scale bars are 500 nm.

Figure 5.27 has (001) pattern with 50 nm a_p and 45-degree rotation, while the crystal is cut in the 0-degree direction. In other words, the cutting is along the (110) plane of the pattern but reveals the (100) plane of the assembled crystal due to strain-induced rotation with respect to the orientation defined by the pattern. Similar to the sample in Figure 5.3c, the cross-sectional image reveals the top two PAE layers, as can be seen in the contrast difference between the two PAE layers. Different from Figure 5.3c, however, there are posts at both layers, so we could also see two layers of the posts.

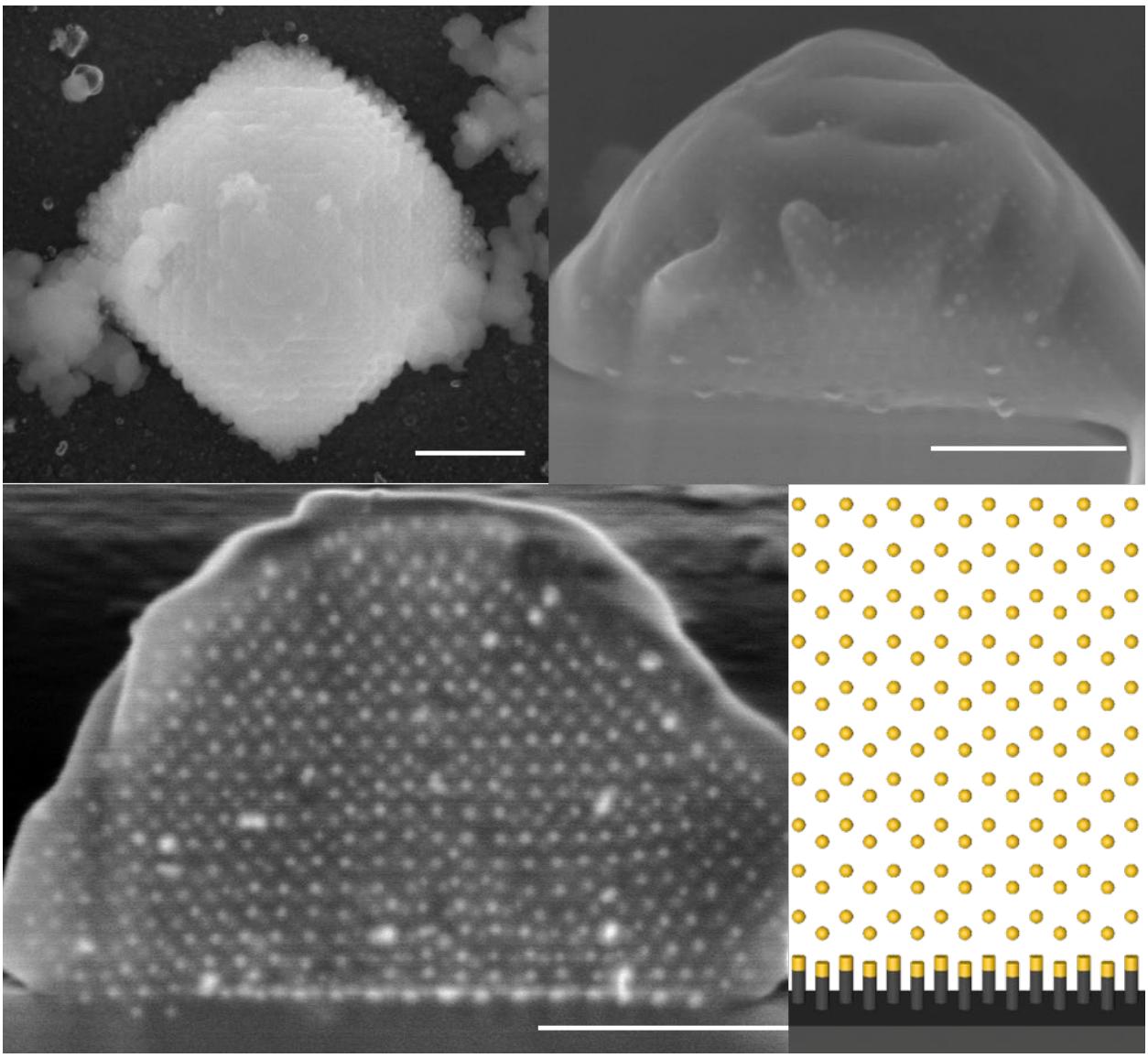

Figure 5.27. Top-down SEM images of crystals before (top left) and after (top right) FIB milling. The crystals are tilted around 75 degrees from the top-down view in order to observe the sectioned surface (bottom left) and a corresponding drawing of the top two layers of posts and nanoparticles (bottom right) is shown for comparison. The (001) pattern lattice constant and rotation are 50 nm and 45 degrees, while the crystal is cut in the 0 degrees, revealing the (100) rather than (110) plane of the crystal. Scale bars are 500 nm.

When there is little lattice mismatch, nanoparticles assemble along the same orientation dictated by the substrate. Figure 5.28 shows another example of (001) pattern with 70 nm a_p and 45-degree rotation, and the crystal is cut in 45-degree (along the (100) plane defined by the

pattern), similar to the one shown in Figure 5.3c. The two cross-sectional nanoparticle arrangements follow the same pattern too, as expected. Figure 5.28 has (001) pattern with lattice constant of 70 nm and 0-degree rotation. The crystal is cut in 0-degree direction, exposing a (100) cross section. Rarely (less than 1% of samples), the crystal assumes an abnormal shape (top left, Figure 5.29). The cross-sectional image shows there are actually two crystals connected by DNA binding. The irregular shape at the lower right is another crystal that likely first grew in solution and attached onto the epitaxially grown crystal at later stage during the growth process. The attachment is non-epitaxial, resulting in lots of defects at the interface.

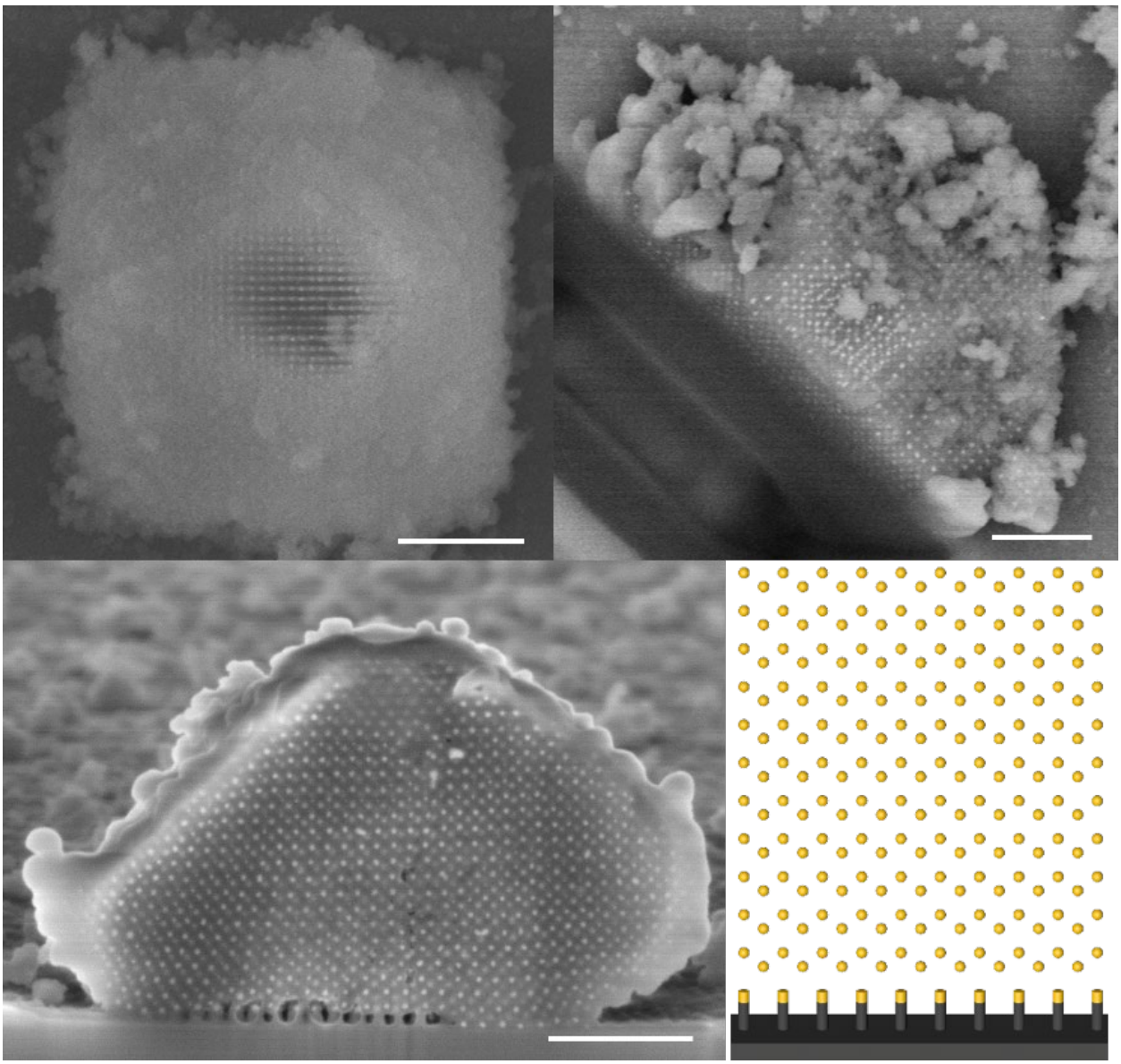

Figure 5.28. Top-down SEM images of crystals before (top left) and after (top right) FIB milling. The crystals are tilted around 75 degrees from the top-down view in order to observe the sectioned surface (bottom left) and a corresponding drawing of the top layer of nanoparticles (bottom right) is shown for comparison. The (001) pattern a_p and rotation are 70 nm and 45 degrees. Scale bars are 500 nm.

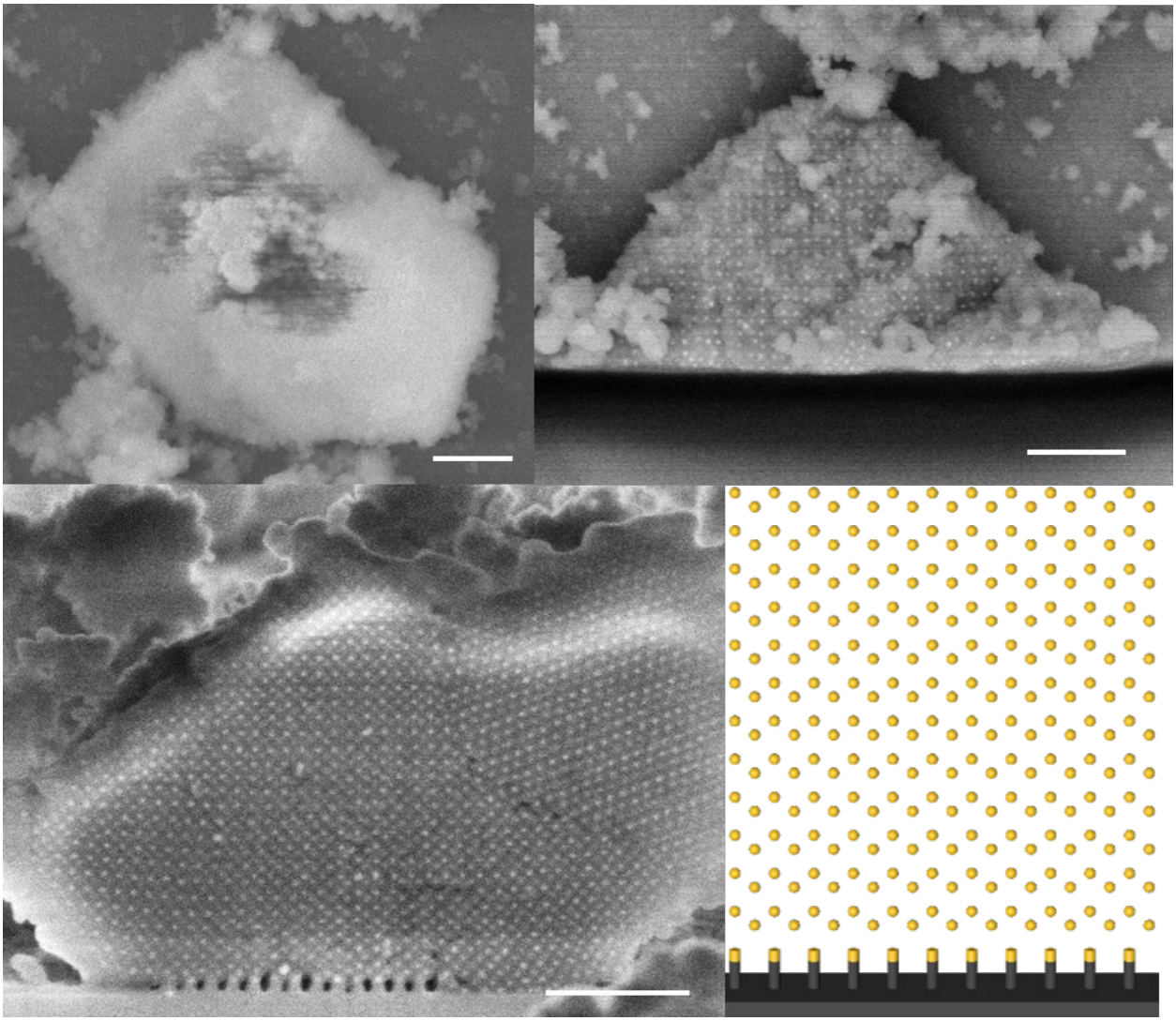

Figure 5.29. Top-down SEM images of crystals before (top left) and after (top right) FIB milling. The crystals are tilted around 75 degrees from the top-down view in order to observe the sectioned surface (bottom left) and a corresponding drawing of the top layer of nanoparticles (bottom right) is shown for comparison. The (001) pattern lattice constant and rotation are 70 nm and 0 degrees. Scale bars are 500 nm.

In Figure 5.30, the (001) pattern has 70 nm a_p and 45-degree rotation, while the crystal cuts in the 0-degree direction, revealing the (110) lattice plane. Note that the cross-sectional SEM images are taken at an angle of 45 degrees from the top-down view. In this example, there is also another crystal attached to the epitaxially grown crystal. Both of the epitaxially-grown and the attached crystals have a more complete shape, since all surfaces are terminated in the (110) lattice plane. As a result, the attachment between the two crystals is epitaxial, and we observe no defects at the attachment interface. The attachment likely happened when the epitaxial growth had finished.

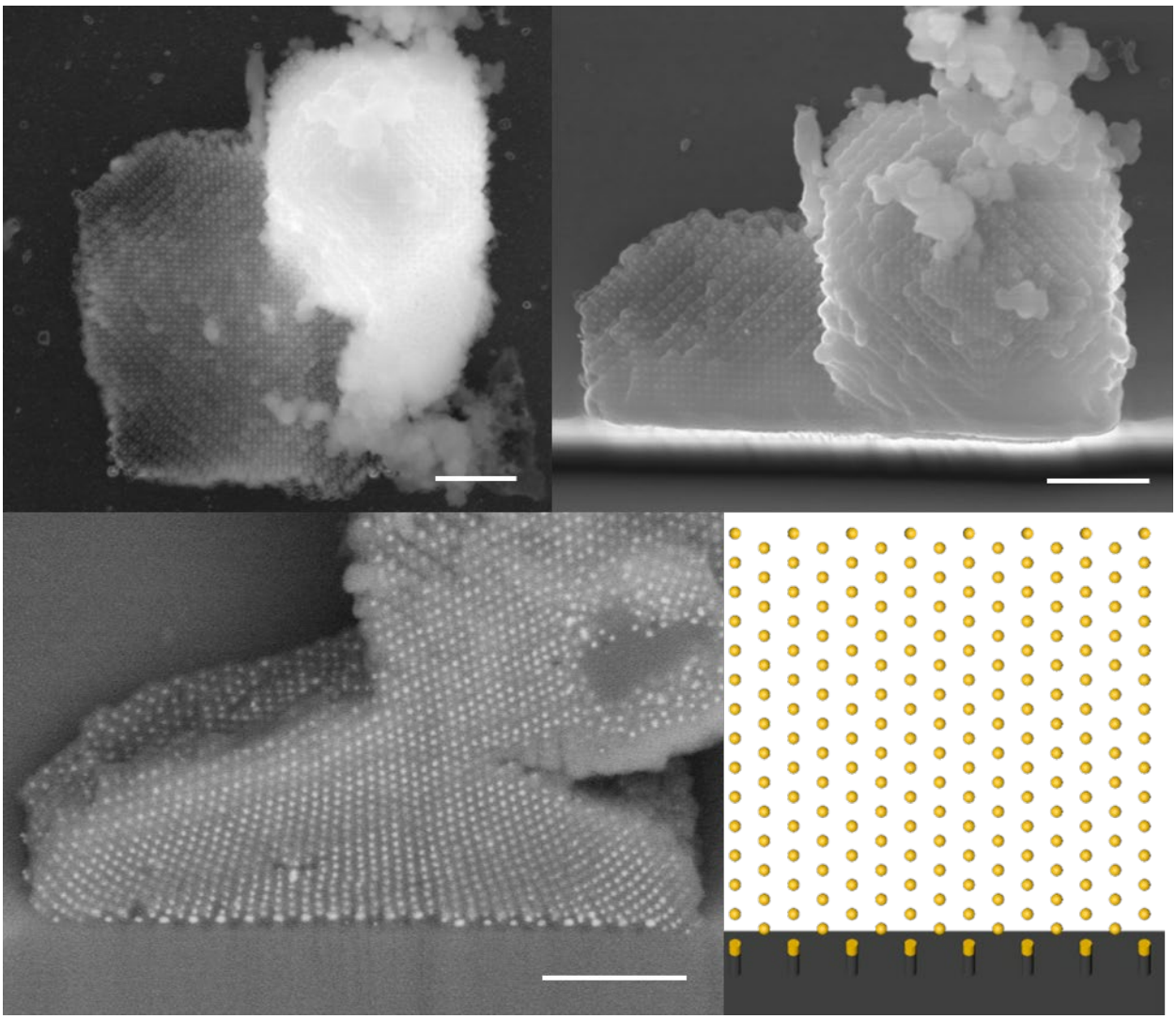

Figure 5.30. Top-down SEM images of crystals before (top left) and after (top right) FIB milling. The crystals are tilted around 45 degrees from the top-down view in order to observe the sectioned surface (bottom left) and a corresponding drawing of the top layer of nanoparticles (bottom right) is shown for comparison. The (001) pattern lattice constant and rotation are 70 nm and 45 degrees. Scale bars are 500 nm.

Figure 5.31 - 5.32 show examples of crystals grown along [001] orientation on (110) and (111) plane with small a_p, respectively. Note that the cross-sectional SEM images are taken at an angle of 38 degrees from the top-down view. Since both planes exposed by the FIB-sectioning are the (001) plane and they are imaged at the same angle, they look identical.

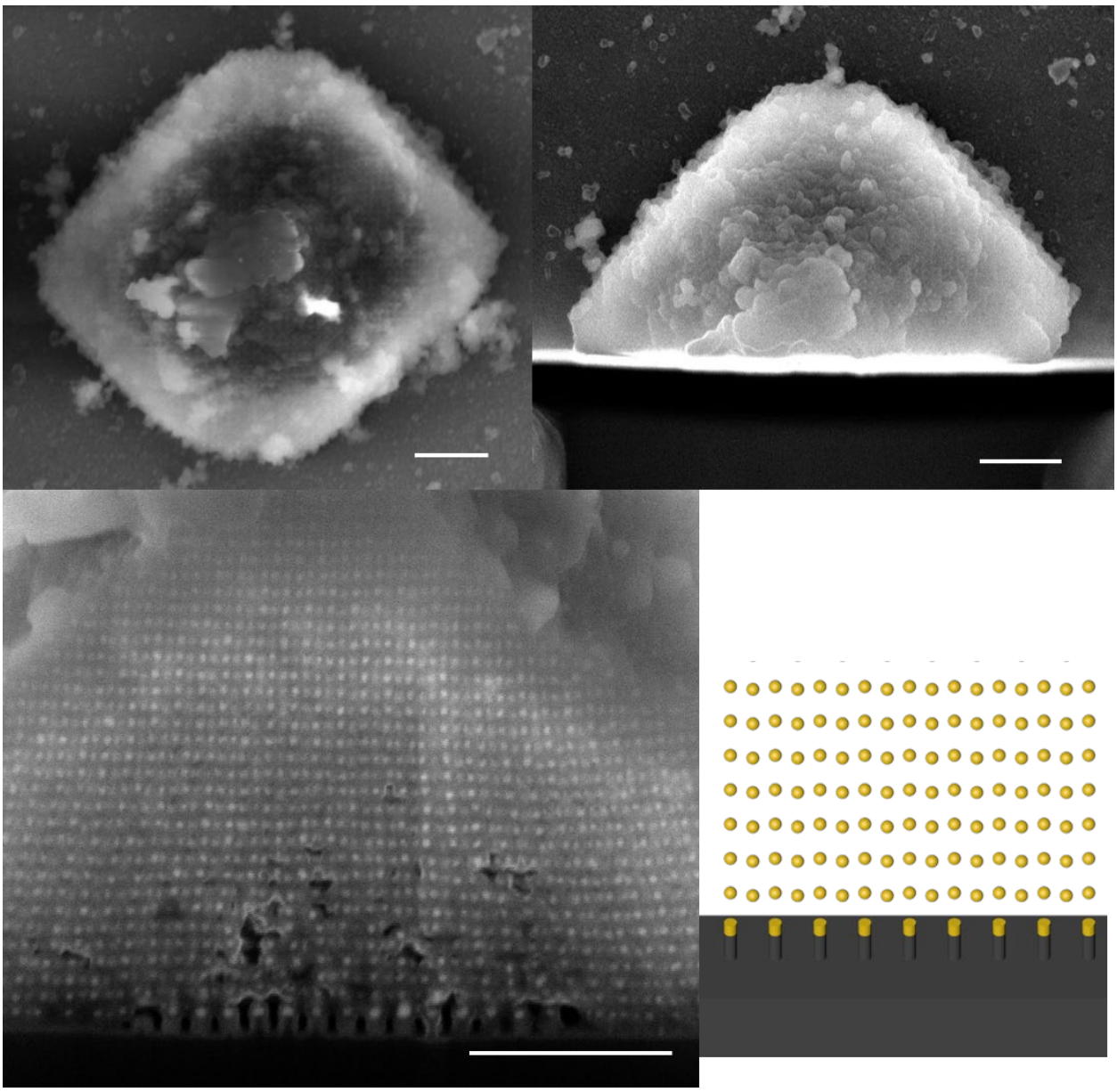

Figure 5.31. Top-down SEM images of crystals before (top left) and after (top right) FIB milling. The crystals are tilted around 38 degrees in order to observe the sectioned surface (bottom left) and a corresponding drawing of the top layer of nanoparticles (bottom right) is shown for comparison. The (110) pattern lattice constant is 60 nm. Scale bars are 500 nm.

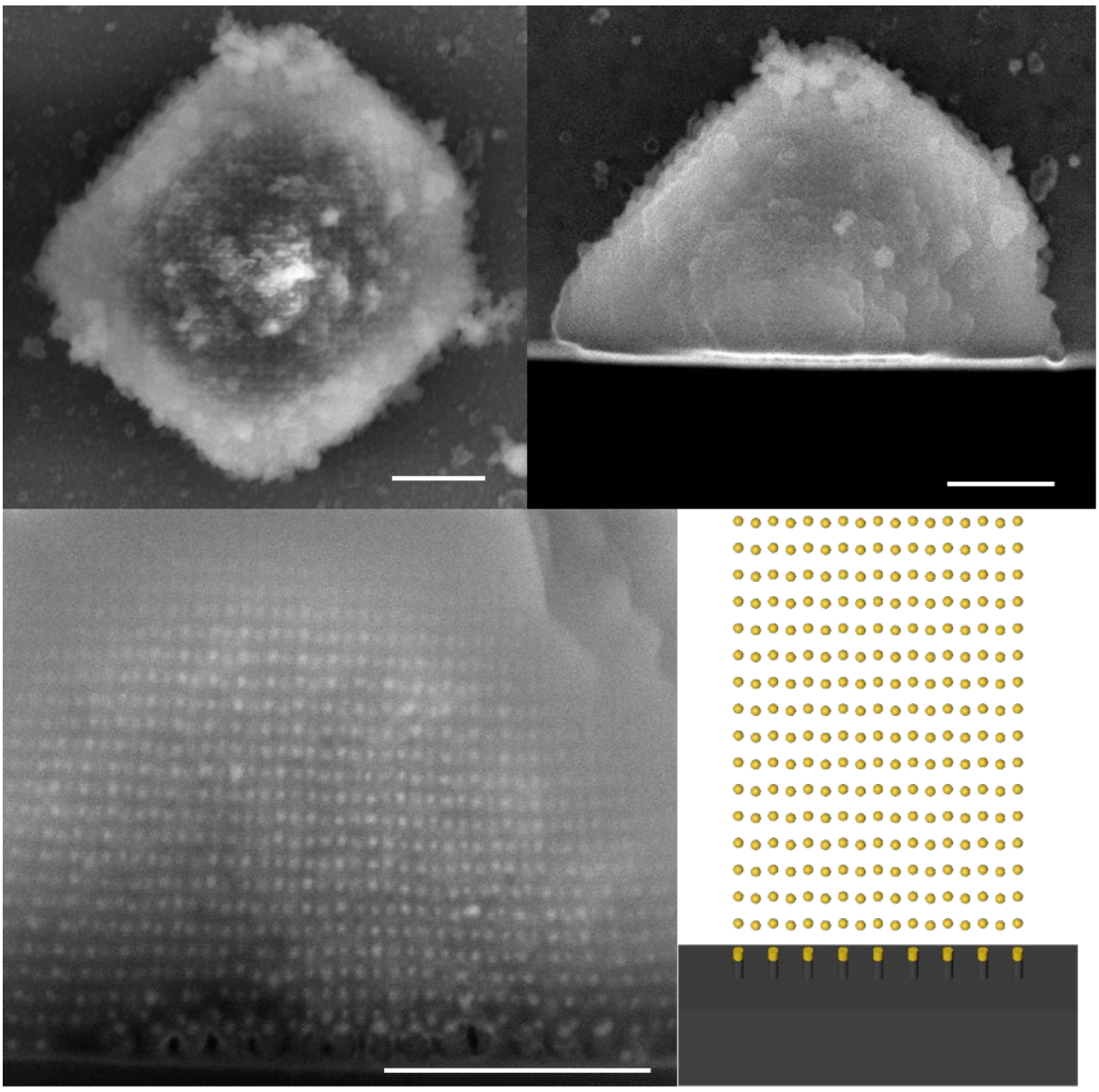

Figure 5.32. Top-down SEM images of crystals before (top left) and after (top right) FIB milling. The crystals are tilted around 38 degrees in order to observe the sectioned surface (bottom left) and a corresponding drawing of the top layer of nanoparticles (bottom right) is shown for comparison. The (111) pattern lattice constant is 50 nm. Scale bars are 500 nm.

5.6.16 Crystals Composed of 20 nm Nanoparticles

While the majority of the analysis we have done is performed on 30 nm nanoparticle crystals, 20 nm nanoparticle crystals can be readily assembled with the same procedure. The only difference is the substrate design, where the size and lattice constants of Au posts should be optimized for the 20 nm system. Figure 5.33a shows the SAXS spectrum of crystals composed of 20 nm NPs and DNA linker n = 2 before silica embedding, and SEM image of these crystals after silica embedding is shown in Figure 5.33b. The intrinsic lattice constant of crystals before silica embedding as calculated from SAXS data is ~ 65.3 nm.

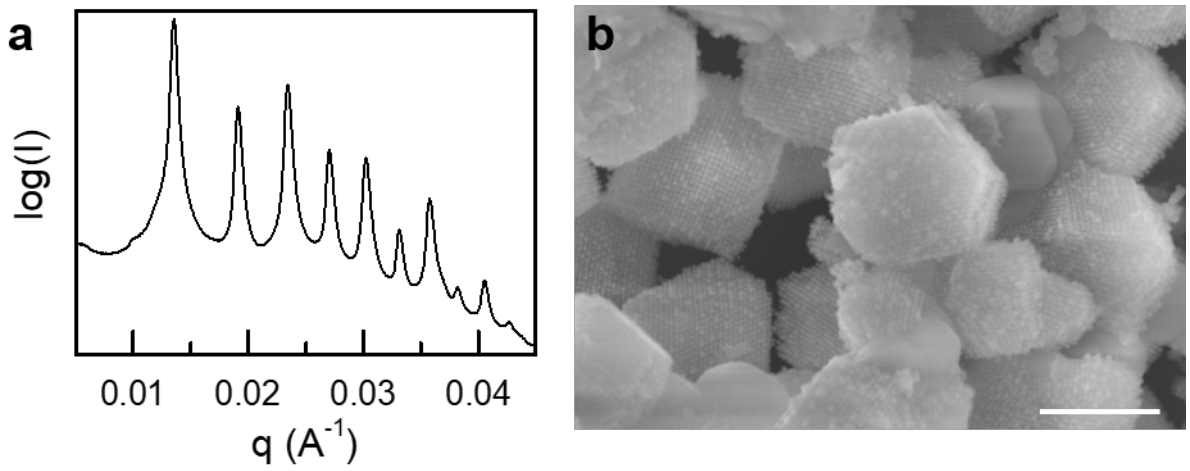

Figure 5.33. SAXS spectrum (a) and SEM images (b) of 20 nm crystals assembled with DNA linker n=2. The SAXS is taken with crystals before silica embedding. The scale bar is 1 μm.

Similar to the 30 nm PAE system, a micron-sized strip of Au is made and processed together with the seed patterns. Figure 5.34 shows a typical example of the 20 nm crystals grown on Au strip (n=2 linker). The 20 nm system also shows similar layer-by-layer (Figure 5.34a), layer-by-layer followed by 3D island growth (Figure 5.34b-d) and island growth (Figure 5.34e-f), similar to the 30 nm system shown in Figure 5.8. However, on average, the 20 nm system shows a higher

PAE coverage on the Au strip and grows into more complete crystals than the 30 nm system. Thus, we suspect the PAE size might also play a role in assembly process on unpatterned Au.

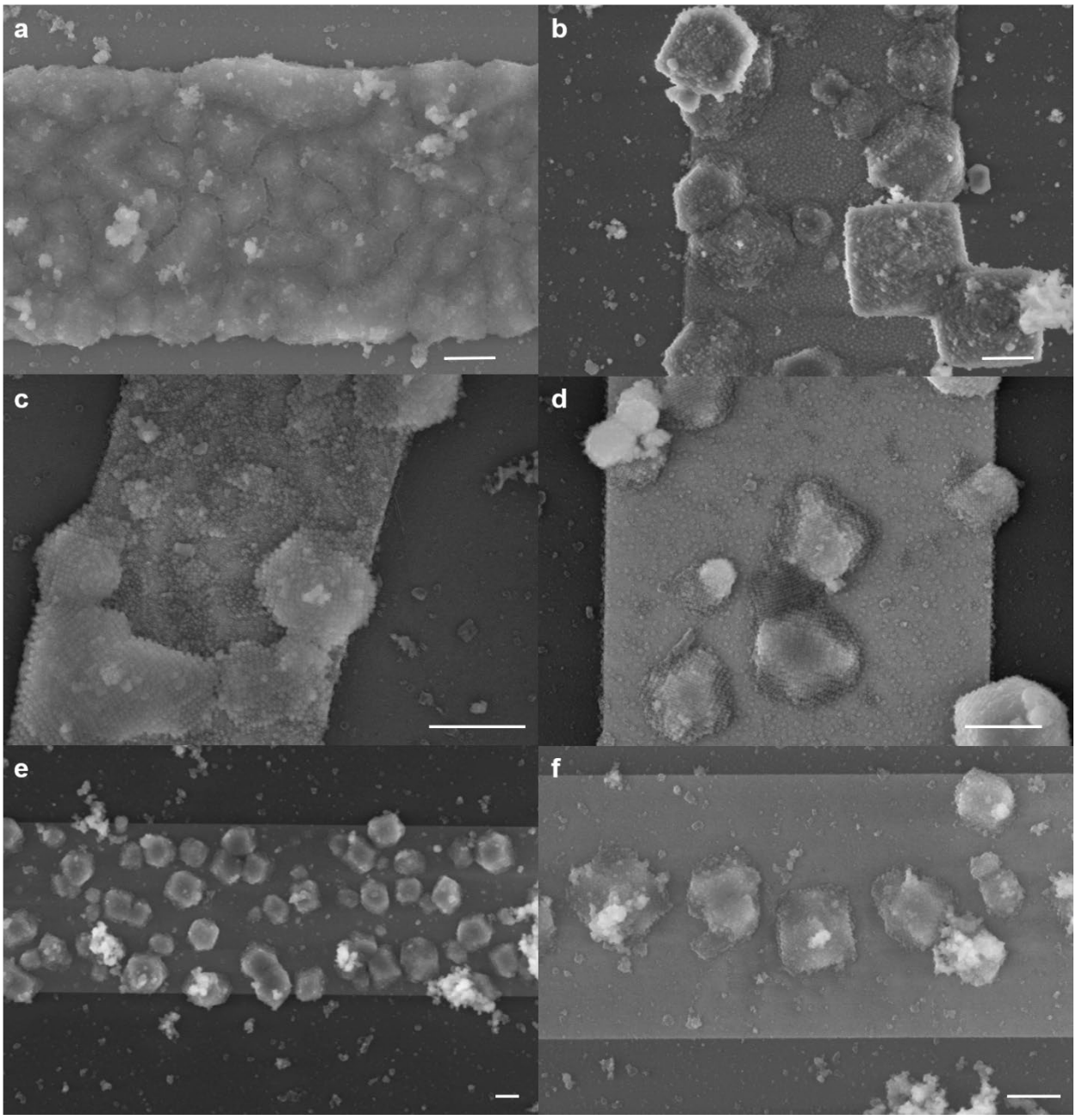

Figure 5.34. SEM images of 20 nm NP crystals grown on a large strip. Depending on the assembly condition, different types of growth processes are observed. In all cases, there is little control on the crystal orientation and exact growth location. DNA linker n=2 is used. Scale bar is 1 μm.

Based on the above information, substrates with post diameter close to 20 nm and a_p close to 65 nm are made. As shown in Figure 5.34, epitaxial assembly of 20 nm NP crystals is achieved in all three orientations that we discussed in the bcc system, namely [001], [110] and [111].

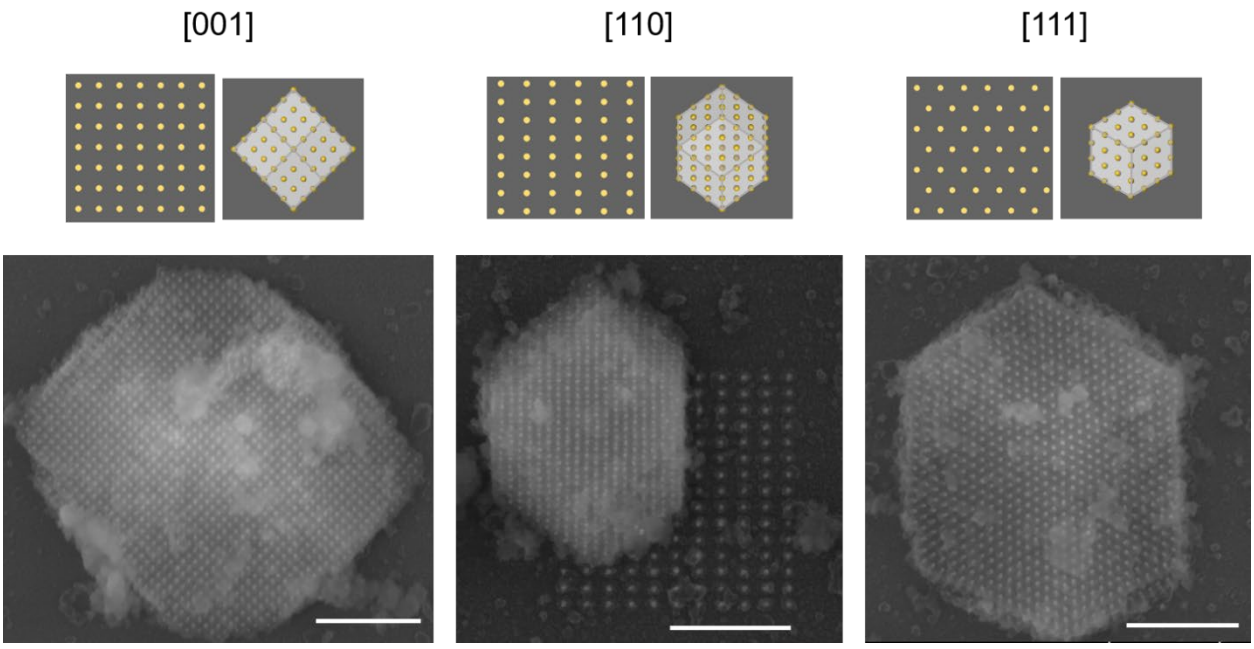

Figure 5.35. Schematic drawing (top) and SEM images (bottom) of 20 nm crystals assembled with DNA linker n=2 on substrate. The three orientations of bcc system, i.e. [001], [110] and [111] are shown on the left, middle and right, respectively. Scale bars are 500 nm.

Moreover, we see that the same level of orientation control, where we can rotate the epitaxially grown crystals by rotating the pattern, is also demonstrated in the 20 nm crystal system. In Figure 5.36, both rows of patterns have (001) lattice symmetry but the top row is rotated 45 degrees compared to the bottom row. Consequently, we expect a corresponding 45-degree rotation of the epitaxially assembled crystal, which is indeed the case as is shown in the SEM images. Again, we see that the shape of the crystals does not follow the overall shape of the pattern.

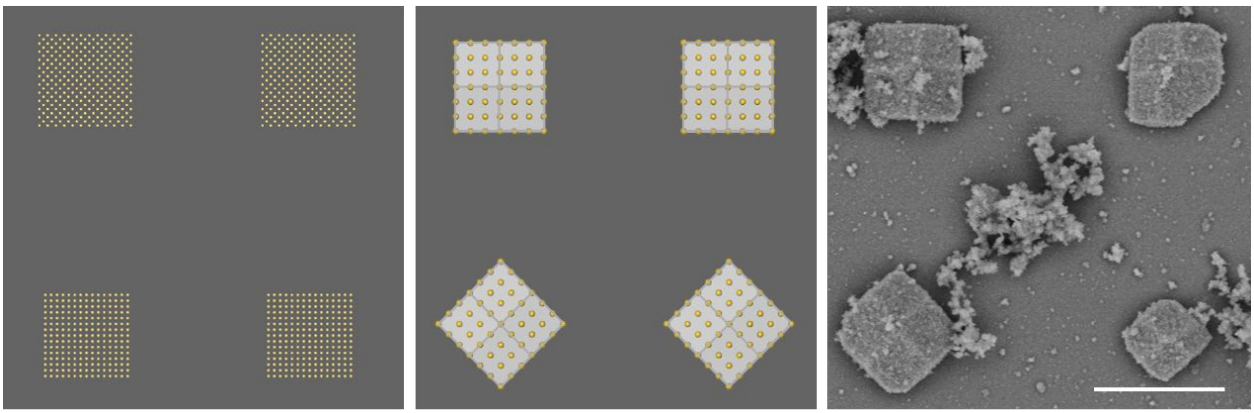

Figure 5.36. Schematic drawing of the substrate pattern (left) and the expected epitaxially grown crystals (middle). Both rows have the same (001) symmetry and lattice constants, but are rotated 45 degrees in plane with respect to each other, thus we expect the same crystal orientation but with 45-degree rotation from the top to the bottom row. SEM image (right) of 20 nm crystals assembled with DNA linker n=2 on substrate (a_p = 60 nm) confirms that it is indeed the case.

CHAPTER SIX

Conclusion and Outlook

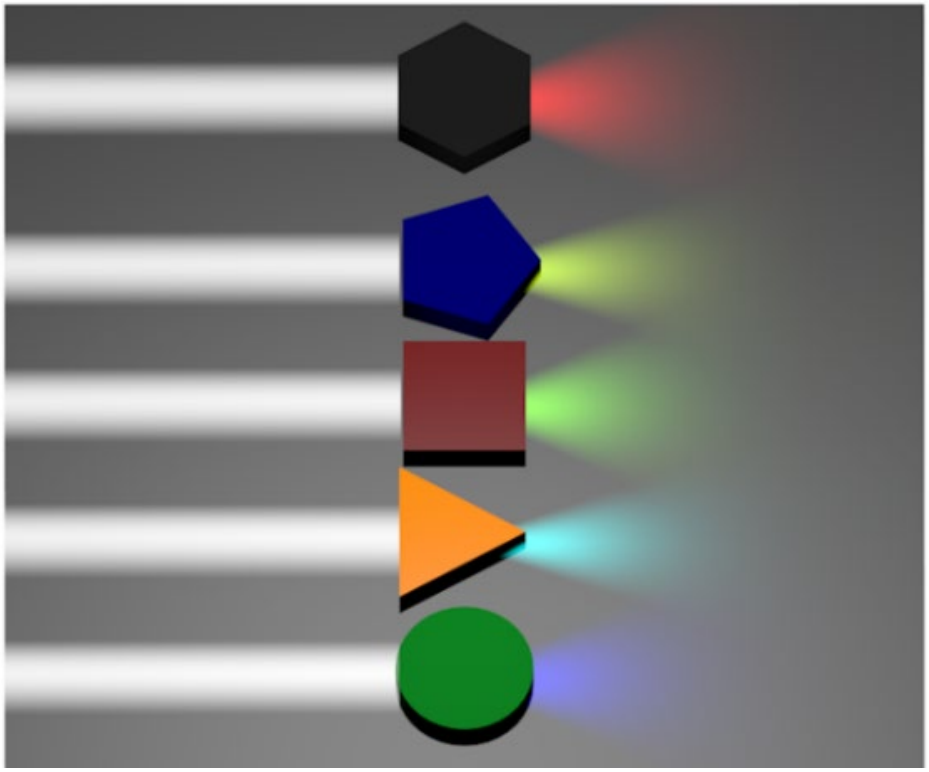

Note: Portions of the material in this chapter is published in the following articles:

1. Directional emission from dye-functionalized plasmonic DNA superlattice microcavities, *Proceedings of the National Academy Sciences USA* **2017**, *114 (3)*, 457-461
2. Clathrate Colloidal Crystals, *Science* **2017**, *355 (6328)*, 931-935

These work were done in collaboration with Dr. Haixin Lin, Dr. Daniel J. Park, Dr. Jessie Ku, Dr. Clotilde M. Lethiec, Dr. Nathaniel P. Stern, Dr. George C. Schatz, Sangmin Lee, Dr. Matthew Spellings, Dr. Michael Engel, and Dr. Sharon C. Glotzer, Wenjie Zhou, Yuanwei Li, Yueh-te chu, Dr. Shunzhi Wang

The work presented in previous chapters, together with those done by other researchers in the field, have shown the unique advantages of utilizing DNA-programmable assembly as a versatile tool in construction optical metamaterials and devices by virtue of its precise structural control down to sub-nanometer length scale and the wide range of nanoparticle building blocks and lattice parameters accessible. Based on these advantages, a plethora of opportunities emerges, and four will be discussed in the follow sections. Specifically, crystals with low structural symmetry and composed of anisotropic nanoparticles might exhibit more exotic optical behavior. Additionally, the majority of this work uses gold nanoparticles as building blocks, due to their strong interaction with light and the resulting localized surface plasmon resonance. However, the potential of DNA-programmable assembly to incorporate a wide variety of nanoparticle core materials can be utilized to provide additional functionality. Moreover, with the newly developed template-guided assembly techniques, a larger library of crystals with tailored orientation and shapes can be assembled on substrate. Combining with a simulation-driven approach, one can envision the fabrication of more complex optical constructs and even integrated devices. Last but not least, one can take the idea of material design further by adopting a machine learning (ML) driven approach to identify optically interesting structures and make them with DNA-mediated assembly.

6.1 Exotic Behavior in Anisotropic Nanoparticle Crystals with Low Structural Symmetries

The lattice structures of crystals studied in this thesis have been *bcc* and *sc*, which fall into the high symmetry category. However, lower-symmetry lattices can be assembled, especially through the use of anisotropic nanoparticles. These crystals can have unique optical properties.

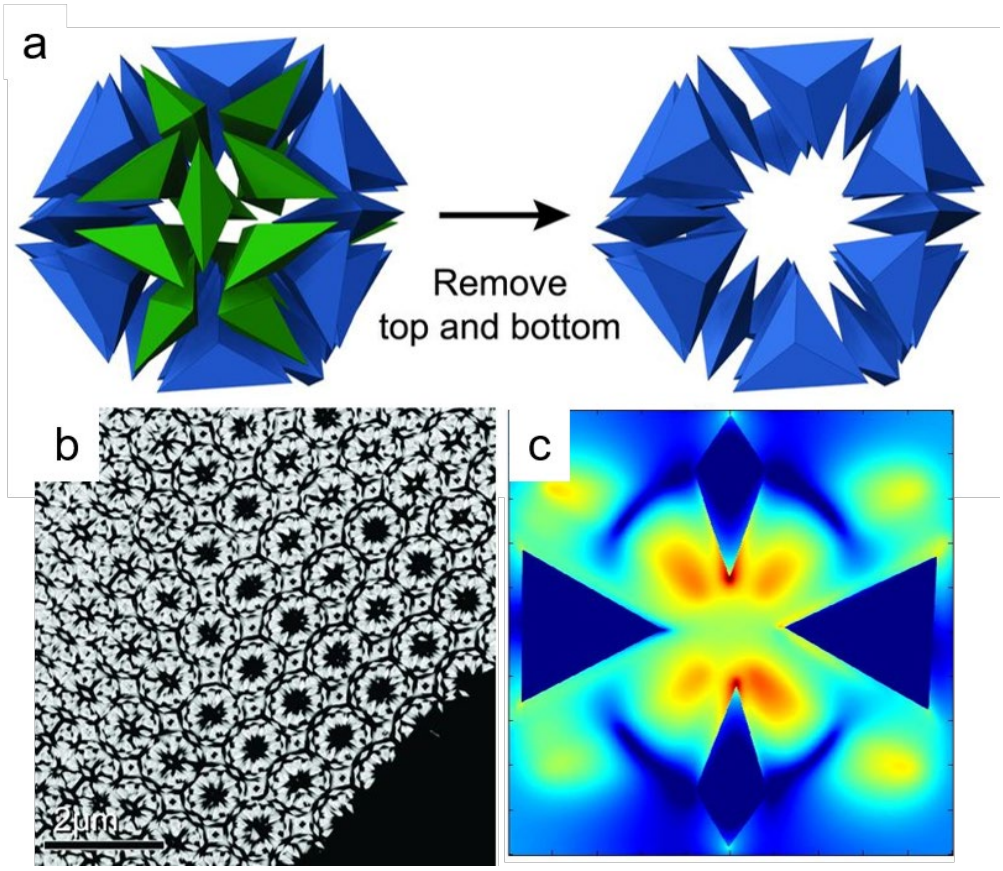

Figure 6.1. Clathrates formed through DNA-assembled triangular bipyramids. (a) Schematic drawing of one typical cage of clathrate structure. (b) TEM image of sectioned clathrates. (c) FDTD simulation of the field distribution of one cross-sectional plane of the cage. Image adapted from ref 127.

For example, triangular bipyramidal NPs can assemble into clathrates, which are structures consisting of polyhedral cages with pores (Figure 6.1).[127] These cages can orient the NPs in such a way that a number of nanoparticle tips are close to one another, which could lead to strong plasmonic coupling and huge field enhancement. Such concentrated optical field could be crucial for a wide variety of applications such as catalyzing host-guest chemistry. Challenges remain, however, that the DNA design used in previous work is too long and the nanoparticles are too far apart to allow strong coupling between neighboring nanoparticles, therefore falling short on

generating extreme field enhancement (Figure 6.1c). Future work could consider using shorter DNA in order to reduce the NP separation.

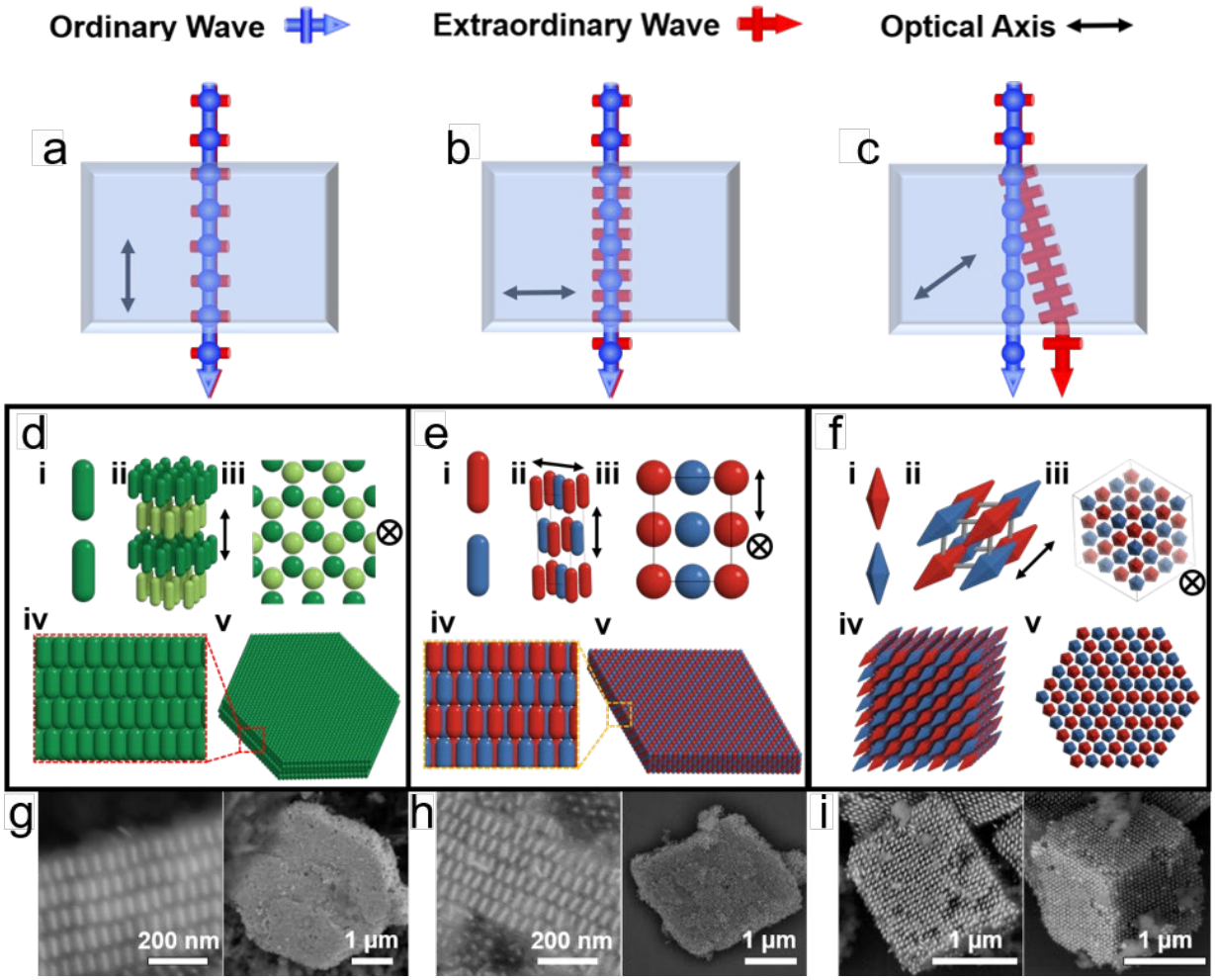

Figure 6.2. Exotic optical behavior in low-symmetry crystals. (a-c) Drawings showing the polarization dependent properties depending on the relative direction between wave propagation and crystal optical axis. (d-i) Crystals made of anisotropic (rod or pentabipyramid) NPs that have optical axes corresponding to the ones above. Image adapted from ref 128.

Additionally, polarization-dependent properties such as birefringence and dichroism can occur in low-symmetry crystals composed of anisotropic NPs.[128] Depending on the light propagation direction and the optical axis inside the crystal, polarization dependent modulation of

the amplitude, phase and direction of light an occur. DNA-programmable assembly allows rational synthesis of low-symmetry crystals with optical axis parallel, perpendicular and oblique to the incident light propagation direction (Figure 6.2). The crystals show birefringent and dichroic properties that have so far only been found in natural crystals like calcite. Additionally, the ability to precisely control and dynamically tune (i.e. stimuli-responsive crystals) the DNA-assembled crystals will bring about unique opportunities not accessible to natural birefringent crystals.[128]

6.2 Incorporation of Excitonic Elements

The main body of this thesis has been focused on using plasmonic NPs as building blocks and investigating the interplay between plasmonic and photonic properties. But the DNA-programmable assembly allows easy incorporation of excitonic components into the crystals.

For example, dye molecules can be inserted at various locations along the DNA strand (Figure 6.3a), allowing control over exciton-plasmon distance down to subnanometer length scale.[80] Thus, in a dye-functionalized *bcc* single crystalline RD crystal, a combination of plasmonic, photonic and excitonic modes exist, leading to complex optical behavior as the one shown in Figure 6.3b. The crystal shows a wavelength-dependent directional emission, where shorter wavelength close to the NP LSPR (~530 nm) is emitted from the top and the tips of the RD, while near IR waves (~700 nm) are emitted from all the RD periphery. Moreover, the unique ability to control surface-plasmon/exciton interactions within superlattice microcavities will catalyze studies involving strong coupling and nonlinear phenomena.

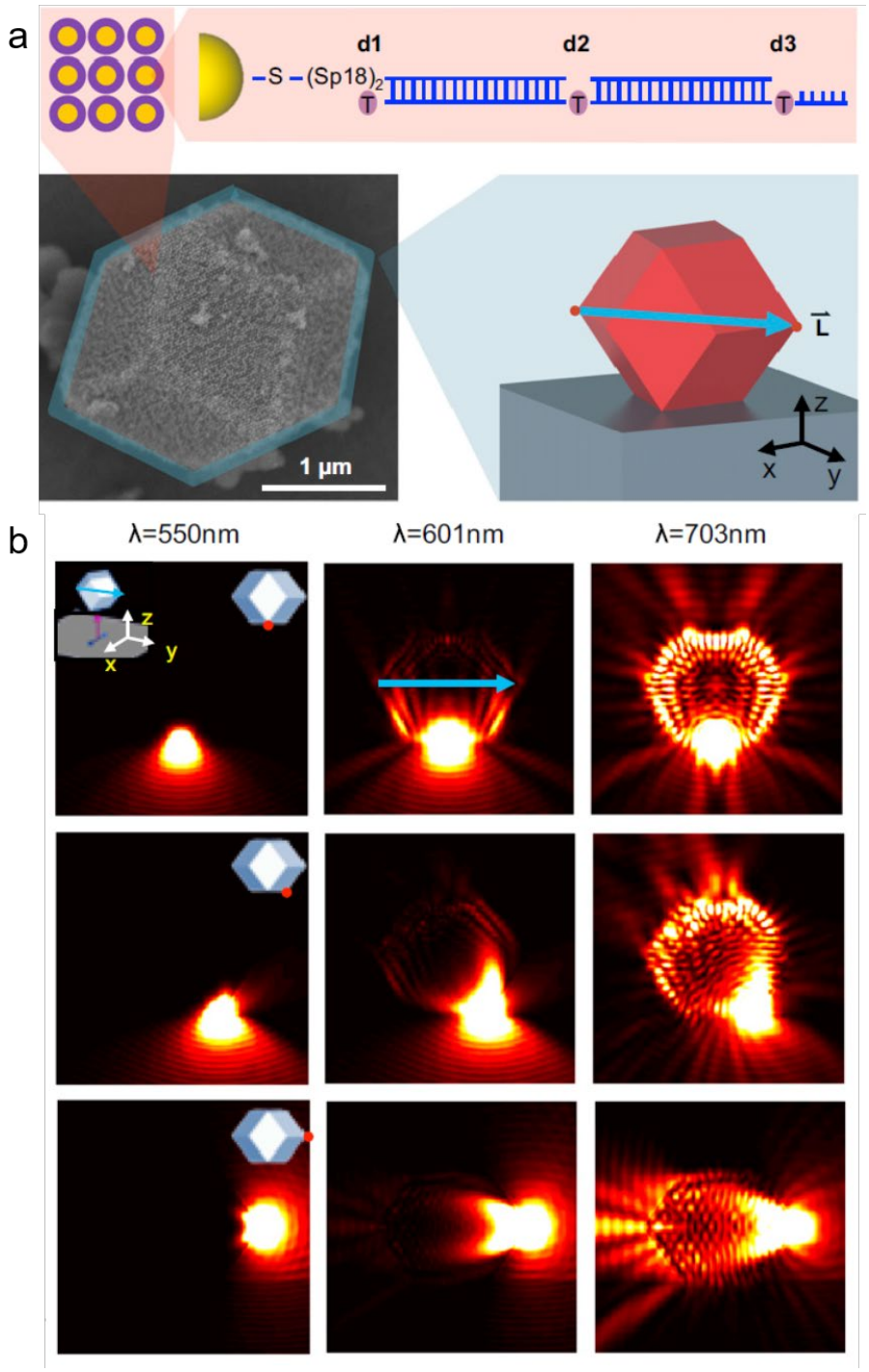

Figure 6.3. Dye molecules can be added into the crystal to enable study of the interactions between plasmonic, photonic, and excitonic components. (a) Schematic representation of the crystal design. Dye molecules can be added to various positions along the DNA strand as indicated by the d1, d2 and d3 points. (b) Optical simulation showing the emission of excitonic dipoles at different wavelengths. The figures are from ref 80.

Additionally, excitonic components can be included as NP core. Rare-earth upconversion nanoparticle (UCNP) cores can be assembled together with Au cores to enhance upconversion efficiency and allow systematic study of the enhancement mechanism. The interaction between Au NP and UCNP can be tuned by changing the Au NP size and DNA length (Figure 6.4a). TEM image of a *bcc* crystal composed of 23 nm β-$NaYF_4$:Yb/Er (20/2 mol%) UCNPs and 20 nm Au NPs is shown in Figure 6.4b. By prepareing a set of samples with different Au NP sizes and DNA lengths, we can systematically study the interaction between plasmonic NPs and UCNP. InFigure 6.4c, sample names are encoded as "NP diameter_DNA used". For example, "20_d0" means Au NP with 20 nm in diameter and DNA design d0, which is the shortest DNA in this system. Different sets of control samples can also be prepared. One direct example is to remove all the Au NPs in the superlattices while leaving UCNP intact. This can be achieved by using potassium cyanide (KCN) to etch away all the Au NPs inside a superlattice (Figure 6.4c, the samples with KCN in its name). By comparing the upconversion efficiencies of the same set of superlattice with and without Au NPs we can clearly see the manifestation of plasmonic enhancement.

Although preliminary data is promising, however, challenge remains. The superlattices were again assembled in solution, and there is little control over their size and shape, therefore limiting a direct comparison of the emission intensity and upconversion efficiency among different samples. This can be overcome by assembling the superlattices on substrate in a layer-by-layer manner, which would allow precise control of the density of Au NPs and UCNPs, enabling a quantitative investigation.

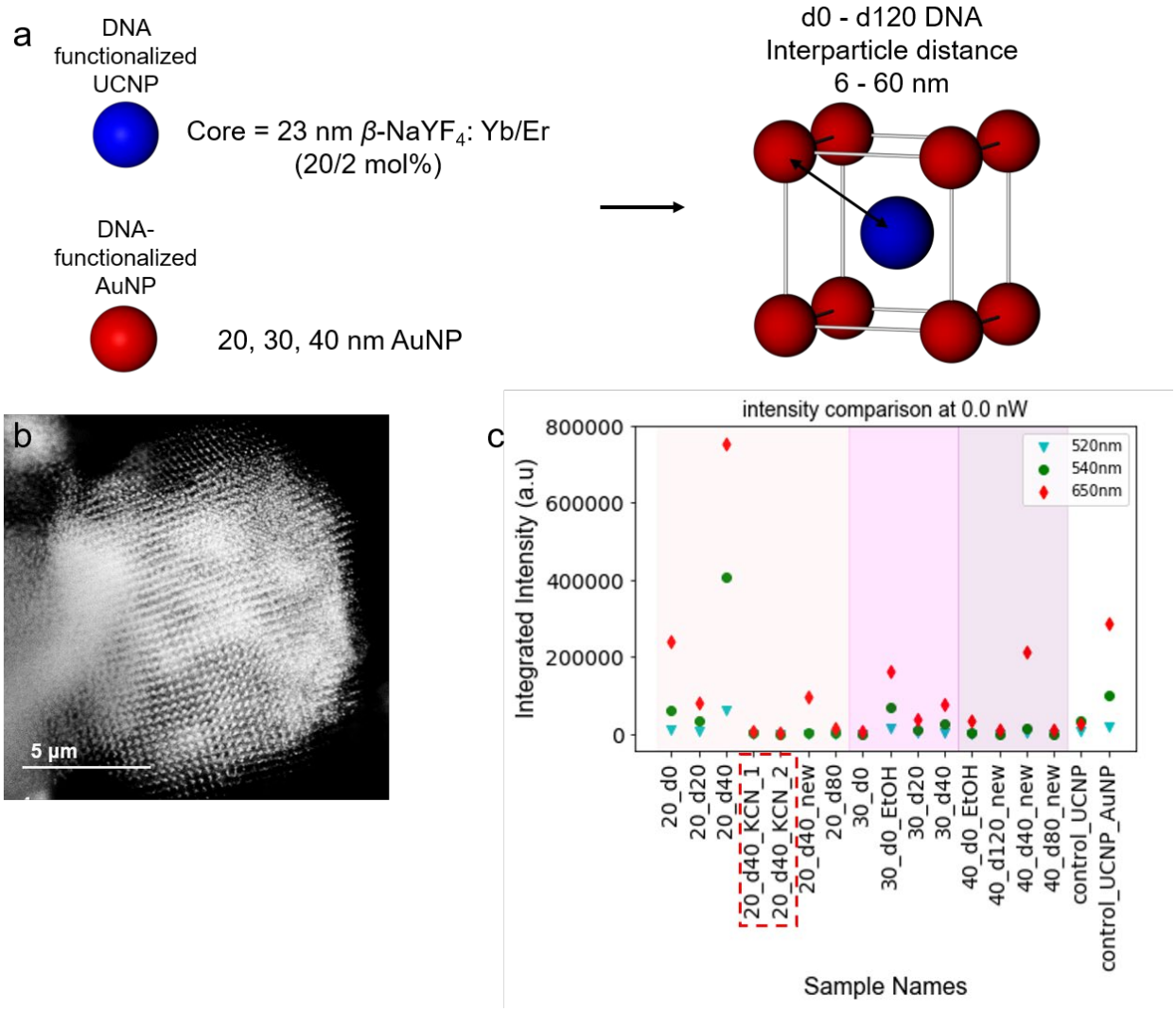

Figure 6.4. Superlattice composed of Au NPs and UCNPs allow systematic study of upconversion enhancement mechanism. (a) A set of *bcc* crystals can be prepared with UCNPs and Au NP. The UCNPs have fixed size, while the size of Au NPs and DNA length vary from sample to sample. (b) A TEM image of one sample. (c) Upconversion emission intensity at three wavelengths (shown in legend) of different samples.

6.3 Fabrication of Complex Optical Structures by Design

In Chapter 5, we only demonstrate epitaxy with *bcc* crystals, one can envision that the technique can be expanded to other crystalline systems. All the 500-plus DNA-assembled nanoparticle crystals that have been previously reported in the literature can potentially be applied

with this technique. For example, DNA-mediated crystallization of nanoparticles with two different hydrodynamic radii leads to the formation of highly hexagonal rod microcrystals with AlB_2 crystallographic symmetry.[107] Thus, one would expect to make hexagonal rod crystal if applying the epitaxy technique to such system (Figure 6.5). In terms of optical application, hexagonal microcavities have been found to support whispering gallery modes, a type of photonic modes that have high quality factor.[129] With the techniques developed in Chapter 4 and 5, large number of crystals with different lattice symmetries and shape can be realized, which can lead to a wide range of optical and photonic properties.

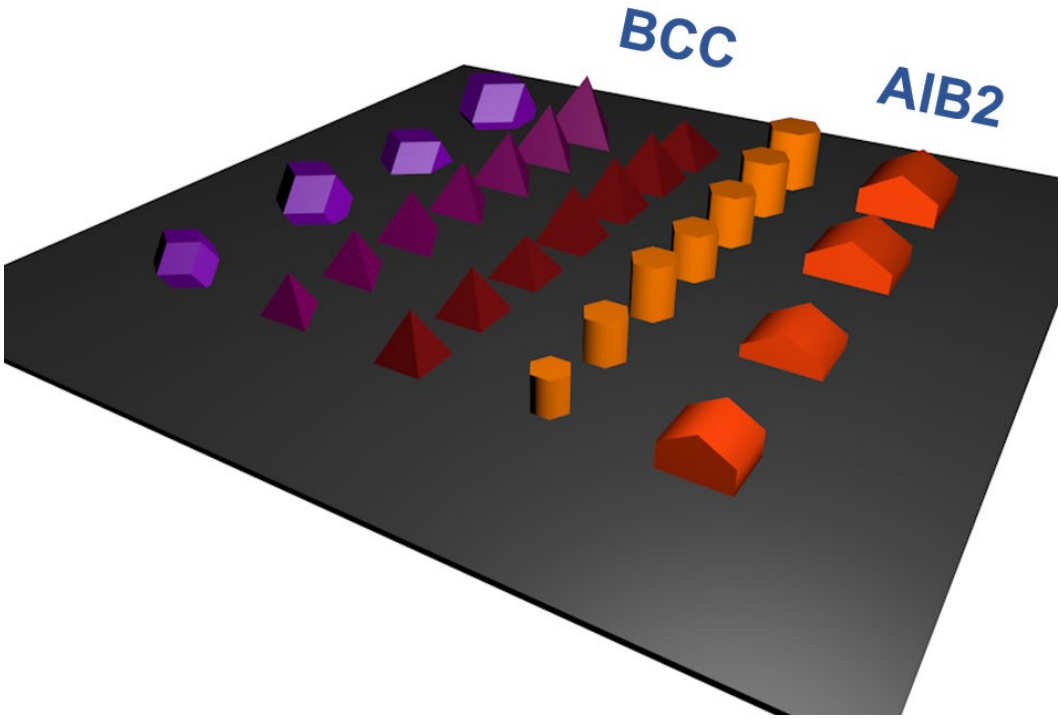

Figure 6.5. A schematic representation of Wulff structure of bcc and AlB*2* epitaxially assembled on substrate. Only bcc and AlB2 cases are shown here, but crystal can be any system that is accessible to the DNA-mediated assembly field.

6.4 Machine-Learning-Driven on-Demand Design of DNA-Assembled Metasurfaces

Chapter 3 provides a glimpse of the potential of the simulation-driven approach. Indeed, simulation has played a significant role for *a priori* prediction and design of optical materials in this thesis. This is enabled by both enormous computing power and the DNA-assembly tool to build designated materials from the bottom up. But doing simulation on more than 500 crystals, more than 40 symmetries, and a large number of NP cores is impractical. The question arises: how do we explore this vast space of different materials and structures efficiently?

The answer might lie in a combined effort of simulation, machine learning (ML) and experimentation. ML, and in particular deep learning, has emerged as a promising tool to aid optical inverse design.[130] Specifically, ML allows both forward mapping and inverse design, where material property prediction and structure design can be simultaneously accomplished. [131] However, the blessing of the versatility of DNA-programmable assembly can also be a curse in the exponentially increasing demand of computing power that scales linearly as the degree of freedom increases (i.e. the "curse of dimensionality"). Thus, choosing the right ML model and an appropriate system and properties to start with should be done with care, and it is reasonable to start with a simpler system without sacrificing the capability to control and tune the structural parameters.

One obvious approach is to reduce the dimensionality of the structure of interests, namely by investigating 2D metasurfaces. DNA-assembled metasurfaces have shown several interesting behavior including stimuli responsiveness, broadband absorption and anomalous reflection.[132] Enabled by the capability to place a range of NPs with different size and shape at designated location and angle, these properties are only a small sample of the potential of this system. ML

techniques such as generative adversarial networks (GAN) can be used to both forward and backward map the structure-function relationship. A few more intuitively straightforward properties, such as broad absorption band, large refractive index, chirality and fano resonance serve as a good starting point.

REFERENCES

1. Schuller, J. A.; Barnard, E. S.; Cai, W.; Jun, Y. C.; White, J. S.; Brongersma, M. L., Plasmonics for extreme light concentration and manipulation. *Nat. Mater.* **2010,** *9* (3), 193-204.
2. Odom, T. W.; Schatz, G. C., Introduction to Plasmonics. *Chem. Rev.* **2011,** *111* (6), 3667-3668.
3. Maier, S. A., *Plasmonics: Fundamentals and Applications*. 1 ed.; Springer: New York, NY, 2007.
4. Tame, M. S.; McEnery, K. R.; Ozdemir, S. K.; Lee, J.; Maier, S. A.; Kim, M. S., Quantum plasmonics. *Nat. Phys.* **2013,** *9* (6), 329-340.
5. Kauranen, M.; Zayats, A. V., Nonlinear plasmonics. *Nat. Photonics* **2012,** *6* (11), 737-748.
6. Stockman, M. I., Nanoplasmonics: past, present, and glimpse into future. *Opt. Express* **2011,** *19* (22), 22029-22106.
7. Zhao, L.; Kelly, K. L.; Schatz, G. C., The Extinction Spectra of Silver Nanoparticle Arrays: Influence of Array Structure on Plasmon Resonance Wavelength and Width. *J. Phys. Chem. B* **2003,** *107* (30), 7343-7350.
8. Ross, M. B.; Mirkin, C. A.; Schatz, G. C., Optical Properties of One-, Two-, and Three-Dimensional Arrays of Plasmonic Nanostructures. *The Journal of Physical Chemistry C* **2016,** *120* (2), 816-830.
9. Haynes, C. L.; McFarland, A. D.; Zhao, L.; Van Duyne, R. P.; Schatz, G. C.; Gunnarsson, L.; Prikulis, J.; Kasemo, B.; Käll, M., Nanoparticle Optics: The Importance of Radiative Dipole Coupling in Two-Dimensional Nanoparticle Arrays. *J. Phys. Chem. B* **2003,** *107* (30), 7337-7342.
10. Tao, A. R.; Ceperley, D. P.; Sinsermsuksakul, P.; Neureuther, A. R.; Yang, P., Self-Organized Silver Nanoparticles for Three-Dimensional Plasmonic Crystals. *Nano Lett.* **2008,** *8* (11), 4033-4038.
11. Fernandez-Dominguez, A. I.; Garcia-Vidal, F. J.; Martin-Moreno, L., Unrelenting plasmons. *Nat Photon* **2017,** *11* (1), 8-10.
12. Halas, N. J.; Lal, S.; Chang, W.-S.; Link, S.; Nordlander, P., Plasmons in strongly coupled metallic nanostructures. *Chemical Reviews* **2011,** *111* (6), 3913-3961.
13. Wang, W.; Ramezani, M.; Väkeväinen, A. I.; Törmä, P.; Rivas, J. G.; Odom, T. W., The rich photonic world of plasmonic nanoparticle arrays. *Materials Today* **2018,** *21* (3), 303-314.
14. Jones, M. R.; Seeman, N. C.; Mirkin, C. A., Nanomaterials. Programmable materials and the nature of the DNA bond. *Science* **2015,** *347* (6224), 1260901.
15. Jones, M. R.; Macfarlane, R. J.; Lee, B.; Zhang, J.; Young, K. L.; Senesi, A. J.; Mirkin, C. A., DNA-nanoparticle superlattices formed from anisotropic building blocks. *Nat. Mater.* **2010,** *9* (11), 913-917.
16. Macfarlane, R. J.; Lee, B.; Jones, M. R.; Harris, N.; Schatz, G. C.; Mirkin, C. A., Nanoparticle Superlattice Engineering with DNA. *Science* **2011,** *334* (6053), 204-208.
17. Auyeung, E.; Li, T. I. N. G.; Senesi, A. J.; Schmucker, A. L.; Pals, B. C.; de la Cruz, M. O.; Mirkin, C. A., DNA-mediated nanoparticle crystallization into Wulff polyhedra. *Nature* **2014,** *505* (7481), 73-77.
18. Kim, Y.; Macfarlane, R. J.; Jones, M. R.; Mirkin, C. A., Transmutable nanoparticles with reconfigurable surface ligands. *Science* **2016,** *351* (6273), 579-582.

19. Senesi, A. J.; Eichelsdoerfer, D. J.; Macfarlane, R. J.; Jones, M. R.; Auyeung, E.; Lee, B.; Mirkin, C. A., Stepwise Evolution of DNA-Programmable Nanoparticle Superlattices. *Angew. Chem. Int. Ed.* **2013,** *52* (26), 6624-6628.
20. Park, D. J.; Zhang, C.; Ku, J. C.; Zhou, Y.; Schatz, G. C.; Mirkin, C. A., Plasmonic photonic crystals realized through DNA-programmable assembly. *Proc. Natl. Acad. Sci. U. S. A.* **2015,** *112* (4), 977-981.
21. Ross, M. B.; Ku, J. C.; Blaber, M. G.; Mirkin, C. A.; Schatz, G. C., Defect tolerance and the effect of structural inhomogeneity in plasmonic DNA-nanoparticle superlattices. *Proceedings of the National Academy of Sciences* **2015,** *112* (33), 10292-10297.
22. Ross, M. B.; Ku, J. C.; Lee, B.; Mirkin, C. A.; Schatz, G. C., Plasmonic Metallurgy Enabled by DNA. *Adv. Mater.* **2016,** *28* (14), 2790-2794.
23. Ross, M. B.; Ku, J. C.; Vaccarezza, V. M.; Schatz, G. C.; Mirkin, C. A., Nanoscale form dictates mesoscale function in plasmonic DNA–nanoparticle superlattices. *Nat. Nanotechnol.* **2015,** *10* (5), 453-458.
24. Ross, M. B.; Blaber, M. G.; Schatz, G. C., Using nanoscale and mesoscale anisotropy to engineer the optical response of three-dimensional plasmonic metamaterials. *Nat. Commun.* **2014,** *5*.
25. Maier, S. A.; Brongersma, M. L.; Kik, P. G.; Meltzer, S.; Requicha, A. A. G.; Atwater, H. A., Plasmonics—A Route to Nanoscale Optical Devices. *Adv. Mater.* **2001,** *13* (19), 1501-1505.
26. Chang, A. S. P.; Kim, Y. S.; Chen, M.; Yang, Z.-P.; Bur, J. A.; Lin, S.-Y.; Ho, K.-M., Visible three-dimensional metallic photonic crystal with non-localized propagating modes beyond waveguide cutoff. *Opt. Express* **2007,** *15* (13), 8428-8437.
27. Luk'yanchuk, B.; Zheludev, N. I.; Maier, S. A.; Halas, N. J.; Nordlander, P.; Giessen, H.; Chong, C. T., The Fano resonance in plasmonic nanostructures and metamaterials. *Nat. Mater.* **2010,** *9* (9), 707-715.
28. Shalaev, V. M.; Cai, W.; Chettiar, U. K.; Yuan, H.-K.; Sarychev, A. K.; Drachev, V. P.; Kildishev, A. V., Negative index of refraction in optical metamaterials. *Opt. Lett.* **2005,** *30* (24), 3356-3358.
29. Rozin, M. J.; Rosen, D. A.; Dill, T. J.; Tao, A. R., Colloidal metasurfaces displaying near-ideal and tunable light absorbance in the infrared. *Nat. Commun.* **2015,** *6*, 7325.
30. Gwo, S.; Chen, H.-Y.; Lin, M.-H.; Sun, L.; Li, X., Nanomanipulation and controlled self-assembly of metal nanoparticles and nanocrystals for plasmonics. *Chem. Soc. Rev.* **2016,** *45* (20), 5672-5716.
31. Tao, A.; Sinsermsuksakul, P.; Yang, P., Tunable plasmonic lattices of silver nanocrystals. *Nat. Nanotechnol.* **2007,** *2* (7), 435-440.
32. Shevchenko, E. V.; Talapin, D. V.; Murray, C. B.; O'Brien, S., Structural Characterization of Self-Assembled Multifunctional Binary Nanoparticle Superlattices. *J. Am. Chem. Soc.* **2006,** *128* (11), 3620-3637.
33. Srivastava, S.; Nykypanchuk, D.; Fukuto, M.; Halverson, J. D.; Tkachenko, A. V.; Yager, K. G.; Gang, O., Two-Dimensional DNA-Programmable Assembly of Nanoparticles at Liquid Interfaces. *J. Am. Chem. Soc.* **2014,** *136* (23), 8323-8332.
34. Zhang, Y.; Lu, F.; Yager, K. G.; van der Lelie, D.; Gang, O., A general strategy for the DNA-mediated self-assembly of functional nanoparticles into heterogeneous systems. *Nat. Nanotechnol.* **2013,** *8* (11), 865-872.

35. Zhang, C.; Macfarlane, R. J.; Young, K. L.; Choi, C. H. J.; Hao, L.; Auyeung, E.; Liu, G.; Zhou, X.; Mirkin, C. A., A general approach to DNA-programmable atom equivalents. *Nat. Mater.* **2013,** *12* (8), 741-746.
36. Ku, J. C.; Ross, M. B.; Schatz, G. C.; Mirkin, C. A., Conformal, Macroscopic Crystalline Nanoparticle Sheets Assembled with DNA. *Adv. Mater.* **2015,** *27* (20), 3159-3163.
37. Fowles, G. R., *Introduction to Modern Optics*. Second ed.; Holt, Rinehart and Winston: New York, 1975.
38. Huang, C.-p.; Yin, X.-g.; Wang, Q.-j.; Huang, H.; Zhu, Y.-y., Long-Wavelength Optical Properties of a Plasmonic Crystal. *Phys. Rev. Lett.* **2010,** *104* (1), 016402.
39. O'Brien, M. N.; Girard, M.; Lin, H.-X.; Millan, J. A.; Olvera de la Cruz, M.; Lee, B.; Mirkin, C. A., Exploring the zone of anisotropy and broken symmetries in DNA-mediated nanoparticle crystallization. *Proc. Natl. Acad. Sci. U. S. A.* **2016,** *113* (38), 10485-10490.
40. O'Brien, M. N.; Lin, H.-X.; Girard, M.; Olvera de la Cruz, M.; Mirkin, C. A., Programming Colloidal Crystal Habit with Anisotropic Nanoparticle Building Blocks and DNA Bonds. *Journal of the American Chemical Society* **2016,** *138* (44), 14562-14565.
41. Senesi, A. J.; Eichelsdoerfer, D. J.; Brown, K. A.; Lee, B.; Auyeung, E.; Choi, C. H. J.; Macfarlane, R. J.; Young, K. L.; Mirkin, C. A., Oligonucleotide flexibility dictates crystal quality in DNA-programmable nanoparticle superlattices. *Adv. Mater.* **2014,** *26* (42), 7235-7240.
42. Macfarlane, R. J.; Jones, M. R.; Senesi, A. J.; Young, K. L.; Lee, B.; Wu, J.; Mirkin, C. A., Establishing the Design Rules for DNA-Mediated Programmable Colloidal Crystallization. *Angew. Chem. Int. Ed.* **2010,** *49* (27), 4589-4592.
43. Auyeung, E.; Macfarlane, R. J.; Choi, C. H.; Cutler, J. I.; Mirkin, C. A., Transitioning DNA-Engineered Nanoparticle Superlattices from Solution to the Solid State. *Adv. Mater.* **2012**.
44. Prodan, E.; Radloff, C.; Halas, N. J.; Nordlander, P., A Hybridization Model for the Plasmon Response of Complex Nanostructures. *Science* **2003,** *302* (5644), 419-422.
45. Shuford, K. L.; Meyer, K. A.; Li, C.; Cho, S. O.; Whitten, W. B.; Shaw, R. W., Computational and Experimental Evaluation of Nanoparticle Coupling. *The Journal of Physical Chemistry A* **2009,** *113* (16), 4009-4014.
46. Gunnarsson, L.; Rindzevicius, T.; Prikulis, J.; Kasemo, B.; Käll, M.; Zou, S.; Schatz, G. C., Confined Plasmons in Nanofabricated Single Silver Particle Pairs: Experimental Observations of Strong Interparticle Interactions. *J. Phys. Chem. B* **2005,** *109* (3), 1079-1087.
47. Auguié, B.; Barnes, W. L., Collective Resonances in Gold Nanoparticle Arrays. *Phys. Rev. Lett.* **2008,** *101* (14), 143902.
48. Kelly, K. L.; Coronado, E.; Zhao, L. L.; Schatz, G. C., The Optical Properties of Metal Nanoparticles: The Influence of Size, Shape, and Dielectric Environment. *J. Phys. Chem. B* **2003,** *107* (3), 668-677.
49. O'Brien, M. N.; Jones, M. R.; Brown, K. A.; Mirkin, C. A., Universal Noble Metal Nanoparticle Seeds Realized Through Iterative Reductive Growth and Oxidative Dissolution Reactions. *J. Am. Chem. Soc.* **2014,** *136* (21), 7603-7606.
50. Auyeung, E.; Macfarlane, R. J.; Choi, C. H. J.; Cutler, J. I.; Mirkin, C. A., Transitioning DNA-engineered nanoparticle superlattices from solution to the solid state. *Advanced Materials* **2012,** *24* (38), 5181-5186.
51. Johnson, P. B.; Christy, R. W., Optical Constants of the Noble Metals. *Phys. Rev. B* **1972,** *6* (12), 4370-4379.

52. Malitson, I. H., Interspecimen Comparison of the Refractive Index of Fused Silica*,†. *J. Opt. Soc. Am.* **1965,** *55* (10), 1205-1209.
53. Joannopoulos, J. D.; Johnson, S. G.; Winn, J. N.; Meade, R. D., Photonic Crystals: Molding the Flow of Light. 2nd Edition ed.; Princeton Univ. Press: 2008.
54. Norris, D. J., Photonic crystals: a view of the future. *Nat. Mater.* **2007,** *6* (3), 177-178.
55. Maldovan, M.; Thomas, E. L., Diamond-structured photonic crystals. *Nat. Mater.* **2004,** *3* (9), 593-600.
56. Huang, M. C. Y.; Zhou, Y.; Chang-Hasnain, C. J., A surface-emitting laser incorporating a high-index-contrast subwavelength grating. *Nat. Photonics* **2007,** *1* (2), 119-122.
57. Yablonovitch, E.; Gmitter, T. J.; Leung, K. M., Photonic band structure: the face-centered-cubic case employing nonspherical atoms. *Phys. Rev. Lett.* **1991,** *67* (17), 2295-2298.
58. Miyake, M.; Chen, Y.-C.; Braun, P. V.; Wiltzius, P., Fabrication of three-dimensional photonic crystals using multibeam interference lithography and electrodeposition. *Adv. Mater.* **2009,** *21* (29), 3012-3015.
59. Hermatschweiler, M.; Ledermann, A.; Ozin, G. A.; Wegener, M.; von Freymann, G., Fabrication of silicon inverse woodpile photonic crystals. *Adv. Funct. Mater.* **2007,** *17* (14), 2273-2277.
60. Vlasov, Y. A.; Bo, X.-Z.; Sturm, J. C.; Norris, D. J., On-chip natural assembly of silicon photonic bandgap crystals. *Nature* **2001,** *414* (6861), 289-293.
61. von Freymann, G.; Kitaev, V.; Lotsch, B. V.; Ozin, G. A., Bottom-up assembly of photonic crystals. *Chem. Soc. Rev.* **2013,** *42* (7), 2528-2554.
62. García-Santamaría, F.; Salgueiriño-Maceira, V.; López, C.; Liz-Marzán, L. M., Synthetic opals based on silica-coated gold nanoparticles. *Langmuir* **2002,** *18* (11), 4519-4522.
63. Jang, S. J.; Song, Y. M.; Yeo, C. I.; Park, C. Y.; Lee, Y. T., Highly tolerant a-Si distributed Bragg reflector fabricated by oblique angle deposition. *Opt. Mater. Express* **2011,** *1* (3), 451-457.
64. Armstrong, E.; O'Dwyer, C., Artificial opal photonic crystals and inverse opal structures - fundamentals and applications from optics to energy storage. *J. Mater. Chem. C* **2015,** *3* (24), 6109-6143.
65. Waterhouse, G. I. N.; Waterland, M. R., Opal and inverse opal photonic crystals: fabrication and characterization. *Polyhedron* **2007,** *26* (2), 356-368.
66. Liu, Y.-S.; Wang, S.; Xie, H.; Kao, T.-T.; Mehta, K.; Jia, X. J.; Shen, S.-C.; Yoder, P. D.; Ponce, F. A.; Detchprohm, T.; Dupuis, R. D., Strain management of AlGaN-based distributed Bragg reflectors with GaN interlayer grown by metalorganic chemical vapor deposition. *Appl. Phys. Lett.* **2016,** *109* (8), 081103.
67. Oh, J. R.; Moon, J. H.; Yoon, S.; Park, C. R.; Do, Y. R., Fabrication of wafer-scale polystyrene photonic crystal multilayers via the layer-by-layer scooping transfer technique. *J. Mater. Chem.* **2011,** *21* (37), 14167-14172.
68. Boles, M. A.; Engel, M.; Talapin, D. V., Self-assembly of colloidal nanocrystals: from intricate structures to functional materials. *Chem. Rev.* **2016,** *116* (18), 11220-11289.
69. Mirkin, C. A.; Letsinger, R. L.; Mucic, R. C.; Storhoff, J. J., A DNA-based method for rationally assembling nanoparticles into macroscopic materials. *Nature* **1996,** *382* (6592), 607-609.
70. Liz-Marzán, L. M., Tailoring Surface Plasmons through the Morphology and Assembly of Metal Nanoparticles. *Langmuir* **2006,** *22* (1), 32-41.

71. Kubo, S.; Diaz, A.; Tang, Y.; Mayer, T. S.; Khoo, I. C.; Mallouk, T. E., Tunability of the refractive index of gold nanoparticle dispersions. *Nano Lett.* **2007,** *7* (11), 3418-3423.
72. Henzie, J.; Grünwald, M.; Widmer-Cooper, A.; Geissler, P. L.; Yang, P., Self-assembly of uniform polyhedral silver nanocrystals into densest packings and exotic superlattices. *Nat. Mater.* **2012,** *11* (2), 131-137.
73. Shevchenko, E. V.; Talapin, D. V.; Kotov, N. A.; O'Brien, S.; Murray, C. B., Structural diversity in binary nanoparticle superlattices. *Nature* **2006,** *439* (7072), 55-59.
74. Karg, M.; Hellweg, T.; Mulvaney, P., Self-assembly of tunable nanocrystal superlattices using poly-(NIPAM) spacers. *Adv. Funct. Mater.* **2011,** *21* (24), 4668-4676.
75. Smith, D. R.; Vier, D. C.; Koschny, T.; Soukoulis, C. M., Electromagnetic parameter retrieval from inhomogeneous metamaterials. *Phys. Rev. E* **2005,** *71* (3), 036617.
76. Munechika, K.; Chen, Y.; Ginger, D. S., Bioenabled nanophotonics. *MRS Bulletin* **2008,** *33* (5), 536-542.
77. Mason, J. A.; Laramy, C. R.; Lai, C.-T.; O'Brien, M. N.; Lin, Q.-Y.; Dravid, V. P.; Schatz, G. C.; Mirkin, C. A., Contraction and expansion of stimuli-responsive DNA bonds in flexible colloidal crystals. *J. Am. Chem. Soc.* **2016,** *138* (28), 8722-8725.
78. Sigalas, M. M.; Chan, C. T.; Ho, K. M.; Soukoulis, C. M., Metallic photonic band-gap materials. *Phys. Rev. B* **1995,** *52* (16), 11744-11751.
79. Ruben, E.; Javier, A.; Garnett, W. B., Strong coupling of single emitters interacting with phononic infrared antennae. *New J. Phys.* **2014,** *16* (1), 013052.
80. Park, D. J.; Ku, J. C.; Sun, L.; Lethiec, C. M.; Stern, N. P.; Schatz, G. C.; Mirkin, C. A., Directional emission from dye-functionalized plasmonic DNA superlattice microcavities. *Proc. Natl. Acad. Sci. U. S. A.* **2017,** *114* (3), 457-461.
81. Engheta, N., Circuits with light at nanoscales: optical nanocircuits inspired by metamaterials. *Science* **2007,** *317* (5845), 1698-1702.
82. Xiao, S.; Drachev, V. P.; Kildishev, A. V.; Ni, X.; Chettiar, U. K.; Yuan, H.-K.; Shalaev, V. M., Loss-free and active optical negative-index metamaterials. *Nature* **2010,** *466* (7307), 735-738.
83. Shiles, E.; Sasaki, T.; Inokuti, M.; Smith, D. Y., Self-consistency and sum-rule tests in the Kramers-Kronig analysis of optical data: Applications to aluminum. *Phys. Rev. B* **1980,** *22* (4), 1612-1628.
84. Hagemann, H. J.; Gudat, W.; Kunz, C., Optical constants from the far infrared to the x-ray region: Mg, Al, Cu, Ag, Au, Bi, C, and Al_2O_3. *J. Opt. Soc. Am.* **1975,** *65* (6), 742-744.
85. O'Brien, M. N.; Jones, M. R.; Brown, K. A.; Mirkin, C. A., Universal noble metal nanoparticle seeds realized through iterative reductive growth and xxidative dissolution reactions. *J. Am. Chem. Soc.* **2014,** *136* (21), 7603-7606.
86. Jones, M. R.; Macfarlane, R. J.; Lee, B.; Zhang, J.; Young, K. L.; Senesi, A. J.; Mirkin, C. A., DNA-nanoparticle superlattices formed from anisotropic building blocks. *Nat. Mater.* **2010,** *9* (11), 913-917.
87. O'Brien, M. N.; Lin, H. X.; Girard, M.; de la Cruz, M. O.; Mirkin, C. A., Programming Colloidal Crystal Habit with Anisotropic Nanoparticle Building Blocks and DNA Bonds. *J. Am. Chem. Soc.* **2016,** *138* (44), 14562-14565.
88. Hurst, S. J.; Lytton-Jean, A. K. R.; Mirkin, C. A., Maximizing DNA loading on a range of gold nanoparticle sizes. *Analytical Chemistry* **2006,** *78* (24), 8313-8318.

89. Butté, R.; Carlin, J. F.; Feltin, E.; Gonschorek, M.; Nicolay, S.; Christmann, G.; Simeonov, D.; Castiglia, A.; Dorsaz, J.; Buehlmann, H. J.; Christopoulos, S.; Högersthal, G. B. H. v.; Grundy, A. J. D.; Mosca, M.; Pinquier, C.; Py, M. A.; Demangeot, F.; Frandon, J.; Lagoudakis, P. G.; Baumberg, J. J.; Grandjean, N., Current status of AlInN layers lattice-matched to GaN for photonics and electronics. *J. Phys. D.* **2007,** *40* (20), 6328.
90. Osting, B., Bragg structure and the first spectral gap. *Appl. Math. Lett.* **2012,** *25* (11), 1926-1930.
91. Ho, K. M.; Chan, C. T.; Soukoulis, C. M., Existence of a photonic gap in periodic dielectric structures. *Phys. Rev. Lett.* **1990,** *65* (25), 3152-3155.
92. Sun, L.; Lin, H.; Kohlstedt, K. L.; Schatz, G. C.; Mirkin, C. A., Design principles for photonic crystals based on plasmonic nanoparticle superlattices. *Proc. Natl. Acad. Sci. U.S.A.* **2018**.
93. Sun, L.; Lin, H.; Park, D. J.; Bourgeois, M. R.; Ross, M. B.; Ku, J. C.; Schatz, G. C.; Mirkin, C. A., Polarization-Dependent Optical Response in Anisotropic Nanoparticle-DNA Superlattices. *Nano Lett* **2017,** *17* (4), 2313-2318.
94. Wu, Y. X.; Zhang, K.; Yang, B., Ordered Hybrid Micro/Nanostructures and Their Optical Applications. *Adv Opt Mater* **2019,** *7* (7).
95. Kagan, C. R., Flexible colloidal nanocrystal electronics. *Chem Soc Rev* **2019,** *48* (6), 1626-1641.
96. Bauer, J.; Meza, L. R.; Schaedler, T. A.; Schwaiger, R.; Zheng, X. Y.; Valdevit, L., Nanolattices: An Emerging Class of Mechanical Metamaterials. *Adv Mater* **2017,** *29* (40).
97. Lee, J. H.; Singer, J. P.; Thomas, E. L., Micro-/Nanostructured Mechanical Metamaterials. *Adv Mater* **2012,** *24* (36), 4782-4810.
98. Inan, H.; Poyraz, M.; Inci, F.; Lifson, M. A.; Baday, M.; Cunningham, B. T.; Demirci, U., Photonic crystals: emerging biosensors and their promise for point-of-care applications. *Chem Soc Rev* **2017,** *46* (2), 366-388.
99. Rabani, E.; Reichman, D. R.; Geissler, P. L.; Brus, L. E., Drying-mediated self-assembly of nanoparticles. *Nature* **2003,** *426* (6964), 271-274.
100. Henzie, J.; Grunwald, M.; Widmer-Cooper, A.; Geissler, P. L.; Yang, P. D., Self-assembly of uniform polyhedral silver nanocrystals into densest packings and exotic superlattices. *Nat Mater* **2012,** *11* (2), 131-137.
101. Klajn, R.; Bishop, K. J. M.; Grzybowski, B. A., Light-controlled self-assembly of reversible and irreversible nanoparticle suprastructures. *P Natl Acad Sci USA* **2007,** *104* (25), 10305-10309.
102. Kalsin, A. M.; Fialkowski, M.; Paszewski, M.; Smoukov, S. K.; Bishop, K. J. M.; Grzybowski, B. A., Electrostatic self-assembly of binary nanoparticle crystals with a diamond-like lattice. *Science* **2006,** *312* (5772), 420-424.
103. Singh, G.; Chan, H.; Baskin, A.; Gelman, E.; Repnin, N.; Kral, P.; Klajn, R., Self-assembly of magnetite nanocubes into helical superstructures. *Science* **2014,** *345* (6201), 1149-1153.
104. Laramy, C. R.; O'Brien, M. N.; Mirkin, C. A., Crystal engineering with DNA. *Nature Reviews Materials* **2019,** *4* (3), 201-224.

105. Auyeung, E.; Li, T. I.; Senesi, A. J.; Schmucker, A. L.; Pals, B. C.; de la Cruz, M. O.; Mirkin, C. A., DNA-mediated nanoparticle crystallization into Wulff polyhedra. *Nature* **2014,** *505* (7481), 73-7.
106. O'Brien, M. N.; Lin, H. X.; Girard, M.; Olvera de la Cruz, M.; Mirkin, C. A., Programming Colloidal Crystal Habit with Anisotropic Nanoparticle Building Blocks and DNA Bonds. *J Am Chem Soc* **2016,** *138* (44), 14562-14565.
107. Seo, S. E.; Girard, M.; Olvera de la Cruz, M.; Mirkin, C. A., Non-equilibrium anisotropic colloidal single crystal growth with DNA. *Nature Communications* **2018,** *9* (1), 4558.
108. Sun, L.; Lin, H.; Kohlstedt, K. L.; Schatz, G. C.; Mirkin, C. A., Design principles for photonic crystals based on plasmonic nanoparticle superlattices. *Proc Natl Acad Sci U S A* **2018,** *115* (28), 7242-7247.
109. Park, D. J.; Ku, J. C.; Sun, L.; Lethiec, C. M.; Stern, N. P.; Schatz, G. C.; Mirkin, C. A., Directional emission from dye-functionalized plasmonic DNA superlattice microcavities. *P Natl Acad Sci USA* **2017,** *114* (3), 457-461.
110. Joannopoulos, J. D.; Villeneuve, P. R.; Fan, S. H., Photonic crystals: Putting a new twist on light. *Nature* **1997,** *386* (6621), 143-149.
111. Arsenault, A.; Fournier-Bidoz, S.; Hatton, B.; Míguez, H.; Tétreault, N.; Vekris, E.; Wong, S.; Ming Yang, S.; Kitaev, V.; Ozin, G. A., Towards the synthetic all-optical computer: science fiction or reality? *Journal of Materials Chemistry* **2004,** *14* (5), 781-794.
112. Wang, M. X.; Seo, S. E.; Gabrys, P. A.; Fleischman, D.; Lee, B.; Kim, Y.; Atwater, H. A.; Macfarlane, R. J.; Mirkin, C. A., Epitaxy: Programmable Atom Equivalents Versus Atoms. *ACS Nano* **2017,** *11* (1), 180-185.
113. Ozin, G. A.; Yang, S. M., The Race for the Photonic Chip: Colloidal Crystal Assembly in Silicon Wafers. **2001,** *11* (2), 95-104.
114. Gabrys, P. A.; Macfarlane, R. J., Controlling Crystal Texture in Programmable Atom Equivalent Thin Films. *ACS Nano* **2019,** *13* (7), 8452-8460.
115. Markov, I. V., *Crystal Growth for Beginners*.
116. Oh, M. H.; Cho, M. G.; Chung, D. Y.; Park, I.; Kwon, Y. P.; Ophus, C.; Kim, D.; Kim, M. G.; Jeong, B.; Gu, X. W.; Jo, J.; Yoo, J. M.; Hong, J.; McMains, S.; Kang, K.; Sung, Y. E.; Alivisatos, A. P.; Hyeon, T., Design and synthesis of multigrain nanocrystals via geometric misfit strain. *Nature* **2020,** *577* (7790), 359-363.
117. Lei, Y.; Chen, Y.; Gu, Y.; Wang, C.; Huang, Z.; Qian, H.; Nie, J.; Hollett, G.; Choi, W.; Yu, Y.; Kim, N.; Wang, C.; Zhang, T.; Hu, H.; Zhang, Y.; Li, X.; Li, Y.; Shi, W.; Liu, Z.; Sailor, M. J.; Dong, L.; Lo, Y.-H.; Luo, J.; Xu, S., Controlled Homoepitaxial Growth of Hybrid Perovskites. **2018,** *30* (20), 1705992.
118. Dong, Q.; Fang, Y.; Shao, Y.; Mulligan, P.; Qiu, J.; Cao, L.; Huang, J., Electron-hole diffusion lengths > 175 μm in solution-grown CH3NH3PbI3 single crystals. *Science* **2015,** *347* (6225), 967-970.
119. Auyeung, E.; Li, T.; Senesi, A. J.; Schmucker, A. L.; Pals, B. C.; de la Cruz, M. O.; Mirkin, C. A., DNA-mediated nanoparticle crystallization into Wulff polyhedra. *Nature* **2014,** *505* (7481), 73-77.
120. Lewis, D. J.; Zornberg, L. Z.; Carter, D. J. D.; Macfarlane, R. J., Single-crystal Winterbottom constructions of nanoparticle superlattices. *Nature Materials* **2020**.

121. Seo, S. E.; Girard, M.; de la Cruz, M. O.; Mirkin, C. A., The Importance of Salt-Enhanced Electrostatic Repulsion in Colloidal Crystal Engineering with DNA. *ACS Central Science* **2019,** *5* (1), 186-191.
122. Tan, C.; Chen, J.; Wu, X.-J.; Zhang, H., Epitaxial growth of hybrid nanostructures. *Nature Reviews Materials* **2018,** *3* (2), 17089.
123. Lee, D.; Noh, T. W., Giant flexoelectric effect through interfacial strain relaxation. **2012,** *370* (1977), 4944-4957.
124. Zhang, C.; Macfarlane, R. J.; Young, K. L.; Choi, C. H. J.; Hao, L.; Auyeung, E.; Liu, G.; Zhou, X.; Mirkin, C. A., A general approach to DNA-programmable atom equivalents. *Nature Materials* **2013,** *12* (8), 741-746.
125. Tan, S. J.; Campolongo, M. J.; Luo, D.; Cheng, W., Building plasmonic nanostructures with DNA. *Nature Nanotechnology* **2011,** *6* (5), 268-276.
126. Girard, M.; Wang, S.; Du, J. S.; Das, A.; Huang, Z.; Dravid, V. P.; Lee, B.; Mirkin, C. A.; Olvera de la Cruz, M., Particle analogs of electrons in colloidal crystals. *Science* **2019,** *364* (6446), 1174-1178.
127. Lin, H.; Lee, S.; Sun, L.; Spellings, M.; Engel, M.; Glotzer, S. C.; Mirkin, C. A., Clathrate colloidal crystals. **2017,** *355* (6328), 931-935.
128. Lin, H., Engineering Optical Axis in Low Symmetry Colloidal Crystals. *in preparation* **2020**.
129. Kudo, H.; Suzuki, R.; Tanabe, T., Whispering gallery modes in hexagonal microcavities. *Physical Review A* **2013,** *88* (2), 023807.
130. Hegde, R. S., Deep learning: a new tool for photonic nanostructure design. *Nanoscale Advances* **2020,** *2* (3), 1007-1023.
131. Yao, K.; Unni, R.; Zheng, Y., Intelligent nanophotonics: merging photonics and artificial intelligence at the nanoscale. **2019,** *8* (3), 339.
132. Lin, Q.-Y.; Mason, J. A.; Li, Z.; Zhou, W.; O'Brien, M. N.; Brown, K. A.; Jones, M. R.; Butun, S.; Lee, B.; Dravid, V. P.; Aydin, K.; Mirkin, C. A., Building superlattices from individual nanoparticles via template-confined DNA-mediated assembly. **2018,** *359* (6376), 669-672.

Lin Sun

810 Sherman Ave. Apt. 2, Evanston, IL 60202 • 847-644-5015 •
lsun@u.northwestern.edu

EDUCATION

Northwestern University, Evanston, IL — June 2020
Ph.D. in Materials Science and Engineering

National University of Singapore (NUS), Singapore — December 2012
B. S. in Engineering Science Program, minors in Math and Physics

RESEARCH EXPERIENCE

Research Assistant, Northwestern University, Evanston, IL — 2014 - present
Advisor: Professor Chad A. Mirkin
"Towards Building Optical Microdevices with DNA-Mediated Assembly: Simulation, Synthesis and Characterization"

- Establish structure-property relationship and design optical functional materials with Finite-Difference Time-Domain simulation and machine learning methods
- Combine top-down nanofabrication with bottom-up DNA-assembled three-dimensional colloidal crystal to build next-generation optical devices
- Lead four research projects, co-authored seven peer-reviewed papers, managing three optical instruments and group server, participated in writing several grant proposals and presented at three conferences
- Mentor two graduate students, assisted teaching in two materials science courses

Research Assistant, NUS Nanoscience and Nanotechnology Institute, Singapore — 2013 - 2014
Advisor: Prof. Ariando
"Investigation of two-dimensional electron gas (2DEG) at the interface of complex transitionmetal oxides for future generation electronic devices"

- Investigated electronic properties of $La_xSr_{1-x}TiO_3/SrTiO_3$ heterostructure and systematically probed the effect of La doping concentration, strain and oxygen vacancy
- Led one research project, co-authored five peer-reviewed papers and presented at two conferences

Summer Undergraduate Research Fellow, California Institute of Technology — May - Aug 2010
Advisor: Professor Julia R. Greer
"Probing the strengthening mechanism in nano-size Copper structure for design of strong yet ultra-light material"

- Measured the mechanical properties of Copper nanopillar down to 50 nm with nanoindentation

PATENTS

Photonic Crystals Comprising Nanoparticles and Spacer Groups, Publication Number WO/2019/152594 — 2019
Wulff-Construct Nanoparticle Crystal Assembly through Epitaxy, filled for Invenstion Disclosure at Northwestern — 2020

PUBLICATIONS

L. Sun†, H. Lin†, Y. Li, W. Zhou, J. Du, C. A. Mirkin, "Wulff-Shaped Superlattice Array with Controlled Orientation and Position Assembled on Substrate", *In preparation*

J. Du†, D. Shin†, T. Stanev, C. Musumeci, Z. Xie, Z. Huang, M. Lai, **L. Sun**, W. Zhou, N. P. Stern, V. P. Dravid, C. A. Mirkin, "Halide Perovskite Nanocrystal Arrays: Multiplexed Synthesis and Size-dependent Emission", *submitted*

D. Liu, Z. Zhou, X. Wang, H. Deng, **L. Sun**, H. Lin, F. Kang, Y. Zhang, Z. Wang, W. Yang, L. Rao, K. Yang, G. Yu, J.Du, Z. Shen, X. Chen, "Yolk-shell nanovesicles endow glutathione-responsive concurrent drug release and T1 MRI activation for cancer theranostics", *Biomaterials* **224**, 119979, (2020)

C. Zheng†, E. Palacios†, W. Zhou†, W. Hadibrata, **L. Sun**, Z. Huang, G. C. Schatz, K. Aydin, C. A. Mirkin, "Tunable Fluorescence from Dye-Modified DNA-Assembled Plasmonic Nanocube Arrays", *Adv. Mater.* **31**, 41, (2019)

L. Sun, H. Lin, G. C. Schatz, C. A. Mirkin, "Design Principles for Nanoparticle Based Photonic Crystals", *Active Photonic Platforms X, SPIE Optics + Photonics 2018 Conference Proceedings* **10721**, 7, (2018)

L. Sun, H. Lin, K. L. Kohlstedt, G. C. Schatz, C. A. Mirkin, "Design principles for photonic crystals based upon plasmonic nanoparticle superlattices", *Proc. Natl. Acad. Sci. U.S.A.* **115**, 28, (2018)

L. Sun, H. Lin, D. J. Park, M. R. Bourgeois, M. B. Ross, J. C. Ku, G. C. Schatz, C. A. Mirkin, "Polarization-dependent optical response in anisotropic nanoparticle - DNA superlattices", *Nano Letters* **17**, 4, (2017)

D. J. Park†, J. C. Ku†, **L. Sun**, C. M. Lethiec, N. Stern, G. C. Schatz, C. A. Mirkin, "Directional emission from dye-functionalized plasmonic DNA superlattice microcavities", *Proc. Natl. Acad. Sci. U.S.A.* **114**, 3, (2017)

H. Lin†, S. Lee†, **L. Sun**, M. Spellings, M. Engel, S. C. Glotzer, C. A. Mirkin, "Clathrate colloidal crystals", *Science* **355**, 6328, (2017)

Z. Xie†, P. Gordiichuk†, Q. Lin, B. Meckes, P. Chen, **L. Sun**, J. S. Du, J. Zhu, Y. Liu, V. P. Dravid, C. A. Mirkin, "Solution-Phase Photochemical Nanopatterning Enabled by High-Refractive-Index Beam Pen Arrays", *ACS Nano* **11**, 8, (2017)

X. Wang†, **L. Sun**†, Z. Huang, W.M. Lu, M.R. Motapothula, A. Annadi, Z.Q. Liu, S.W. Zeng, T. Venkatesan, Ariando, "Parallel charge sheets of electron liquid and gas in $La_{0.5}Sr_{0.5}TiO_3$ heterostructures", *Scientific Reports* **5**, 18282, (2015)

C. J. Li, W. M. Lü, X. R. Wang, X. P. Qiu, **L. Sun**, S. W. Zeng, Z. Q. Liu, Z. Huang, Y. L. Zhao, Ariando, T. Venkatesan, "Nature of electron scattering in LaAlO3/SrTiO3 interfaces near the critical thickness", *Adv. Matter. Interfaces* **2**, 1400437 (2015) - Featured on the cover

Z. Huang, Z.Q. Liu, M. Yang, S.W. Zeng, A. Annadi, W.M. Lu, X.L. Tan, P.F. Chen, **L. Sun**, X. Renshaw Wang, Y.L. Zhao, C.J. Li, J. Zhou, K. Han, W.B. Wu, Y.P. Feng, J.M.D. Coey, T. Venkatesan, Ariando, "Biaxial Strain Induced Transport Property Changes in Different Atomically Tailored SrTiO3-based Systems", *Phys. Rev. B* **90**, 125156 (2014)

Z. Q. Liu, W. Lu, S. W. Zeng, J. W. Deng, Z. Huang, C. J. Li, M. Motapothula, W. M. Lü, **L. Sun**, K. Han, J. Q. Zhong, P. Yang, N. N. Bao,W. Chen, J. S. Chen, Y.P. Feng, J. M. D. Coey, T. Venkatesan, Ariando, "Bandgap control of the oxygen-vacancy-induced two-dimensional electron gas in SrTiO3", *Adv. Mater. Interfaces* **1**, 1400155 (2014) - Featured on the cover

Z. Q. Liu, **L. Sun**, Z. Huang, C. J. Li, S. W. Zeng, K. Han, W. M. Lü, T Venkatesan, and Ariando, "Dominant role of oxygen vacancies in electrical properties of unannealed LaAlO3/SrTiO3 interfaces", *J. Appl. Phys.* **115**, 054303 (2014)

Note: † equal contribution

POSTER PRESENTATIONS

L. Sun, H. Lin, K. L. Kohlstedt, G. C. Schatz, C. A. Mirkin, "Design Principles for Photonic Crystals Based Upon Metallic Nanoparticle Superlattices", *Argonne National Labroratory Center for Nanoscale Materials 10th Anniversary Symposium*, Lemont, IL 2017

L. Sun, H. Lin, D. J. Park, M. R. Bourgeois, M. B. Ross, J. C. Ku, G. C. Schatz, C. A. Mirkin, "Polarization-Dependent Optical Response in Anisotropic Nanoparticle-DNA Superlattices", *2016 Materials Research Society Fall Meeting & Exhibit*, Boston, MA 2016

L. Sun, X. Wang, Z. Huang, W.M. Lu, M.R. Motapothula, A. Annadi, Z.Q. Liu, S.W. Zeng, T. Venkatesan, Ariando, "Coexistence of Two Types of Carrier in $La_xSr_{1-x}TiO_3/SrTiO_3$ Heterostructure", *20th Workshop on Oxide Electronics*, Singapore 2013

L. Sun, X. Wang, Z. Huang, W.M. Lu, M.R. Motapothula, A. Annadi, Z.Q. Liu, S.W. Zeng, T. Venkatesan, Ariando, "Coexistence of Two Types of Carrier in $La_xSr_{1-x}TiO_3/SrTiO_3$ Heterostructure", *7th International Conference on Materials for Advanced Technologies,* Singapore (Best Poster Award winner) 2013

ORAL PRESENTATION

L. Sun, H. Lin, G. C. Schatz, C. A. Mirkin, "Design Principles for Nanoparticle Based Photonic Crystals", *SPIE Optics + Photonics 2018*, San Diego, CA 2018